A NOVEL MUON SPECTROMETER USING MULTI-LAYER PRESSURIZED GAS CHERENKOV RADIATORS FOR MUON TOMOGRAPHY

by

Junghyun Bae

A Dissertation

Submitted to the Faculty of Purdue University

In Partial Fulfillment of the Requirements for the degree of

Doctor of Philosophy

School of Nuclear Engineering

West Lafayette, Indiana

May 2022

THE PURDUE UNIVERSITY GRADUATE SCHOOL
STATEMENT OF COMMITTEE APPROVAL

Dr. Stylianos Chatzidakis, Chair

School of Nuclear Engineering, Purdue University

Dr. Lefteri Tsoukalas

School of Nuclear Engineering, Purdue University

Dr. Yunlin Xu

School of Nuclear Engineering, Purdue University

Dr. Wei Xie

Department of Physics and Astronomy, Purdue University

Approved by:

Dr. Seungjin Kim

This dissertation is dedicated to my parents, HyungO Bae and SoonRan Park, whose love and support have led me to where I am today.

ACKNOWLEDGMENTS

This dissertation was supported by my mentor and academic advisor, Professor Stylianos Chatzidakis. I especially would like to acknowledge his invaluable mentorship and guidance for me throughout the years. I also would like to acknowledge (i) ANS for awarding me the winner of the "Pitch your PhD" competition in the 2021 ANS Winter Meeting and Graduate Scholarship, (ii) Roy G. Post Foundation for bequeathing me the Graduate Scholarship, (iii) ASME for awarding me the Best Paper Award during the ICONE28, (iv) APS (GIMS and Braslau Family) and IEEE for supporting my travels, (v) KSEA for nominating me for the Best Presentation award and conferring me the KSEA-KUSCO Graduate Scholarship, and (vi) School of Nuclear Engineering and College of Engineering at Purdue University for granting me assistantships, scholarships, awards, and supporting me throughout my Ph.D. program.

I would also like to inform that some chapters in this dissertation were reprinted from our recent publications in the open access journals, (i) Bae, J. and Chatzidakis, S. (2022) Fieldable muon spectrometer using multi-layer pressurized gas Cherenkov radiators and its applications. *Scientific Reports*, **12**, 2559 (DOI: 10.1038/s41598-022-06510-2), (ii) Bae, J. and Chatzidakis, S. (2022) A new semi-empirical model for cosmic ray muon flux estimation. *Progress of Theoretical and Experimental Physics*, **2022**, 4 (DOI: 10.1093/ptep/ptac016), and (iii) Bae, J. and Chatzidakis, S. (2022) Momentum-Dependent Cosmic Ray Muon Computed Tomography using a Fieldable Muon Spectrometer, *Energies*, **15** (7), 2666 (DOI: 10.3390/en15072666).

TABLE OF CONTENTS

LIST OF TABLES

LIST OF FIGURES

LIST OF ABBREVIATIONS

Abbreviations	Meaning
ART	Algebraic Reconstruction Technique
ATLAS	A Toroidal Large hardon collider ApparatuS
AUC	Area Under Curve
BR	Branching Ratio
CMS	Compact Muon Solenoid
CR	Classification Rate
CT	Computed Tomography
EM	Electromagnetic
FA	Fuel Assembly
GeV	Giga-election volt, 10^9 eV
HEU	High Enriched Uranium
IR	Infrared
KE	Kinetic Energy
LEU	Low Enriched Uranium
LHC	Large Hadron Collider
MCS	Multiple Coulomb Scattering
MIP	Minimum Ionization Particle
mPoCA	Momentum-Integrated PoCA
μCT	Muon Computed Tomography
OTR	Optical Transition Radiation
PID	Particle Identification
PMT	Photomultiplier Tube
PoCA	Point-of-Closest Approach
PWR	Pressurized Water Reactor
RICH	Ring Image Cherenkov Detector
ROC	Receiver Operating Characteristic

Continued on next page

SiPM	Silicon Photomultiplier
SNF	Spent Nuclear Fuel
SNM	Special Nuclear Material
SNR	Signal to Noise Ratio
SPAD	Single-Photon Avalanche Diode
SQ	Significant Quantity
TeV	Tera-electron volt, 10^{12} eV
ToF	Time of Flight
ToP	Time of Propagation
UV	Ultraviolet
VIS	Visible
WLS	Wavelength Shifter
WOM	Wavelength-Shifting Optical Module
XTR	X-ray Transition Radiation

NOMENCLATURE

Greek symbols	Meaning
α	Fine-structure constant (≈1/137)
α_m	Molecular polarizability
β	Ratio of particle's speed to the speed of light
δ	Multiplication factor of the dynode
	Half-plane projected angle (Section 2.1.3)
γ	Euler-Mascheroni numerical constant (≈ 0.57721) (Section 2.2.2)
	Lorentz factor ($= 1/\sqrt{1-\beta^2}$)
ϵ_0	Permittivity of the vacuum
θ	Scattering angle
θ_C	Cherenkov angle
$K^{\pm}$	Charged kaon
$\mu^{\pm}$	Charged muon
ν	Neutrino
$\bar{\nu}$	Anti-neutrino
$h\nu$	Photon energy
$\pi^{\pm}$	Charged pion
σ_X	Measurement uncertainty in quantity X
τ	Mean life time (Chapter 2)
	Decay time constant (Chapter 3)
φ	Zenith angle
Φ	Work function
χ_c	Characteristic angle
χ_a	Screening angle
Ω	Solid angle
Ω_{eff}	Effective solid angle

Continued on next page

Other symbols	Meaning
A_m	Molecular refractivity
a_0	Bohr radius ($4\pi\varepsilon_0\hbar^2/m_e e^2$ = 5.29177 × 10^{-11} m)
E_C	Critical energy
e	Euler's number (≈ 2.71828)
h	Plank's constant (≈ 6.62607 × 10^{-34} $J{\cdot}s$)
$\hbar$	Reduced Plank's constant (= $h/2\pi$)
I	Muon intensity
I_0	Vertical muon intensity
k	Wave number
k_B	Birks' coefficient
M	Mach number
$m_\mu c^2$	Muon rest mass (≅105.66 MeV)
$m_e c^2$	Electron rest mass (≅0.511 MeV)
n	Index of refraction
R	Radiation length number
V_{br}	Breakdown voltage
X_0	Radiation length

ABSTRACT

Nuclear waste management and nonproliferation are among the critical tasks to be addressed for the advancement of nuclear energy in the United States. In this regard, monitoring spent nuclear fuel (SNF) and special nuclear materials (SNM) is important to continue reliable stewardship of SNF management and prevent SNM proliferation. Cosmic ray muons have been used for imaging large and dense objects, e.g., SNF dry casks, the Fukushima Daiichi unit-1 reactor, and the great pyramid of Giza. Despite their potential and success, the wide application of cosmic ray muons is limited by the naturally low intensity at sea level, approximately 10^4 $m^{-2}min^{-1}$. For example, when imaging large objects, time consuming measurements typically in the order of several days or even weeks, are frequently needed to collect a statistically significant amount of muon samples to reconstruct images using muon tomography. However, when scanning time is of essence, e.g., treaty verification, low resolution imaging can result in potentially undetected diversion of nuclear materials.

To maximize the utilizability of cosmic ray muons in engineering and physics applications, two important quantities–scattering angle and momentum–must be measured. Although many studies have demonstrated that there are significant benefits when measuring momentum in muon applications, measuring both the muon scattering angle and muon momentum in the field remains a challenge. To fill this critical gap, a novel concept using multi-layer pressurized gas Cherenkov radiators that is fieldable to allow muon momentum measurement in the field is presented in this dissertation. The proposed Cherenkov muon spectrometer is: (i) accurate (~90%) in classifying muon momentum, (ii) lightweight (< 10 kg) for easy transport and deployment in the field, (iii) compact (< 1 m^3), and (iv) easily coupled with existing muon tomographic systems. Although muon momentum measurement resolution of spectrometers used in high energy physics laboratories, such as CMS or ATLAS of LHC at CERN, is less than 5% for low energy muons, these spectrometers typically (i) use bulky and large solenoidal or toroidal magnets and (ii) interfere with muon trajectories to measure momentum. These characteristics make them unsuitable for field deployment.

In this work, the feasibility of using the proposed Cherenkov muon spectrometer coupled with current muon tomographic systems is explored and evaluated using Monte Carlo simulations and reconstruction algorithms. It is shown the use of the proposed Cherenkov muon spectrometer

has the potential to improve muon tomographic imaging resolution or reduce measurement time by a factor of 10 or more when used to identify a missing fuel assembly from a SNF dry cask. In addition, a new imaging algorithm is developed that integrates muon momentum and muon scattering without significantly increasing computational cost. Advances in momentum-integrated muon tomography have the potential to improve monitoring and imaging efficiency in various nuclear engineering applications. For example, it can expand current capabilities to continue reliable stewardship in nuclear material management, i.e., Continuity of Knowledge, and prevent SNM proliferation to unauthorized states and parties. The benefit of such an approach is a compact, lightweight, and portable spectrometer that can be deployed in the field to improve existing or explore new engineering applications: muon tomography, geological studies, and cosmic radiation measurement in space.

1. INTRODUCTION

In many engineering and physics applications, cosmic ray muons have been acknowledged as a promising radiographic probe mostly due to their high penetration depth, especially in dense materials. For example, a muon of energy 3 GeV can travel approximately 10 m in water (ρ = 1.0 g/cm^3) and 0.5 m in uranium (ρ = 19.1 g/cm^3) whereas the mean free path for high-energy photons is approximately 0.25 and 0.01 m for water and uranium, respectively (Borozdin et al., 2003). Electrons and protons also have been considered to monitor large and dense objects. However, high-energy electrons emit a large amount of Bremsstrahlung radiation and their penetration depth is only a few centimeters in lead. Although accelerated protons have a penetration depth of a few meters in dense materials, it requires particle accelerator (Gustafsson, 2005). On the other hand, cosmic ray muons barely emit Bremsstrahlung radiation while they interact with matter because they are minimum ionization particles (MIP). In addition, muons do not necessitate the use of particle accelerators or other expensive infrastructure because the energy range of cosmic ray muons extends from 0.2 GeV to 2 TeV (Hagiwara et al., 2002). Cosmic ray muons constantly shower from the sky as a result of decay of pions and kaons produced by interactions between atmospheric molecules and primary cosmic radiations on Earth, i.e., protons, electrons, and heavy ions such as O^+ and N^+. Although the intensity of cosmic ray muons at sea level is often approximated to 10^4 m^{-2}min^{-1} (Allkofer et al., 1968), it depends on various conditions, i.e., zenith angle, longitude, latitude, solar activity, and detector configuration. To provide an accurate estimation of cosmic ray muon flux, a couple of analytical and empirical models have been developed for various environmental conditions (Autran et al., 2018; Junghyun Bae et al., 2021; Junghyun Bae & Chatzidakis, 2022a; Bahmanabadi, 2019a; Sato, 2016).

It is noted that the recent advancement of cosmic ray muon applications has been successfully acknowledged in various engineering fields, including nuclear reactor and spent nuclear fuel cask imaging (Bonneville et al., 2017; S. Chatzidakis et al., 2017), homeland security (Anghel et al., 2010; Kamaev et al., 2019), geotomography (Guardincerri et al., 2017; Schouten, 2018), and archaeology (Morishima et al., 2017). Despite the potential and success, the wide application of cosmic ray muons is often limited by the naturally low intensity. Because it is not practical to deploy either a particle accelerator or muon beam in the field, it is important to measure muon momentum to maximize the utilizability of each cosmic ray muon (Junghyun Bae &

Chatzidakis, 2021b; Stylianos Chatzidakis, Liu, et al., 2017). However, it is still challenging to measure muon momentum in the field without resorting to a large solenoid or toroidal magnets, Cherenkov ring imagers, or time-of-flight detectors (Abratenko et al., 2017; Boezio et al., 2003; Salvucci, 2011). Although recent efforts at Canadian Nuclear Laboratory (CNL) and Istituto Nazionale Fisica Nucleare (INFN) aim to infer momentum knowledge from multiple Coulomb scattering measurements (Anghel et al., 2015; Vanini et al., 2018), at present no portable spectrometer exists that can measure muon momentum in the field. By portable, it is meant a spectrometer that can be transported by commercial vehicle and deployed at different facilities or sites without the need for permanent structures.

To fill this critical gap, a novel muon spectrometer using multi-layer pressurized gas Cherenkov radiators is developed and presented in this dissertation. Because muons are charged particles, they can induce Cherenkov radiation in optically transparent media. Unlike solid or liquid Cherenkov radiators, the refractive index of a gas radiator can be varied by changing gas pressure and temperature. We can then find the optimal muon threshold momentum levels by carefully selecting the gas pressure for each radiator. As a result, radiators will emit Cherenkov radiation only when the threshold momentum is less than the actual muon momentum even though a muon passes through all radiators. Therefore, by measuring the Cherenkov signals in each radiator, we can estimate the actual muon momentum. The benefit of such an approach is a compact, lightweight, and portable spectrometer that can be deployed in the field to improve existing or explore new engineering applications: muon tomography, geological studies, and cosmic radiation measurement in space.

To demonstrate the feasibility and applicability of the proposed Cherenkov muon spectrometer, this dissertation focuses on (i) theoretical background, (ii) operational principles, (iii) detailed Geant4 (Geometry And Tracking) modeling and simulations, and (iv) reconstruction algorithm that integrates muon momentum and muon scattering, and (v) application to different scenario to evaluate improvements in resolution and measurement time. The results show that the proposed spectrometer has the potential to measure muon momentum with high accuracy (~ 90%) for a wide muon momentum range (0.1–10.0 GeV/c) and with a resolution of ±0.5 GeV/c which is sufficient for most engineering applications.

One of the current radiographic techniques using cosmic ray muons, muon scattering tomography, uses the Point-of-Closest Approach (PoCA) algorithm and reconstructs images by

assigning scattering angle values, i.e., rad or rad^2/cm, in a voxel. In momentum integrated muon tomography, however, a new value, *M*, which mathematically integrates muon momentum and scattering angle as a single value without significantly increasing computational cost is introduced.

Muon tomography is especially important for SNF cask monitoring. Although preceding work on SNF cask monitoring using muon tomography has shown promising results in image reconstruction and monitoring the integrity of used nuclear fuel assemblies (FA), they either (i) used both muon transmission and scattering tomography techniques simultaneously for a long measurement time or (ii) collected cosmic muon data in various aspects by rotating muon detectors to improve image resolution (Liu et al., 2017; Poulson et al., 2019; Vanini et al., 2018; Yang et al., 2019). In this work, we investigate the applicability of our Cherenkov muon spectrometer to reconstruct a high-resolution SNF cask image and accurately locate a missing fuel assembly without transmission technique and shorter scanning times by measuring muon momentum. We used a VSC-24 canister (EPRI, 2010) as our model SNF cask and a Cherenkov muon spectrometer (Junghyun Bae & Chatzidakis, 2022b) to measure the muon scattering angle and momentum at the same time in the field. Our objective is to visually and systematically identify the location of one missing FA in the cask using momentum integrated muon tomography. This scenario is challenging because the missing FA is surrounded by other FAs that tend to blur the image. The results show that the image resolution is significantly improved when measuring muon momentum with a momentum resolution of 0.1 GeV/c and it reduces scanning time by a factor of 10 or more compared to existing PoCA imaging algorithm in terms of systematically finding a missing FA in the cask.

1.1 The Author's Role and Contribution

The development of a fieldable muon spectrometer using multi-layer pressurized gas Cherenkov radiators is interdisciplinary research because the potential applications widely extend from nuclear engineering to high energy physics. This research covers various disciplines including muon physics, radiation instrumentation and detection, nuclear security, safeguards, computational imaging, and algorithm development. In this dissertation, the author led and conducted high-quality research to expand the knowledge in muon research and its applications. In order to achieve the research objectives, the author performed the following activities:

1. Conceptualization of the idea for measuring muon momentum using multi-layer pressurized gas Cherenkov radiators.
2. Design of methodology in the development of a novel fieldable Cherenkov muon spectrometer.
3. Implementation of (i) Geant4 simulations for Monte-Carlo muon transportation and interactions, (ii) MATLAB for numerical analysis and algorithm development, and (iii) ParaView for visualization of image reconstructions.
4. Performed experiments for cosmic ray muon measurement to develop a semi-empirical muon flux estimation model.
5. Sharing ideas and results with colleagues and researchers by publishing original papers in interdisciplinary peer-reviewed journals and delivering presentations at international professional conferences.

1.2 Scope of Dissertation

This dissertation consists of three pillars: (i) development of a novel Cherenkov muon spectrometer, (ii) momentum integrated PoCA imaging algorithms, and (iii) momentum integrated muon tomography system for nuclear security applications.

Chapter 2 presents the background knowledge of cosmic ray muons and state-of-art scientific instrumentation in muon research. The characteristics of cosmic ray muons and their interactions with matter are discussed. In addition, types of muon detectors, optical sensors, and muon spectrometers are summarized. At the end of Chapter 2, two muon radiographic techniques–muon scattering tomography and muon transmission radiography–are also presented.

Chapter 3 details the theory and principles in the development of a muon spectrometer using multi-layer pressurized gas Cherenkov radiators. It includes not only the analytical and numerical analyses but also extensive Geant4 simulation results. Finally, the feasibility and performance of our proposed muon spectrometer are evaluated and methods to maximize the signal-to-noise ratio (SNR) are suggested.

Chapter 4 introduces momentum integrated imaging algorithm. It provides the mathematical and physical background to develop new PoCA imaging algorithms, mPoCA. Each mPoCA algorithm has a benefit depending on the types of target materials and monitoring conditions.

Chapter 5 presents the implementation of the Cherenkov muon spectrometer in various security and nuclear material management applications. It details the methodology to reconstruct images for lead-shielded special nuclear materials (SNM) and spent nuclear fuel (SNF) dry casks. Finally, the results are visually and systematically compared with those of the original PoCA imaging algorithm.

Chapter 6 summarizes and concludes the main discussions and remarks of this dissertation. It also details our future work for selecting materials, calibration, and maximizing the SNR in the experiments.

2. BACKGROUND

A portion of this chapter was previously published by *Progress of Theoretical and Experimental Physics*, **2022** (4) (2022), "A new semi-empirical model for cosmic ray muon flux estimation," Bae. J and Chatzidakis, S. [DOI: 10.1093/ptep/ptac016]

In this chapter, characteristics of cosmic ray muons, physics in the muon interaction with matter, scientific instruments in muon research, and muon radiographic techniques are presented. In Section 2.1, the cosmic ray muon energy spectrum, zenith angle distribution, and flux estimation models are discussed. Two major physical phenomena when a muon interacts with matter– scattering and energy loss–are outlined in Section 2.2. In addition, a brief summary of state-of-art technologies for muon detectors (trackers), photon detectors, and muon spectrometers appears in Section 2.3. Section 2.4 provides the fundamentals of two muon imaging techniques, muon scattering tomography and muon transmission radiography. Finally, a summary of Chapter 2 is presented in Section 2.5.

2.1 Cosmic Ray Muons

The existence of muons was first predicted by the Japanese physicist Yukawa Hideki in 1935 (Yukawa, 1935) and they were discovered by the American Physicists Carl Anderson and Seth Neddeermeyer in 1936 (Anderson & Neddermeyer, 1936; Neddermeyer & Anderson, 1937). Muons are elementary particles in the standard model of particle physics as shown in Table 2.1. They are similar to electrons, with a positive or negative charge, and spin-half. However, they are approximately 207 times more massive than electrons. A muon is unstable with a mean lifetime of 2.2 μsec and it decays to electron/positron and two kinds of neutrinos, electron and muon neutrinos (Particle Data Group, 2020). We begin this section with a distinction between primary and secondary cosmic rays in Section 2.1.1. The characteristics of cosmic ray muons at sea level such as the energy spectrum and zenith angle dependency are outlined in Section 2.1.2. Finally, in Section 2.1.3, various analytical approaches to estimate the muon flux: cosine-power, PARMA (Sato, 2016), and effective solid angle models (Junghyun Bae & Chatzidakis, 2022a), and experimental results are presented.

2.1.1 Cosmic rays at Earth

The primary cosmic rays predominantly consist of protons, alpha particles, and heavier nuclei with an energy ranging from 10^6 to 10^{18} eV per particle (Engelmann et al., 1990). They include stable charged particles and nuclei that have a mean lifetime of millions of years or longer. High energetic interactions between the primary cosmic rays and atmospheric nuclei, such as nitrogen and oxygen cause successive particle showers that result in the massive production of mesons and secondary particles. The most abundant particles from the hadronic interactions are pions and kaons. If these secondary particles have sufficient energy, they continue new hadronic interactions and cause extensive air showers. Otherwise, unstable particles such as charged pions and kaons begin to decay. Vertical fluxes of primary and secondary cosmic rays at various altitudes are shown in Figure 2.1.

Table 2.1. The standard model of particle physics.

	Fermions (Matter particles) †			Bosons (Force carriers)	
Quarks	$\boldsymbol{u}$ (up)	$\boldsymbol{c}$ (charm)	$\boldsymbol{t}$ (top)	$\boldsymbol{g}$ (gluon)	$\boldsymbol{H}$ (Higgs)
	$\boldsymbol{d}$ (down)	$\boldsymbol{s}$ (strange)	$\boldsymbol{b}$ (bottom)	$\boldsymbol{\gamma}$ (photon)	
sLeptons	$\boldsymbol{e}$ (electron)	$\boldsymbol{\mu}$ (muon)	$\boldsymbol{\tau}$ (tau)	$\boldsymbol{Z^0}$ (Z boson)	
	$\boldsymbol{\nu_e}$ (electron neutrino)	$\boldsymbol{\nu_\mu}$ (muon neutrino)	$\boldsymbol{\nu_\tau}$ (tau neutrino)	$\boldsymbol{W^\pm}$ (W boson)	

†*Note: All fermions have the antiparticles.*

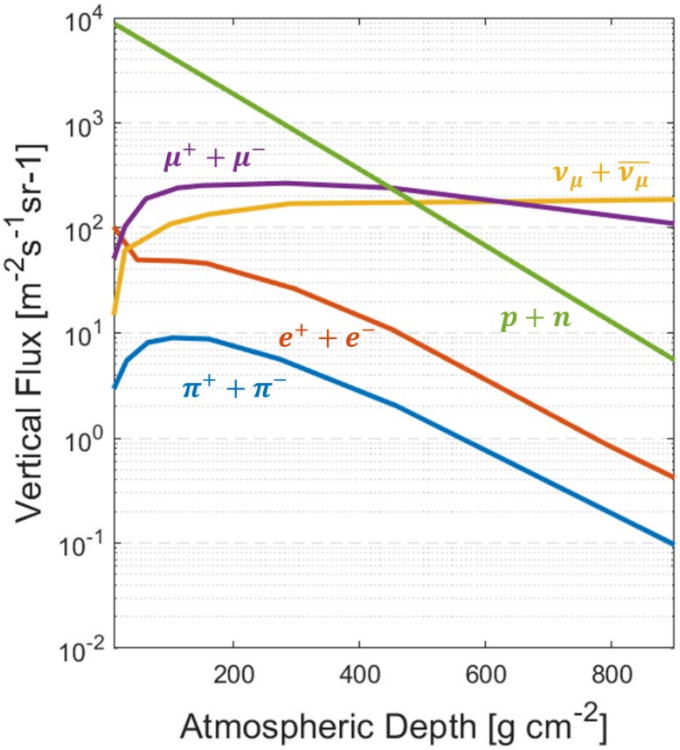

Figure 2.1. Vertical fluxes of major cosmic particles in Earth's atmosphere (Grieder, 2001).

2.1.2 Cosmic ray muons at sea level

With the exception of neutrinos and protons, muons are the most abundant secondary cosmic particles at sea level. As described in Section 2.1.1, cosmic ray muons are produced as a product of charged pion ($\pi^{\pm}$) or kaon ($K^{\pm}$) decay at an altitude of approximately 15 km. Pions ($m_{\pi\pm}$ = 139.6 MeV/c^2) decay into muons and neutrinos with a mean lifetime of 2.6033×10^{-8} seconds and branching radio of 0.9999. Similarly, kaons ($m_{K\pm}$ = 493.7 MeV/c^2) also decay into muons and neutrinos with a mean lifetime of 1.2380×10^{-8} seconds and branching radio of 0.6355 (P.A. Zyla et al., 2020). The productions of muons and neutrinos by pion and kaon decays with a branching ratio are

$$\pi^{\pm} \rightarrow \mu^{\pm} + \nu_\mu \left(\bar{\nu}_\mu\right) \qquad BR \approx 100\% \tag{2-1}$$

$$K^{\pm} \rightarrow \mu^{\pm} + \nu_{\mu}\left(\bar{\nu}_{\mu}\right) \qquad BR \approx 63.5\% \tag{2-2}$$

Muons also decay into electrons or positrons and two types of neutrinos with a branching ratio of 1.0000.

$$\mu^{\pm} \rightarrow e^{\pm} + \nu_e\left(\bar{\nu}_e\right) + \bar{\nu}_{\mu}(\nu_{\mu}) \qquad BR \approx 100\% \tag{2-3}$$

As an example, the Feynman diagram for μ- decay is shown in Figure 2.2. Since the muon neutrinos are produced by (2-1) and (2-3) in charged pion decays, the expected ratio of muon to electron neutrinos is (Grieder, 2001)

$$\frac{\nu_{\mu} + \bar{\nu}_{\mu}}{\nu_e + \bar{\nu}_e} \approx 2 \tag{2-4}$$

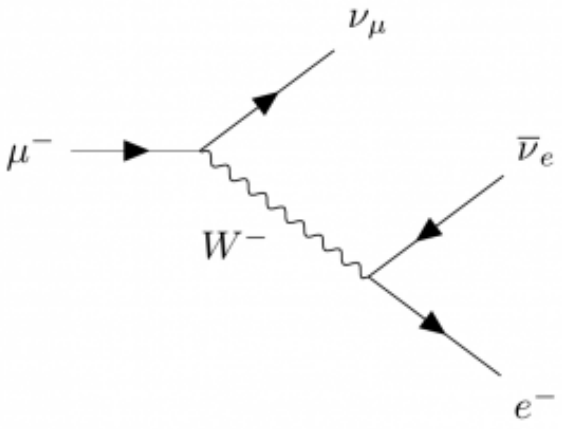

Figure 2.2. Feynman diagram for μ- decay.

The average energy loss of cosmic ray muons due to the multiple interactions with air molecules is about 2 GeV and the mean energy of muons at sea level is approximately 3 to 4 GeV. Approximated vertical flux of cosmic ray muons (p_{μ} > 1 GeV/c) is 70 $m^{-2}s^{-1}sr^{-1}$ at sea level (Hagiwara et al., 2002). The vertical differential cosmic ray muon momentum spectrum in the range of 0.2 to 10 GeV/c at sea level is shown in Figure 2.3 (Allkofer et al., 1968). The Gaisser

formula for the muon energy spectrum which is valid when a low zenith angle ($\theta < 70°$) is given by (T. K. Gaisser et al, 2016)

$$\frac{dN_\mu}{dE_\mu d\Omega} \approx \frac{0.14 E_\mu^{-2.7}}{\text{cm}^2 \text{ s sr GeV}} \times \left[\frac{1}{1 + 1.1 E_\mu \cos\theta / (115 \text{ GeV})} + \frac{0.054}{1 + 1.1 E_\mu \cos\theta / (850 \text{ GeV})} \right] \quad (2\text{-}5)$$

where θ and Ω are the zenith and solid angles. N_μ and E_μ are the muon intensity and energy. The first and second terms represent the contribution of pion and kaon, respectively.

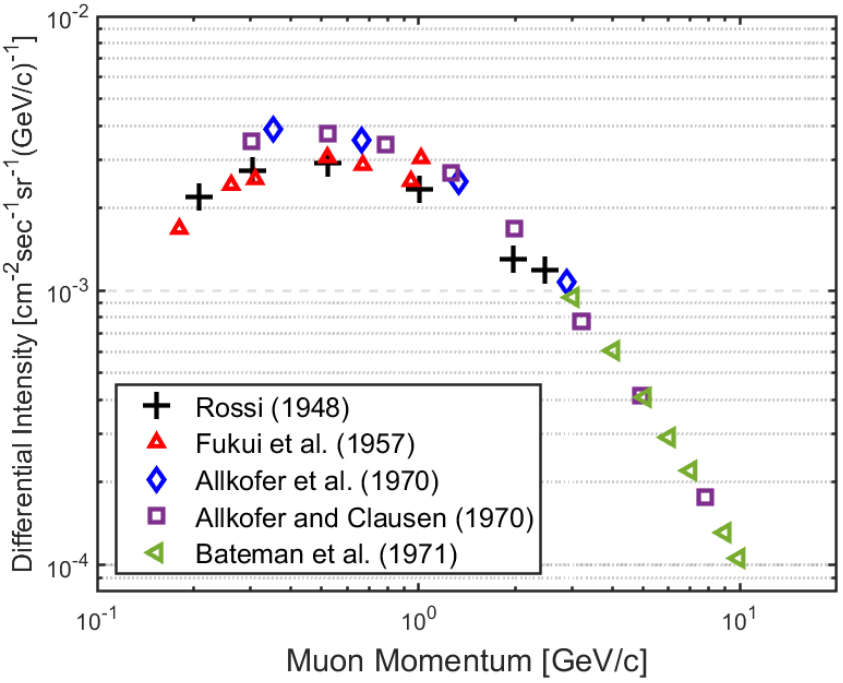

Figure 2.3. Vertical differential cosmic ray muon momentum spectrum in the range of 0.2–10 GeV/c (Grieder, 2001).

After pion and kaon decays, muons travel dozens or hundreds of kilometers through the Earth's atmosphere depending on their flight directions until they reach the Earth's surface. Although cosmic ray muons are highly penetrative, a muon intensity decreases as the flight

distance increases. The zenith angle distribution of cosmic ray muons at the ground is known to follow the cosine-power law (Bahmanabadi, 2019b)

$$I(\varphi) = I_0 \cos^{n(h,E)} \varphi \tag{2-6}$$

where φ is the zenith angle, I_0 is the vertical muon intensity. The exponent, n (h, E) is a function of muon energy, E, and vertical length of muon path, h. $n \cong 2$ at sea level. Even though the muon intensity depends on various factors such as the longitude, azimuthal angle, Earth's movement in the universe, and solar activity, the variance is not significant compared to the zenith angle dependency (Bahmanabadi, 2019b; Cheng, 2000). Figure 2.4 shows the zenith angle distribution of cosmic ray muons at sea level in the range of 0 to 89°.

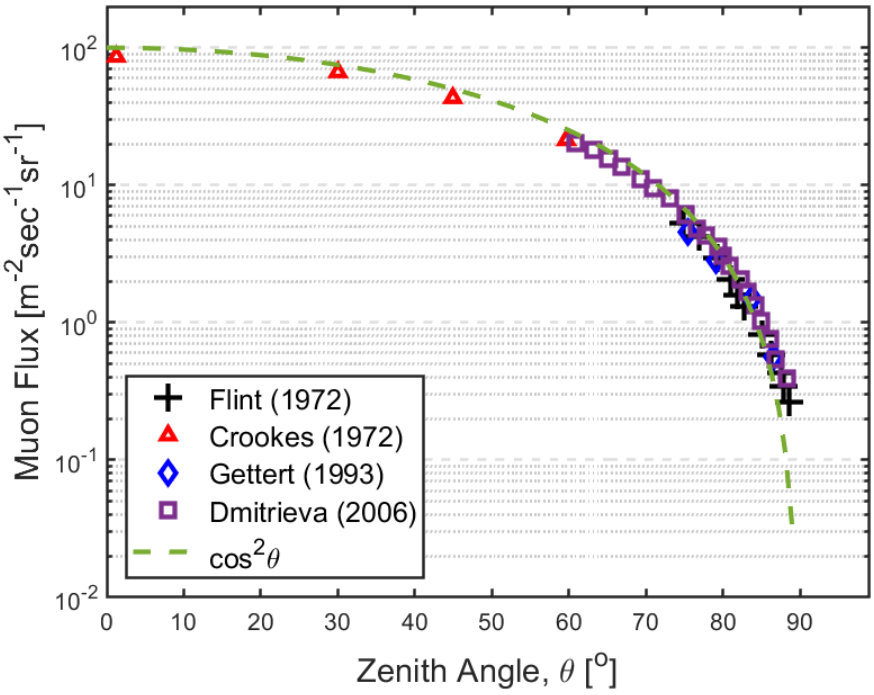

Figure 2.4. The variation of cosmic ray muon flux with zenith angles in the range of 0 – 89° at sea level (Grieder, 2001).

2.1.3 Cosmic ray muon flux estimation models

One widely used empirical model for the relationship between cosmic particle flux and zenith angle is the cosine-power model. For cosmic ray muons at sea level, the exponent is often approximated to 2, then the (2-6) can be written by

$$I(\varphi) = I_0 \cos^2 \varphi \tag{2-7}$$

However, the cosine-squared model (n = 2) is often limited due to its assumption of point-detector geometry. Cosmic ray muons can be measured at any zenith angle and there exist radiographic techniques using horizontal muon detectors (Christopher L Morris et al., 2014; Tanaka et al., 2005). Although various accurate analytical models for a terrestrial cosmic ray flux estimation have been developed (Sato, 2015, 2016), detector geometry and configuration are not taken into account in these models. To address this limitation, we focus on the development of a new model which can easily estimate the muon flux in all zenith angles at sea level. To integrate the geometry and configuration of a detector in the cosmic muon flux estimation, we developed a new approach, an effective solid angle. The equation for the effective solid angle is given by

$$\Omega_{\text{eff}}(i) = \Omega'_{\text{eff}}(i) F(i) \tag{2-8}$$

where

$$\Omega'_{\text{eff}}(i) = \frac{2\pi}{I_0} \int_{\varphi_i - \gamma}^{\varphi_i + \gamma} I(\phi) \sin\phi \, d\phi \tag{2-9}$$

$$F(i) = \frac{A_{\text{cap}}}{A_{2\pi}(i)} = \frac{1 - \cos\gamma}{\cos(\varphi_i - \gamma) - \cos(\varphi_i + \gamma)} \tag{2-10}$$

where $I(\phi)$ is the muon intensity, I_0 is the maximum intensity, φ_i is the ith centerline pointing angle (zenith angle), γ is the half-plane projected angle, A_{cap} is the cap area, and $A_{2\pi}$ is a circular area between $\varphi \pm \gamma$. A full derivation of (2-8) to (2-10) are detailed in Appendix A.

The results of four approaches for cosmic ray muon flux estimation at sea level and experimental measurements: (i) cosine-squared model, (ii) PARMA model, (iii) Monte-Carlo simulation, and (iv) effective solid angle model are shown in Figure 2.5.

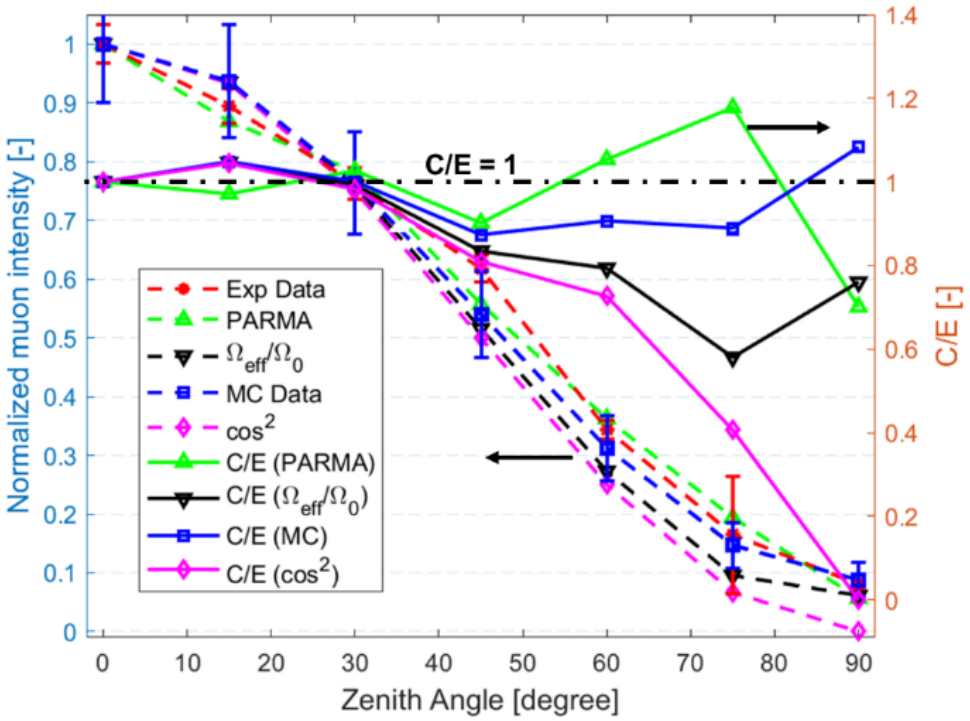

Figure 2.5. Comparison of experimental measurement data and four approaches for cosmic ray muon flux estimation: (i) cosine-squared model, (ii) PARMA model (Sato, 2015), (iii) Monte-Carlo simulation, and (iv) effective solid angle model and their C/E (right y-axis) when D = 8 cm and r_d = 2.54 cm. Reprinted from Bae (2021), with the permission of Oxford Press.

2.2 Muon Interaction with Matter

The energy transfer from a charged particle to the matter occurs mainly in three ways: (i) nuclear collision, (ii) electronic interactions such as ionization and excitation, and (iii) Bremsstrahlung radiation. The predominant energy loss mechanism is determined by the particle energy. In a practical example, a mean energy loss rate of cosmic ray muons is close to the minimum, and they are called "minimum ionizing particle (MIP)". A detailed discussion of muon energy loss mechanisms in the matter is discussed in Section 2.2.1. When a muon interacts with a matter, not only does it lose energy but also is deflected due to the inelastic collision with electrons and nuclei (K. Nakamura et al., 2010). The analytical models for muon scattering and multiple Coulomb scattering (MCS) approximation are presented in Section 2.2.2. At the end of Section 2.2, two important characteristic quantities of matter, radiation length and critical energy, are described in Section 2.2.3.

2.2.1 Mean rate of energy loss of muon

When a cosmic muon travels through matter, electronic interactions are the predominant energy loss mechanism because cosmic ray muons are minimum ionizing particles. For instance, the mean rate of energy loss, $\langle -dE/dx \rangle$, of a positive muon in copper as a function of muon momentum in GeV/c and $\gamma\beta$ is shown in Figure 2.6 (P.A. Zyla et al., 2020). For low energy muons, a nuclear energy loss mechanism dominates whereas a radiative energy loss such as Bremsstrahlung radiation emission dominates in the high energy region. The majority of cosmic ray muon momentum spectrum extends from 0.1 to 100 GeV/c in which "Bethe" region in Figure 2.6. In the Bethe region where the Bethe equation is valid, the ionization energy loss mechanism dominates over both nuclear and radiative energy loss mechanisms. The momentum range of cosmic ray muons has a low mass stopping power including the minimum ionization point. The mean rate of energy loss, or the mass stopping power in MeV cm^2/g can be estimated using the Bethe equation

$$-\left.\frac{dE}{dx}\right|_{avg} = Kz^2\frac{Z}{A}\frac{1}{\beta^2}\left[\frac{1}{2}\ln\frac{2m_e c^2\beta^2\gamma^2 W_{max}}{I^2} - \beta^2 - \frac{\delta(\beta\gamma)}{2}\right]. \quad (2\text{-}11)$$

Notations, constants, and symbols used in (2-11) are summarized in Table 2.2. Bethe equation is valid for $0.1 < \beta\gamma < 1000$ in which the cosmic ray muon energy range is included. Figure 2.6 shows the mass stopping power for a muon as a function of $\beta\gamma$ in different states and materials using the Bethe equation. The values of the minimum and maximum energy loss per unit length in various materials within the cosmic muon range are summarized in Table 2.3. The minimum ionization point, $\langle -dE/dx\rangle_{\min}$ of mass stopping power for different materials has a linear relation with an atomic number, Z, and the fitted correlation ($Z > 6$) is described by

$$\langle -dE/dx\rangle_{\min} = 2.35 - 0.28\ln Z \quad (Z > 6) \quad (2\text{-}12)$$

In a practical case, it is valid to assume that a cosmic ray muon is a minimum ionizing particle (MIP) because the mean energy loss rate is at nearly minimum ionization point in the Bethe equation.

Table 2.2. Summary of symbols, notations, and values used in (2-11).

Notation	Definition	Units or value
W_{max}	Maximum energy transfer in a single collision from a fast-charged particle to the electron. $W_{max} = \frac{2m_e c^2 \beta^2 \gamma^2}{1 + 2\gamma\left(\frac{m_e}{M}\right) + \left(\frac{m_e}{M}\right)^2}$ (2-13)	MeV
M	Target (absorber) mass.	$\mathrm{MeV/c^2}$
m_e	Electron mass.	$\mathrm{MeV/c^2}$
Z	Target (absorber) charge and atomic number.	–
A	Target (absorber) atomic number.	g/mol
z	Atomic number of the incident particle.	–
K	$4\pi N_{Av} r_e^2 m_e c^2$	0.307 MeV cm^2/mol
β	v/c	–
γ	$1/\sqrt{1-\beta^2}$	–
I	Mean excitation energy (potential).	eV
$\delta(\beta\gamma)$	Density effect correction to ionization energy loss. Details are available in "Sternheimer Density Effect calculator".	–

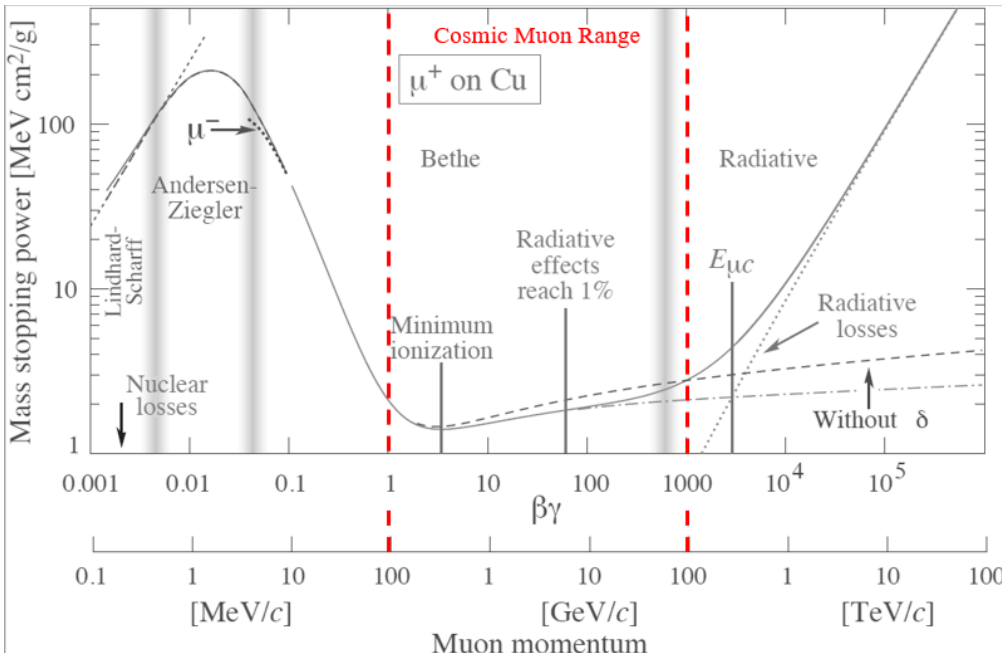

Figure 2.6. Mean energy loss rate for muons in copper as a function of $\beta\gamma = p/Mc$ (P.A. Zyla et al., 2020). The approximated cosmic muon energy range is indicated with vertical dashed lines.

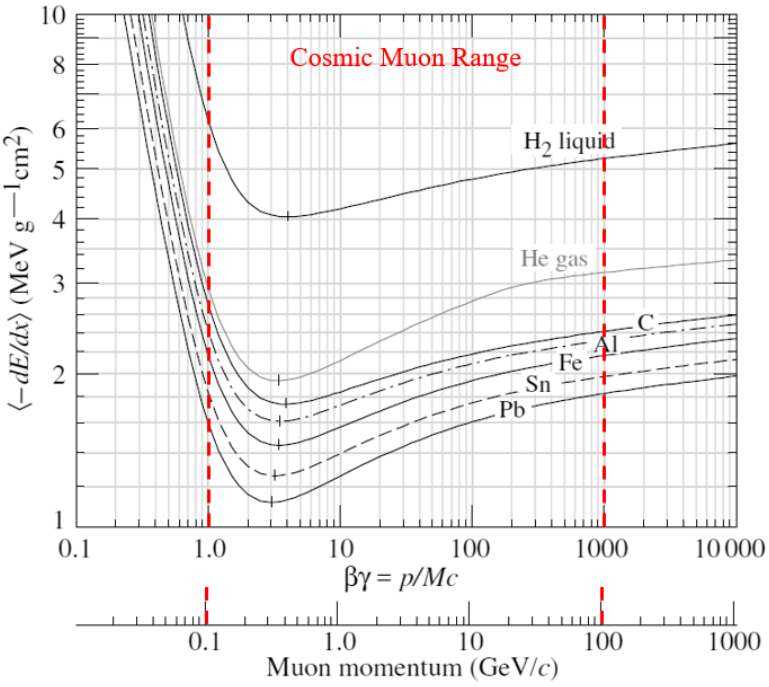

Figure 2.7. Mean energy loss rate of for muons in iron as a function of $\beta\gamma = p/Mc$ in various states and materials (P.A. Zyla et al., 2020). The approximated cosmic muon energy range is indicated with vertical dashed lines.

Table 2.3. Minimum and maximum energy loss rates of muons for different materials within the cosmic muon energy range (0.1 to 100 GeV/c).

	Atomic number	Density (g/cm^3)	ΔE_{min} (MeV/cm)	ΔE_{max} (MeV/cm)
H_2 (Liquid)	1	0.0709	0.284	0.382
He (Gas)	2	0.000178	0.00034	0.00057
Fe	26	7.9	11.46	17.38
Pb	82	10.7	12.31	19.26
U	92	19.1	21.01	30.56

In practical cases such as spent nuclear fuel assemblies and shielded special nuclear materials, they typically do not exist as a single material but a mixture or compound. The mean rate of energy loss for the mixture is given by

$$\left(\frac{dE}{dx}\right)_{avg} = \sum \omega_i \left(\frac{dE}{dx}\right)_{i,avg} \tag{2-14}$$

where ω_i and $(dE/dx)_i$ are the weight fraction and mean rate of energy loss for *i*th element. For compounds,

$$\langle Z/A \rangle = \sum \omega_i \, (Z/A)_i. \tag{2-15}$$

2.2.2 Multiple Coulomb scattering

Molière theory

When a muon interacts with matter, it is deflected because of (i) inelastic collision with electrons and (ii) consecutive collisions with nuclei, or multiple Coulomb scattering (MCS). The theoretical model for the MCS angle distribution was studied by Molière (Molière, 1948) and extended by Bethe and Meyer (Bethe, 1953; Meyer, 1961). The general form of MCS angle distribution for a point-like nucleus is given by

$$F(\theta,t)\theta d\theta = 2\chi e^{-\chi^2}\left[1+\frac{b_0+b_2\chi^2+\sum_{\nu=2}^{\infty}b_{2\nu}\chi^{2\nu}}{B}\right]d\chi \tag{2-16}$$

where θ is the muon scattering angle, χ and coefficients are defined in (2-17) and (2-18). The first term shown in the RHS of (2-16), $\chi e^{-\chi^2}$, represents a sum of consecutive large number of small angle deflections and the second term is the results from a single scattering with a large angle.

$$b_0 = 0.423, \qquad b_2 = -1.423, \qquad b_{2\nu} = \frac{(\nu-2)!}{(\nu!)^2} \tag{2-17}$$

$$\chi \equiv \frac{\theta}{\chi_c\sqrt{B}} \tag{2-18}$$

The parameter B shown in (2-16) and (2-18) can be determined by solving the transcendental equation

$$B = -\ln\left(\frac{\chi_a^2}{\chi_c^2}\frac{\boldsymbol{\gamma}^2}{\boldsymbol{e}B}\right) \tag{2-19}$$

where $\boldsymbol{e}$ is the Euler constant (≈ 2.71828) and $\boldsymbol{\gamma}$ is the Euler-Mascheroni numerical constant (≈ 0.57721). χ_c is the characteristic angle and χ_a is the screening angle defined by Molière as follow

$$\chi_c^2 = 0.157\left(\frac{Z(Z+1)\rho L}{A}\right)\left(\frac{1}{p\beta}\right)^2 \tag{2-20}$$

$$\chi_a^2 = 2.007\times10^{-5}Z^{\frac{2}{3}}\left[1+3.34\left(\frac{Z\alpha}{\beta}\right)^2\right]\frac{1}{p^2} \tag{2-21}$$

where p is the muon momentum in MeV/c, β is the particle velocity, and α is the fine structure constant (≈ 1/137). L, ρ, Z, and A are the length in cm, density in g/cm^3, charge, and atomic weight

of the scattering medium, respectively (Lynch & Dahl, 1991). In the original Molière's work, Z^2 was used in (2-20) instead of $Z(Z+1)$. Later, the original equation was modified to take into account atomic electron interactions with heavy particles by Beth and Kulchisky & Latyshev (Bethe, 1953; L. A. Kulchitsky & Latyshev, 1942).

Geant4 simulation algorithm

In the Monte-Carlo particle transport code, Geant4 (Geant4 Collaboration, 2017), the Goudsmit-Saunderson and Lewis' model has been implemented as the basis of the multiple scattering algorithm (Goudsmit & Saunderson, 1940; Lewis, 1950). The deflected angular distribution using the Legendre polynomials, $P_l(\cos\theta)$, is given by

$$F(\theta,t)=\sum_{l=0}^{\infty}\frac{2l+1}{4\pi}e^{-\frac{t}{\lambda_l}P_l(\cos\theta)} \tag{2-22}$$

when

$$\frac{1}{\lambda_l}=\exp\left(-2\pi tN\int_{-1}^{1}\left(1-P_l(\cos\theta)\right)\frac{d\sigma(\theta)}{d\Omega}d(\cos\theta)\right) \tag{2-23}$$

where λ_l is the lth transport mean free path, N is the atom number density of scattering medium. The single scattering differential cross section, $d\sigma(\theta)/d\Omega$, was initially derived by Rutherford (Rutherford, 1911) and extended by Wentzel (Wentzel, 1926). The cross section of the single Coulomb scattering angle including screening effect by orbiting electrons is described by

$$\frac{d\sigma(\theta)}{d\Omega}=\left(\frac{zZe^2}{8\pi\epsilon_0 mv_0^2}\right)^2\left(\sin^2\frac{\theta}{2}+\frac{1}{4k^2a^2}\right)^{-2} \tag{2-24}$$

where ze and Ze are the charges of the projectile and target material, m and v_0 are the mass and initial speed of projectile. ϵ_0 is the vacuum permittivity, k is the projectile's wave number, and a is the Thomas-Fermi radius,

$$a = 0.885 a_0 Z^{-1/3} \tag{2-25}$$

where a_0 is the Bohr radius.

In Geant4 simulations, a discrepancy exists between the length of true muon scattering trajectory due to the multiple Coulomb scattering and geometrical scattering path as show in Figure 2.8. The mean geometrical path length is given by

$$\langle z \rangle = \lambda_l [1 - e^{-L/\lambda_l}] \tag{2-26}$$

where L is the true path length. The mean scattering angle and its variance after each step is expressed by (Greis, 2017)

$$\langle \cos\theta \rangle = e^{L/\lambda_l} \tag{2-27}$$

$$\sigma^2(\cos\theta) = \frac{1}{3}\left[1 + 2e^{-2\kappa(L/\lambda_l)} - 3e^{-2(L/\lambda_l)}\right] \tag{2-28}$$

where

$$\kappa = \lambda_1/\lambda_2 \tag{2-29}$$

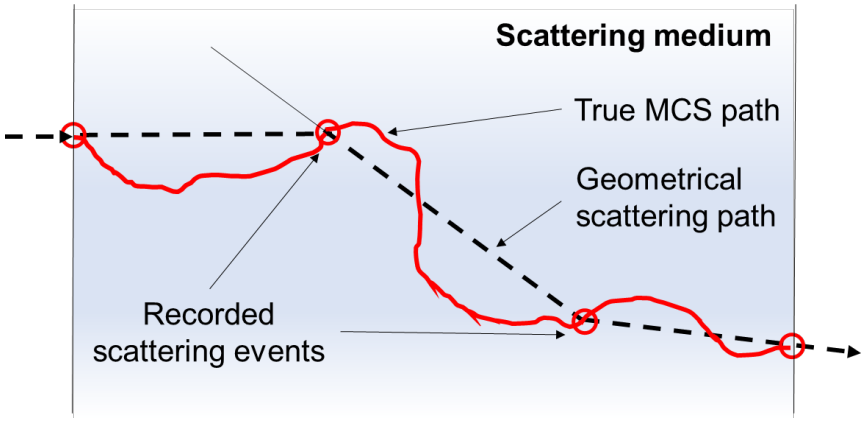

Figure 2.8 Illustration of true (solid red curve) and geometrical (dashed straight lines) scattering paths in the medium between the recorded scattering events.

Multiple Coulomb scattering approximation

The multiple Coulomb scattering (MCS) approximation using Gaussian distribution has been developed by Highland (Highland, 1975) and Lynch-Dahl (Lynch & Dahl, 1991) to search a simple representation of the complex physics models. The initial form of MCS approximation for a singly charged particle was devised by Rossi and Greisen (Rossi, Bruno and Greisen, 1941). The standard deviation, σ_θ, can be estimated by (i) material properties and (ii) muon momentum and it is given by

$$\sigma_\theta = 15\ [\mathrm{MeV}]\frac{\sqrt{X/X_0}}{p\beta} \tag{2-30}$$

where X is the length of scattering medium, X_0 is the radiation length, p and β are the momentum and speed of singly charged particle. Radiation length, X_0, is one of the nuclear properties and it can be found in the Particle Data Group library (Particle Data Group, 2020; Tsai, 1974). For composite and unconventional material, the X_0 value can be fairly (< 1% error) approximated by the following analytical formula (P.A. Zyla et al., 2020)

$$X_0[g/cm^3] = \frac{716.4A}{z(z+1)\ln\left(\frac{287}{\sqrt{z}}\right)} \tag{2-31}$$

where A is the atomic mass.

In 1974, (2-30) was extended by Highland by including a correction term which is proportional to the logarithm of X/X_0

$$\sigma_\theta = 14.1[\mathrm{MeV}]\frac{\sqrt{X/X_0}}{p\beta}\left[1+\frac{1}{9}\log_{10}(X/X_0)\right] \tag{2-32}$$

Without a large number of hard scatterings (scatterings with a large angle) which result in a longer tail than Gaussian distribution, (2-30) and (2-32) successfully estimated the MCS angle distribution. However, the error level increases up to 20–30% for high-Z scattering materials and they only take into account singly charged particles, z=1. The improved MCS approximation model was developed by Lynch and Dahl in 1991 and it is given by

$$\sigma_\theta = \frac{13.6\ [\mathrm{MeV}]}{p\beta} z \sqrt{\frac{X}{X_0}} \left[1 + 0.088 \log_{10}\left(\frac{Xz^2}{X_0\beta^2}\right)\right] \tag{2-33}$$

This model successfully estimates MCS angle distribution within 11% error for every material (better for low-Z and worse for high-Z materials).

Unless a target object is extremely thin, a muon will undergo the multiple Coulomb scattering and the sum of successive random deflection angles can be approximated Gaussian distribution with a zero mean and (2-33) (Bethe, 1953)

$$f_{space}\left(\theta_{space} \mid 0, \sigma_\theta^2\right) = \frac{1}{2\pi\sigma_\theta^2} \exp\left(-\frac{1}{2}\frac{\theta_{space}^2}{\sigma_\theta^2}\right) d\Omega \tag{2-34}$$

$$f_{plane}\left(\theta_{plane} \mid 0, \sigma_\theta^2\right) = \frac{1}{\sqrt{2\pi}\,\sigma_\theta} \exp\left(-\frac{1}{2}\frac{\theta_{plane}^2}{\sigma_\theta^2}\right) d\theta_{plane} \tag{2-35}$$

where θ_{space} and θ_{plane} are the deflected angles in space and plane, and $d\Omega \approx d\theta_{plane,x} \times d\theta_{plane,y}$. The angular defection distribution in x- and y- directions are independent and $\theta^2_{space} \approx \theta^2_{plane,x} + \theta^2_{plane,y}$. Necessary quantities to describe the multiple Coulomb scattering are indicated in Figure 2.9. The incoming and outgoing (deflected) muons are denoted as μ and μ'. The initial muon direction is defined as z-axis, vertical and horizontal scattering directions are x- and y-axis, respectively. x_{plane} and y_{plane} are deflected lengths in x- and y-direction in the plane. The 2D scattering angle intensity map is illustrated in color. Red represents the high intensity of the muon scattering angle. The y-z plane projection is also included in Figure 2.9. The root mean square of y-directional deflection length is given by

$$y_{\mathrm{plane}}^{\mathrm{rms}} = \frac{1}{\sqrt{3}} z\, \sigma_\theta \tag{2-36}$$

where z is the z-directional length of the scattering medium shown in Figure 2.9.

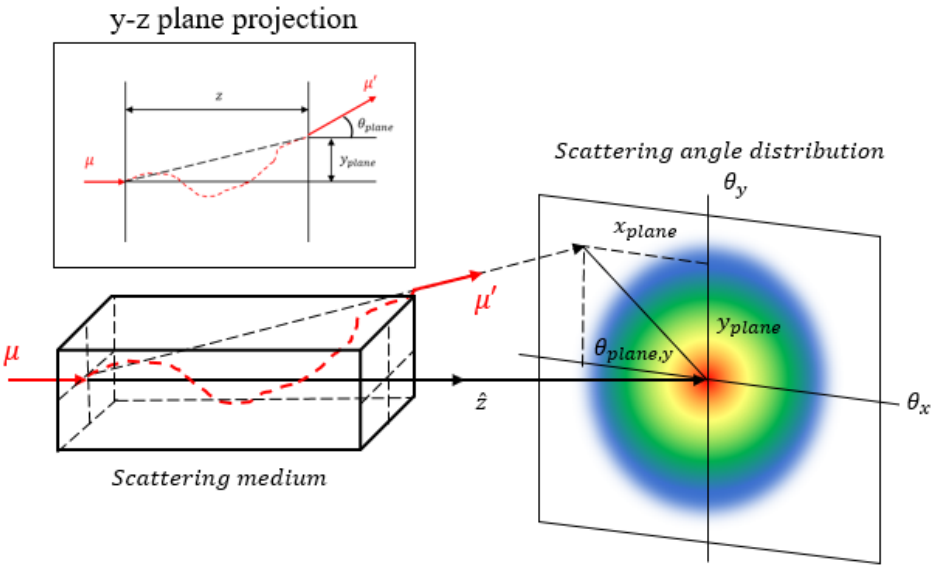

Figure 2.9. Multiple Coulomb scattering of a muon in the scattering medium and the estimated MCS angle distribution using 2D Gaussian approximation. Red and blue represent the high and low intensity of muon scattering angles, respectively.

2.2.3 Radiation length

Radiation length is defined as a mean distance over which a high energy electron loses all but *1/e* (≈ 0.3679) of its energy by the Bremsstrahlung radiation emission. For example, the radiation length, X_0, and critical energy, E_c, of an electron in copper are 12.86 g/cm^2 and 19.63 MeV as shown in Figure 2.10. The characteristic radiation length for various particles and materials can be calculated by

$$X_0 = \frac{A(4\alpha r_e^2 N_A)^{-1}}{Z^2[L_{rad} - f(z)] + ZL'_{rad}} \tag{2-37}$$

where Z, A, α, and N_A are the material atomic number and mass, fine structure constant, and Avogadro number, respectively. L_{rad}, L'_{rad}, and $f(Z)$ are defined as:

$$L_{rad} = \ln(184.15\, Z^{-1/3}) \tag{2-38}$$

$$L'_{rad} = \ln(1194\, Z^{-2/3}) \tag{2-39}$$

and

$$f(z) = z\sum_{n=1}^{\infty} n(n^2 + z) \approx 1.202z - 1.0369z^2 + 1.008\frac{z^3}{1+z} \qquad (2\text{-}40)$$

where $z = (\alpha Z)^2$ (Biscossa et al., 1998; Davies et al., 1954).

Especially, in high-Z number materials, such as tungsten ($Z = 74$), lead ($Z = 82$), uranium ($Z = 92$), plutonium ($Z = 94$), a high-energy charged particle predominantly loses its energy by the Bremsstrahlung radiation whereas the low- and intermediate-energy charged particles lose their energy by collisions and ionization, respectively. Figure 2.10 shows the electron energy loss rate in copper by the ionization and Bremsstrahlung for the energy range of 2 to 50 MeV. Energy loss by the Bremsstrahlung radiation emission becomes significant beyond the critical energy, E_c. Critical energy can be defined in either way as the energy in which two energy loss mechanisms, ionization, and Bremsstrahlung are equal or $|dE/dx|_{brem} \cong E/X_0$ (Rossi, 1965). Both definitions of E_c represent the energy when the Bremsstrahlung energy loss dominates the total energy loss of electrons.

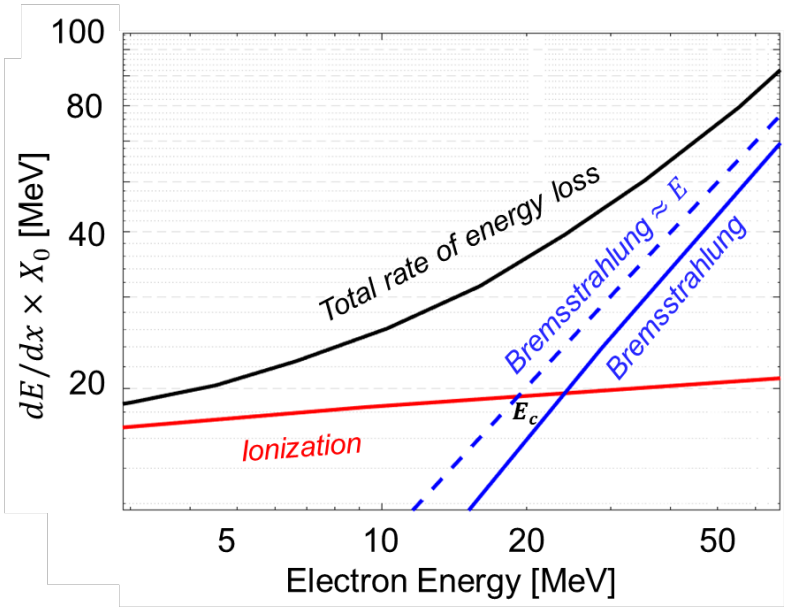

Figure 2.10. The rate of energy loss of electrons in copper ($X_0 = 12.86$ g/cm^2, $E_c = 19.63$ MeV) by the ionization and Bremsstrahlung for energy range 2 to 50 MeV.

2.3 Scientific Instruments in Muon Research

To develop a new scientific instrument, understanding and reviewing existing technologies must be ahead of everything. In this section, three major instruments in muon research are outlined: (i) muon detectors (trackers), (ii) photon detectors or optical sensors, and (iii) muon spectrometers. Muon detectors record incoming and outgoing muon signals using various types of radiation detectors. In general, a high-resolution muon detector is used to reconstruct the incoming and outgoing muon trajectories. In Section 2.3.1, two types of muon trackers–scintillator or gas drift tube detector–are presented. In many scientific instrumentations for nuclear and particle physics, photon signals are often utilized to detect radiation and measure particle momentum. Section 2.3.2 provides the characteristics of two major photon detectors, photoelectric and semiconductor optical sensors. In Section 2.2.3, four existing techniques to measure muon momentum, or muon spectrometers are extensively reviewed: (i) toroid and solenoid magnets, (ii) time-of-flight, (iii) Cherenkov ring imager, and (iv) time-of-propagation.

2.3.1 Muon tracker

In many cosmic ray muon applications such as muon tomography, the incoming and outgoing muon trajectories are reconstructed by measuring the location and direction of muons at the detectors. In this section, two types of muon trackers, scintillators and gas drift-tube detectors, are explored which are typically used to track muon trajectories (Anghel et al., 2015; Salvucci, 2011). In general, scintillation muon trackers have a worse spatial resolution (a few millimeters to centimeters) and efficiency compared to the gas drift-tube muon tracker. However, scintillation muon trackers are also widely used because they are easy to install and operate.

Scintillation fibers

At least two three-dimensional coordinates are required to reconstruct the straight muon trajectory in the space. A typical configuration of muon tracking system using scintillation fibers is shown in Figure 2.11. Each muon tracker consists of horizontal and vertical arrays of scintillation fibers to provide x- and y-coordinates, respectively (x-, y-, and z-directions are shown in Figure 2.11). For instance, since the heights (z-coordinate) of upper and lower muon trackers (1 and 2) are given by z_1 and z_2, two three-dimensional coordinates for the incoming muon trajectory

are successfully reconstructed. In the same manner, the outgoing muon trajectory is also reconstructed using two muon trackers (z_3 and z_4). The methods and mathematical processes to reconstruct muon trajectories in the muon tomographic imaging algorithm will be discussed in Section 2.4.

Gas drift-tube detectors

Similar to the scintillation fiber muon trackers, arrays of gas drift tube muon detectors are placed horizontally and vertically to provide x- and y-coordinates of muon position. However, a gas drift-tube provides additional spatial information within the detector because electrons emitted by muon interaction in the gas are attracted by the anode in the center as shown in Figure 2.12. By measuring the time from each gas drift-tube in a few nanosecond level, the spatial resolution can be improved by approximately 50–100 μm (Kume et al., 2016; Salvucci, 2011). The high spatial resolution in reconstructing muon trajectory leads to the high momentum measurement resolution in the magnetic spectrometers and high imaging resolution in muon tomography.

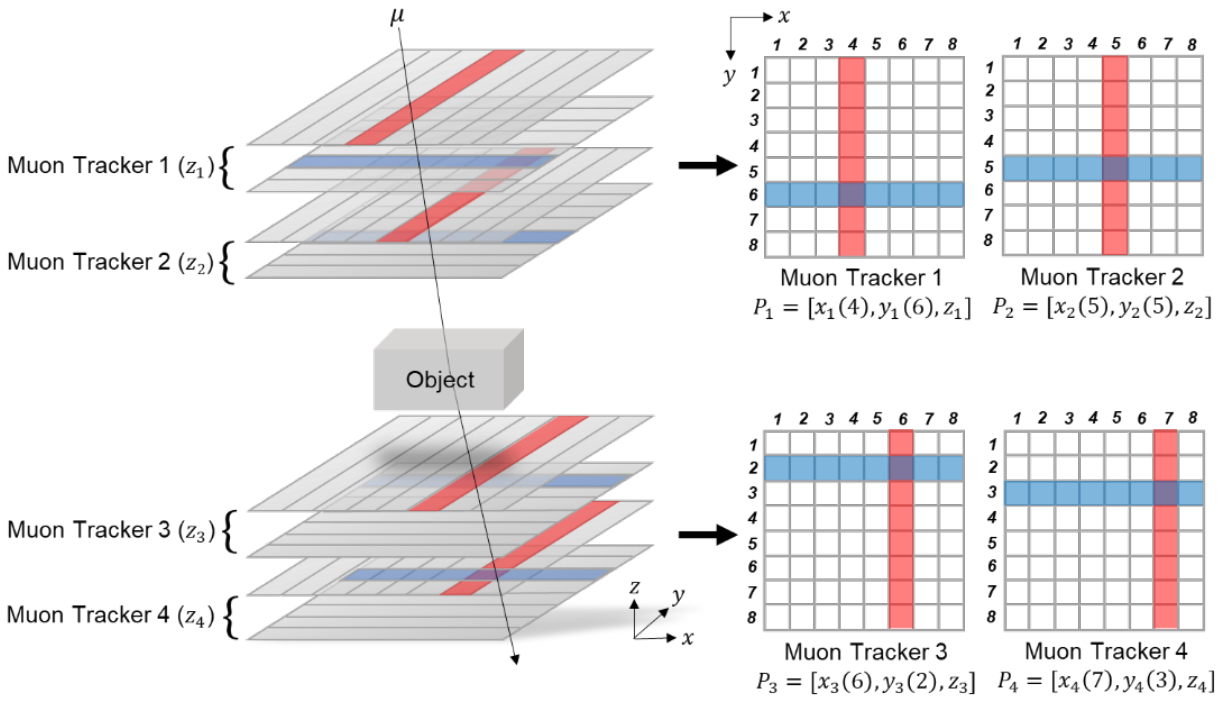

Figure 2.11. Overview of a typical configuration of upper and lower two-fold scintillation muon trackers to reconstruct incoming and outgoing muon trajectories.

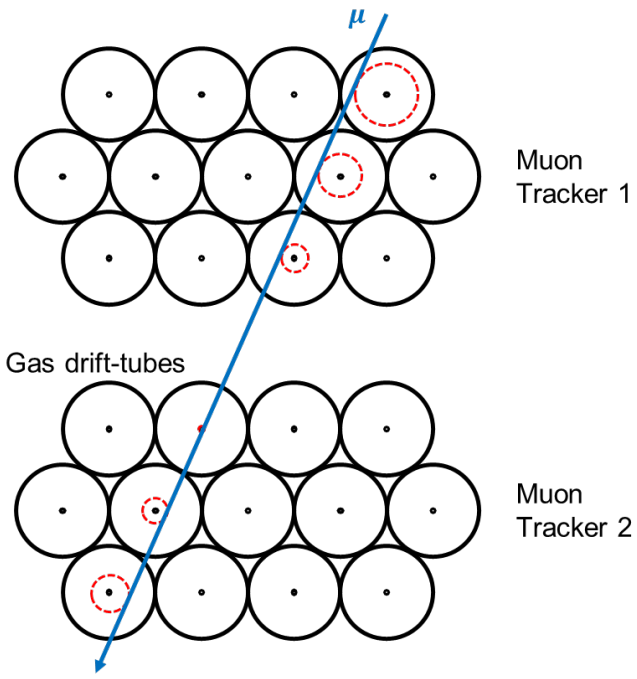

Figure 2.12. The Schematic diagram of tracking a muon trajectory using two arrays of gas drift tubes.

2.3.2 Photon detector

In nuclear and particle physics, photon signals which are produced by the interactions between particles and matter, provide significant information such as particle identification (PID) and energy. In many physics and engineering applications, photon signals are recorded and analyzed to detect radiation or identify particle signals. The electromagnetic (EM) waves have a wide range of wavelength spectrum. Figure 2.13 shows the EM spectrum and general classifications in terms of wavelength. Most photon detectors are sensitive to the ultraviolet (UV), visible (VIS), and infrared (IR) lights in the EM wavelength spectrum. Therefore, a high-energy particle or even photon with a high frequency, e.g., x-rays or gamma-rays, needs to be converted to the UV, VIS, or IR photons to be efficiently detected by photon detectors. Then, the detected photons are converted to electric signals to be read out. In this Section, two major photon detectors are reviewed: (i) photoelectric and (ii) semiconductor optical sensors. In addition, a wavelength shifting fiber that guides photons to the detector is also presented.

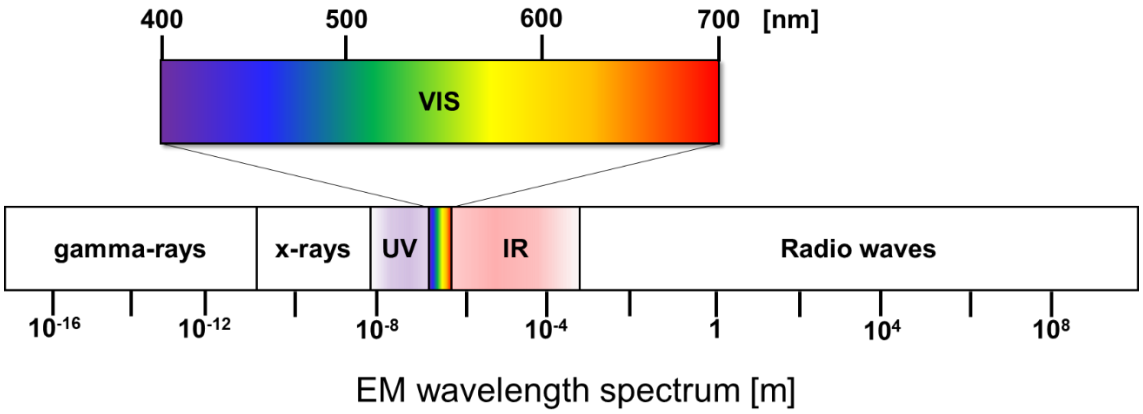

Figure 2.13. Electromagnetic wavelength spectrum and general classifications in terms of wavelength.

Photoelectric detectors

Emission of photoelectrons

The photoelectric detector is built based on the photocathode which emits electrons when a material absorbs incident photons and transfers enough energy to electrons. The excited electrons migrate to the surface of the photocathode and ultimately escape from it. These electrons are called photoelectrons. To generate photoelectrons, an incident photon must have enough energy so that the excited electron overcomes a potential barrier of metal. A general condition of the photoelectric effect is

$$h\nu > \Phi \tag{2-41}$$

where $h\nu$ is the single Incident photon energy and Φ is the work function, or a potential barrier of metal. The maximum electron kinetic energy, $E_{e,max}$, is given by

$$E_{e,max} = h\nu - \Phi \tag{2-42}$$

Using the condition for the photoelectric effect in (2-41) and (2-42), the threshold photon wavelength can be determined. In general, the potential barrier level of metal, Φ, is greater than 3 eV. It means that the corresponding electromagnetic wave has to have a wavelength shorter than approximately 400 nm. In order to be sensitive to visible and infrared lights, the semiconductor

which has a lower potential barrier can be considered. In addition, the photocathode has to have a thin layer, a few nanometers, to minimize the surface barrier and maximize the electron emission rate. Photoelectrons are easily absorbed by the photocathode metal since their energy is normally too small to overcome the potential and surface barriers once they lose energy due to the Coulombic interactions.

Photoelectron Multiplication

Photoelectrons from the photocathode are accelerated to the dynode using applied voltage and emit more than one electron on its surface. The overall multiplication factor of the dynode is defined as (Knoll, 2010)

$$\delta = \frac{\text{number of electron emission on the suface of a dynode}}{\text{number of incident electron}} \tag{2-43}$$

BeO, MgO, and Cs_3Sb are commonly used for dynode metals because they emit 5 to 10 secondary electrons regardless of the incident electron energy. Since the signal from secondary electrons with a single dynode is too weak to measure, a series of dynodes are installed in the photomultiplier tube (PMT). For example, if δ is 5 and the number of dynodes (N) is 10, the expected number of secondary electrons at the final stage is approximately $\delta^N \approx 10^6$. Figure 2.14 depicts the major components and principles of PMT. When a thousand photoelectrons are produced from an incident photon in the photocathode and the scintillation pulse rate is 10^5, the average anode current, $\langle I \rangle$ is given by

$$\langle I \rangle = 10^3 \left[\frac{\text{primary } e_{ph}^-}{\text{photon}}\right] \times 10^6 \left[\frac{\text{secondary } e_{ph}^-}{\text{primary } e_{ph}^-}\right] \times 10^5 \left[\frac{\text{photons}}{\text{sec}}\right] \times (1.6 \times 10^{-19})\,[C/e] = 16\,\mu A \tag{2-44}$$

This current level is measurable.

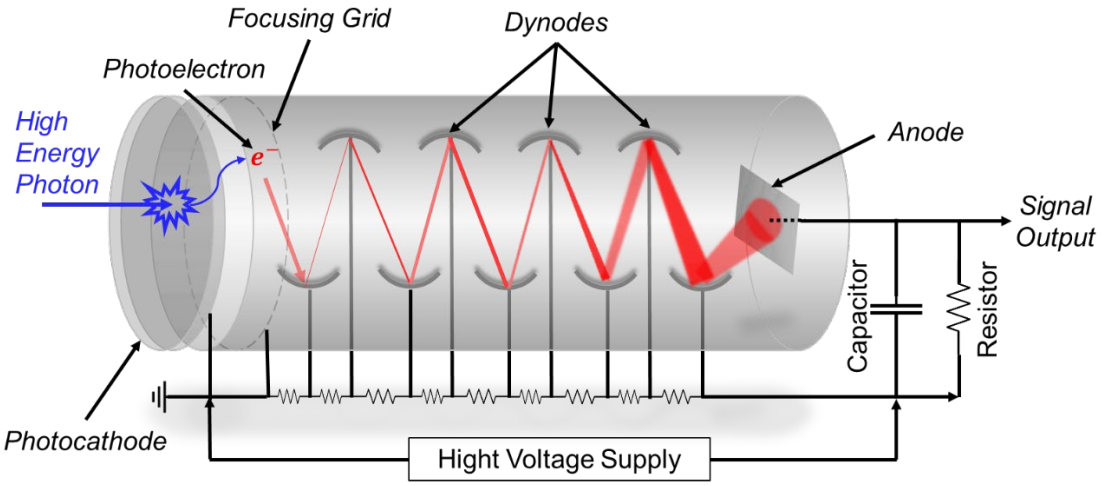

Figure 2.14. Operation principles and major components of photomultiplier tube (PMT).

Semiconductor detectors

Principle of semiconductor detectors

For semiconductor materials, silicon (Si) and germanium (Ge) are known as ideal materials to build a particle detector. The average energies to produce a single electron-hole pair for Si and Ge are 3.76 and 2.96 eV at 77 K, respectively. More properties of Si and Ge semiconductors are summarized in Table 2.4. At room temperature, however, the numbers of free charge carriers in Si and Ge are much larger than the created electron-hole pairs by an incident particle. Therefore, it requires a depletion region fabrication which is a photodiode. It is a type of *p*-*n* junction semiconductor diode at reverse biased conditions. For example, in the silicon crystal, doping silicon with arsenic (As) becomes an n-type conductor (donor), and doping silicon with boron (B) becomes a *p*-type conductor (acceptor). A contact of *p*- and *n*-type conductors makes a diode and creates a depletion region in which charges are depleted. By applying the biased voltage, a depletion region is extended to the entire diode, becoming a near insulator. Under this condition, the currents only occur when an incident particle produces electron-hole pair in the depletion region as shown in Figure 2.15.

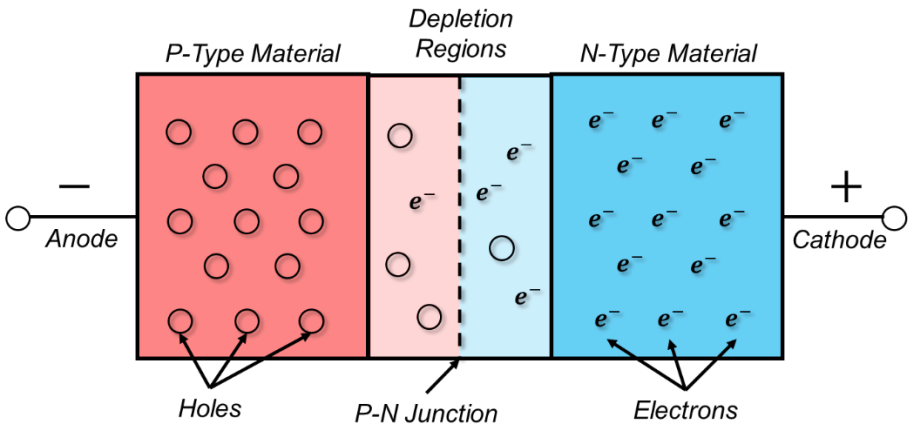

Figure 2.15. Holes, electrons, and depletion regions near *p-n* junction.

Table 2.4. Properties of silicon and germanium semiconductor materials.

		Silicon (Si)	Germanium (Ge)	Unit
	Atomic number (Z)	14	32	
	Forbidden Gap	1.115	0.665	Volts
300 K	Electron mobility (μ_e)	1450	3900	cm^2/Vs
	Hole mobility (μ_h)	500	1900	cm^2/Vs
	Energy per electron-hole pair	3.63	N/A	eV
77 K	Electron mobility (μ_e)	2.1×10^4	3.5×10^4	cm^2/Vs
	Hole mobility (μ_h)	1.1×10^4	4.2×10^4	cm^2/Vs
	Energy per electron-hole pair	3.76	2.96	eV

Silicon Photomultiplier (SiPM)

In the *p-n* junction silicon semiconductor diode, avalanche processes occur in the silicon structure when a reverse-biased voltage increases near the breakdown point. The avalanche process in the silicon semiconductor diode is analogous to the Townsend avalanche which occurs when electrons are strongly accelerated by the applied voltage and cause further ionization in the gas-filled detector (Paschen, 1889; Raizer, 1991). Beyond the breakdown voltage, V_{br}, the silicon semiconductor diode enters the Geiger mode region in which a single photon can build enough current to be measured. The current level changes over the reversed bias voltage in the Si

semiconductor diode and three different modes along the biased voltage and breakdown voltage of a *p-n* junction silicon semiconductor diode are illustrated in Figure 2.16. All processes happen in a single diode, called a single-photon avalanche diode (SPAD). In the Geiger mode region, the SPAD response (current pulse out) remains unchanged regardless of the number of absorbed photons. The SPAD is not able to provide information about the magnitude of incoming photons. To provide proportional signals to the number of incoming photons, an array of microcells (SPAD + quenching resistor) are designed and it is called a silicon photomultiplier (SiPM). If a spatial resolution (size of microcell) is small enough, each microcell is triggered by a single photon. Since the signals are accumulated in the SiPM system, the output signal is proportional to the incoming photon amplitude. In order to decrease the dead time of SiPM signals, a capacitor can be added to the microcell. Figure 2.17 shows the comparison of signal outputs of the standard and improved SiPM.

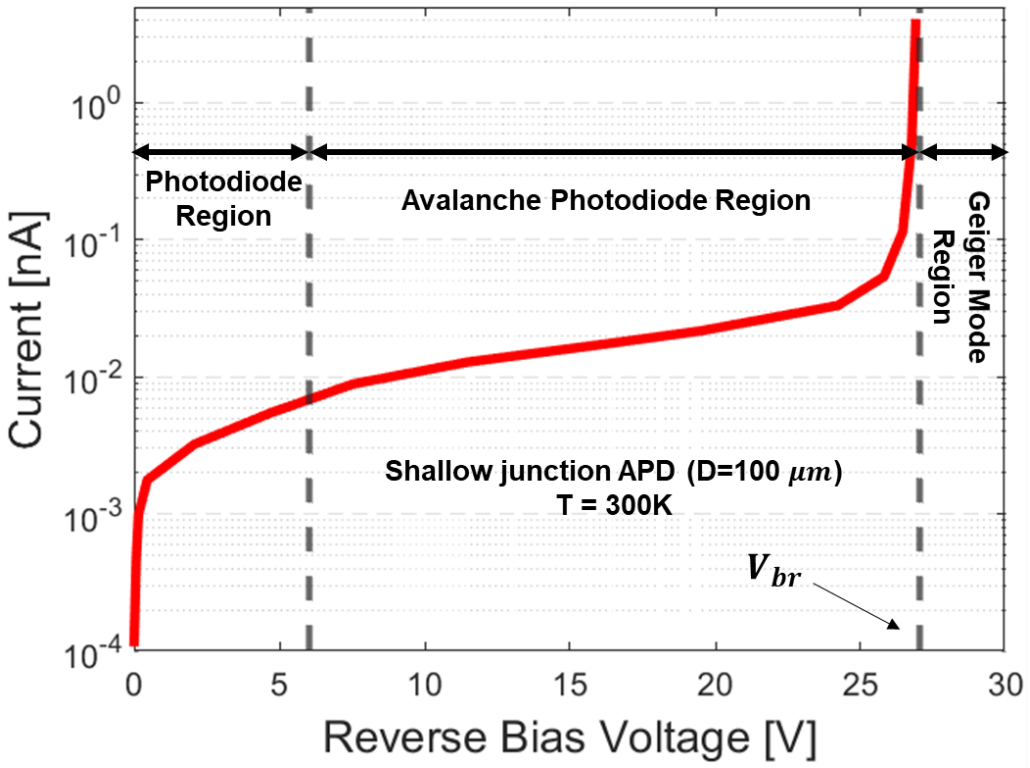

Figure 2.16. Current level changes over the reverse biased voltage in the solid-state silicon detector. V_{br} represents the breakdown voltage (Stewart et al., 2006).

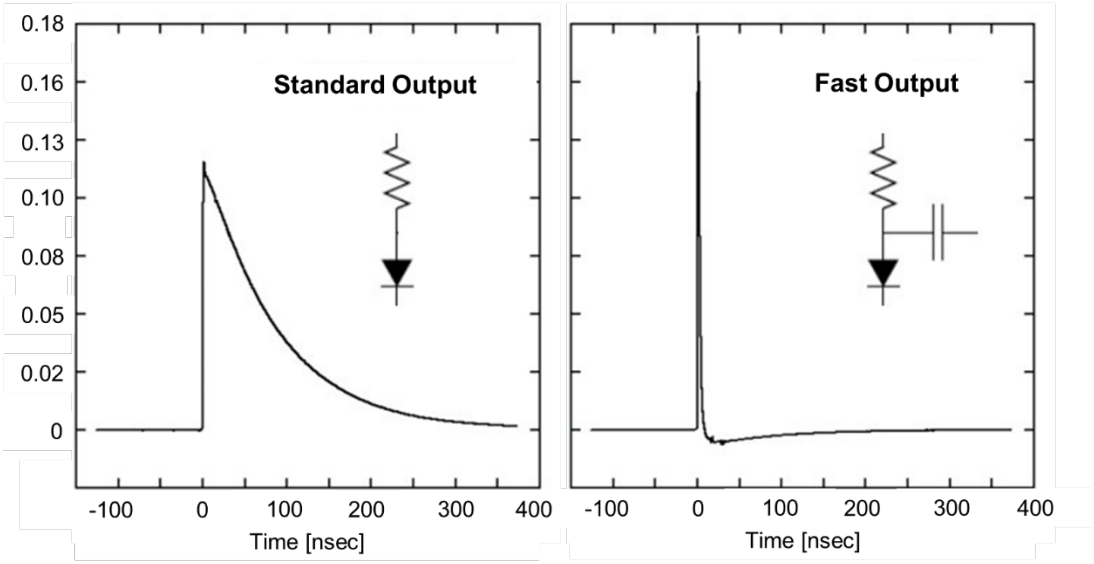

Figure 2.17. Examples of pulse output signal of standard (left) and improved (right) SiPMs (SensL, 2011).

PMT and SiPM

The technical characteristics of PMT and SiPM are summarized and compared in Table 2.5. In many applications, both photomultipliers are often used because neither one of them can perfectly replaces the other and each has unique advantages. For instance, more than 13,000 PMTs are instrumented in the huge neutrino observatory in Japan, Super-Kamiokande, to detect light from Cherenkov radiation emitted from the 50,000 metric tons of ultrapure water (Abe et al., 2014). However, a conventional PMT is replaced by SiPM because a fast response time and its compactness are preferred in medical imaging applications.

Table 2.5. Characteristics of PMT and SiPM.

	Photomultiplier Tube (PMT)	Silicon Photomultiplier (SiPM)
Principle	Vacuum tube	Solid state
Gain	$\sim 10^6$	$\sim 10^6$
Response time	$\sim 2\ ns$	$\sim 100\ ps$
Size	$5 \sim 10\ cm$	Single Si photodiode: $\sim 25\ \mu m$ SiPM Array: $\sim mm^2$
Operating Voltage	$\sim kV$	$\sim V$
Quantum Efficiency	$< 20\%$	$\sim 90\%$
Electric and Magnetic field	Affected	Immunity
Photon Resolution	Low	High
Dark current noise	Low ($< kHz$ per mm^2)	High ($\sim 100\ kHz$ per mm^2)

Wavelength shifter

A wavelength shifter is a scintillator. However, it is specifically designed for shifting the wavelength of EM wave from UV to VIS or IR light. A wavelength shifting (WLS) fiber is a combination of wavelength shifter and optical fiber such as an optical fiber doped with WLS material. A wavelength shifter is made of a material that absorbs high-frequency photons and emits low-frequency photons. In the particle detector, WLS is used to absorb blue and ultraviolet photons (200–450 nm) and emit lights wavelength of 450–600 nm (green in the EM wavelength spectrum) in which the spectral photon detection efficiency of PMT or SiPM is maximized (Figure 2.18). A WLS is widely used as a form of guide tube, fiber, or plastic to be flexibly applied to various geometries of photon emitters and detectors. For example, a wavelength-shifting optical module (WOM) is developed for application in the ice-Cherenkov neutrino detectors (Hebecker et al., 2016).

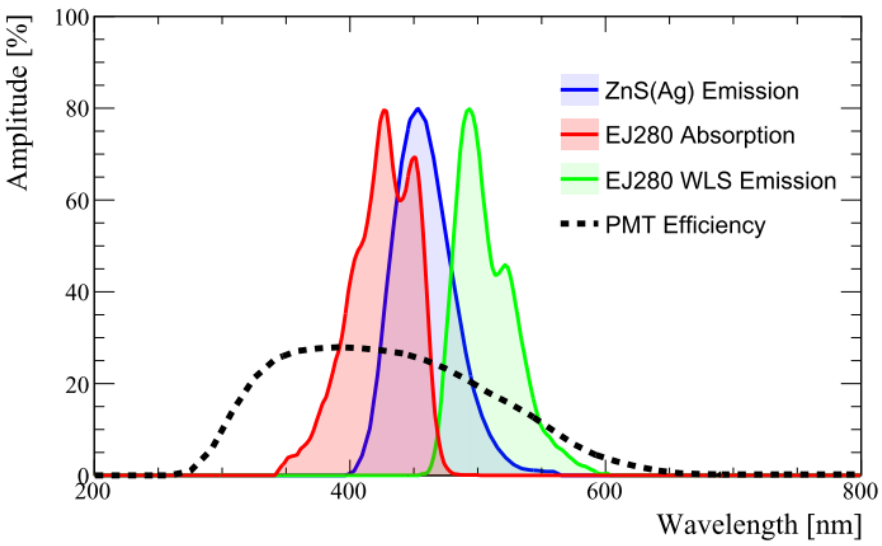

Figure 2.18. Example of absorption and emission spectra of wavelength shifters (Stowell et al., 2021). Reprinted from Stowell et al. (2021), with the permission of IOPscience.

2.3.3 Muon spectrometer

Although muons have a very small nuclear interaction cross-section, they are easily detected because they are charged and have a relatively long-lifetime, 2.2 μsec. A muon momentum measurement typically requires complex and huge spectrometers such as CMS (Compact Muon Solenoid) (CMS-Collaboration, 2010), ATLAS (A Toroidal Large hardon collider ApparatuS) (CERN & LHCC, 1997) at LHC, LEP detectors Cosmo-Aleph (Grupen et al., 2008), and L3+C (Adriani et al., 2002). For the atmospheric muon detection, techniques using a strong magnetic field, transition radiation, or muon scattering angle are mainly considered. For example, MACRO detector uses transition radiation to measure high-energy muons (100 GeV to 1 TeV) and rock absorber layers to measure low-energy muons (< 40 GeV) instead of using a strong magnetic field (Baldetti et al., 1988). On the other hand, both Okayama muon telescope and BESS-TeV spectrometer use uniform magnetic field strengths of 1.8 and 1 T, respectively (Motoki et al., 2003; Wadaa et al., 1996). In order to integrate muon momentum information into the existing muon tomography system, following parameters must be considered in a new muon spectrometer design, (i) compactness, (ii) low muon attenuation and absorption rate, (iii) good resolution, (iv) low muon scattering and deflection rate, and (v) high efficiency. Most existing muon spectrometers only satisfy one or two conditions. As a reference, four muon spectrometers

are introduced in the following sections: spectrometers based on (i) a strong magnetic field, (ii) time-of-flight, (iii) Cherenkov ring images, and (iv) time-of-propagation.

Magnetic spectrometer

Strong magnets are used in CMS (solenoid, B ≅ 4 T) and ATLAS (toroid, B ≅ 1 T) (Campi et al., 2007; Kate, 2006) to measure muon momentum. In both designs, muon momentum is calculated by measuring a curvature of muon trajectory under a uniform magnetic field. The bending radius of muon trajectory, R, is given by

$$R = \frac{p_\mu}{q|\boldsymbol{B}|} \tag{2-45}$$

where $|\boldsymbol{B}|$ is the strength of magnetic field, p_μ and q are the muon momentum and charge, respectively. Using gas drift-tube muon trackers, the sagitta and chord length of muon trajectory are measured and they are shown in Figure 2.19. Muon momentum can then be expressed in terms of measured quantities when $s \ll L$ using the following equation

$$p_\mu[GeV/c] = \frac{0.3}{8}\frac{|\boldsymbol{B}|L^2}{s} \tag{2-46}$$

where L is the chord length and s is the sagitta. The relative momentum resolution depends on the number of measurement points and it is derived by R. Gluckstern (R.L.Gluckstern, 1963)

$$\left.\frac{\sigma_p}{p}\right|_{\vec{B}} = \frac{\sigma_x p_\mu}{0.3|\boldsymbol{B}|L^2}\sqrt{\frac{720}{(N+4)}} \quad (\text{for } N \geq 10) \tag{2-47}$$

where σ_p and σ_x are the momentum and position resolutions, N is the number of equidistant measurement points, x_1, x_2, ..., x_N. For instance, a muon spectrometer using a strong magnet requires a characteristic dimension of approximately 3.2 m in order to measure a 3 GeV/c muon

momentum with a 10% resolution when strength of the magnetic field is 3 T, a spatial resolution is 1 cm, and the number of measurement points is three.

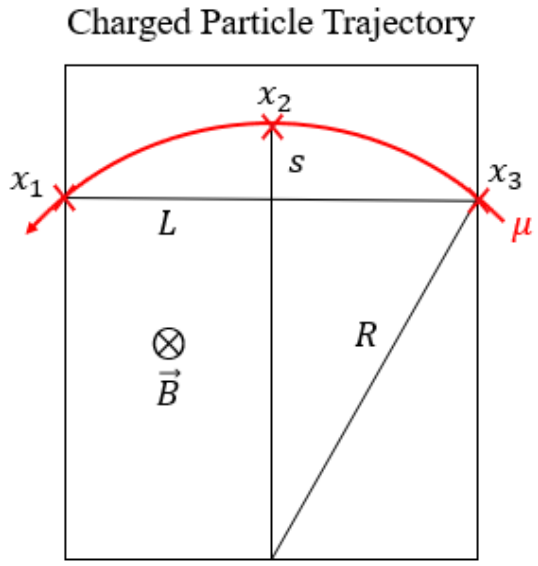

Figure 2.19. A charged particle trajectory under the action of a uniform magnetic field, ***B***.

A Toroidal LHC ApparatuS (ATLAS)

One example of muon spectrometer using a strong magnetic field can be found in the ATLAS in the Large Hadron Collider (LHC) at CERN. The inner components of ATLAS are mostly designed for measuring energies of hadrons and other elementary particles using electromagnetic and hadron calorimeters whereas the outer components are specifically designed to detect and measure muon momentum. Because muons can penetrate meters even for high-Z materials, they barely interact with inner components of ATLAS. Outer components of ATLAS are made of dense and thick layers of tracking devices. In addition, a superconducting toroid is installed to apply a strong magnetic field. The momentum measurement resolution of the ATLAS muon spectrometer is about 10–15% when a traverse muon momentum, p_T, is 1 TeV/c and 4% when p_T = 3 to 100 GeV/c. To guarantee the maximum muon momentum measurement resolution, the spatial error in sagitta, σ_s, must be less than 50 μm. The overview of ATLAS muon spectrometer is presented in Figure 2.20. Characteristic interactions of various particles–photon, electron, neutron, proton, neutrino, and muon–with calorimeters, trackers, and spectrometers of ATLAS are also illustrated in Figure 2.20 (Aefsky, 2012).

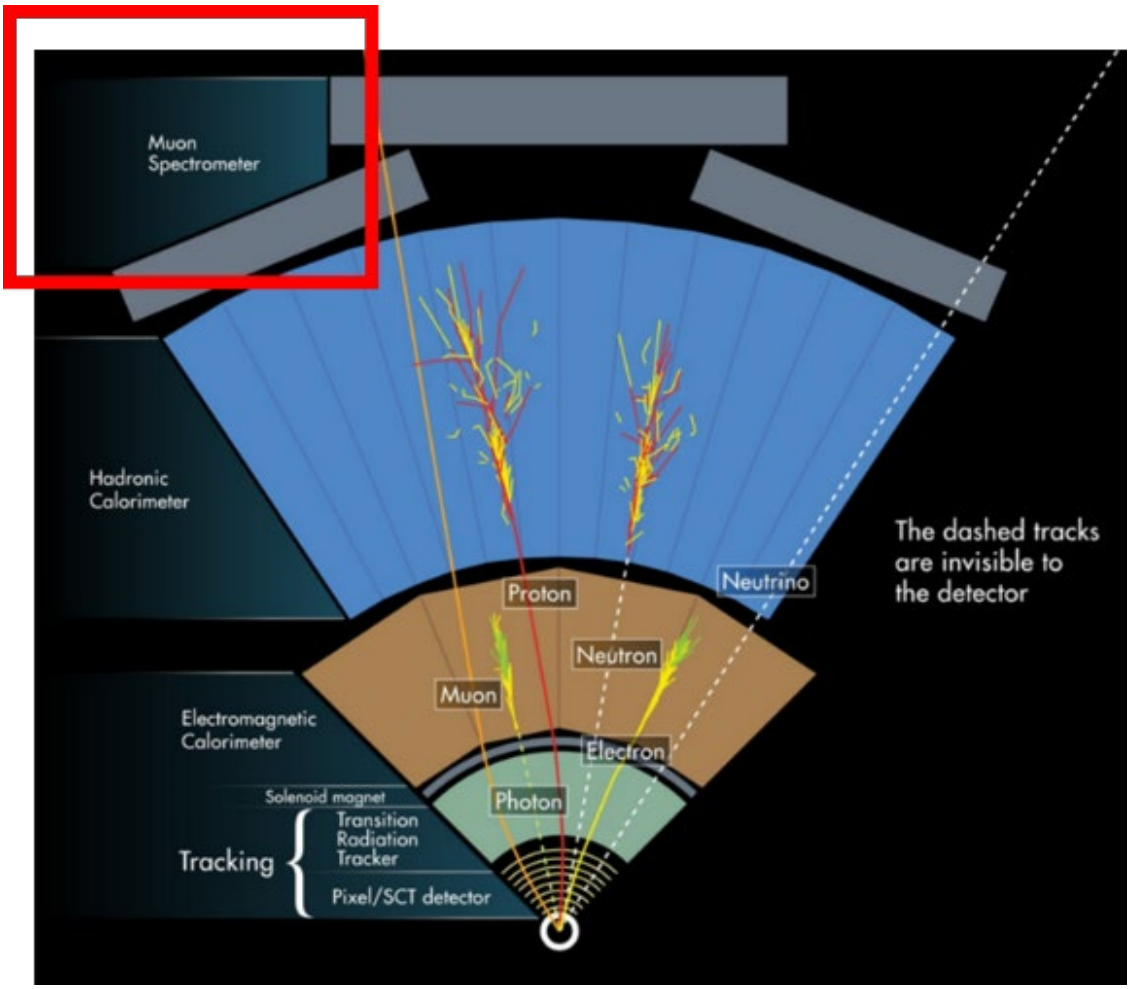

Figure 2.20. The overview of muon spectrometer in ATLAS at CERN (Aefsky, 2012). Reprinted from Aefsky on behalf of the ATLAS Collaboration (2012), with the permission of Elsevier.

Time-of-flight spectrometer

The principle of a time-of-flight muon spectrometer is to measure time difference between two detectors when a muon is detected by both muon detectors as shown in Figure 2.21. Muon velocity, v, can be determined by measuring the time difference, Δt, when the flight distance, L, is fixed. Given cosmic ray muons generally have high energy, they must be considered as relativistic particles. The relativistic momentum is given by

$$p = \gamma m_0 v \tag{2-48}$$

where m_0 and p are the particle rest mass and momentum, respectively. γ is the Lorentz factor defined as $(1-\beta^2)^{-1/2}$ and $\beta \equiv v/c$. Using the momentum-energy equation, we can write particle momentum, p, in terms of time and distance

$$E = \sqrt{(pc)^2 + (m_0c^2)^2} \tag{2-49}$$

$$p = \frac{m_0 cL}{\sqrt{c^2\Delta t^2 - L^2}}. \tag{2-50}$$

Although we assume that the rest mass of particle, m_0, has no uncertainty, there are certain levels of uncertainties in time and distance measurements. The uncertainty of particle momentum can be derived from measurement uncertainties of time and distance

$$\sigma_p^2 = \left(\frac{\partial p}{\partial t}\right)^2 \sigma_t^2 + \left(\frac{\partial p}{\partial L}\right)^2 \sigma_L^2 \tag{2-51}$$

$$\left(\frac{\partial p}{\partial t}\right)^2 = \frac{c^6 m_0^2 \Delta t^2}{(c^2\Delta t^2 - L^2)^3} \cdot L^2 \tag{2-52}$$

$$\sigma_p^2 = \frac{c^2\Delta t^2 (m_0c^2)^2}{(c^2\Delta t^2 - L^2)^3} \cdot [L^2\sigma_t^2 + \Delta t^2 \sigma_L^2] \tag{2-53}$$

$$\frac{\sigma_p^2}{p^2} = \left[\left(\frac{pc}{m_0c^2}\right)^2 + 1\right]^2 \cdot \left[\frac{\sigma_t^2}{\Delta t^2} + \frac{\sigma_L^2}{L^2}\right] \tag{2-54}$$

$$\left.\frac{\sigma_p}{p}\right|_{ToF} = \gamma^2 \sqrt{\frac{\sigma_t^2}{\Delta t^2} + \frac{\sigma_L^2}{L^2}} \tag{2-55}$$

The relative error of particle momentum, σ_p/p, depends on particle velocity, relative uncertainties in time and distance. For example, when a muon has momentum of 3 GeV/c and it passes two detectors with a distance, L, and the particle velocity is measured using timers with a time resolution of $\sigma_t = 1\times10^{-9}$ s and the spatial resolution of $\sigma_L = 1$ mm. Then the estimated distance to have a momentum resolution of 10 % is 8 m.

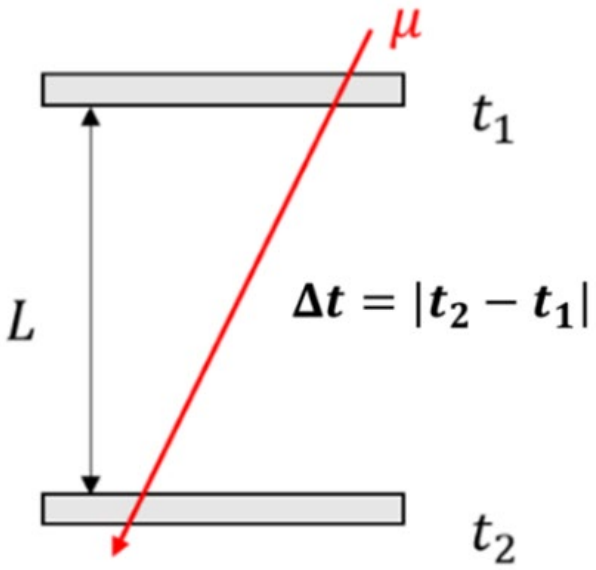

Figure 2.21. The principle of a time-of-flight muon spectrometer.

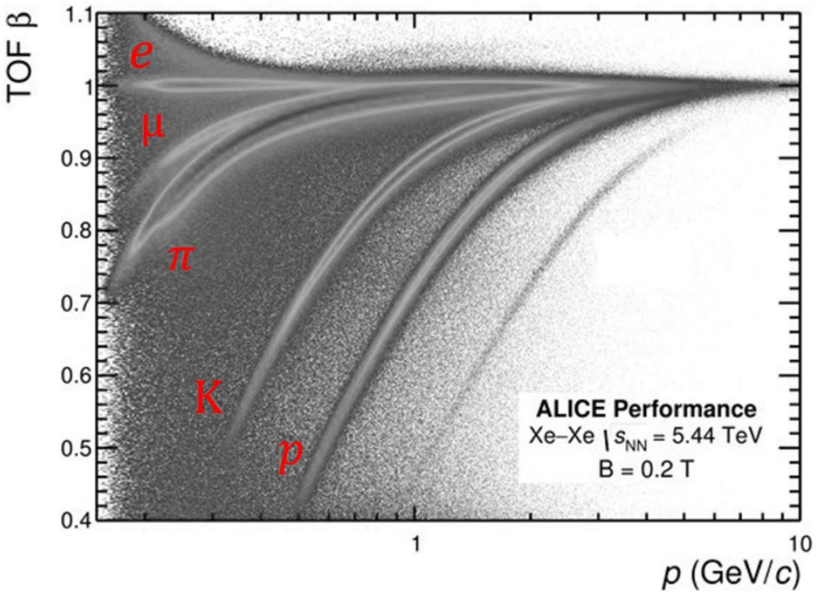

Figure 2.22. TOF experiment data for PID and momentum estimation in ALICE detector at CERN (Ragoni, 2018).

Cherenkov Detectors

Since the Cherenkov radiation was discovered by Pavel Cherenkov in 1934 (Cherenkov, 1934), it has been widely used in nuclear and particle physics to identify high-energy particles and measure particle velocity and mass. There exist various types of Cherenkov detectors including, (i) threshold Cherenkov detectors, (ii) Ring image Cherenkov detectors (RICH), (iii) time-of-propagation (TOP), and (iv) time-of-flight (TOF) Cherenkov detectors. In this section, we provide a brief overview of fundamentals of these four types of Cherenkov detectors. The background physics of the Cherenkov effect will be discussed and detailed in Section 3.1.

Threshold Cherenkov detector

Cherenkov radiation is observed only when the momentum of incident charged particle exceeds the threshold momentum level of optically transparent medium which is determined by (i) types of particle, or particle rest mass, mc^2, and (ii) index of refraction of the medium, n

$$p_{th}c = \frac{mc^2}{\sqrt{n^2 - 1}} \tag{2-56}$$

where p_{th} is the threshold momentum, c is the speed of light in a vacuum. For example, the expected Cherenkov threshold momentum for muons in the water is approximately 0.120 GeV/c when the rest mass of muon, $m_\mu c^2$ = 105.658 MeV and the refractive index of water is 1.33. As described in (2-56), Cherenkov threshold momentum depends on the type of particle and refractive index of the medium. Examples of threshold momenta for various particles and media are tabulated in Table 2.6. As shown in Table 2.6, each particle has a characteristic Cherenkov threshold momentum in a certain medium and these characteristics are used for the particle identification (PID). The experimental results of the PID separation using two aerogel media (n = 1.015, 1.030) in the momentum range between 0 to 6 GeV/c are shown in Figure 2.23 (Asaturyan et al., 2005).

Table 2.6. Cherenkov threshold momenta for various particles in various media.

Type of particle	Rest mass, m in MeV	Cherenkov threshold momentum, p_{th} in GeV/c		
		Water ($n = 1.33$)	Aerogel ($n = 1.015$)	CO_2 ($n = 1.0004$)
$\mu^{\pm}$	105.658	0.120	0.608	3.735
$\pi^{\pm}$	139.570	0.159	0.803	4.934
$K^{\pm}$	493.677	0.563	2.840	17.452
p	938.272	1.070	5.397	33.170

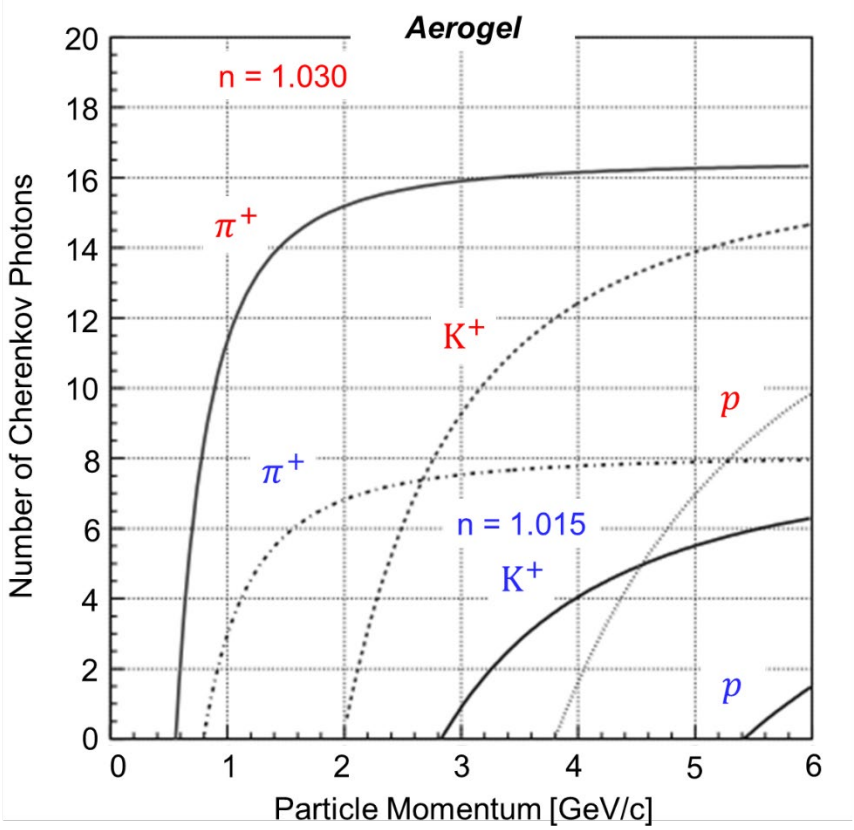

Figure 2.23. Expected number of Cherenkov photons in high-energy particle separation using aerogels of n = 1.015 and 1.030 (Asaturyan et al., 2005).

Ring Image Cherenkov detector (RICH)

One of the characteristics of Cherenkov radiation is that Cherenkov light is emitted toward the traveling direction as shown in Figure 2.24. The Cherenkov light emission direction depends on the phase velocity of the traveling charged particle and the refractive index of the medium. The

light emission direction is forward-biased and the Cherenkov angle, θ_c, is determined by the angle between the particle moving direction and wave front. Frank and Tamm theorized this relationship in 1937 (Frank, I. Tamm, 1937)

$$\cos\theta_c = \frac{1}{\beta n} \tag{2-57}$$

where β is the phase velocity of the charged particle. For example, when a muon has a velocity of β = 0.999 and travels in the water (n = 1.33), the corresponding Cherenkov angle will be approximately 41.2°. The Cherenkov angle is a key parameter to estimate muon momentum for the Ring image Cherenkov detector (RICH). The isotropic Cherenkov photon emission with θ_c results in the ring image as shown in Figure 2.24. The estimated muon momentum using the ring image is given by

$$\beta_\mu = \frac{1}{n}\sqrt{1+\frac{r^2}{L^2}} \tag{2-58}$$

$$p_\mu = m_\mu c\left[\frac{1}{\beta_\mu^2}-1\right]^{-1/2} \tag{2-59}$$

where r is the radius of the Cherenkov ring image and L is the muon traveling distance to the screen. The momentum resolution can be expressed with respect to spatial measurement resolutions for Cherenkov ring radius and distance, σ_r and σ_L.

$$\left.\frac{\sigma_p}{p}\right|_{RICH} = \frac{\gamma^2}{(r/L)^2+1}\sqrt{\frac{\sigma_r^2}{\mathrm{r}^2}+\frac{\sigma_L^2}{L^2}} \tag{2-60}$$

For instance, when a spatial resolution for both screen optical sensors and distance is 1 cm, the length of gas radiator is 1 m, and we assume that there is no uncertainty in the refractive index (n = 1.001), the momentum resolution of 3 GeV/c muon is approximately 26%.

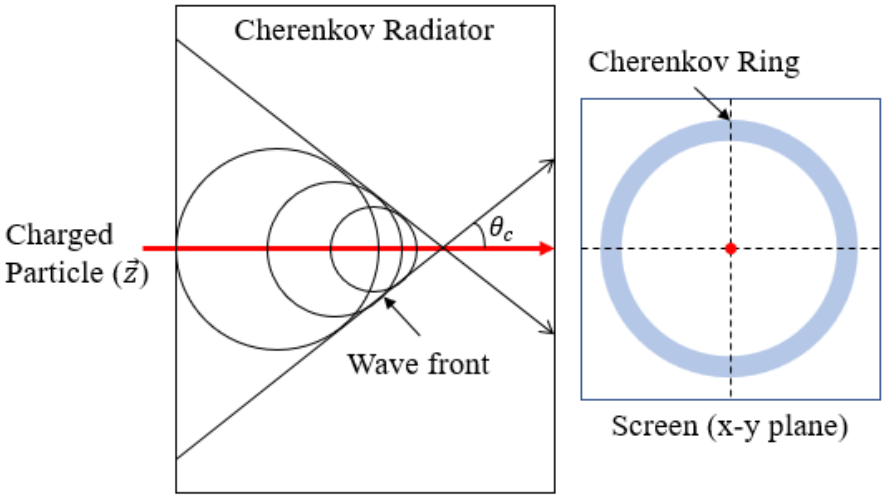

Figure 2.24. The wave front, Cherenkov ring image, and Cherenkov angle are shown when a charged particle travels in the Cherenkov medium (radiator). Forward-biased Cherenkov photon emission builds the Cherenkov ring on the screen (reconstructed by a array of optical sensors).

Ring image Cherenkov detector (RICH) provides a velocity information of particles by measuring the Cherenkov angle. The RICH detector can be incorporated with a magnetic tracker to obtain the PID accurately. Particle mass and velocity can be identified by measuring the curvature of particle track and radius of Cherenkov ring image, respectively. The reconstructed Cherenkov ring images for pion, kaon, and proton based on photon signals on the screen (array of optical sensors) in the RICH detector are shown in Figure 2.25 (Graf et al., 2010). Although all three particles have an identical momentum, 40 GeV/c, a proton has the smallest Cherenkov ring radius whereas a pion has the largest ring image because a proton is the most massive particle among them. The relationship between Cherenkov angle and particle momentum is shown in Figure 2.26 for various charged particles. The PID separation becomes more difficult as particle momentum increases because particle velocity, β, approaches unity. In order to exaggerate the PID separation, measured data can be reprocessed in terms of θ_c^2 and $1/p^2$ instead of θ_c and p. Both relationships, θ_c versus p and θ_c^2 versus $1/p^2$, are shown in Figure 2.26 (Abbon et al., 2011).

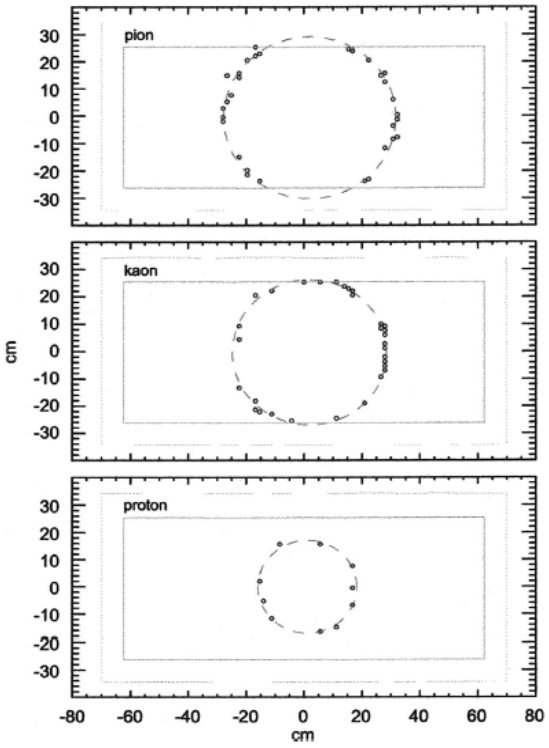

Figure 2.25. Reconstructed Cherenkov ring images of pion, kaon, and proton in RICH counter. All three particles have an identical momentum, 40 GeV/c (Graf et al., 2010). Reprinted from Graf et al. (2010), with the permission of Elsevier.

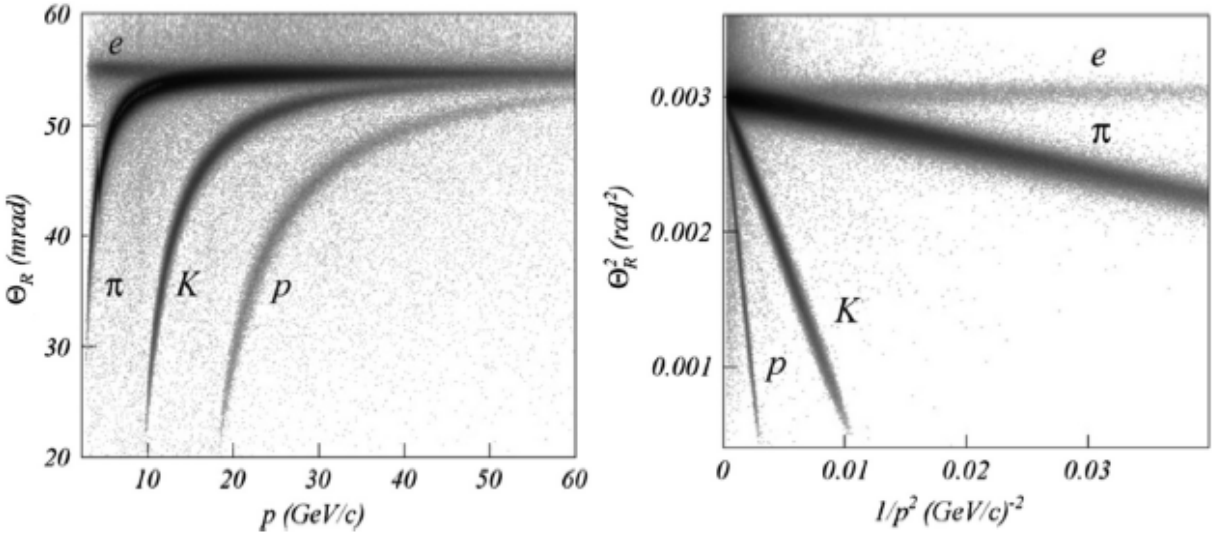

Figure 2.26. The PID using RICH experimental data of C_4F_{10} gas radiator. Cherenkov angle, θ_R (in this literature, authors used the subscription, R) in mrad versus particle momentum p in GeV/c (left). Reprocessed data, θ_c^2 versus $1/p^2$ (right) (Abbon et al., 2011). Reprinted from Abbon et al. (2011), with the permission of Elsevier.

Time-of-propagation (TOP) Cherenkov detector

When two different particles emit Cherenkov radiation, the heavier one has a more acute Cherenkov angle than the other. A time-of-propagation (TOP) Cherenkov detector uses the characteristic Cherenkov angle for PID separation. It measures a propagation time variance of different particles inside of a quartz bar of which all surfaces are highly reflective except one side where a photon detector is placed. If the Cherenkov angle is acute, more reflections within the quartz occur until Cherenkov photons arrive at the detector surface earlier than photons with a broad angle. For example, Cherenkov photons produced by a kaon have a small Cherenkov angle and take longer propagation time due to more reflections than that of a pion. The TOP Cherenkov detector requires a long and narrow bar radiator to enhance propagation time variance. According to the experimental results (Inami, 2011), the TOP variance between 2 MeV/c K^+ and π^+ is approximately 200 picoseconds in a 255×40×2 cm^3 quartz radiator. The schematic of Cherenkov radiation by kaon and pion in the TOP quartz radiator is shown in Figure 2.27.

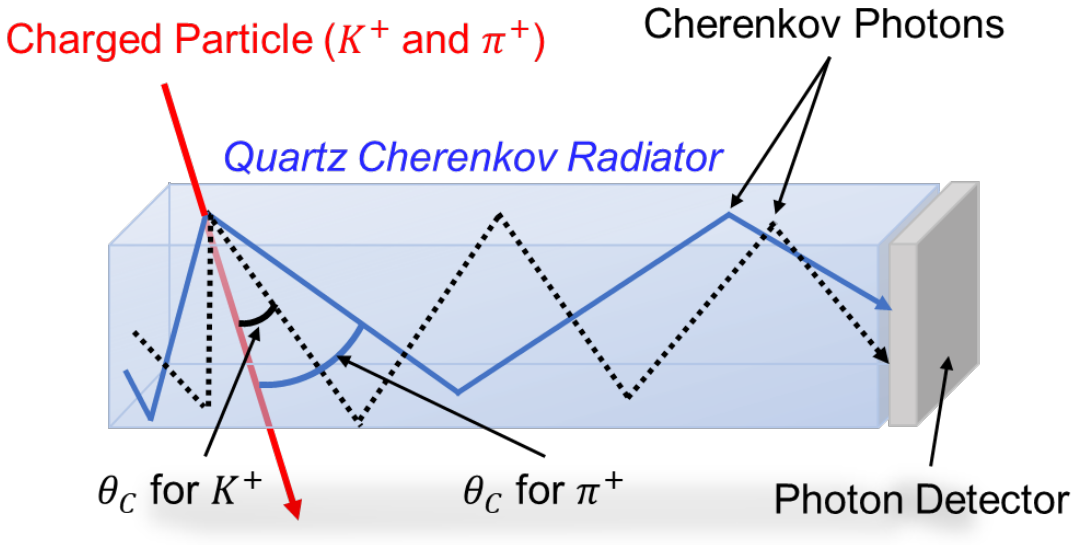

Figure 2.27. Schematic diagram of Time-of-propagation (TOP) of Cherenkov photons by K^+ and π^+ in a quartz radiator (Toru Iijima, 2010).

Time-of-flight (TOF) Cherenkov detector

Given the particle momentum is known, the time-of-flight (TOF) measurement yields the mass information of particle, and vice versa. For example, when there are two particles that have

the same momentum, p, but different mass, m_A and m_B, the flight time difference between two particles, $|t_A - t_B|$, is given by (Lippmann, 2012)

$$|t_A - t_B| = \frac{L}{c}\left|\sqrt{1+\left(\frac{m_A c}{p}\right)^2} - \sqrt{1+\left(\frac{m_B c}{p}\right)^2}\right| \tag{2-61}$$

where L is the given distance, c is the speed of light in a vacuum. The TOF method is incorporated with a RICH detector to produce photon signals for measurements. Additional time difference occurs when two particles produce Cherenkov rings on the screen due to the propagation time differences. Figure 2.28 describes the concept of the TOF-RICH measurement system. The time difference is determined using (2-61), $\Delta TOF = |t_{\pi+} - t_{K+}|$ and there is an additional term, ΔTOP which is a propagation time difference between two particles. Typically, the TOF method requires either a fine time resolution or a long distance to ensure precise measurement. For example, ΔTOF of the momentum of 2 and 4 GeV/c, are 147 and 37 picoseconds, respectively (T Iijima et al., 2008).

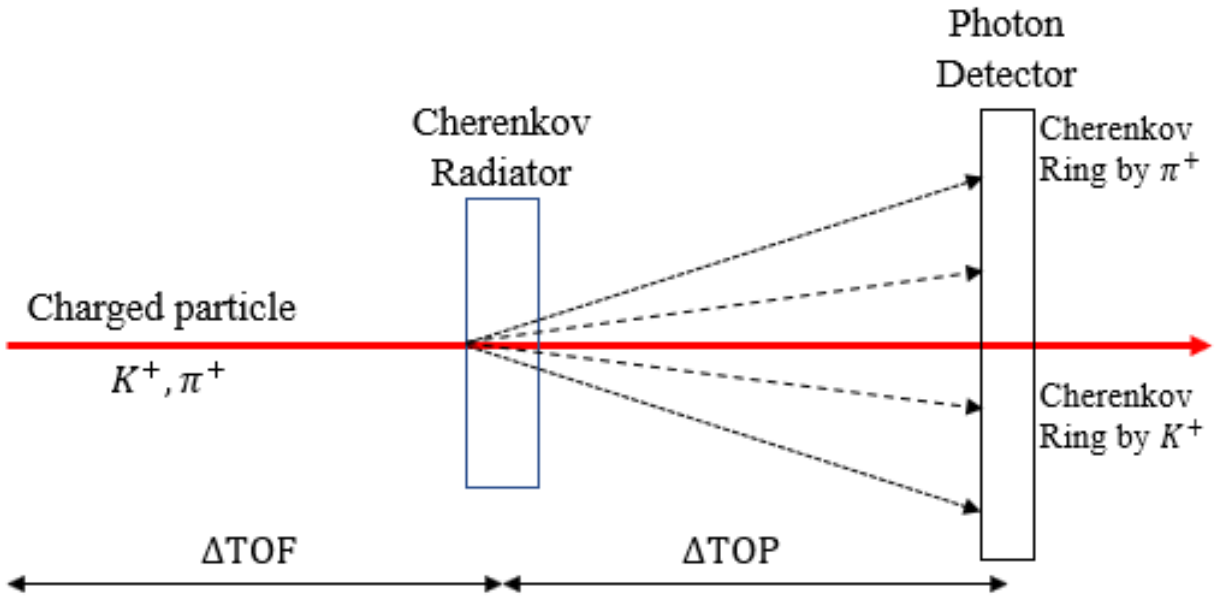

Figure 2.28. TOF-RICH detector to differentiate K^+ and π^+ (T Iijima et al., 2008).

2.4 Muon Radiography

Muon radiography, or muography, is one of the nondestructive imaging techniques to estimate the properties of materials and components using cosmic ray muons without causing physical damage. Especially, muon radiography becomes significant in monitoring large and dense materials such as spent nuclear fuel cask imaging (Stylianos Chatzidakis & Tsoukalas, 2015; Poulson et al., 2017), cargo scanning (Baesso et al., 2014), geotomography (Marteau et al., 2012; Tanaka et al., 2005) because conventional radiographic methods are limited, e.g., x-rays and gamma rays. For example, x-rays only penetrate a few centimeters in lead (Borozdin et al., 2003), and the increased x-ray photon energy does not improve the penetrating capability due to the pair production. In this Section, two major muon radiographic techniques, (i) muon transmission radiography and (ii) muon scattering tomography, are discussed. Muon transmission radiography uses the fraction of transmission and absorption of cosmic ray muons in the object whereas muon scattering tomography uses the multiple Coulomb scattering of cosmic ray muon. Although the muon transmission radiography is straightforward, simple, and fast, it suffers from the blurred images due to multiple Coulomb scattering and low signal-to-noise ratio (Lesparre et al., 2010; Nishiyama et al., 2016). The principles and imaging algorithms for muon transmission radiography and scattering tomography are detailed in Sections 2.4.1 and 2.4.2.

2.4.1 Muon transmission radiography

The first muon radiography was developed based on the fraction of transmission and absorption of cosmic ray muons in objects similar to the x-ray computed tomography. In the 1950s, the muon transmission radiographic technique was used by E. George to investigate the depth of the rock layer covering the underground tunnels in Australia (George, 1955). About 10 years later, L. Alvarez used the muon transmission radiographic technique to investigate the hidden chamber in the Great Pyramid of Giza (Alvarez et al., 1970).

Muon transmission radiography (also referred to as μCT) analyzes the absorption and transmission rate of cosmic ray muons. The μCT is analogous to the x-ray computed tomography (CT) because the CT reconstructs three-dimensional human body images using the multiple slices of planar images taken by x-rays. Similar to the x-ray CT, the forward and filtered back projection can be applied to the muon tomographic image reconstruction. The example of forward-projection

method for a square object in various perspectives are shown in Figure 2.29. The fraction of muon transmission or absorption is represented using a projected signal. $f(x,y)$ is a square density function and $R_\theta(x')$ is a projection onto the x' axis tilted at angles of θ with respect to x-axis. The projection intensity is given by

$$R_\theta(x') = \int_{-\infty}^{\infty} f(x,y)dy' \tag{2-62}$$

In practical cases, both $R_\theta(x')$ and $f(x,y)$ are not continuous functions, but functions of discrete variables. The system of equations using i number of muon events and j pixels is written by

$$r_i = \sum_{j=1}^{M} A_{ij} f_j \qquad \text{where } i = 1, 2, \dots N \tag{2-63}$$

$$\begin{bmatrix} r_1 \\ r_2 \\ \vdots \\ r_N \end{bmatrix} = \begin{bmatrix} A_{11}f_1 + A_{12}f_2 + \cdots + A_{1M}f_M \\ A_{21}f_1 + A_{22}f_2 + \cdots + A_{2M}f_M \\ \vdots \qquad\qquad \vdots \qquad\qquad \vdots \\ A_{N1}f_1 + A_{N2}f_2 + \cdots + A_{NM}f_M \end{bmatrix} \tag{2-64}$$

where r_i and f_j are the ith muon ray projection and jth pixel density function, A_{ij} is the material property of i–j pixel. To solve (2-64), various algorithms have been developed such as Algebraic Reconstruction Technique (ART) which is commonly used in the medical industry. The example of the forward-projection method for a two-dimensional arbitrary object is described in Figures 2.29 and 2.30. The practical examples of muon transmission radiography can be found in the investigation of the underground cavities at Mt. Echia performed by INFN (Amato et al., 2017) and one-sided muon tomography at CNL (Erlandson et al., 2018).

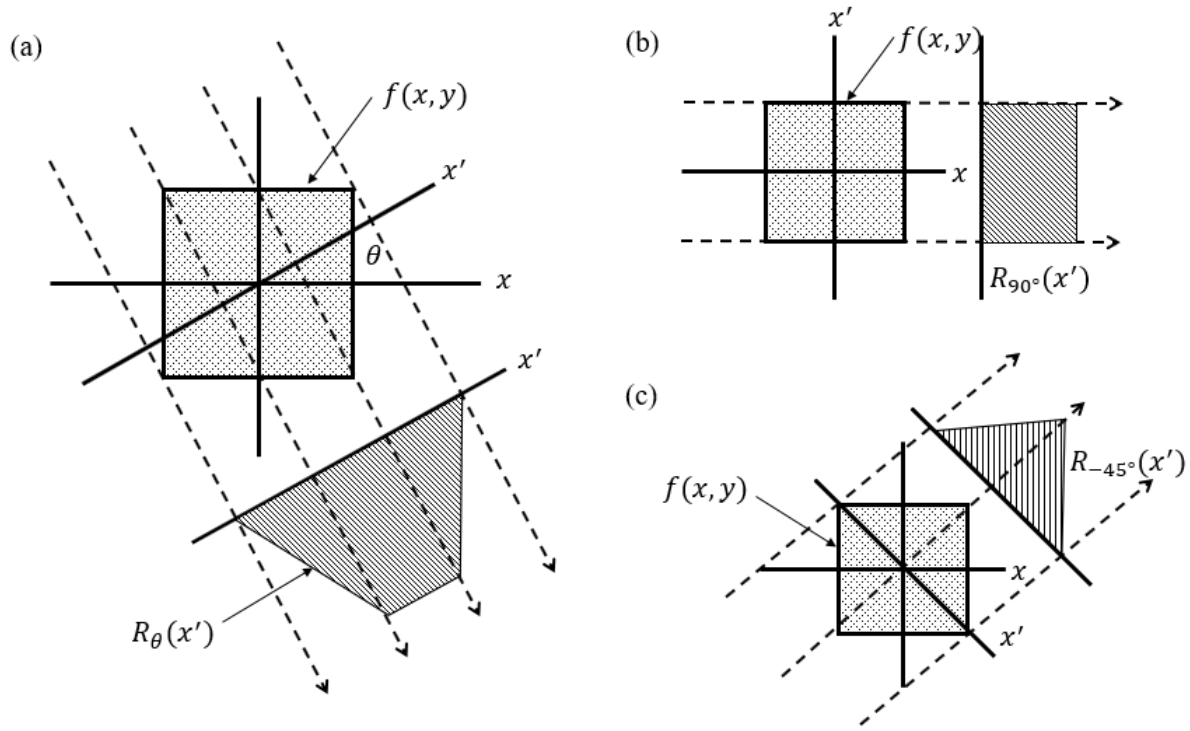

Figure 2.29. Forward projection for a two-dimensional square object in various perspectives: (a) arbitrary angle, θ, with respect to x axis, (b) 90°, and (c) -45° (Prince & Links, 2006).

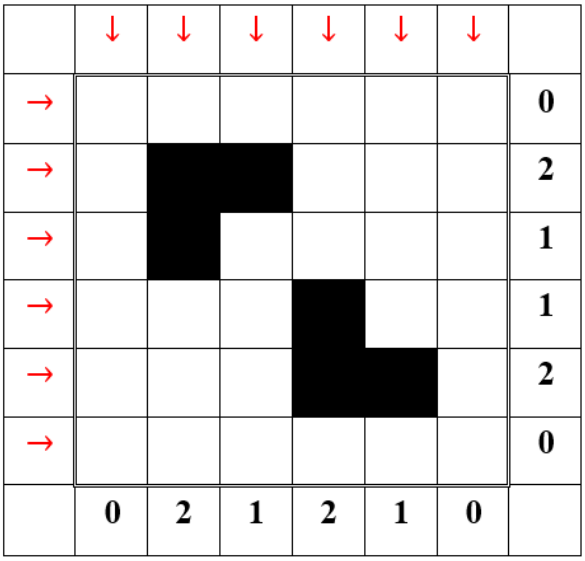

Figure 2.30. Forward projection for two-dimensional arbitrary object geometries (black) and muon beams (arrows).

- Arrows represent vertical and horizontal muon beams.
- Bold numbers represent the counts of black blocks that each beam encounters while it passes its row and column.
- $R_\theta(x')$: $\theta = 0°$ and $90°$, $x'_{0°}$ is x-axis and $x'_{90°}$ is y-axis.
- Number of detectors $(N) = 6$
- Number of pixels $(M) = 6$
- A: Property of pixel i, j. Here black or white.
- f: Assigned values. Black = 1, White = 0.

For 90° (Horizontal),

$$\begin{bmatrix} r_1 \\ r_2 \\ r_3 \\ r_4 \\ r_5 \\ r_6 \end{bmatrix} = \begin{bmatrix} A_{11}(0) + A_{12}(0) + \cdots + A_{16}(0) \\ A_{21}(0) + A_{22}(1) + \cdots + A_{26}(0) \\ \vdots \\ \vdots \\ \vdots \\ A_{61}f_1 + A_{62}f_2 + \cdots + A_{66}f_6 \end{bmatrix} = \begin{bmatrix} 0 \\ 2 \\ 1 \\ 1 \\ 2 \\ 0 \end{bmatrix}$$

Figure 2.31. Description of the forward projection method for two-dimensional arbitrary object geometries shown in Figure 2.30.

2.4.2 Muon scattering tomography

Muon scattering tomography was first developed by scientists in the Los Alamos National Laboratory in 2003. Unlike muon transmission radiography, it uses a cosmic ray muon scattering angle to estimate the properties of materials and components. Muon scattering tomography is especially useful to monitor and investigate large and dense (high-Z) materials in a background of low-Z materials such as a cargo scanning for special nuclear materials. As one of the efficient and fast image reconstruction algorithms for muon scattering tomography, the Point of Closest Approach (PoCA) algorithm developed by LANL is often used (L J Schultz et al., 2004) as an analogous to proton radiography (C. L. Morris et al., 2016). In the PoCA algorithm, muon multiple Coulomb scattering is not considered but a single muon scattering point is assigned to a voxel to reconstruct object images.

Point of Closest Approach Algorithm

We demonstrate that the unknown material can be specified using the MCS approximation by analyzing the muon scattering angle in Section 2.2.2. In addition to the muon scattering angle, we need to locate in which the scattering occurs to complete the 3D muon tomography. However, it is not possible to reconstruct the actual scattering history of muons in the medium because it is not only the result of randomized Coulomb scattering processes but also a sum of small deflection angles. Improved models to reconstruct multiple muon scattering trajectory in the scattering medium were developed based on Bayesian estimation and maximum likelihood expectation minimization (MLEM) (Benettoni et al., 2013; Stylianos Chatzidakis et al., 2018; Larry J Schultz et al., 2007; Wang et al., 2009). Nevertheless, one common imaging technique, a Point-of-Closest Approach (PoCA) (L J Schultz et al., 2004) is widely used to efficiently locate a scattering position because it is simple and fast enough for online analysis. It is noted that there is an assumption in the PoCA algorithm: (i) it only yields a single scattering point and (ii) incoming and outgoing muon trajectories are straight regardless of the actual muon trajectory. To find the PoCA point, we need to measure incoming and outgoing muon trajectories. The incoming muon trajectory, or initial muon trajectory before interacting with target objects, is reconstructed using two muon trackers. The outgoing muon trajectory, a final muon trajectory after interacting with target objects, is also reconstructed in the same manner. A scattering angle point is approximated by finding a midpoint of the shortest perpendicular line between incoming and outgoing muon trajectories. Then a corresponding voxel that includes a PoCA point is assigned as a PoCA voxel. The single muon scattering point using the PoCA algorithm in 3D and voxelated space of interest that surrounds target objects is graphically described in Figure 2.32.

To measure incoming and outgoing muon trajectories, typically two sets of muon trackers are installed above and below the target objects. Each set of muon trackers consists of two muon detectors and each detector yields muon position information. The measured muon positions in terms of Cartesian coordinate at four muon detectors, 1, 2, ,3 and 4 (from top to bottom), are

$$p_i = (x_i, y_i, z_i) \quad i = 1, 2, 3, \text{and } 4 \tag{2-65}$$

The unit vectors of incoming and outgoing muon trajectories, $\boldsymbol{u_1}$ and $\boldsymbol{u_2}$, can be written by

$$\boldsymbol{u_1} = \frac{p_2 - p_1}{\|p_2, p_1\|} \quad \text{and} \quad \boldsymbol{u_2} = \frac{p_4 - p_3}{\|p_4, p_3\|} \tag{2-66}$$

Both unit vectors can be extrapolated using coefficient vectors (2-68) and sets of extrapolated line segments, L_1 and L_2, are given by

$$L_1 = \boldsymbol{k_1} \cdot \boldsymbol{u_1} \quad \text{and} \quad L_2 = \boldsymbol{k_2} \cdot \boldsymbol{u_2} \tag{2-67}$$

$$\boldsymbol{k_1} = \left[k_{1,x}\,, k_{1,y}\,, k_{1,z}\right]^T \quad \text{and} \quad \boldsymbol{k_2} = \left[k_{2,x}\,, k_{2,y}\,, k_{2,z}\right]^T \tag{2-68}$$

The closest distance between two straight lines can be estimated by finding minimum distance between two points, l_1 and l_2, on lines, L_1 and L_2, respectively

$$D = \min\left\|l_{1,i},\ l_{2,i}\right\| \quad i = 1, \dots, N_L \tag{2-69}$$

where D is the distance and N_L is the number of points on L_1 and L_2. A PoCA point is defined as the closest point from L_1 and L_2, hence it is a midpoint of l_1 and l_2 and given by

$$P(x, y, z) = \frac{1}{2}\left[l_{1,m}(x, y, z) + l_{2,n}(x, y, z)\right] \tag{2-70}$$

where $l_{1,m}$ and $l_{2,n}$ are the points where $\| l_{1,\mathrm{m}}\,, l_{2,\mathrm{n}} \|$ equals to the line distance, D.

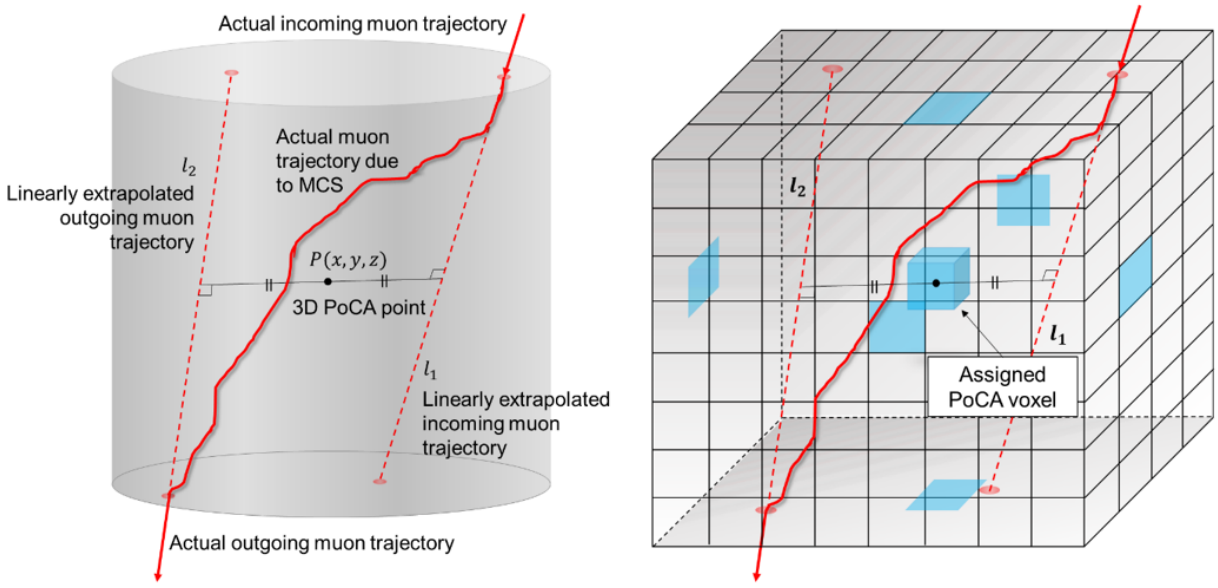

Figure 2.32. A single muon scattering point estimation using a PoCA algorithm. Two extrapolated straight lines, incoming and outgoing muon trajectories, l_1 and l_2, are reconstructed using two measured points in upper and lower muon trackers, respectively. A midpoint of the shortest perpendicular line between l_1 and l_2 is a PoCA point in 3D (left). A corresponding voxel PoCA which includes PoCA point is assigned in voxelated space.

To reconstruct the image of a target object, a muon scattering angle must be estimated using incoming and outgoing muon trajectories as shown in Figure 2.32. In 3D space, projected scattering angles on x-z and y-z planes for both incoming and outgoing muon trajectories are given by

$$\theta^{\text{in}}_{\text{xz-plane}} = \text{atan}\left(\frac{|p_{2,z} - p_{1,z}|}{|p_{2,x} - p_{1,x}|}\right) \tag{2-71}$$

$$\theta^{\text{out}}_{\text{xz-plane}} = \text{atan}\left(\frac{|p_{4,z} - p_{3,z}|}{|p_{4,x} - p_{3,x}|}\right) \tag{2-72}$$

$$\theta_{\mathrm{yz-plane}}^{\mathrm{in}} = \mathrm{atan}\left(\frac{\left|p_{2,z} - p_{1,z}\right|}{\left|p_{2,y} - p_{1,y}\right|}\right) \tag{2-73}$$

$$\theta_{\mathrm{yz-plane}}^{\mathrm{out}} = \mathrm{atan}\left(\frac{\left|p_{4,z} - p_{3,z}\right|}{\left|p_{4,y} - p_{3,y}\right|}\right) \tag{2-74}$$

where *i* and *C* represent muon detector numbers (*1, 2, 3,* or *4*) and components (*x, y,* or *z*) in the form of Cartesian coordinates, $p_{i,C}$. Furthermore, a spatial muon scattering angle, θ, can be estimated using computed projected plane angles, (2-71) to (2-74)

$$\theta \approx \sqrt{\Delta\theta_{xz}^2 + \Delta\theta_{yz}^2} \tag{2-75}$$

$$\Delta\theta_{xz} = \left|\theta_{\mathrm{xz-plane}}^{\mathrm{in}} - \theta_{\mathrm{xz-plane}}^{\mathrm{out}}\right| \tag{2-76}$$

$$\Delta\theta_{yz} = \left|\theta_{\mathrm{yz-plane}}^{\mathrm{in}} - \theta_{\mathrm{yz-plane}}^{\mathrm{out}}\right| \tag{2-77}$$

The computed spatial muon scattering angle is tagged along with a designated PoCA point (voxel in 3D or pixel in 2D) and these values are utilized for imaging and material identification. When two or more spatial muon scattering angles are recorded in a PoCA voxel (or pixel), the average scattering angle will be used

$$\theta = \frac{1}{N_{Voxel}} \sum \theta_i \qquad i = 1, 2, \ldots, N_{Voxel} \tag{2-78}$$

where N_{Voxel} is the number of recorded scattering angles in a PoCA voxel. Sometimes, a scattering angle is replaced by a scattering angle value or density, s_i, to magnify the scattering angle density in imaging reconstruction (Stylianos Chatzidakis et al., 2016)

$$s_i = \frac{1}{2}\left[{\Delta\theta_{xz}}^2 + {\Delta\theta_{yz}}^2\right] \tag{2-79}$$

2.5 Summary

Section 2.1 and 2.2 presented characteristics of cosmic ray muons and fundamental physics of muon interaction with matters such as energy loss and scattering mechanisms. In Section 2.3, the properties of state-of-art scientific instruments in muon research, e.g., muon detectors, optical sensors, and muon spectrometers, were summarized. At the end of Chapter 2, two muon radiographic technologies, muon transmission and scattering tomography, were outlined in Section 2.5.

3. MUON SPECTROMETER USING MULTI-LAYER PRESSURIZED GAS CHERENKOV RADIATORS

A portion of this chapter was previously published by *Scientific Reports*, **12**, 2559 (2022), "Fieldable muon spectrometer using multi-layer pressurized gas Cherenkov radiators and its applications," Bae. J and Chatzidakis, S. [DOI: 10.1038/s41598-022-06510-2]

A new method to measure muon momentum using multi-layer pressurized gas Cherenkov radiators is extensively discussed from methods to performance evaluations in this chapter. The fundamental physics, operational principle, and methods are outlined in Section 3.1. Then, the properties of four widely used Cherenkov gas radiators, CO_2, C_3F_8, C_4F_{10}, and R1234yf, are presented to be investigated as candidates for Cherenkov gas radiator in Section 3.2. In the Cherenkov muon spectrometer, Cherenkov lights are measured as signals whereas other optical light emissions are considered as noise. In Section 3.3, three major optical photon emission mechanisms in the gas medium, Cherenkov radiation, scintillation, and transition radiation, are discussed. The results from analytical models are compared with Geant4 Monte-Carlo muon transport simulations in Section 3.4. In the end of this section, the performance of Cherenkov muon spectrometer is evaluated in various perspectives and approaches. Section 3.4 not only describes methods for post-signal processing and noise analysis but also presents the results of reconstructed cosmic ray muon spectrum and system classification rate.

3.1 Operational Principle

Because muons are charged particles, they can induce Cherenkov radiation in the optically transparent media. In addition, unlike a solid or liquid medium, the index of refraction of gas medium can be varied by pressurizing and changing temperature. Therefore, the necessary muon threshold momentum levels for gas can be determined by carefully selecting the gas pressure. When a muon passes multiple gas radiators that are placed side-by-side, they will emit Cherenkov lights only when the actual muon momentum exceeds the threshold momentum. By measuring the Cherenkov signals in each radiator, we can then estimate the range of actual muon momentum.

3.1.1 Cherenkov effect

The idea of Cherenkov effect was firstly predicted by Oliver Heaviside in 1889. But it was not noticed because neither an electron nor theory of relativity was discovered until J. J. Thompson (1897) and A. Einstein (1905). Later, Cherenkov effect was re-discovered by Pavel Cherenkov (1934) and theoretically interpreted by I. Frank and I. Tamm (1937). Cherenkov radiation is a forward directional electromagnetic wave when a charged particle, e.g., an electron or a muon, travels in a dielectric medium at a velocity exceeding the speed of light in the medium. It is often compared to the sonic boom and shockwave fronts which occur when an object travels faster than the speed of sound (Mach number, $M > 1$) as shown in Figure 3.1 (L'Annunziata, 2016).

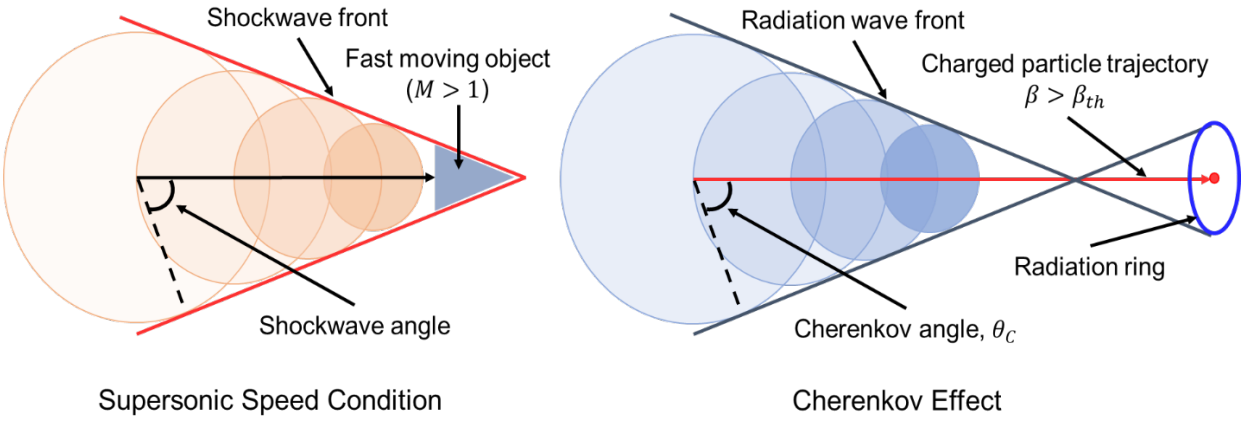

Figure 3.1. Conical waves created by a supersonic speed object ($M > 1$) in the air (left) and a charged particle traveling at the super-speed of light, $\beta > \beta_{th}$ in the transparent medium (right).

The threshold condition to induce Cherenkov radiation in the medium is given by

$$\beta > \frac{1}{n} \quad (\beta \equiv v/c) \tag{3-1}$$

where v is the velocity of the charged particle, c is the speed of light in a vacuum, and n is the refractive index of the medium. The velocity of the particle, β, is a function of particle's kinetic energy, E, and rest mass energy, $m_o c^2$ (Jelley, 1961)

$$\beta = \sqrt{1 - \left(\frac{1}{E/m_0c^2 + 1}\right)^2} \tag{3-2}$$

Cherenkov threshold velocity, energy, momentum, and angle

The threshold condition for a particle velocity can be written as a reciprocal of refractive index of the medium

$$\beta_{th} = 1/n \tag{3-3}$$

The corresponding threshold energy can be expressed by substituting (3-3) into (3-2),

$$E_{th} = m_0c^2\left[\frac{1}{\sqrt{1 - \frac{1}{n^2}}} - 1\right] \beta = \sqrt{1 - \left(\frac{1}{E/m_0c^2 + 1}\right)^2} \tag{3-4}$$

where γ_{th} is the threshold Lorentz factor, $(1 - \beta_{th}^2)^{-1/2}$. The threshold momentum is also a function of refractive index and the particle mass which described by (Asaturyan et al., 2005)

$$p_{th}c = \frac{m_0c^2}{\sqrt{n^2 - 1}} \tag{3-5}$$

Besides the Cherenkov threshold conditions, another important property of Cherenkov radiation is its directional photon emission. As described previously, Cherenkov photons are emitted as conical waves toward the direction of the particle's path. According to the theoretical model developed by Frank and Tamm, Cherenkov angle, θ_c, is a function of particle velocity and refractive index of the medium (Wilkinson, 2004)

$$\cos\theta_c = \frac{1}{\beta n} \tag{3-6}$$

The examples of Cherenkov threshold momenta and angles for various particles in the different media are summarized in Table 3.1.

Table 3.1. Cherenkov threshold momenta and angles for various particles in the different media.

Medium			Type of particles (mass in MeV)			
	$n-1$	p_{th} in GeV/c θ_c in degree	Electron (0.511)	Muon (105.658)	Pion (139.570)	Proton (938.272)
Air	2.73×10^{-4}	p_{th}	0.022	4.52	5.97	40.15
		θ_c	1.34	-	-	-
CO_2	4.5×10^{-4}	p_{th}	0.017	3.52	4.65	31.27
		θ_c	1.72	-	-	-
C_4F_{10}	1.4×10^{-3}	p_{th}	0.0097	2.00	2.64	17.73
		θ_c	3.03	2.32	1.64	-
Water	0.33	p_{th}	0.0006	0.12	0.16	1.07
		θ_c	41.25	41.21	41.18	39.27
Glass	0.45	p_{th}	0.0005	0.10	0.13	0.89
		θ_c	46.40	46.37	46.34	44.76

Note: Cherenkov threshold angles are computed when the incident particle has momentum of 3 GeV/c. Cherenkov radiation is not observed when p_{th} is greater than 3 GeV/c.

3.1.2 Lorentz-Lorenz equation

Unlike solid or liquid Cherenkov radiator, the index of refraction of gas can be changed by varying its pressure and temperature. The Lorentz-Lorenz equation describes the refractive index of a substance to its molecular polarizability and it is named after L. Lorenz and H. Lorentz. The original form of the Lorentz-Lorenz equation is

$$\frac{n^2-1}{n^2+2} = \frac{4\pi}{3} N\alpha_m \tag{3-7}$$

where n is the refractive index, α_m is the mean molecular polarizability, and N is the number of molecules per unit volume. For a gas radiator, $n^2 \approx 1$, the refractive index can be approximated using the molecular refractivity, A_m

$$n \approx \sqrt{1 + \frac{3A_m p}{RT}} \tag{3-8}$$

where R is the universal gas constant with a unit of *J/mol-K*, p and T are pressure in Pa and temperature in K. The molecular refractivity, A_m, has a unit of m^3/mol which is described as a function of the mean molecular polarizability, α_m in 10^{-30} m^3 that describes the relative tendency of charge distribution in isotropic media

$$A_m = \frac{4\pi}{3} N_A \alpha \tag{3-9}$$

where N_A is the Avogadro number. Hence, the muon momentum threshold in (3-5) can be selected by manipulating the gas temperature and pressure. In other words, one can pressurize gas Cherenkov radiators differently so that they are only activated by muons with a momentum exceeding their threshold levels.

3.1.3 Methods

To measure muon momentum, we use multiple gas Cherenkov radiators that are differently pressurized to provide necessary pre-determined threshold momentum levels for muons. The Cherenkov threshold momentum for muons in terms of both gas pressure and temperature, p_{th}, can be written by substituting (3-8) into (3-5)

$$p_{th}c = m_\mu c^2 \sqrt{\frac{R}{3A_m}\frac{T}{p}} \tag{3-10}$$

where $m_\mu c^2$ is the rest mass of the muon which is 105.66 MeV/c. From (3-10) we find out that the Cherenkov threshold momentum is proportional to $T^{1/2}$ and $p^{-1/2}$. As a result, by changing either pressure or temperature, the threshold muon momentum can be changed without the need to replace the material.

In our Cherenkov muon spectrometer, each gas radiator is designed to be triggered when the actual muon momentum exceeds the pre-selected threshold momentum level. In other words, when a muon passes all radiators, none to all gas Cherenkov radiators can be triggered depending on the actual incoming muon momentum. For the lowest threshold momentum level, p_{th} = 0.1 GeV/c, a solid radiator was inevitably used to reach a necessarily high-refractive index otherwise not possible with a pressurized gas radiator. The schematic diagram describing the measurement principle and signal flows to estimate muon momentum using multiple gas Cherenkov radiators is depicted in Figure 3.2. In this example, a muon passes all six radiators with a momentum of 3.1 GeV/c. They have threshold momentum levels of 0.1, 1.0, 2.0, 3.0, 4.0, and 5.0 GeV/c, respectively. The first four radiators emit Cherenkov radiation because the muon momentum is greater than 3.0 GeV/c, whereas last two radiators do not emit Cherenkov radiation because their threshold momentum levels are greater than 3.0 GeV/c. It records '1' for triggered radiators and '0' for the non-triggered ones. After the signal analysis, the final signal correctly indicates the range of actual muon momentum, $3.0 < p_\mu < 4.0$ GeV/c as shown in Figure 3.2.

The wavelength shifters and photon absorber liners are placed on the bottom of each radiator. The wavelength shifter converts the UV lights to VIS lights and the light guide transfers them to optical sensors in order to convert photon signals to electrical signals. Strong photon absorbers are used on all inner surfaces of radiator containers to prevent photons from escaping the assigned container. In addition, muon trackers, e.g., scintillation muon detectors, are installed to selectively record muon signals and minimize background noise. Figure 3.3 shows the overview of Cherenkov muon spectrometer. A digital signal analyzer receives signals from two inputs: (i) the coincidence logic gate to record muon signals and (ii) twelve photon counters to measure Cherenkov photons.

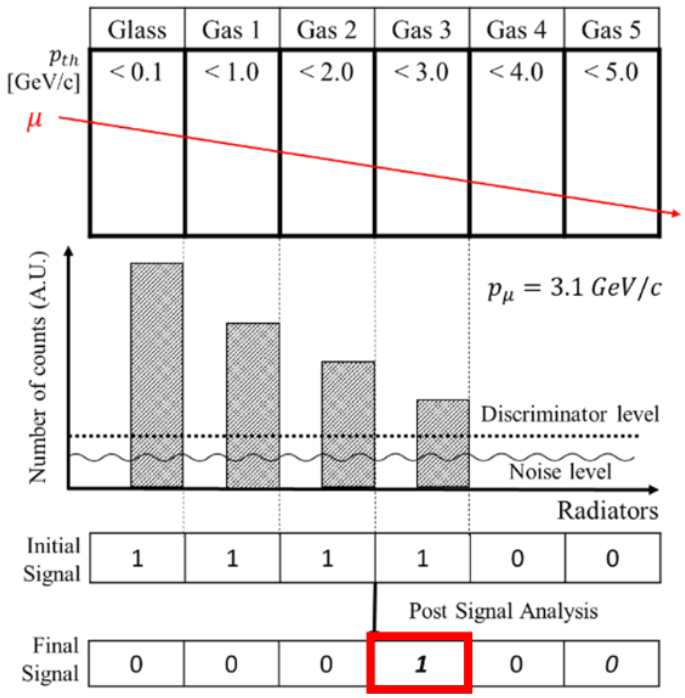

Figure 3.2. The schematic diagram describing the principle of muon momentum estimation using multiple gas Cherenkov radiators (Junghyun Bae & Chatzidakis, 2022b).

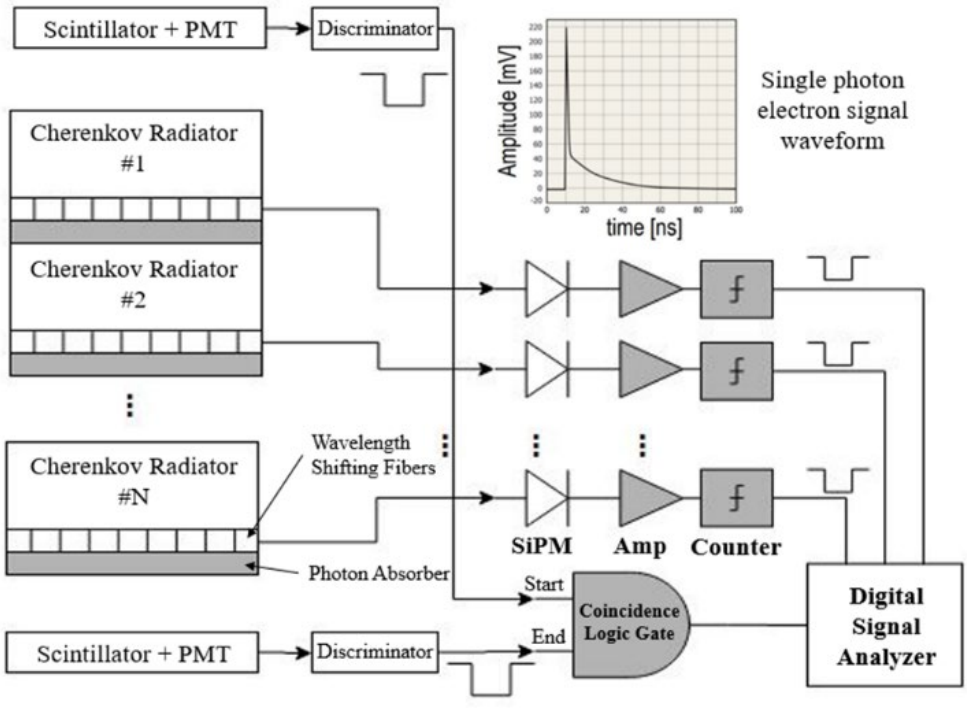

Figure 3.3. The block diagram of Cherenkov muon spectrometer and scintillation muon detectors (J. Bae & Chatzidakis, 2021).

3.2 Selection of Gas Cherenkov Radiators

To choose a Cherenkov gas radiator, four well-known Cherenkov gas radiators, C_3F_8 (Octafluoropropane), $C_3H_2F_4$ (R1234yf), C_4F_{10} (Perfluorobutane), and CO_2 are investigated. C_4F_{10} and CO_2 are used for Cherenkov radiators in the Jefferson Lab (Neil, 1998). The refrigerant, R1234yf, is a promising substitute radiator due to its low Ozone Depletion Potential (ODP) to replace R12 (CCl_2F_2) (Harvey et al., 2018). C_3F_8 is also considered as an alternative for the C_4F_{10} because C_4F_{10} cannot be pressurized higher than 3 atm without condensation at room temperature. Material properties of four gas Cherenkov radiators are presented in Table 3.2. In addition, Figures 3.4 and 3.5 show the variations of Cherenkov threshold muon momentum, p_{th}, and the refractive index, n, as a function of pressure and temperature for four radiators, respectively. Based on the results from Figures 3.4, 3.5, and Table 3.2, we choose CO_2 gas as our Cherenkov gas radiator because it covers a wider range of threshold momenta and it is commercially available in large quantities at a minimal cost. Even though C_3F_8 gas would be a good candidate, it has a smaller vapor pressure and is more expensive than those of CO_2.

Table 3.2. Material properties for four Cherenkov gas radiators at room temperature (Harvey et al., 2018; Hayes, 2018; Richter et al., 2011).

Selected gas radiators	$\mathbf{C_3F_8}$	**R1234yf**	$\mathbf{C_4F_{10}}$	$\mathbf{CO_2}$
Vapor pressure [MPa]	0.820	0.673	0.380	5.7
Vapor density [kg/m^3]	12.5	37.6	24.6	1.977
Molecular weight [g/mol]	188.02	114.04	236.03	44.01
Refractive index [$-$]	1.0011	1.0010	1.0015	1.00045
Polarizability, α [$\times 10^{-30}$ m^3]	7.4	6.2	8.44	2.59

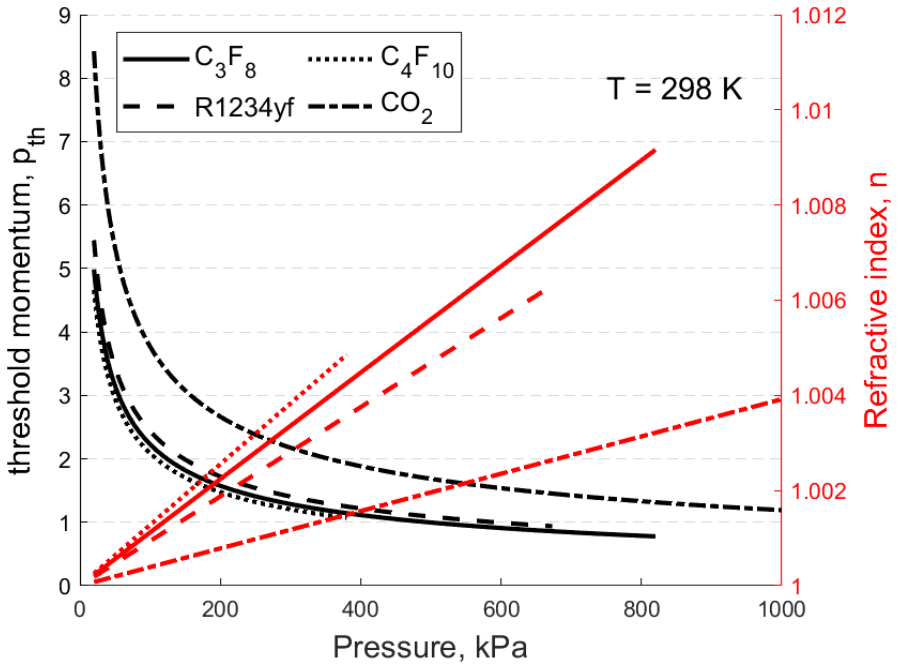

Figure 3.4. Cherenkov threshold momentum for muons and refractive index for C_3F_8, R1234yf, C_4F_{10}, and CO_2 gas radiators as a function of gas pressure. Note: C_4F_{10} and R1234yf cannot be pressurized above their vapor pressure without condensation (Junghyun Bae & Chatzidakis, 2022d).

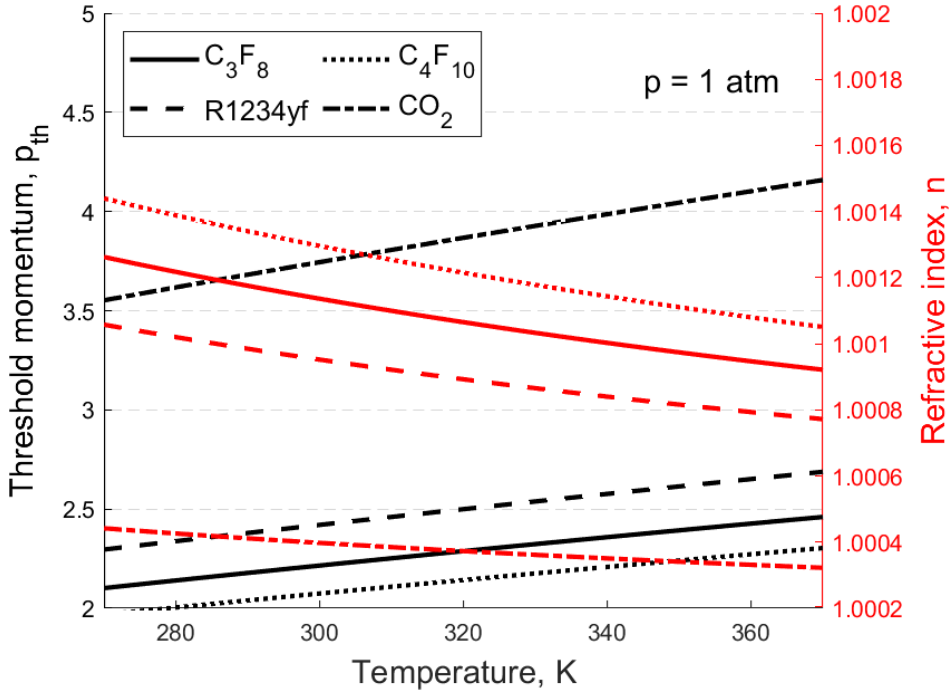

Figure 3.5. Cherenkov threshold momentum for muons and refractive index for C_3F_8, R1234yf, C_4F_{10}, and CO_2 gas radiators as a function of gas temperature (Junghyun Bae & Chatzidakis, 2022d).

3.3 Optical Photon Emission

Three dominant optical photon emission mechanisms, (i) Cherenkov radiation, (ii) scintillation, and (iii) transition radiation, when a muon interacts with a gas radiator are discussed in this section. The theory and characteristics of light emission of Cherenkov radiation, scintillation, and transition radiation are outlined in the following sections 3.3.1 to 3.3.3, respectively. The practical example and analysis for three light emission mechanisms are detailed in Appendix B.

3.3.1 Cherenkov radiation

Cherenkov radiation photon is the emission of electromagnetic radiation when polarized molecules in the dielectric medium return to the normal states while a charged particle travels at a speed greater than the speed of light. The details of background physics and theory of the Cherenkov effect are discussed in Section 3.1.1. The Cherenkov photon wavelength spectrum is continuous and extends from the near ultraviolet (UV) to the visible (VIS) region, 200 to 700 nm peaking at near 420 nm. Only an insignificant amount of Cherenkov photons is found in the IR regions. Assuming that muon phase velocity, β, is a constant, the analytical expression of the Cherenkov photon intensity within the wavelength interval between λ_1 and λ_2 is given by (Sowerby, 1971)

$$\frac{dN_{ch}}{dx} = 2\pi\alpha \int_{\lambda_1}^{\lambda_2} \left(1 - \frac{1}{n^2(\lambda)\beta^2}\right) \frac{d\lambda}{\lambda^2} \tag{3-11}$$

where dN_{ch} is the expected number of Cherenkov photons in a unit path length dx, α is the fine structure constant ($e^2/4\pi\epsilon_0\hbar c \cong 1/137$) and $n(\lambda)$ is the refractive index of the radiator gas. The estimated Cherenkov optical photon yield is proportional to the refractive index of a radiator, muon velocity, and traveling path length whereas it is inversely proportional to the light wavelength. If only VIS photons (400–700 nm) are considered, (3-11) can be reduced by

$$\frac{dN_{ch}}{dx} \cong 490 \sin^2 \theta_c \tag{3-12}$$

where θ_c is Cherenkov angle which is defined in (3-6). When the UV photon region is included, 200–700 nm, (3-11) can be reduced by

$$\frac{dN_{ch}}{dx} \cong 1150 \sin^2 \theta_c \tag{3-13}$$

Cherenkov light flash

Cherenkov effect is the result of instant physical disorder caused by the incident charged particle. The Cherenkov photon response time is much shorter than that of scintillation photon production because it is not associated with absorption, excitation, or relaxation. The time duration of Cherenkov light flash, Δt, was firstly predicted by Jelly (Burden & Hieftje, 1998; Jelley, 1958)

$$\Delta t_{ch} = \frac{r}{\beta_\mu c}[\tan \theta_c(\lambda_2) - \tan \theta_c(\lambda_1)] \tag{3-14}$$

where $\theta_c(\lambda_1)$ and $\theta_c(\lambda_2)$ are the Cherenkov angles for λ_1 and λ_2, and r is the distance to the observer. The estimated light flash duration of Cherenkov for high-energy muons is less than 1×10^{-9} sec.

3.3.2 Scintillation

Scintillation is a light flash caused by the incident particle in a transparent medium. When the energy of particle is transferred to molecules, atoms are vibrated against one another or electrons are excited, then they release energies as a form of light. The light emission spectra of scintillation highly depend on materials. There are various types of scintillator, i.e., organic, inorganic, gas, glass, and plastic scintillators. A sodium iodide doped with thallium, NaI (Tl), and cesium iodide, CsI (Tl), are typically used for inorganic scintillator because of their high light yields and emission spectra. The scintillation light emission spectra of NaI (Tl) and CsI (Tl) are

well matched with the sensitive wavelength range of typical photocathodes as shown in Figure 3.6. For gas scintillators, high-purity noble gases, e.g., xenon, helium serve as a scintillation medium. The typical response time of the gas scintillation is a few nanoseconds.

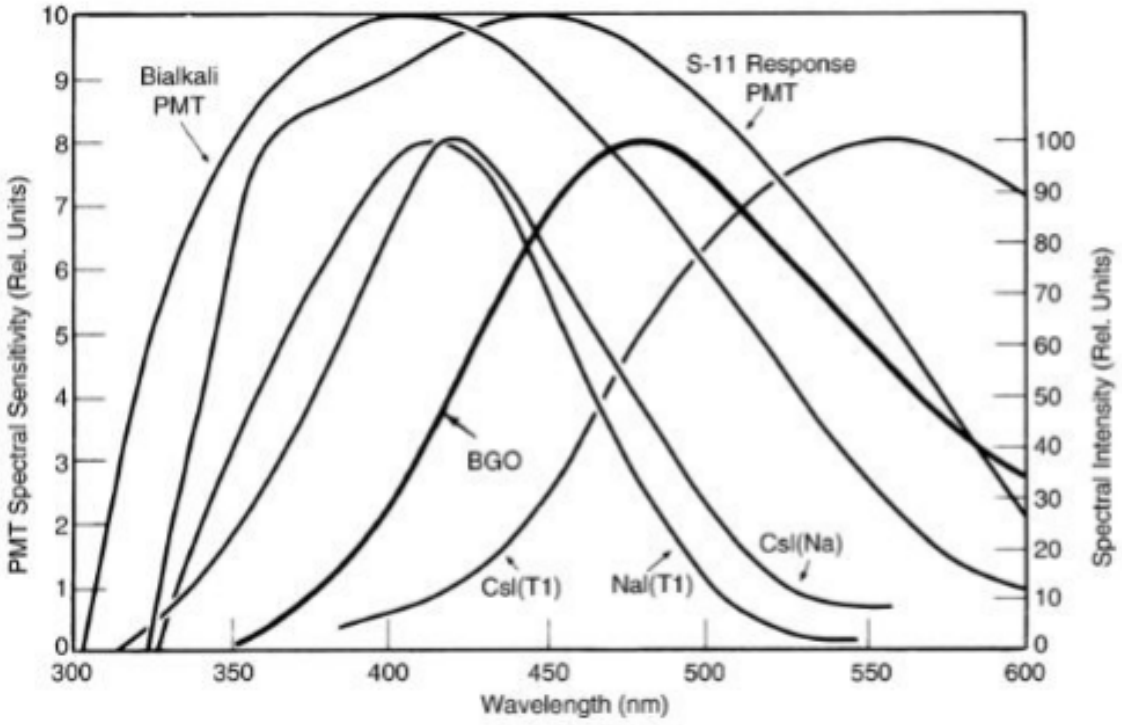

Figure 3.6. Scintillation photon emission spectra of common inorganic scintillators and PMT spectral sensitivity (Wilkinson, 2004). Reprinted from *Emission Tomography: Chapter13-Scintillators* by F. Wilkinson.

Scintillation spectrum and photon yields

Scintillation photon yield depends on the amount of energy loss and path length of incident particle before being absorbed or escaped. In general, the scintillation photon yield linearly increases as particle energy increases as shown in Figure 3.7. The wavelength of scintillation photon is extended approximately 200–700 nm depending on types of scintillation materials (Knoll, 2010). Therefore, the scintillation photon yield depends on the muon energy deposited in the radiators. The mean number of scintillation photons per unit distance, dN_{sc}/dx, is given by (Birks, 1951):

$$\frac{dN_{sc}}{dx} = S\frac{dE/dx}{1 + k_B(dE/dx)} \tag{3-15}$$

where S is the scintillation efficiency, k_B is the Birks' coefficient, and dE/dx is the muon mass stopping power that can be computed using the Bethe equation (Bethe, 1953). When the scintillation medium is gas and E ≥ 300 keV, the Birks' coefficient, $k_B \approx 0$. The scintillation efficiency is defined as a mean number of scintillation photon per 1 MeV energy loss. Scintillation efficiencies for various gas scintillator are tabulated in Table 3.3. The expected number of scintillation photons in non-scintillation materials is much smaller than that of Cherenkov radiation.

The light flash duration time of scintillation is associated with photon absorption, excitation, and relaxation. Time response of the prompt fluorescence of scintillation is given by (Bengtson & Moszynski, 1974)

$$I/I_0 = f(t)e^{-t/\tau} \tag{3-16}$$

where I/I_0 is the normalized light intensity, $f(t)$ represents the characteristic Gaussian function, and τ is the time constant describing decay. The scintillation light flash duration is mainly determined by a decay constant that is the order of μsec for inorganic and few *nsec* for organic scintillation materials (Knoll, 2010). Figures 3.8 and 3.9 show the estimated flash time responses and light emission wavelength spectra for Cherenkov and scintillation, respectively. Using a significant timing difference between two light emission mechanisms and fast timing techniques, we are able to discriminate scintillation photon signals from Cherenkov radiation using (Kaptanoglu et al., 2019).

Table 3.3. Scintillation efficiency of various gas media (Morii et al., 2004).

Gas	$S = \langle dN_{sc}/dE \rangle$
N_2	141 ± 2.1
Air	25.45 ± 0.43
O_2	0.61 ± 0.22
CO_2	5.09 ± 0.28
CH_4	1.39 ± 0.09

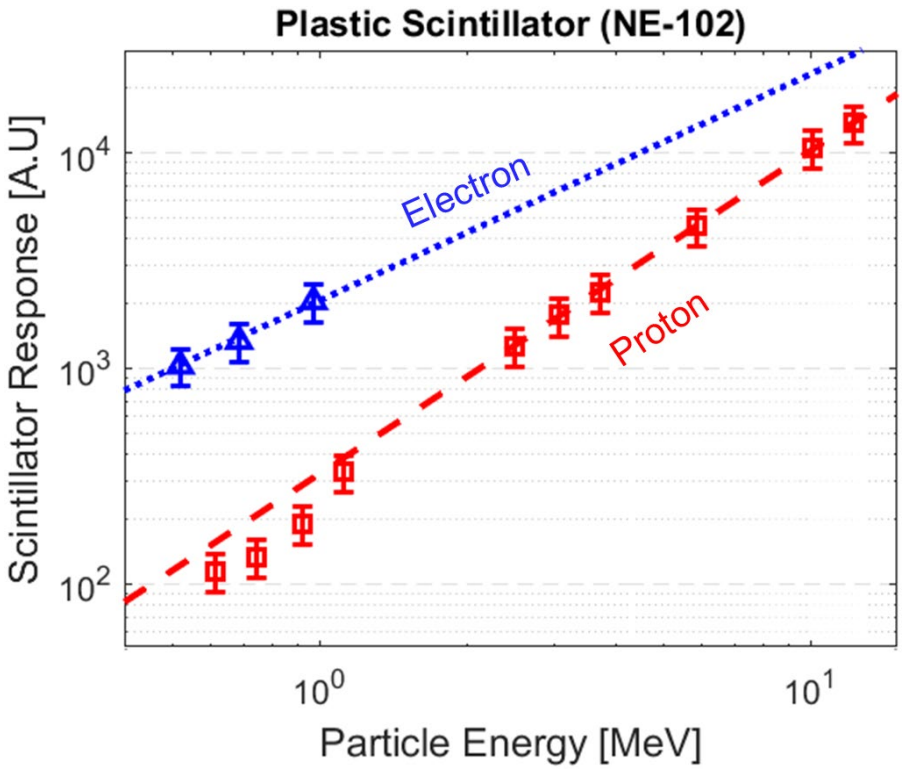

Figure 3.7. Scintillation photon response for the NE-102 plastic scintillator for electrons and protons (Craun & Smith, 1970).

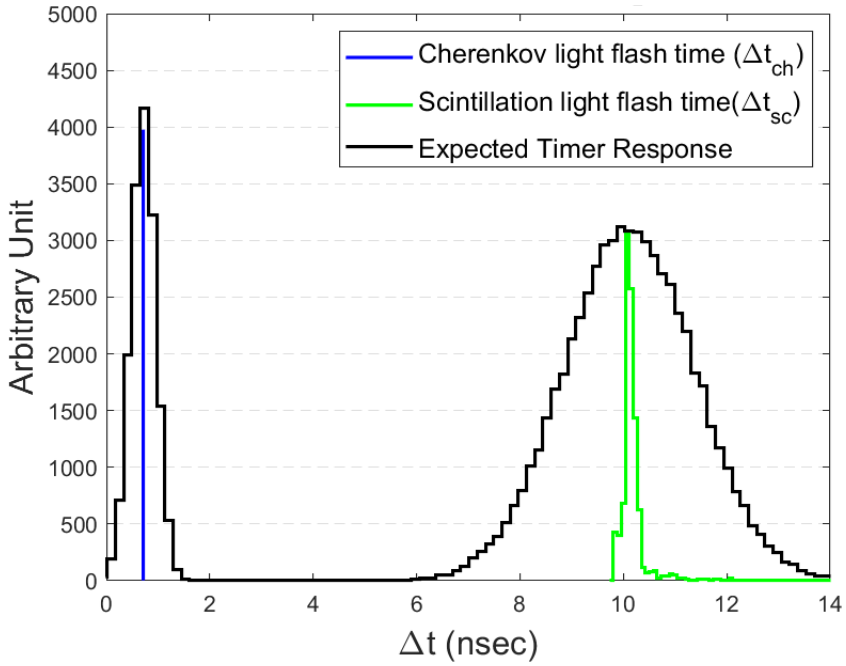

Figure 3.8. The expected Cherenkov and scintillation light flash time responses. Cherenkov light flashing time has a fast pulse ($< 1\times10^{-9}$ sec) because it is the result of instant physical disorder caused by the incident muon whereas scintillation light flash time has a slow distribution with a tail due to the decay constant ($\gg 1\times10^{-9}$ sec) because it is a fluorescence process of scintillation (Junghyun Bae & Chatzidakis, 2022b).

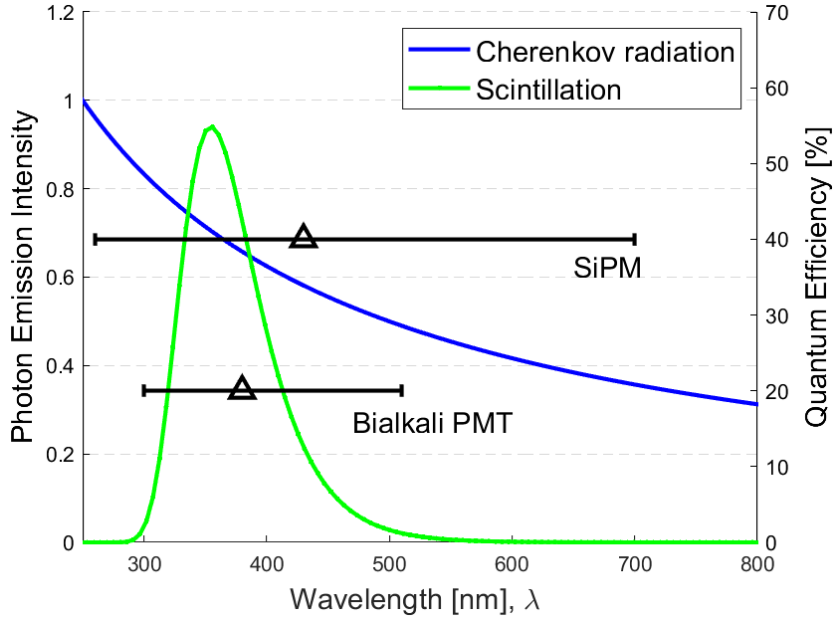

Figure 3.9. Typical Cherenkov and scintillation light wavelength spectra with quantum efficiency ranges for bialkali PMT and SiPM (Alharbi et al., 2020). Triangular markers and horizontal bars indicate the peak and 90% range of quantum efficiency spectra.

3.3.3 Transition radiation

Transition Radiation is emitted when a charged particle travels through inhomogeneous materials such as a boundary between two different media. The transition radiation effect is a result of the reformation of the dielectric field when a particle travels from one medium to another. The presence of transition radiation as a form of electromagnetic radiation was predicted by Frank and Ginzburg in 1947 (Ginzburg & Frank, 1947). The transition radiation emission is neither related to particle energy loss by collisions at boundaries nor deacceleration of the particle. The polarization of media is a source of transition radiation. Transition radiation, sometime is misinterpreted as Cherenkov or the Bremsstrahlung radiation. However, the transition radiation occurs even at any particle velocity and does not lose particle energy by deacceleration. Figure 3.10 describes the difference between the transition and Cherenkov radiation. As shown in Figure 3.10, the transition radiation is observed at the boundary of two dielectric media and emitted in both directions with an angle that is proportional to the $1/\gamma$. On the other hand, Cherenkov radiation occurs within a dielectric medium and its angle depends on $1/\beta n$.

Transition radiation spectrum and photon yields

A charged particle emits transition radiation at the boundary in two directions, forward and backward. The peak intensity angle, θ, is approximately $1/\gamma$. The angular distributions of transition radiation for various electron energies are shown in Figure 3.11. The transition radiation that emits in the backward direction with a visible wavelength is called optical transition radiation (OTR). The photon yields of OTR, when $\gamma \gg 1$ and the emitted photon frequency is greater than plasma frequency, ω_p, per interface is given by (John David Jackson, 1962)

$$N_{tr} = \frac{z^2 \alpha}{\pi}\left[(\ln \gamma - 1)^2 + \frac{\pi^2}{12}\right] \tag{3-17}$$

where N_{tr} is the mean number of photons by OTR, z is the particle charge, α is the fine structure constant, and $1/\gamma^2 \cong 0$. As shown in Figure 3.12, the transition radiation photon yield is insignificant. There is another type of transition radiation called x-ray transition radiation (XTR). XTR is normally observed when $\gamma > 10^3$ and photon yield is smaller than that of OTR. For instance, a particle of $\gamma \sim 2\times10^3$, the mean number of XTR photons is approximately 0.1. Besides, general

photocathodes and semiconductor counters are not sensitive to x-ray range (λ = 10^{-2}–10 nm) photons.

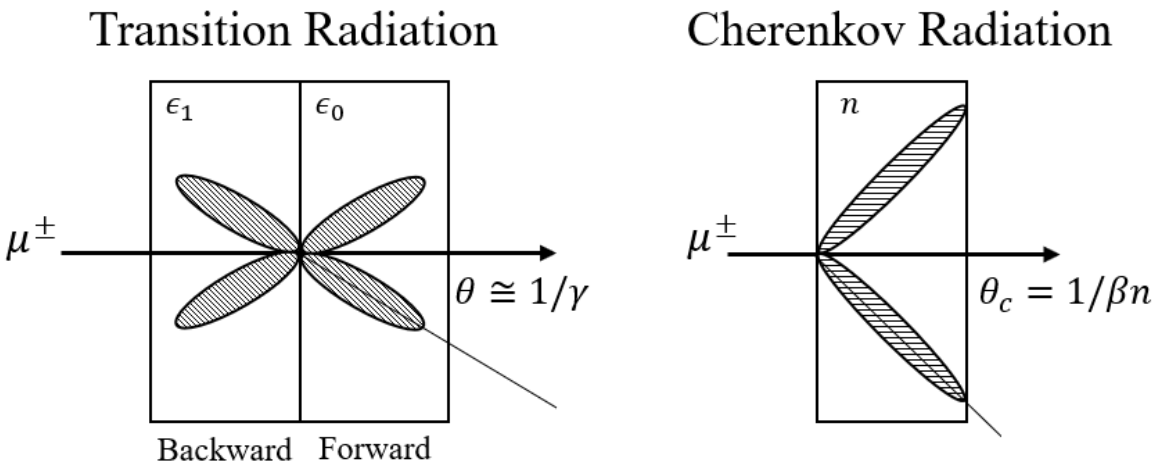

Figure 3.10. Characteristics of transition and Cherenkov radiation when a muon passes through the media (photon emission angles are exaggerated).

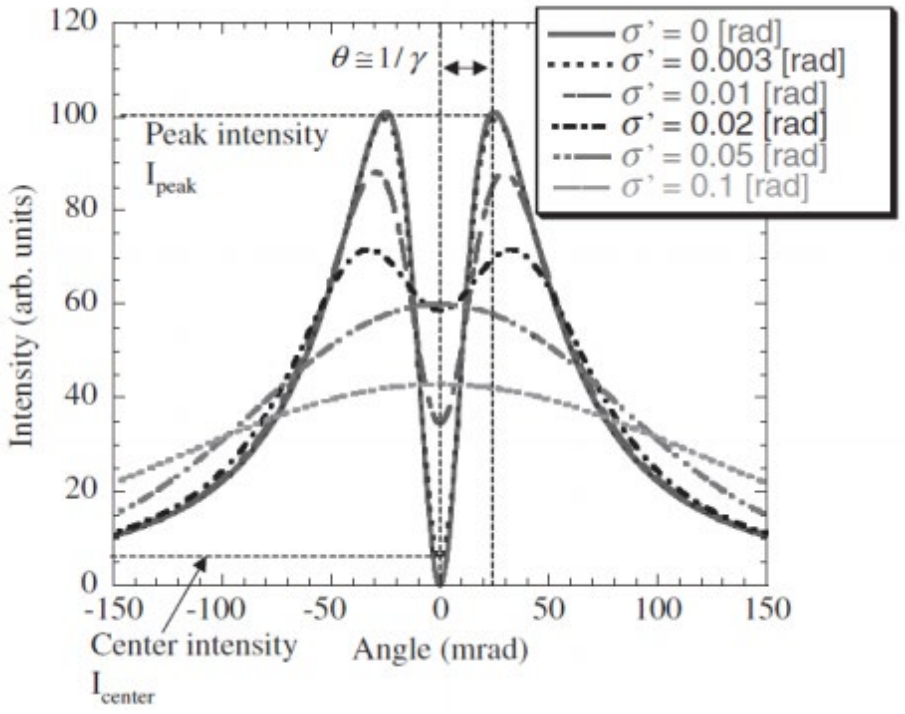

Figure 3.11. Transition radiation angular distributions of electrons at various energy levels (Sakamoto et al., 2005). Reprinted from F. Sakamoto, et. al (2005), with the permission of IOPscience.

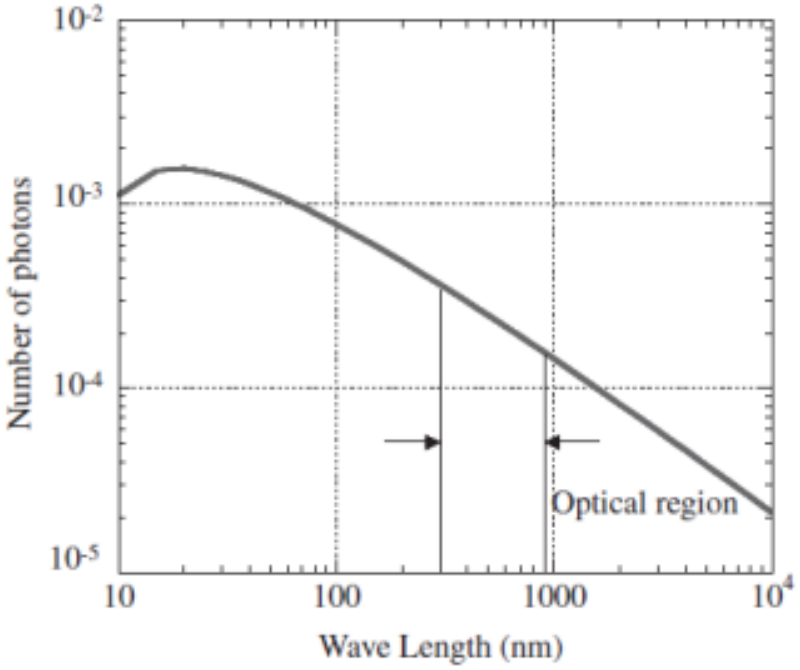

Figure 3.12. Electromagnetic wavelength spectrum of transition radiation (Sakamoto et al., 2005). Reprinted from F. Sakamoto, et. al (2005), with the permission of IOPscience.

The expected optical photon emission intensity of transition radiation is not significant, approximately 10^{-3} to 10^{-4}, when the number of physical boundaries is small and the momentum range is not greater than 10 GeV/c (Sakamoto et al., 2005). The expected optical photon yields by Cherenkov, scintillation, and transition radiation and their signal to noise ratios (SNR), $N_{ch}/(N_{sc}+N_{tr})$, as a function of the radiator length for pressurized CO_2 and C_3F_8 are shown in Figures 3.13 and 3.14. It demonstrates that the Cherenkov light emission yield increases rapidly than scintillation photon emission. In addition, the expected number of optical photons by transition radiation is negligible.

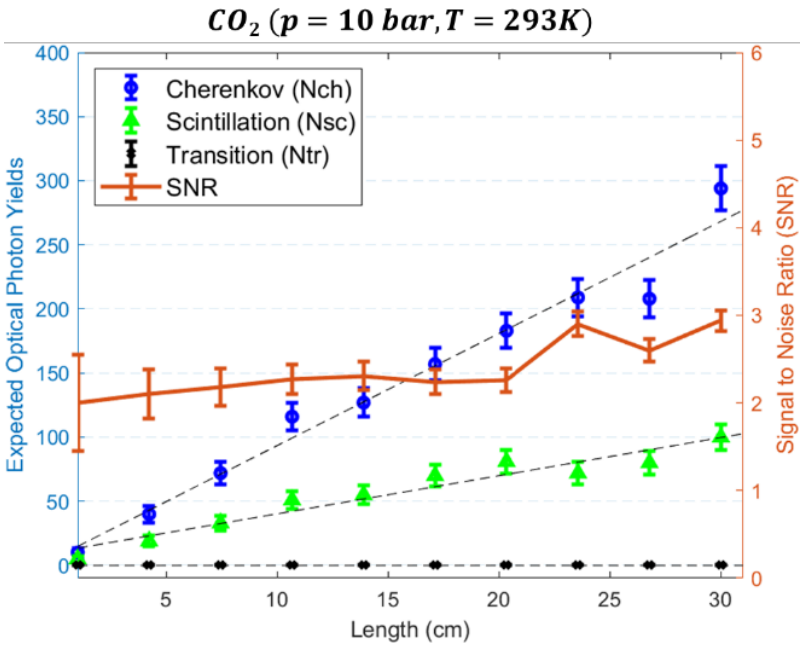

Figure 3.13. The expected photon emission intensities by Cherenkov radiation, scintillation, and transition radiation. They depend on a muon path length in the pressurized CO_2 gas. It shows the estimated photon intensity and SNR as a function of length when E_μ = 4 GeV/c. Error bars represent 1σ.

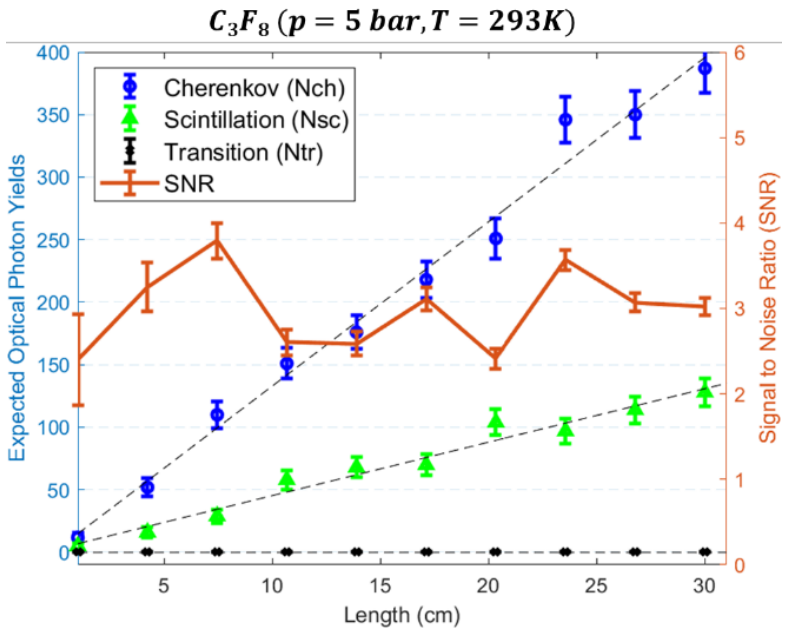

Figure 3.14. The expected photon emission intensities by Cherenkov and scintillation. They depend on a muon path length in the pressurized C_3F_8 gas. It shows the estimated photon intensity and SNR as a function of length when E_μ = 4 GeV/c. Error bars represent 1σ.

3.4 Geant4 Simulations

Geant4 (Geometry ANd Tracking) is a computational tool developed by CERN for the Monte-Carlo particle transport simulations in many applications such as high-energy, nuclear, accelerator, medical, and space physics (Agostinelli et al., 2003; Allison et al., 2006). We use the Geant4 to simulate muon interactions with matters, secondary particle production, scattering, absorption, and light emission in our proposed Cherenkov muon spectrometer. In Section 3.4.1, we perform two benchmarking simulations: (i) cosmic ray muon scattering angle distribution, and (ii) energy loss, to verify the Geant4 model. Section 3.4.2 details our Cherenkov muon spectrometer model in Geant4 such as geometry, materials, and list of physics. The Geant4 simulation results are presented and analyzed in Section 3.4.3.

3.4.1 Analytical model benchmarking

To verify the Geant4 code for muon transport simulations, we benchmarked two muon physics, (i) scattering angle distribution and (ii) mean rate of muon energy loss in the medium. The simulation results are compared with analytical models which were successfully developed based on multiple Coulomb scattering approximation and Beth equation, respectively.

Scattering angle distribution

When a muon travels through the material, it is randomly deflected due to the Coulomb interactions with the atomic nuclei and electrons. The result of multiple Coulomb scattering is approximated using Gaussian distribution and its root mean square (rms) is described in (2-33). When a muon travels the inhomogeneous materials, the effective radiation length is given by

$$\frac{X_{total}\rho_e}{X_{0,e}} = \sum_i \frac{X_i \rho_i}{X_{0,i}} \tag{3-18}$$

where X_{total} is the total length, ρ_e is the effective density of materials. X_i, $X_{0,i}$ and, ρ_i are the length, radiation length, and density of ith material component. All parameters used to compute effective radiation length, $X_{0,e}$ are summarized in Table 3.4. In addition, the rms of the plane displacement of muons, σ_{plane} is related to σ_θ

$$\sigma_{plane} = X\sigma_{\theta} \tag{3-19}$$

The analytical calculation of muon scattering angle distribution is shown as a circle centered at the origin (initial muon x-y coordinate). The estimated radii (1σ, 2σ, and 3σ) of muon scattering displacement distributions for selected muon energies, 0.5, 1.0, 4.0, and 10.0 GeV, and Geant4 simulations are in good agreement and the results are shown in Figure 3.15.

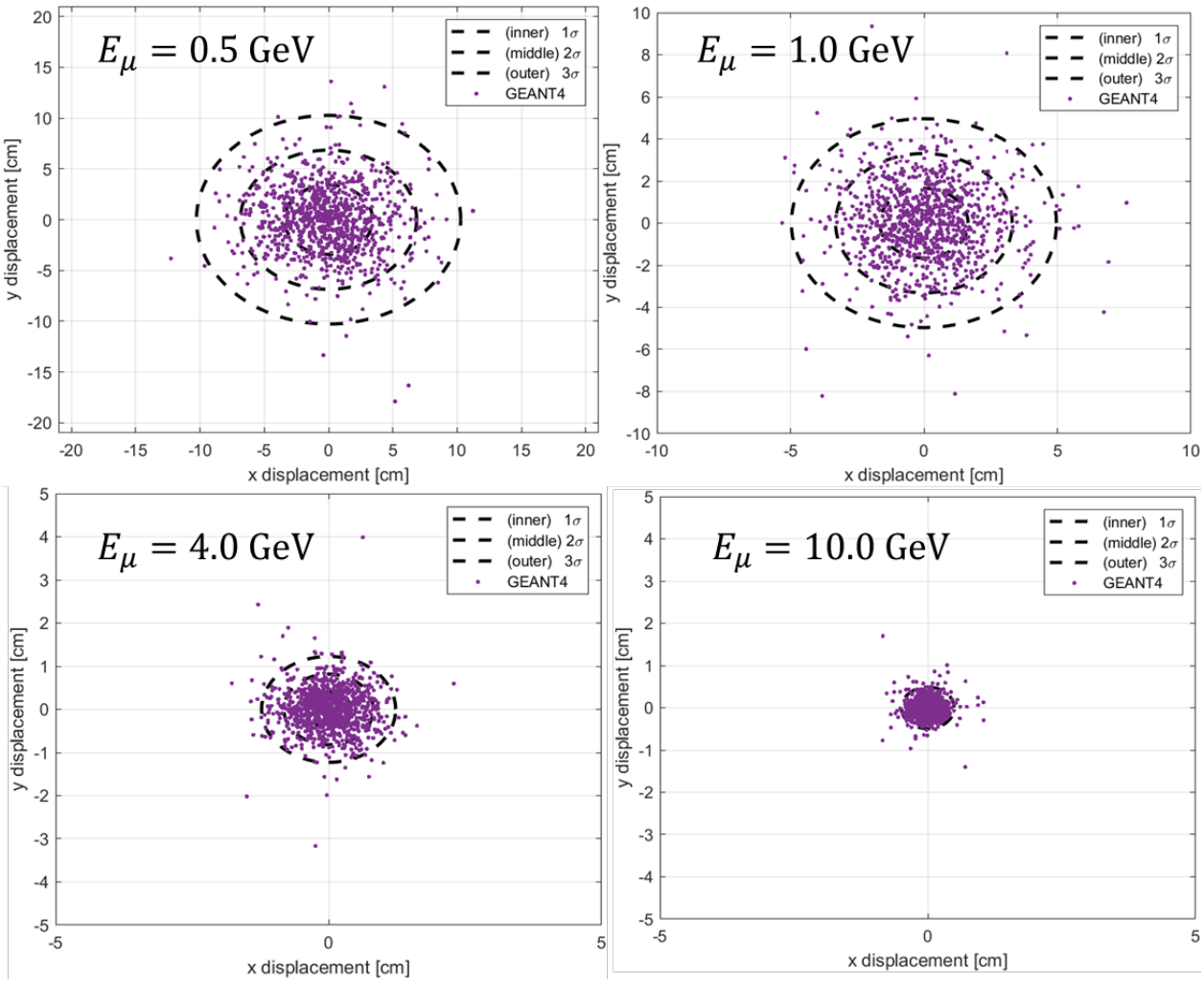

Figure 3.15. Muon scattering angle distributions for various muon energies using Geant4 simulations and analytical estimation using Gaussian approximation. Each projected Gaussian circular area represents 1σ (inner), 2σ (middle), and 3σ (outer). Note: Different x- and y-axis ranges are used.

Muon energy loss

Since the muon energy loss by ionization dominates in major cosmic ray muon energy ranges (0.1 to 100 GeV/c), the mean muon mass stopping power can be estimated by the Bethe equation (P.A. Zyla et al., 2020). Figure 3.16 shows the simulation results of muon energy loss in the radiators as a function of muon energy using 10^4 muon samples. Even though the amount of muon energy loss varies slightly from 7 to 12 MeV depending on muon energy, the fraction of energy loss to initial muon energy is insignificant, < 1%. Computed results using Bethe equation and Geant4 simulations are in good agreement with each other.

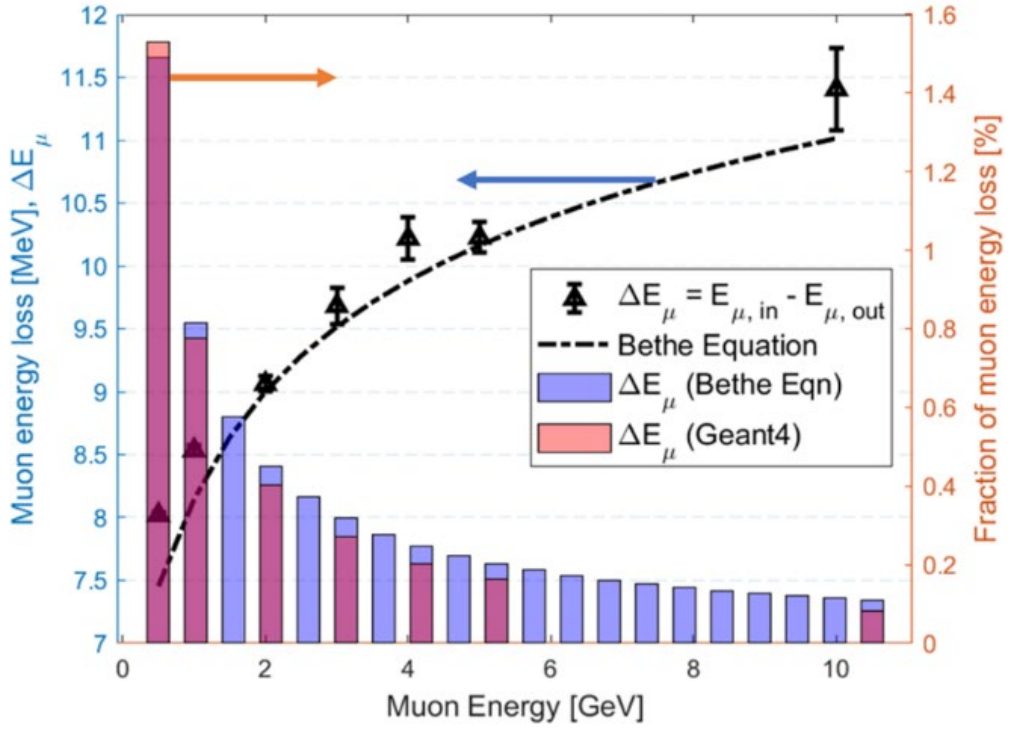

Figure 3.16. Muon energy loss computed by using Bethe equation (curve) and simulations using 10^4 muon samples (bars). Even though the amount of muon energy loss varies slightly from 7 to 12 MeV depending on muon energy, the fraction of the energy loss to initial muon energy is insignificant, < 1%. The computed fraction of muon energy loss to incident energy as a function of initial muon energy using simulations and analytical approach is also presented.

3.4.2 Modeling

To demonstrate the functionality of proposed muon spectrometer, a high-fidelity stochastic muon transport simulation using Geant4 is performed. The underlying principle of the proposed Cherenkov muon spectrometer is illustrated in Figure 3.17 (Junghyun Bae & Chatzidakis, 2021a, 2022b). It shows characteristics of photon emissions by Cherenkov, scintillation, and transition radiation in radiator A ($p_\mu > p_{th}$) and B ($p_\mu < p_{th}$). All surfaces of gas radiator containers are wrapped by strong photon absorbers so that emitted photons are isolated within the radiators. Moreover, the optical sensors are installed on one side of each radiator container to measure photon signals. In this way, we can efficiently discriminate scintillation photon signals from Cherenkov photon signals because scintillation photons are emitted in all directions whereas Cherenkov photons are emitted forward-biased directions.

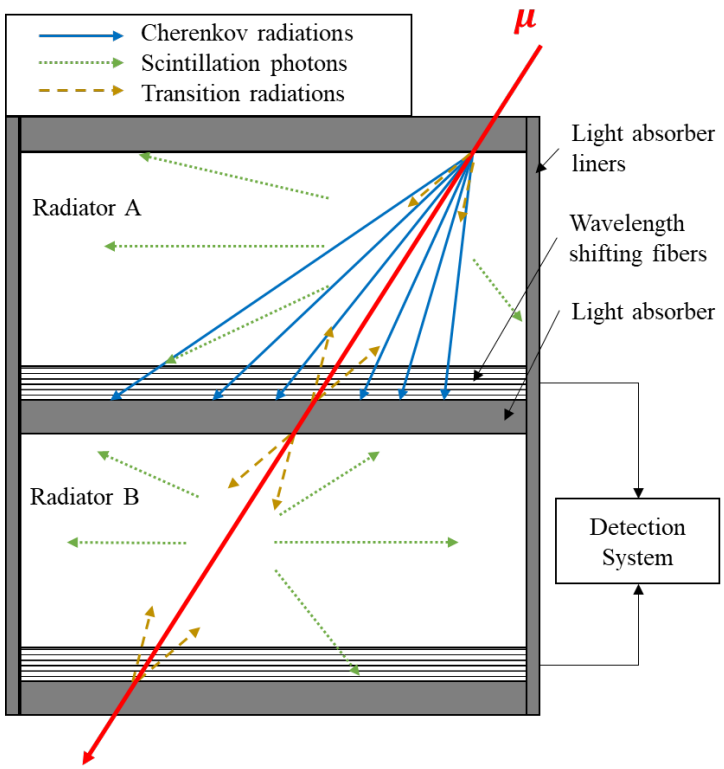

Figure 3.17. The characteristics of photon emissions by Cherenkov, scintillation, and transition radiation in two radiators. Radiator A (top) emits Cherenkov photons since $p_\mu > p_{\text{th}}$ whereas radiator B (bottom) does not because $p_\mu < p_{\text{th}}$. However, both radiators emit scintillation and transition radiation regardless of actual muon momentum. Due to the forward-biased directional photon emission of Cherenkov radiation, scintillation photon signals can be efficiently discriminated (Junghyun Bae & Chatzidakis, 2022b).

We chose CO_2 as a gas radiator because it can be pressurized up to 5.7 MPa without condensation although the refractive index of CO_2 gas is lower than gas radiators such as C_4F_{10} or R1234yf. Five sequential threshold momentum levels, p_{th} = 1.0, 2.0, …, 5.0 GeV/c are obtained using pressurized CO_2 gas radiators. However, a solid radiator (SiO_2) has to be used to provide the lowest threshold momentum level, 0.1 GeV/c, because it is not possible to obtain this threshold momentum level using any pressurized gas radiator at room temperature.

The overall length of muon spectrometer is 51.7 cm and the active surface area is 20×20 cm^2. It consists of a 1 cm glass radiator, five 10 cm pressurized CO_2 gas radiators, and 0.1 cm photon absorber liners. The overall weight is less than 10 kg since it mostly made of gas radiators. However structural frames and photon detectors weigh approximately 8 kg. A standard SiO_2 (n = 1.45) is used for a glass radiator and sequentially pressurized CO_2 are used for gas radiators to provide necessary refractive indices and threshold momentum levels for muons. Because the Cherenkov threshold momentum at atmospheric pressure is approximately 3.5 GeV/c, some CO_2 radiators are technically depressurized to achieve p_{th} = 4 and 5 GeV/c. In Geant4 simulations, any optical photon events are immediately terminated when they reach either photon absorbers or outside of "world" volume during the simulations. Figure 3.18 illustrates the overview of Cherenkov muon spectrometer configuration with dimensions and materials of components. The characteristic parameters used in Genat4 simulation for solid and gas radiators are summarized in Table 3.4. Black aluminum foils are chosen to simulate strong photon absorbers. Once the optical photons arrive at the absorber surface, all disappear.

Cosmic ray muons and physics list

All muons were initially generated 10 cm from the center of solid radiator surface. All major physics, i.e., three optical photon emission mechanisms by both primary muons and secondary particles, scattering and absorption, decays, energy loss, are included in the Geant4 reference physics list, QGSP_BERT (Geant4 Collaboration, 2017). All optical photons are accordingly tagged by types of mother particle (primary muon or secondary particle) and light emission mechanisms (Cherenkov, scintillation, and transition radiation).

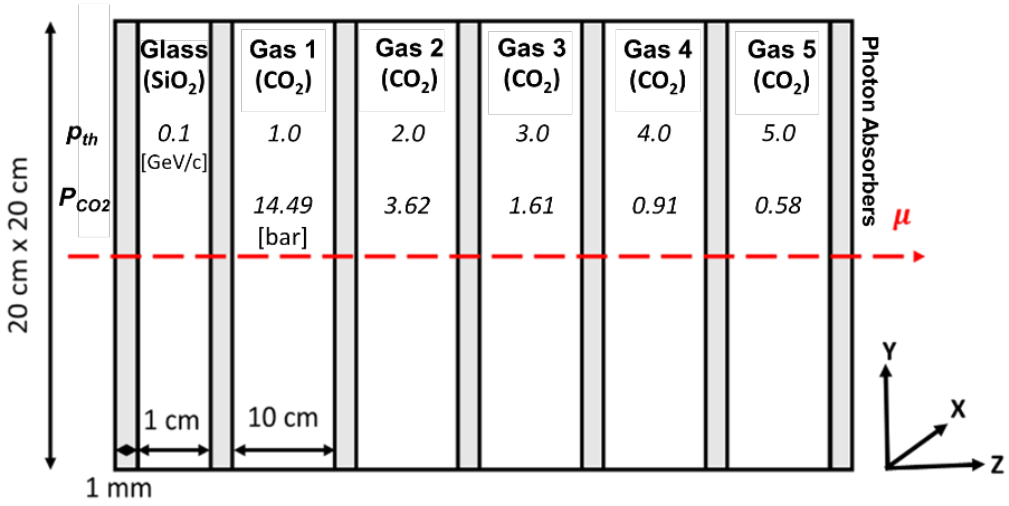

Figure 3.18. The schematic of proposed Cherenkov muon spectrometer. It shows dimensions and materials of components. In addition, threshold momentum and CO_2 gas pressure of each radiator are also presented. Note: The figure is not proportional to the actual size (Junghyun Bae & Chatzidakis, 2022b).

Table 3.4. Properties and parameters of materials used in Geant4 simulations.

Radiator ID	**1**	**2**	**3**	**4**	**5**	**6**	**Absorber**
Material	SiO_2	CO_2	CO_2	CO_2	CO_2	CO_2	Al
$< Z/A >$ [-]	0.4973	0.4999	0.4999	0.4999	0.4999	0.4999	0.4818
Length [cm]	1	10	10	10	10	10	0.1
p_{th} [GeV/c]	0.1	1.0	2.0	3.0	4.0	5.0	-
Refractive index [-]	1.45	1.00557	1.00139	1.00062	1.00035	1.00022	-
Pressure [bar]	-	14.4857	3.6214	1.6095	0.9054	0.5794	-
Density [kg/m^3]	2500	27.83	6.55	2.88	1.61	1.03	2700
Radiation Length [cm]	10.69	1.93E4	1.96E4	1.96E4	1.97E4	1.97E4	8.90

3.4.3 Simulation results

Various mono-energetic muons are generated to evaluate the functionality of the muon spectrometer in Geant4 simulations. The measured photon signals are classified into two categories, Cherenkov photons (signals) and others (noise). The optical photon emissions by the scintillation and transition radiation are excluded during the first simulation in order to focus on the Cherenkov photon emission. Two mono-energetic muons, p_μ = 3.25 and 10.0 GeV/c, vertically enter the Cherenkov muon spectrometer and travel through all radiators as shown in Figure 3.19. When p_μ = 3.25 GeV/c, only the first four radiators emit conical-shaped Cherenkov radiation because their threshold momenta are less than the incident muon momentum. On the other hand, all radiators emit Cherenkov radiation when p_μ = 10.0 GeV/c because threshold momentum levels for all radiators are lower than 10.0 GeV/c. In next simulations, scintillation and transition radiation are included, however, all other parameters remain unchanged. More optical photons are observed in the radiators because of optical photon emission by scintillation and transition radiation. It is noted that scintillation photons can be differentiated from Cherenkov photons due to (i) the characteristic photon emission direction (θ_c vs 4π) and (ii) light flash duration as shown in Figure 3.8. No transition radiation is observed in Figure 3.19 because it is a highly rare event for a few GeV muons and for the small number of boundary systems.

It is noted that there are some additional Cherenkov photons ($N_{ch} \neq 0$ when $p_\mu < p_{th}$) that are observed in Figure 3.19 and they are also found in Figure 3.20. They occurs due to either Compton scattering or Cherenkov photon emissions by secondary particles, mainly electrons, which can be produced by muon decays and muon to electron conversions (R. Donghia, 2017).

$$\mu^- \rightarrow e^- \bar{\nu}_e \nu_\mu \tag{3-20}$$

$$\mu^+ \rightarrow e^+ \nu_e \bar{\nu}_\mu \tag{3-21}$$

$$\mu N_{Al} \rightarrow e N_{Al} \tag{3-22}$$

Equation (3-20) and (3-21) represent radiative decays of $\mu\pm$ with a mean lifetime of $\tau_\mu \cong 2.2$ μsec. Radiative muon decays are the primary source of secondary charged particles, electrons. Equation (3-22) represents the muon to electron conversion. Muons can be captured by the *1s* orbital of

aluminum, then mono-energetic electron emits with an absence of neutrino (Litchfield, 2014). Even though the muon capture cross-section is not significant, it has to be considered because a photon absorber is made of black aluminum foils.

Total numbers of optical photons and Cherenkov photons as a function of muon energy are shown in Figure 3.21. It is noted that the rapid increases in the total number of emitted photons at the muon threshold momentum levels (vertical dashed lines) and they are due to the Cherenkov radiation by muons. Then, it gradually increases as muon energy increases. It demonstrates that our proposed Cherenkov muon spectrometer is feasible because muon energies are clearly identified by analyzing optical photon signals from radiators.

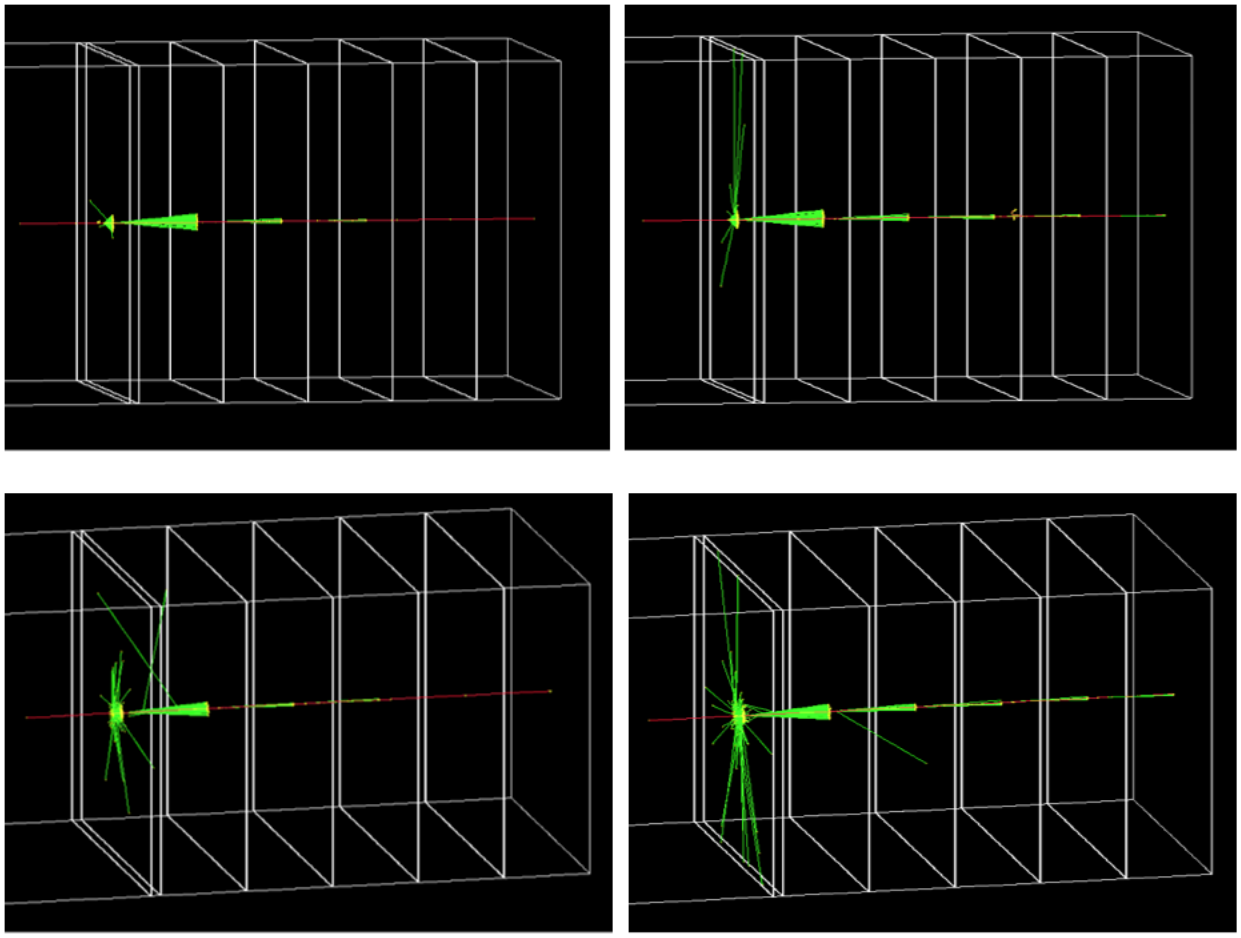

Figure 3.19. Visualized GEANT4 simulation results: (a) Cherenkov radiation only (top row), (b) Cherenkov radiation, scintillation and transition radiation (bottom row) when E_{μ} = 3.25 (left column) and 10.0 GeV (right column). Green and red represent optical photons and negative muons, respectively (Junghyun Bae & Chatzidakis, 2022b)s.

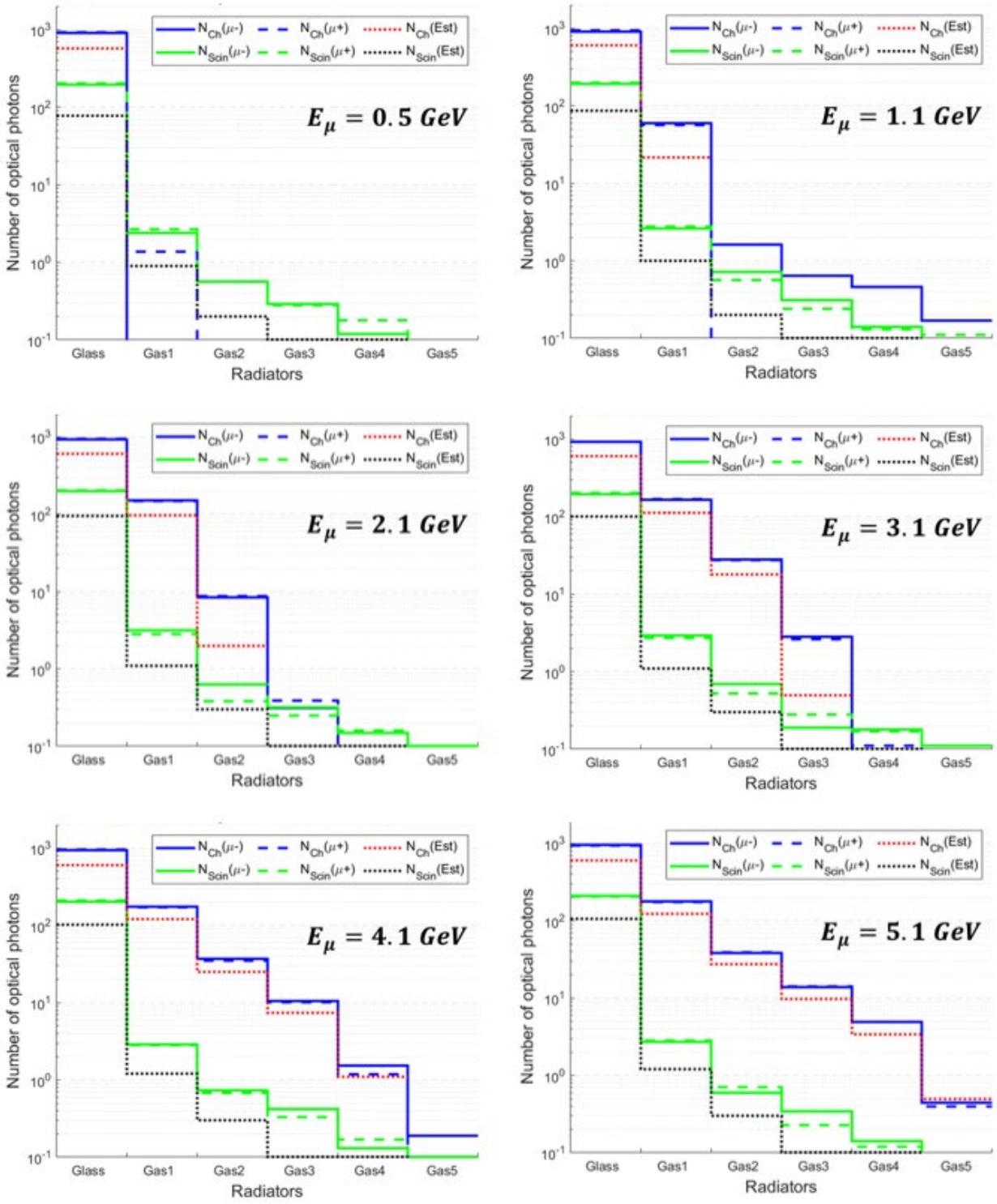

Figure 3.20. Estimated number of optical photon emission by Cherenkov and scintillation in the glass and CO_2 gas radiators for various muon energies using analytical models (dotted) and GEANT4 simulations using 10^4 μ- (solid) and μ+ (dashed).

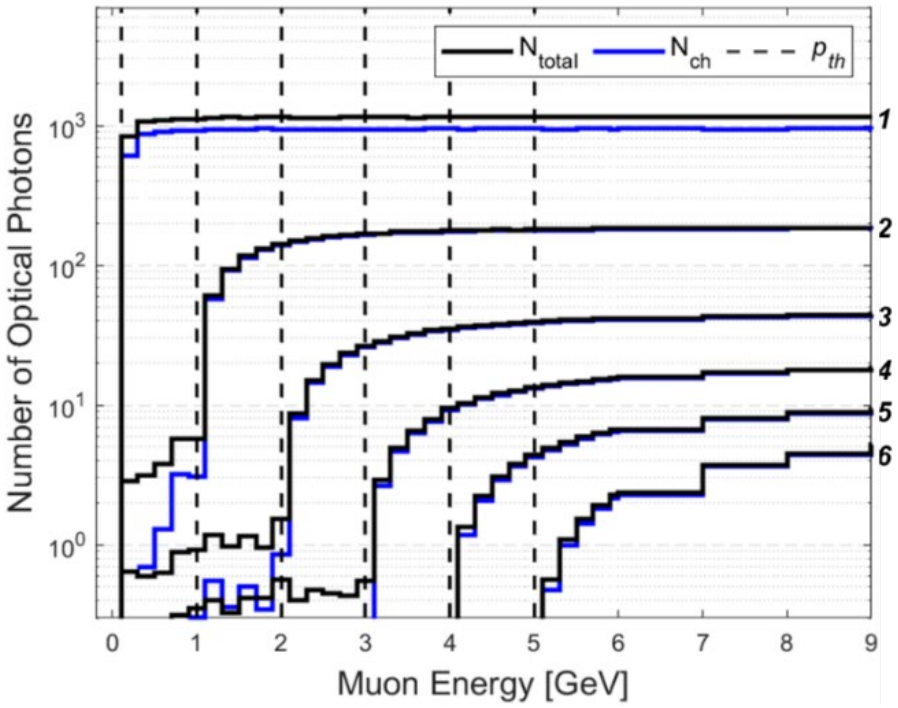

Figure 3.21. Expected number of optical photon emission as a function of muon energy. The rapid increments at the threshold momentum levels (vertical dashed lines) are observed because of the Cherenkov radiation emission above the threshold momentum levels. Then, it gradually increases as muon energy increases. The italic numbers (*1* to *6*) on the right represent the radiator IDs (Junghyun Bae & Chatzidakis, 2022b).

3.5 Optical Photon Emission

Method to measure muon momentum using the proposed Cherenkov muon spectrometer was discussed in Section 3.1.3. Section 3.5.1 details a signal processing algorithm to estimate muon momentum when both signals and noise are simultaneously recorded in the optical sensors of radiators. The quantitative analysis of the performance and functionality of Cherenkov muon spectrometer and post-signal processing to minimize noise are discussed in Section 3.5.2. At the end of this section, we present the simulation results of reconstructed cosmic ray muon spectrum using our muon spectrometer and the results are compared with the actual spectrum in Section 3.5.3.

3.5.1 Signal analysis

Signal processing

As described in Section 3.1.3, the system only records binary signals according to the presence of photon signals regardless of their amplitude. It will record "*1*" for triggered radiators if optical photon signals are detected, otherwise record "*0*" for non-triggered radiators. Without noise, the system correctly estimates the actual muon momentum by analyzing the presence of Cherenkov photons. However, in practice, there exist various noise sources, e.g., optical photons except from Cherenkov photons by muons, background radiation, or electronic noise. When optical photons are emitted by radiators and detected by optical sensors, a digital signal analyzer receives signals, then assigns "*0*" or "*1*" for each radiator. The signal processor reads signals from low to high threshold momentum levels and converts the initial binary signals from "*1*" to "*0*" until it encounters "*0*". After the signal process, "*1*" indicates the estimated muon momentum. The examples of Monte-Carlo simulation data and signal processing when p_μ = 1.5 and 3.5 GeV/c are shown in Figures 3.22.

(a)

Radiator ID	**1**	**2**	**3**	**4**	**5**	**6**
p_{th} [GeV/c]	0.1	1.0	2.0	3.0	4.0	5.0
Counts	308	122	0	0	0	0
Signal	*1*	*1*	*0*	*0*	*0*	*0*
			↓ Signal processing			
Final signal	*0*	***1***	*0*	*0*	*0*	*0*

(b)

Radiator ID	**1**	**2**	**3**	**4**	**5**	**6**
p_{th} [GeV/c]	0.1	1.0	2.0	3.0	4.0	5.0
Counts	325	144	50	21	0	0
Signal	*1*	*1*	*1*	*1*	*0*	*0*
			↓ Signal processing			
Final signal	*0*	*0*	*0*	***1***	*0*	*0*

Figure 3.22. Examples of optical photon counts in six radiators when (a) p_μ = 1.5 GeV/c and (b) 3.5 GeV/c. After the signal processing, the actual muon momentum is correctly estimated (red box) from binary signal outputs.

Noise analysis

The dominant noise source in our proposed Cherenkov muon spectrometer system is the scintillation photon signals. However, other noise sources, e.g., transition radiation, electronic noise, and background radiation can mislead the measurement as well. Although scintillation photons can be differentiated from Cherenkov photons using a flash time difference, light emission direction, or peak wavelength, it is challenging to clearly separate Cherenkov lights from other photon signals in the field. Hence, we assume that all optical photons are indiscriminately recorded by detectors. In Geant4 simulations, used a total number of photons, $N_{ph} = N_{ch}+N_{sc}+N_{tr}$, as a signal output without background noise. To investigate the effect of noise, we used the same signal analysis for muons with a momentum of 1.5 and 3.5 GeV as described in the previous section and the results are shown in Figures 3.23. Due to the presence of a noise signal, the system incorrectly indicates the actual muon momentum. Specifically, it overestimates the actual muon momentum to 2–3 GeV/c and 5.0 GeV/c or greater.

(a)

Radiator ID	**1**	**2**	**3**	**4**	**5**	**6**
p_{th} [GeV/c]	0.1	1.0	2.0	3.0	4.0	5.0
Counts	307	112	1	0	1	0
Signal	*1*	*1*	*0*	*0*	*0*	*0*
			↓ Signal processing			
Final signal	*0*	***0***	***1***	*0*	*0*	*0*

(b)

Radiator ID	**1**	**2**	**3**	**4**	**5**	**6**
p_{th} [GeV/c]	0.1	1.0	2.0	3.0	4.0	5.0
Counts	311	138	58	18	2	1
Signal	*1*	*1*	*1*	*1*	*1*	*1*
			↓ Signal processing			
Final signal	*0*	*0*	*0*	***0***	*0*	***1***

Figure 3.23. Examples of optical photon counts in six radiators with noise when (a) p_μ = 1.5 GeV/c and (b) 3.5 GeV/c. After the signal processing, the actual muon momentum is overestimated due to the noise (red box).

Signal discriminator

The accuracy of Cherenkov muon spectrometer is decreased due to the noise as shown in Figure 3.23. As discussed in previous sections, the potential noise sources are scintillation, transition radiation, electronic noise, and background radiation. To efficiently eliminate predictable noise optical signals introduced in Section 3.3, we used a logical signal discriminator which deducts 1, 2, or 3 from the recorded photon counts. If an initial count is already *0*, however, it remains at *0*. Because the expected yield of noise photon signal in the gas radiator is insignificant whereas that of Cherenkov radiation is significant, the noise level can be compressed without increasing computational costs by uniformly deducting a few signals. Figure 3.24 shows the Geant4 simulation results using various levels of the logical signal discriminator, 1 and 2.

(a)

Radiator ID	**1**	**2**	**3**	**4**	**5**	**6**
p_{th} [GeV/c]	0.1	1.0	2.0	3.0	4.0	5.0
Counts	307	112	1	0	1	0
↓ Signal discriminator level of ***1***						
Adjusted counts	306	111	0	0	0	0
Signal	*1*	*1*	*0*	*0*	*0*	*0*
↓ Signal processing						
Final signal	*0*	***1***	*0*	*0*	*0*	*0*

(b)

Radiator ID	**1**	**2**	**3**	**4**	**5**	**6**
p_{th} [GeV/c]	0.1	1.0	2.0	3.0	4.0	5.0
Counts	311	138	58	18	2	1
↓ Signal discriminator level of ***2***						
Adjusted counts	309	136	56	16	0	0
Signal	*1*	*1*	*1*	*1*	*0*	*0*
↓ Signal processing						
Final signal	*0*	*0*	*0*	***1***	*0*	*0*

Figure 3.24. Examples of optical photon counts in six radiators with noise when (a) p_μ = 1.5 GeV/c and (b) 3.5 GeV/c. By using a signal discriminator, noise signals are efficiently suppressed. After the signal processing, the actual muon momentum is correctly estimated (red box) from binary signal outputs.

3.5.2 Classification rate

To quantify the muon spectrometer measurement accuracy, we introduced a classification rate (CR) which is the probability that the system correctly identifies the actual muon momentum. The Geant4 simulation results of computed CRs using 10^4 mono-energy muons in the pressurized CO_2 gas radiator as a function of muon momentum with various logical signal discriminator levels, 0, 1, and 2, within the momentum range of 0.1–10 .0 GeV/c are shown in Figure 3.25. The uniform discrimination levels were used in the final stage of signal process to cut off predictable noise from total signals. When $p_{th} < 1.0$ GeV/c, the overall CR is less than 60% due to the high scintillation photon intensity in the glass radiator. Therefore, the CR is improved by using a higher discrimination level at this level. When $1.0 < p_{th} < 4.0$ GeV/c, all gas radiators show high CRs because the signals from Cherenkov and scintillation are clearly discriminated by using a linear discriminator. However, when $4.0 < p_{th} < 6.0$ GeV/c, the CR is decreased because the expected Cherenkov photon yields are too low due to the rarefied CO_2 gas (approximately a 0.5 atm) in the high muon threshold momentum level. When $p_{th} > 6.0$ GeV/c, the CR rebounds and increases because Cherenkov photon yields gradually increase as muon momentum increases. However, it is not sufficient to use any linear discriminator in the high threshold levels (> 5.0 GeV/c). In addition, it is noteworthy that the repeated dips of CRs are observed in Figure 3.25 because muon momentum near the threshold momentum boundaries, 0.1, 1.0, … 5.0 GeV/c, typically has a high false classification rate.

3.5.3 Cosmic ray muon spectrum reconstruction

We evaluate the performance of Cherenkov muon spectrometer by reconstructing the cosmic ray muon spectrum at sea level. The analytical models and experimental measurements of cosmic ray muon spectrum at sea level can be found in many literatures (Grieder, 2001; Rossi, 1964; T. K. Gaisser et al, 2016). We used the open-source Monte Carlo muon generator to generate cosmic ray muons in Geant4 simulations, "Muon_generator_v3 (S. Chatzidakis & Tsoukalas, 2016)" which is developed based on the semi-empirical model by Smith and Duller (Smith & Duller, 1959). The maximum muon momentum is limited to 10.0 GeV/c because more than 90% of cosmic ray muon has a momentum less than 10.0 GeV/c as shown in Figure 3.26. The result of reconstructed cosmic ray muon spectrum using six momentum groups is shown in Figure 3.27.

The last bin in a histogram shows a great disagreement with the actual cosmic ray muon spectrum because all muons that have momentum greater than 5.0 GeV/c are categorized in ">5.0 GeV/c" bin.

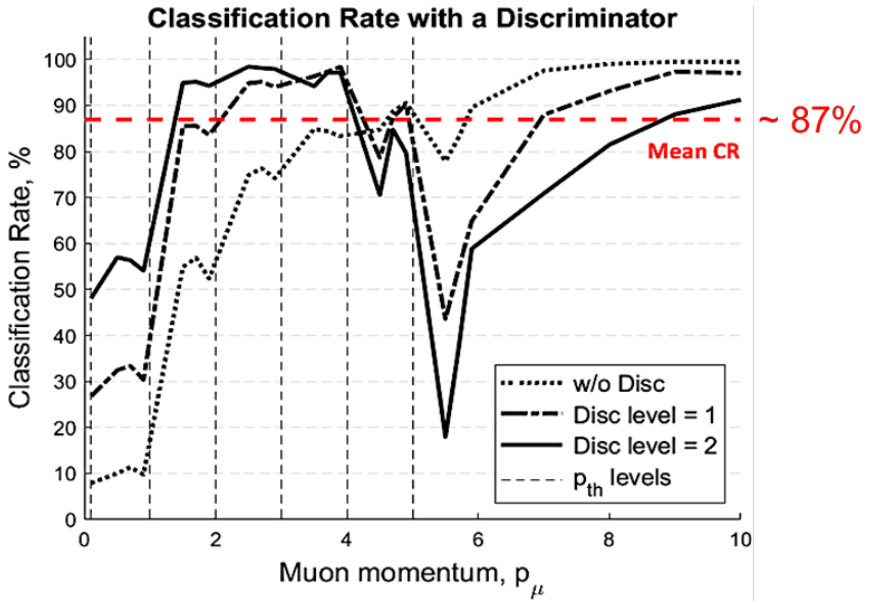

Figure 3.25. Geant4 simulation results of the computed CRs using 10^4 mono-energy muons in the pressurized CO2 gas radiator as a function of muon momentum with various logical signal discriminator levels, 0, 1, and 2, from 0.1 to 10.0 GeV/c. Repeated dips of CRs are observed because muon momentum near the threshold momentum boundaries has a high false classification rate (Junghyun Bae & Chatzidakis, 2022b).

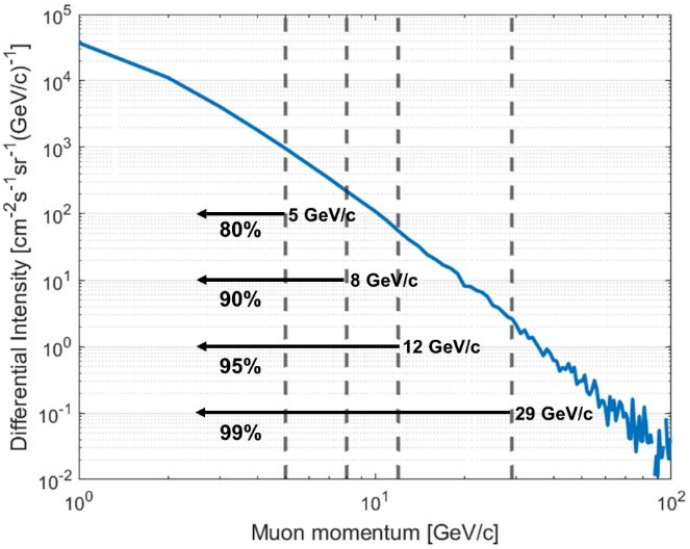

Figure 3.26. Approximated fraction of muon momentum in the cosmic ray muon spectrum.

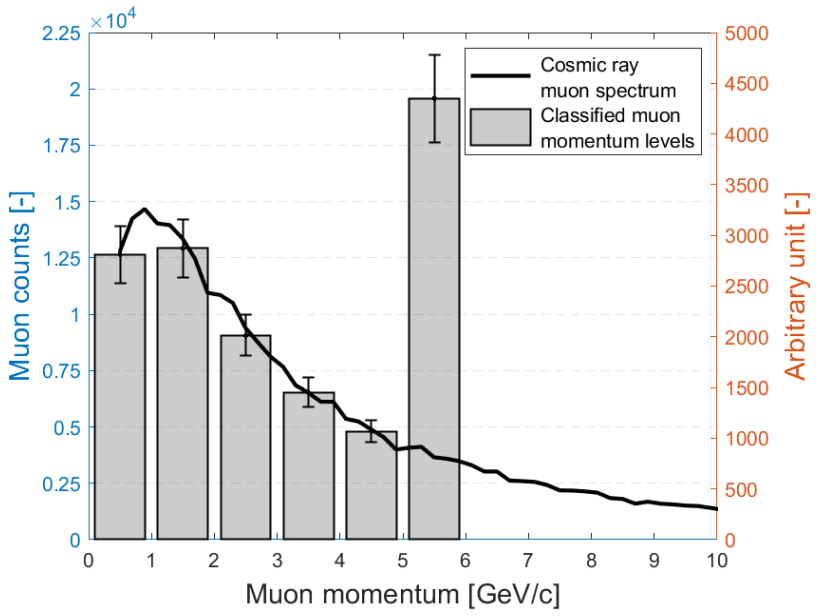

Figure 3.27. Reconstructed cosmic ray muon spectrum using six momentum groups. The last bin (> 5.0 GeV/c) has the largest muon counts which differs from cosmic ray muon spectrum (solid) because all muons that have momentum greater than 5.0 GeV/c are categorized in the last bin.

To address the maximum measurable momentum threshold problem in Figure 3.27, we increase the number of radiators and extend the momentum range. Since the momentum resolution depends on the number of radiators, we consider four scenarios to demonstrate the performance of muon spectrometer using 10^4 muon samples: (i) 10^2 radiators (fine measurement resolution, σ_p = ±0.05 GeV/c and $\sigma_p/p|_{\text{mean}}$= 3.35%) without noise, (ii) 10^2 radiators with noise (i.e., including scintillation and transition photon emission), (iii) 10 radiators (coarse resolution, σ_p = ±0.5 GeV/c and $\sigma_p/p|_{\text{mean}}$= 21.33%) without noise, and (iv) 10 radiators with noise. Although the increased number of radiators improves absolute resolution, σ_p, and mean relative resolution, $\sigma_p/p|_{\text{mean}}$, it will negatively impact the signal-to-noise ratio (SNR) due to the decreased expected Cherenkov signals. The results are shown in Figure 3.28. The cosmic ray muon spectrum is successfully reconstructed using 100 radiators, and it has a nearly identical shape to the actual spectrum. When noise is included, however, the spectrum is slightly shifted to the right. In this simulation, noise is the random generation of scintillation and transition radiation signals. Therefore, the additional photon signals create noise which then increases the possibility that the system overestimates the actual muon momentum. However, we can improve the performance by eliminating noise using signal discriminators because the momentum overestimation due to noise is predictable. For the scenario

with 10 radiators (iii and iv), the recorded muon counts in each bin are greater than that of the previous scenario with 100 radiators. Even with fewer radiators, the spectrum is reconstructed adequately. When the random noise is added, the reconstructed spectrum is also shifted due to the overestimation of counted signals. The results from these scenarios demonstrate that the proposed spectrometer behaves as expected and it can successfully reconstruct the cosmic ray muon spectrum without any sophisticated signal processing. In the case where noise is present, there is a predictable shift that can be reduced or eliminated using a discrimination technique as discussed in Section 3.5.1.

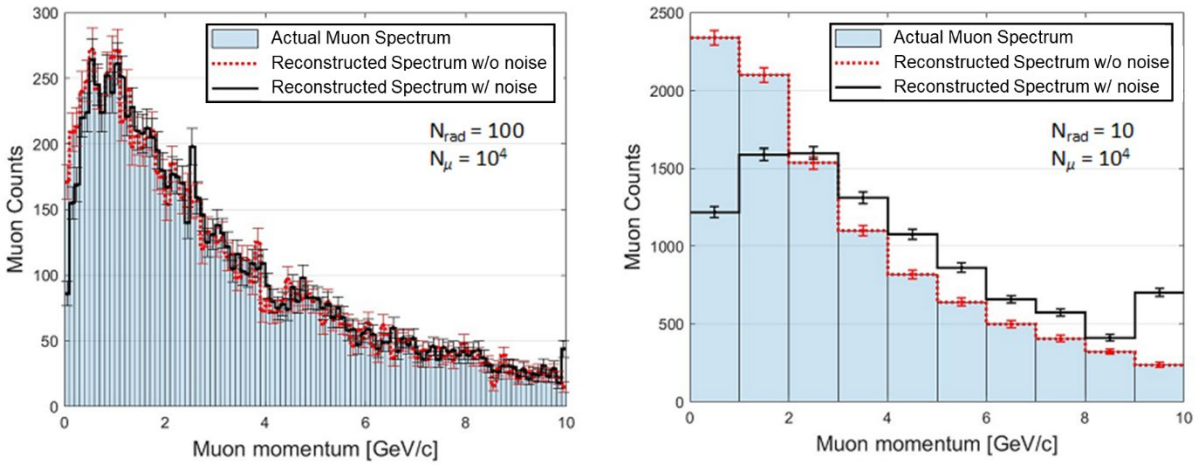

Figure 3.28. Reconstructed cosmic ray muon spectra using the 10^2 (left) and 10 (right) radiators without (dotted line) and with noise (solid line) with 10^4 muon samples. Histogram represents the classified cosmic ray muon spectrum using 10 momentum levels (Junghyun Bae & Chatzidakis, 2022c).

3.6 Summary

The extensive discussion of proposed Cherenkov muon spectrometer using multi-layer pressurized Cherenkov gas radiators were presented in this chapter. Two theories in physics, the Cherenkov effect and Lorentz-Lorenz equation, that motivated to develop of our Cherenkov muon spectrometer were outlined in Section 3.1. In addition, the brief operational principle and circuit diagram of a new Cherenkov muon spectrometer were presented. Section 3.2 details the results of a thorough investigation in searching gas Cherenkov radiators (C_3F_8, R1234yf, C_4F_{10}, and CO_2)

and rationales for choosing CO_2 gas for our prototype muon spectrometer. The theory and simple Monte-Carlo simulations for three dominant optical photon emission mechanisms in gas radiators, Cherenkov radiation, scintillation, and transition radiation, were discussed in Section 3.3. To verify the fidelity of Geant4 code for our Cherenkov muon spectrometer simulations, two muon physics were performed using Geant4, muon scattering angle distribution, and energy loss in Section 3.4. The results were compared with analytical models, the multiple Coulomb scattering approximation and Beth equation, respectively. Section 3.5 described the quantitative analysis of the performance and functionality of the Cherenkov muon spectrometer by presenting the algorithms for signal processing and noise elimination. At the end of Section 3.5, a cosmic ray muon spectrum was reconstructed using the current prototype (6 radiators and $\sigma_p = \pm 0.5$) and the extended number of radiators, 10 and 100. To evaluate and improve the results of cosmic ray muon spectrum reconstruction, concepts of classification rate and signal discriminator were presented.

4. MOMENTUM INTEGRATED IMAGING ALGORITHM

Although the benefits of measuring muon momentum in muon tomography have been demonstrated in various preceding studies (Junghyun Bae & Chatzidakis, 2021b; Stylianos Chatzidakis, Hausladen, et al., 2017), (i) it is still challenging to measure muon momentum in the field and (ii) the proper momentum integrated imaging algorithm does not exist. In the current muon scattering tomography algorithm, multiple Coulomb scattering (MCS) approximation and Point-of-Closest Approach (PoCA) are often used as discussed in Section 2.4.2. Due to the difficulty to measure muon momentum in the field, a mean or mode momentum value of cosmic ray muon (3–4 GeV/c) is used to represent the entire cosmic ray muon spectrum. This approximation often results in the increased measurement times and low image resolution that hampers the expansion of muon tomography to real-world applications. To overcome this shortcoming, several techniques have been proposed including a collection of a large number of muon samples or carefully excluding outlier data points, however, none of these approaches efficiently improves imaging quality and require significantly long measurement times. In this section, we introduce two momentum integrated PoCA algorithms: (i) material classification mPoCA and (ii) generalized mPoCA. The material classification mPoCA has an advantage in its capability to identify the type of target materials, however, it requires pre-calculated data and additional processes (Section 4.1). On the other hand, despite the generalized mPoCA is not able to specify the target material, it significantly improved the imaging quality without increasing computation times compared to that of the original PoCA algorithm (Section 4.2).

4.1 Material Classification mPoCA

In Section 2.4.2, we reviewed the muon scattering tomography using the PoCA imaging algorithm. Because it is not possible to accurately locate the history of muon scattering in the medium, a simple and fast PoCA algorithm has been developed based on Multiple Coulomb scattering approximation. In the original PoCA algorithm, a coordinate of PoCA point and muon scattering angle, are recorded for each muon event. As discussed in Chapter 3, muon momentum can be measured using a Cherenkov muon spectrometer in the field. Therefore, the estimated muon momentum is additionally tagged in the PoCA point along with a scattering angle to integrate

momentum into the PoCA algorithm (i.e., momentum integrated PoCA), Then, all muon event vectors include five values, three Cartesian components of PoCA point (P_x, P_y, and P_z), reconstructed spatial muon scattering angle, θ, and measured muon momentum, p_μ

$$\boldsymbol{X_i} = \left[P_x, P_y, P_z, \theta, p_\mu\right]_i \quad i = 1, \dots, N_\mu \tag{4-1}$$

where N_μ is the total number of muon events. All measured muon momenta can be classified by a finite number of momentum groups, N_p, depending on the functionality of the muon spectrometer. To reconstruct image of target object, the volume of interest is discretized into $N_X \times N_Y \times N_Z$ voxels and the designated PoCA point is denoted as $V_{l,m,n}$ where $l = 1, \dots, N_X$, $m = 1, \dots, N_Y$, and $n = 1, \dots, N_Z$ (l, m, and n are integers). Therefore, the muon event matrix, $\boldsymbol{X_i}$, can be decomposed with respect to momentum and PoCA voxel

$$\boldsymbol{X^T} = \left[\vec{X}_1^T, \vec{X}_2^T, \dots, \vec{X}_{N_p-1}^T, \vec{X}_{N_p}^T\right] \tag{4-2}$$

$$\vec{X}_j = \left[\binom{V_{l,m,n}(1)}{\theta_1} \binom{V_{l,m,n}(2)}{\theta_2} \cdots \binom{V_{l,m,n}(L)}{\theta_L}\right]_j \tag{4-3}$$

where L is the length of X_j. Because the expected muon scattering angle distribution depends on muon momentum, each $\boldsymbol{X_j^T}$ will have a unique scattering angle distribution. After the $\boldsymbol{X_i}$ decomposition process, (i) a designated voxel as PoCA, (ii) scattering angle, and (iii) momentum group data will be recorded for all muon events

$$\boldsymbol{Y_{i,j}} = \left[V_{l,m,n}, \theta_i, \pi(j)\right]_i \tag{4-4}$$

where θ_i is the ith muon event in the jth muon momentum group, $\pi(j)$. To reconstruct image of target materials using mPoCA algorithm, materials are classified with respect to their Z number (atomic number) because radiation length, X_0, depends on Z as described in (2-31). All materials

can be classified by M_N material classes using M_N-1 threshold scattering angles, θ_{th}. The threshold scattering angles are estimated by finding the intersection of two expected scattering angle distributions of threshold materials

$$f\left(\boldsymbol{\theta_{th}}; k, \pi(j)\right) = f\left(\boldsymbol{\theta_{th}}; k+1, \pi(j)\right) \quad k = 1, \dots, M_N - 1 \tag{4-5}$$

where $f\,(\theta_{th};\, k,\, \pi(j))$ is the expected muon scattering angle Gaussian distribution for a threshold material, $Z_{th}\,(k)$ when the muon momentum group is $\pi(j)$. By comparing the measured muon scattering angle to threshold angles, the most probable material class can be identified. The material classification process is then repeated for all momentum groups. Then, all muon events will have a PoCA voxel and expected material class, M_k. Hence, the muon event vector, (4-4), can be modified by

$$\boldsymbol{Y_{i,j,k}} = \left[V_{l,m,n}, M_k, \pi(j)\right]_i \tag{4-6}$$

By assigning a unique color for each material class in all PoCA voxels, the imaging process by muon scattering tomography using mPoCA algorithm is completed. A comparison of pseudocodes for PoCA and mPoCA algorithms in muon scattering tomography is shown in Figure 4.1.

4.1.1 Muon momentum groups

According to the results from Section 3.5.4, cosmic ray muon momentum can be categorized in six levels using a prototype of Cherenkov muon spectrometer, 0.1–1.0, 1.0–2.0, …, and > 5.0 GeV/c. To investigate the effect of muon momentum in scattering angle distribution, we generate 10^5 muons with a cosmic ray muon energy spectrum and cylindrical tungsten sample (D = 10 cm and H = 10 cm) in Geant4 simulations. All muon events are rearranged with respect to their momentum group, $\boldsymbol{X_1}$, …, $\boldsymbol{X_6}$. The results of scattering angle distributions for $\boldsymbol{X_i}$ and its subsets, $\boldsymbol{X_j^T}$, are shown in Figure 4.2. The most probable muon scattering angle peak, θ_{mode}, moves to lower-left because muon scattering angle is inversely proportional to momentum and expected muon counts decrease as momentum increases. It is noted that $\boldsymbol{X_6}$ (> 5.0 GeV/c) spectrum is out of trend due to the large muon counts.

1) Retrieve four Cartesian coordinates, $p_i = [x_i, y_i, z_i]$ where $i = 1, 2, 3,$ and 4, from muon trackers.
2) Reconstruct incoming and outgoing muon trajectories, l_1 and l_2, using two upper and lower coordinates, respectively.
3) Compute scattering angle, θ, by analyzing the incoming and outgoing muon trajectory angles.
4) Determine 2D or 3D PoCA points.
   IF two-dimension **THEN** find the intersection of two lines, l_1 and l_2. $\rightarrow P_{\text{PoCA}|2D}$
   ELSE find the closest point from two lines, l_1 and l_2. $\rightarrow P_{\text{PoCA}|3D}$
   ENDIF
5) Collect the coordinate of PoCA points, $P_{x,y,z}$, and scattering angles for all muon samples, N_μ, and save in the muon event vectors, $X_i = [P_x, P_y, P_z, \theta]_i$ where $i = 1, \ldots, N_\mu$.
6) Discretize the volume of interest for image reconstruction in $N_X \times N_Y \times N_Z$ voxels.

PoCA	**mPoCA**
7a) Save the scattering angle data into the PoCA voxel and update the muon event vector. $\rightarrow Y_i = [V_{l,m,n}, \theta]_i$ where $V_{l,m,n}$ is the designated voxel coordinate as a PoCA point. **IF** more than one muon samples are recorded in a PoCA voxel **THEN** use the mean scattering angle. **END IF**	7b) Include muon momentum data into the muon event vector X_i. $\rightarrow X_i = [P_x, P_y, P_z, \theta, p_\mu]_i$
	8b) Proceed (7a) $\rightarrow Y_i = [V_{l,m,n}, \theta, p_\mu]_i$
	9b) Momentum classification. **FOR** each muon momentum groups, 1 to N_p. Classify all muon samples by its momentum groups, $\pi(j)$ where $j = 1, \ldots, N_p$. **END FOR** $\rightarrow Y_{i,j} = [V_{l,m,n}, \theta, \pi(j)]_i$
8a) Assign a relative colormap for each PoCA voxel with respect to recorded muon scattering angles.	10b) Define material classes based on the Z number and determine the threshold scattering angles, θ_{th}, for all momentum groups. $\rightarrow Y_{i,j,k} = [V_{l,m,n}, M_k, \pi(j)]_i$
	11b) Assign a unique color for each material class in the PoCA voxels.

Figure 4.1. A comparison of pseudocodes for PoCA and mPoCA algorithms for muon scattering tomography.

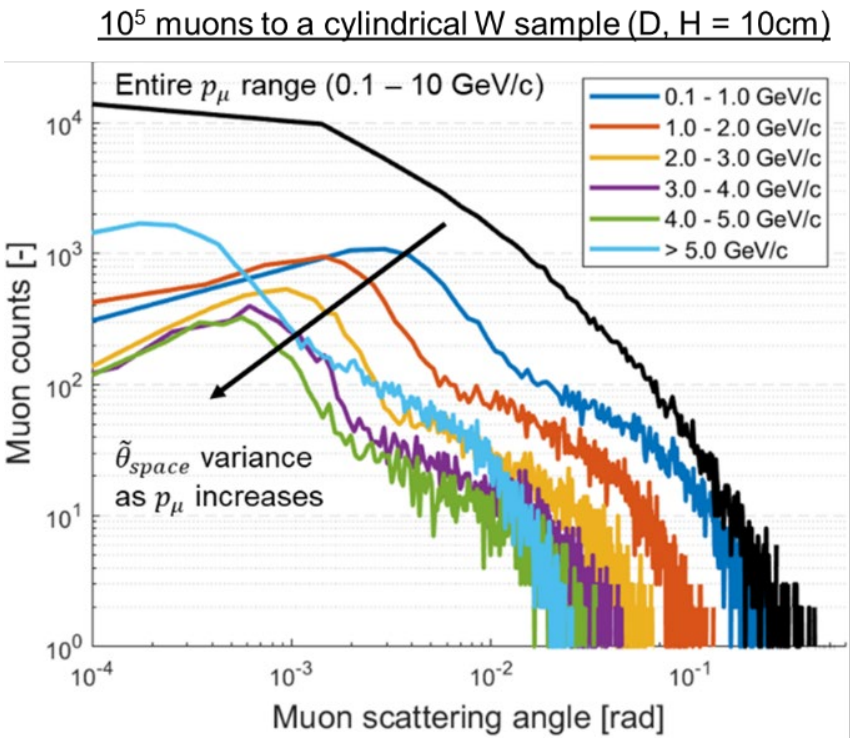

Figure 4.2. Six independent muon scattering angle distributions are plotted with respect to muon momentum groups, 0.1–1.0, …, 4.0–5.0, and > 5.0 GeV/c. It is noted that a peak of distribution moves from 10^{-2} to 10^{-4} radian as muon momentum increases.

4.1.2 Material classification

In this section, we used four material classes to identify a type of target materials: (i) gas or liquid (Z < 11), (ii) light structural materials (Z ~20), (iii) heavy structural or shielding materials (Z ~74), and (iv) potential special nuclear materials (Z > 90). The nuclear properties of various selected threshold materials (Z_{th} = 11, 20, 74, and 90) are summarized in Table 4.1. The computed scattering angle distributions for four threshold materials when muon momentum is 0.5, 1.5, 2.5, 3.5, 4.5, and 5.5 GeV/c are shown in Figure 4.3. The intersections of two distributions are found for material classification (threshold scattering angles, θ_{th}) and they are shown as vertical dashed lines in Figure 4.3. To identify the type of material, the most probable material class is designated (M_1, M_2, M_3, or M_4) for each muon event by comparing measured muon scattering angle with threshold angles. However, because a width of muon scattering angle distribution, σ_θ, is a function of two variables, p_μ and X/X_0, the threshold angles also vary along with them. For example, threshold angle values for $<p_\mu>$ = 0.5, 1.5, … 5.5 GeV/c when the length of scattering medium, is 10 cm, are tabulated in Table 4.2.

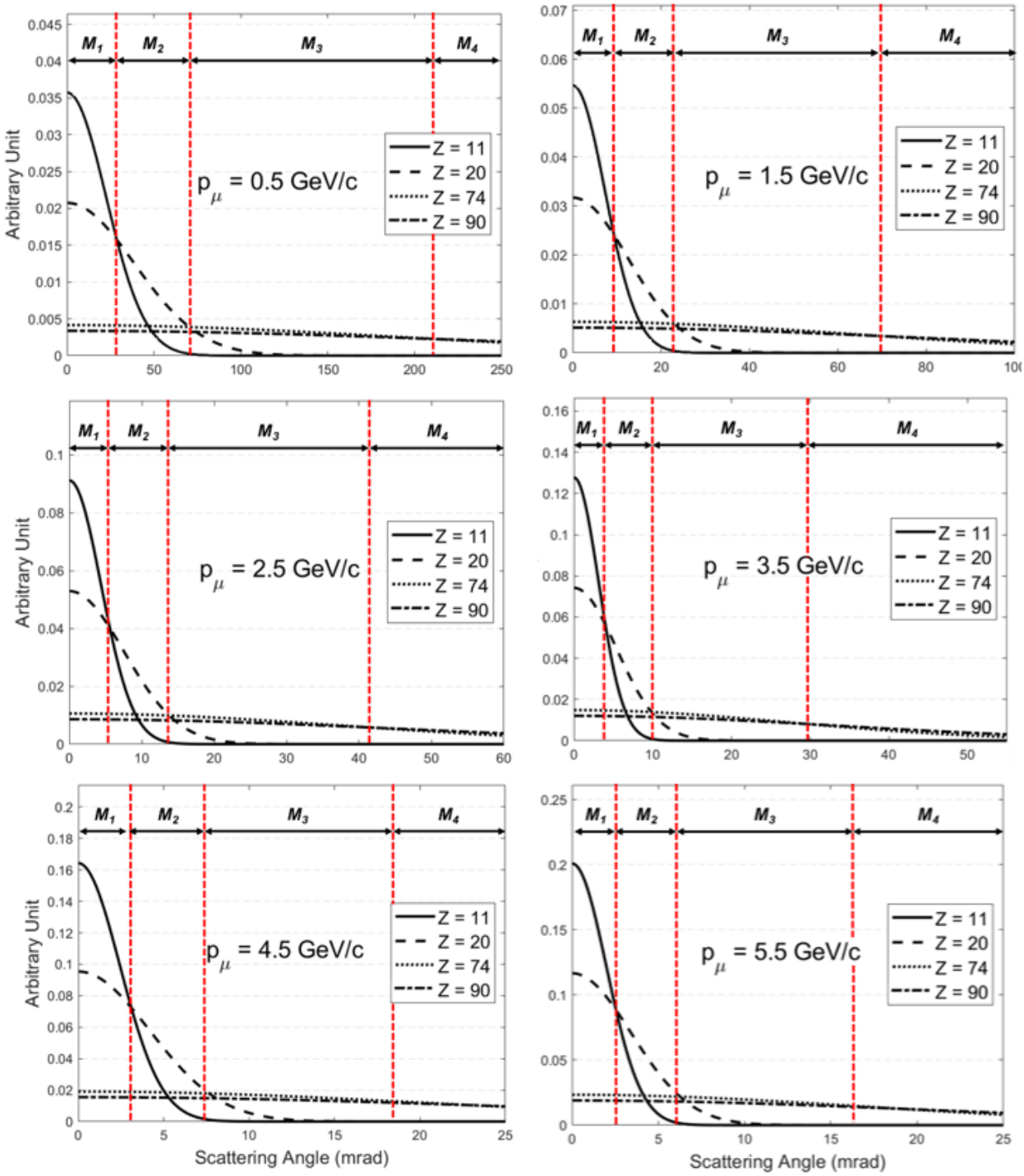

Figure 4.3. Expected scattering angle distributions for threshold materials (Z_{th} = 11, 20, 74, and 90) based on multiple Coulomb scattering approximation when p_μ = 0.5, 1.5, 2.5, 3.5, and, 5.5 GeV/c. Scattering angles at each intersection of two distributions represent threshold angles (vertical dashed lines). The threshold angles are tabulated in Table 4.2.

Table 4.1. Nuclear properties of selected threshold materials (Z_{th} = 11, 20, 74, and 90) and materials used in Geant4 simulations (Particle Data Group, 2020).

	Atomic number	Atomic mass [g/mol]	Density [g/cm^3]	Radiation Length [g/cm^2]
Air	-	-	1.205E-3	36.62
Na	11	22.99	0.9710	27.74
Al	13	26.98	2.699	24.01
Ca	20	40.08	1.550	16.14
Fe	26	55.85	7.874	13.84
W	74	183.84	19.30	6.76
Pb	82	207.21	11.35	6.37
Th	90	232.04	11.72	6.07
U	92	238.03	18.95	6.00

Table 4.2. Threshold scattering angles for various muon momentum groups in material classifications.

θ_{th} [mrad]	<p_μ> [GeV/c]					
	0.5	**1.5**	**2.5**	**3.5**	**4.5**	**5.5**
$M_1 - M_2$	28.6	9.1	5.5	4.0	3.1	2.3
$M_2 - M_3$	74.3	24.3	14.1	10.4	8.0	6.6
$M_3 - M_4$	212.2	69.1	41.5	29.7	18.2	15.6

Using the computed threshold angles for each momentum group, estimated material IDs, i.e., M_1, M_2, M_3, or M_4, are assigned for all muon events. Therefore, the muon event vectors are given by

$$\boldsymbol{Y_{i,j,k}} = \left[V_{l,m,n}, M_k, \pi(j)\right]_i \quad i = 1, \dots N_\mu; j = 1, \dots, 6; k = 1, \dots 4 \tag{4-7}$$

For imaging, each designated PoCA voxel is colored according to the assigned color of material ID for all muon events instead of using gradient colormap based on the scattering angle distribution. By assigning the different color for each material ID, we were able to identify materials based on material classification table (Table 4.2) because the results show absolute colors (colormap based on types of materials) instead of relative colors of materials (colormap based on scattering angle distribution).

4.2 Generalized mPoCA

Unlike the material classification mPoCA, a generalized mPoCA does not rely on material classification (material ID) nor threshold scattering angles to reconstruct images in muon tomography. Instead, we introduce a new value, M, which mathematically integrates muon momentum and scattering angle as a single value without increasing computational cost. It replaces scattering angles, i.e., rad or rad^2/cm, that are used for the original mPoCA imaging algorithm. The generalized mPoCA algorithm was developed to overcome limitations of the multiple Coulomb scattering (MCS) approximation and original PoCA algorithm. The limitations of MCS approximation are summarized in Section 4.2.1. The mathematical and physical backgrounds of a new value, M, and imaging algorithm using M-values are discussed in Section 4.2.2.

4.2.1 Limitations of multiple Coulomb scattering approximation

According to the MCS approximation, muon scattering angle distribution follows the Gaussian distribution with a zero mean. Although the standard deviation of that Gaussian distribution varies depending on two variables, p_μ and X/X_0, it assumes that a mean or mode value of muon scattering angle is always zero. However, the most probable scattering angle, or mode scattering angle, $mod(\theta)$, not only has a non-zero value but also varies depending on two variables, p_μ and X/X_0, as shown in Figure 4.2. Muon multiple Coulomb scattering distributions using MCS approximation, Molière model, and Geant4 simulation when 10^4 3 GeV mono-energy muons interact with 10 cm uranium sample are shown in Figure 4.4. Although the Molière model successfully estimates the hard scatterings (long tail) than MCS approximation, it was developed for small radiation length objects, $X/X_0 < 1$. Therefore, the discrepancy level with Geant4 simulation results increases for large muon scattering angles.

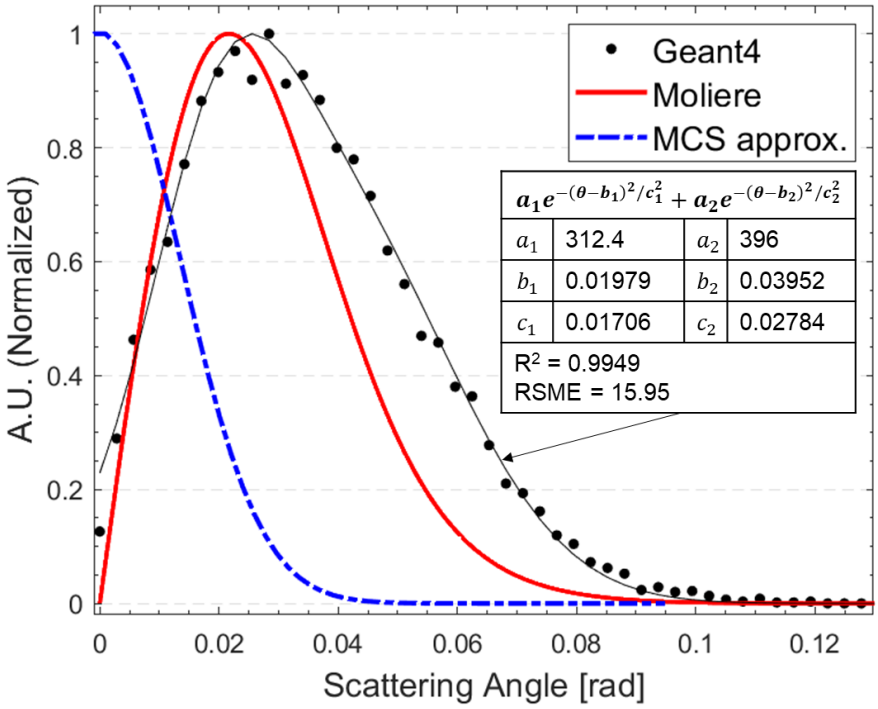

Figure 4.4 Normalized muon multiple Coulomb scattering angle distributions using (i) MCS approximation, (ii) Molière model, and (iii) Geant4 simulation ($N\mu = 10^4$) in the uranium sample (L = 10 cm) when $p_\mu = 3$ GeV/c.

The Geant4 simulation results and MCS approximations for mode and standard deviation of muon scattering angle distribution is shown in Figure 4.4. In the MCS approximation, when muon momentum increases, a mode of scattering angle distribution remains zero, however, the width of Gaussian distribution is narrowed as the standard deviation is decreased. On the other hand, Geant4 simulations show that both mode and standard deviation exponentially decrease as the muon momentum increases. To accurately compare the difference between MCS approximation and Geant4 simulation results, we used a folded Gaussian distribution for the MCS so that all computed scattering angles have absolute values. The variance of the folded Gaussian distribution is given by

$$\sigma_f^2 = \sigma^2\left(1 - \frac{2}{\pi}\right) \tag{4-8}$$

where σ^2 is the variance of the original Gaussian distribution (2-33). Although Geant4 simulation results show the scattering angle distribution has a non-zero mode value, they have similar variances with σ_f^2

$$\sigma_{G4}^2 \sim \sigma_f^2 \tag{4-9}$$

To quantify the shape of scattering angle distributions by MCS (folded Gaussian) and Geant4 simulations, we also present the skewness of distribution as shown in Figure 4.5.

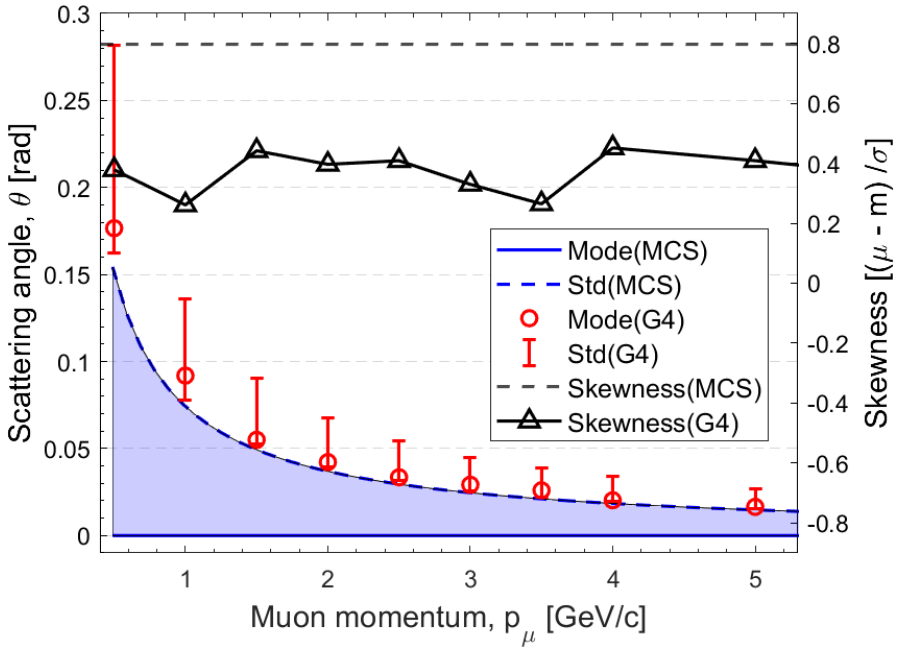

Figure 4.5. Mode and standard deviation of muon scattering angle distributions as a function of muon momentum using MCS approximation and Gean4 simulations. The skewness of distributions is also plotted to help image their shapes.

4.2.2 M–value

As shown in Figure 4.4, there is a clear relationship between mode scattering angle, *mod(θ)*, and momentum, *p*. This correlation can be linearized by taking logarithms of both *mod(θ)* and *p*. Then, the correlation is written by

$$\log_{10} mod(\theta) = k \log_{10} p + M \tag{4-10}$$

where k is the slope and M is the y-intersection. The plots of (4-10) for various materials and sizes, are shown in Figures 4.6 and 4.7. Despite k varies from –2.38 for uranium to –2.23 for aluminum, it is convenient to assume as a constant to reduce one variable because a type and size of materials more highly and clearly depend on M than k. Since we have two measurements, scattering angle and momentum, for each muon event in the momentum integrated muon tomography, we can use a new function, $M(p, \theta)$, to replace scattering angle density

$$M(p,\theta) \equiv \log_{10}\left(\frac{\theta}{p^k}\right) \tag{4-11}$$

when k is assumed as the average value, -2.3, (4-11) becomes

$$M = \log_{10}(\theta\ [rad] \times p\ [GeV/c]^{2.3}) \tag{4-12}$$

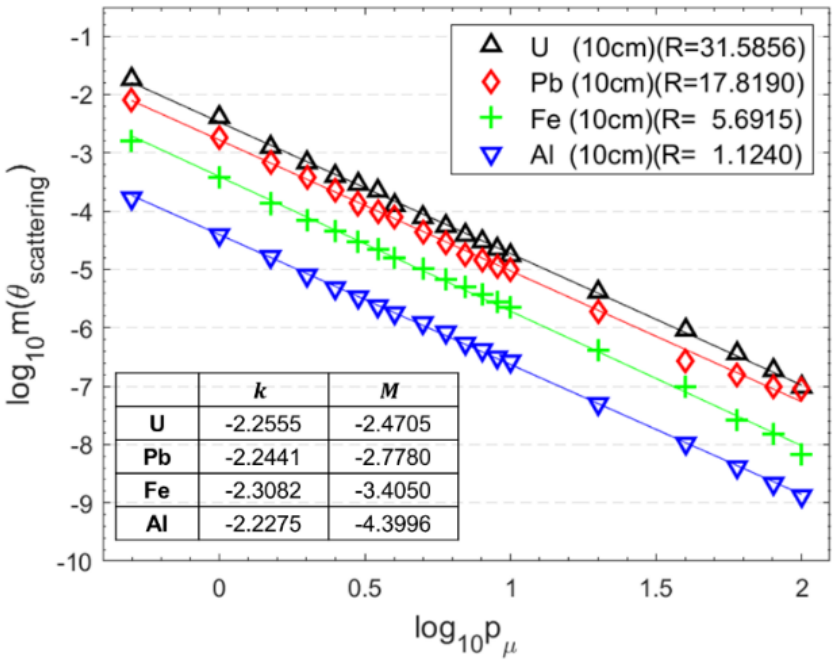

	k	M
U	-2.2555	-2.4705
Pb	-2.2441	-2.7780
Fe	-2.3082	-3.4050
Al	-2.2275	-4.3996

Figure 4.6. The linear relationship between $\log_{10} p_\mu$ and $\log_{10} mod(\theta)$ for various sample materials: U, Pb, Fe, and Al with a length of 10 cm. Each material has a unique radiation length number, R. k (slope) and M-values (y-intersection) for all samples are also presented in tables.

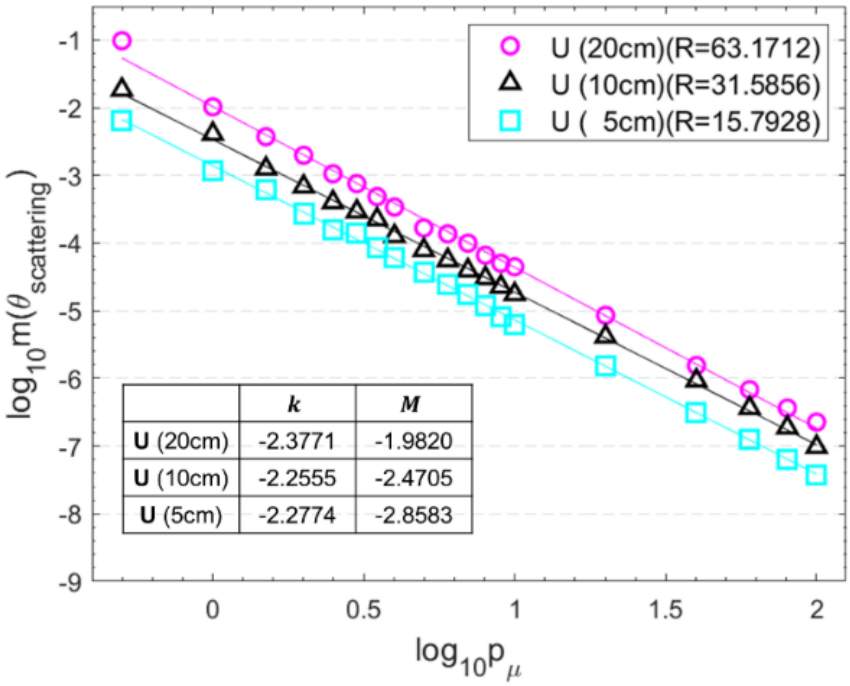

Figure 4.7. The linear relationship between $\log_{10} p_\mu$ and $\log_{10} mod(\theta)$ for various sizes: 5, 10, and 15 cm of uranium samples. Each size of uranium has a unique radiation length number, R. k (slope) and M-values (y-intersection) for all samples are also presented in tables.

To demonstrate that the M-value can represent the material type and size, we found the correlation between M-values and X/X_0. To take into account both material type and size, a new dimensionless number, or radiation length number, R, is defined

$$R \equiv X/X_0 \tag{4-13}$$

The M-values for various size and types of materials are plotted and it shows the linear correlation between M and $\log_{10}(R)$. As shown in Figure 4.8, we can estimate R from M-values using coefficients, a (slope) and b (y-intersection), because it has a linear correlation.

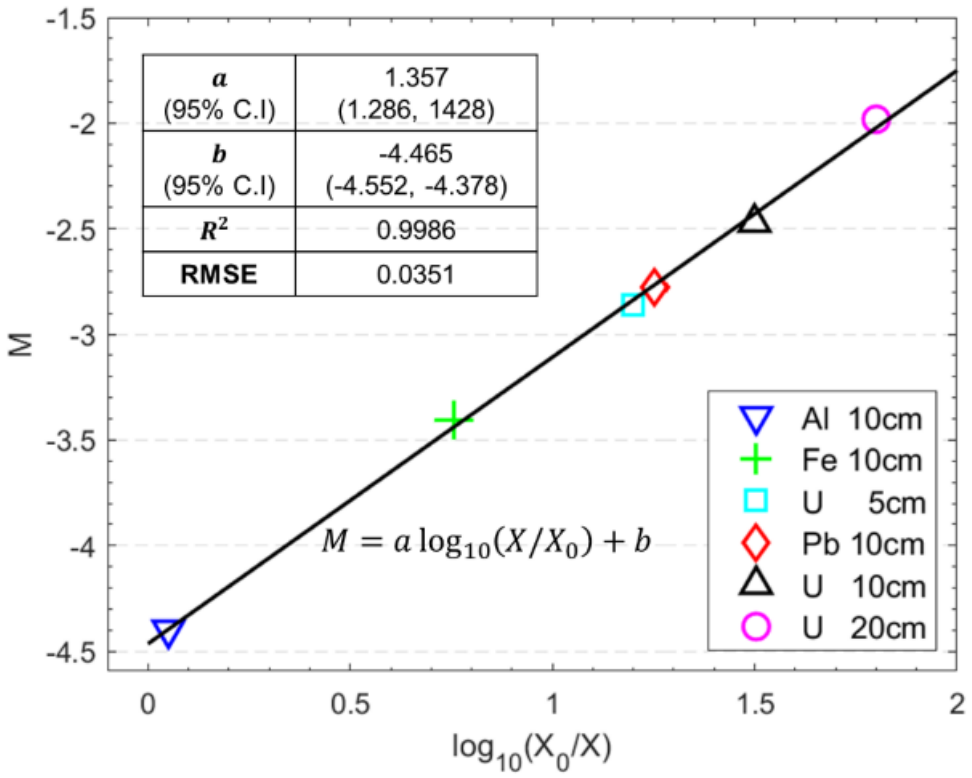

Figure 4.8. The linear correlation between $\log_{10}(R)$ and M for various size and types of materials.

4.3 Summary

Two momentum integrated imaging algorithms for muon scattering tomography: (i) material classification mPoCA and (ii) generalized mPoCA, were presented in this chapter. In the material classification mPoCA, the muon momentum information is included along with a 3D Cartesian coordinate of a PoCA point for each muon event. The method to integrate momentum information in the tomography imaging algorithm and applications of material classification mPoCA were presented in Section 4.1. Specifically, the material classification mPoCA has an advantage in its capability to identify the type of target materials such as cargo scanning or SNM investigation. However, reference database and additional processes must be provided in this algorithm which requires increased computational costs. In Section 4.2, the principle and applications of the generalized mPoCA imaging algorithm were introduced. In the generalized mPoCA imaging algorithm, a scattering angle or scattering angle value which are sued in the original PoCA algorithm are replaced by the *M*-value. Hence, a quantity recorded in each voxel in the tomographic imaging process is a *M*-value instead of scattering angles. Because the generalized mPoCA also reconstructs images using a relative colormap like the original PoCA (scattering angle vs *M*-value), this algorithm works more efficiently when the target materials are known such as SNF dry cask or reactor imaging. It significantly improves the imaging quality and reduces scanning times without increasing computational times compared to that of the original PoCA algorithm.

5. MOMENTUM INTEGRATED MUON TOMOGRAPHY

A portion of this chapter was previously published by *Energies*, **15** (7), 2666 (2022), "Momentum-Dependent Cosmic Ray Muon Computed Tomography using a Fieldable Muon Spectrometer," Bae, J. and Chatzidakis, S. [DOI: 10.3390/en15072666]

Nuclear material and waste management are among the critical tasks to be addressed for the advancement of nuclear energy. In this regard, monitoring of spent nuclear fuel (SNF) and special nuclear materials (SNM), is important to continue reliable stewardship of used fuels and radioactive material management. As extensively discussed in Chapter 2, cosmic ray muons have promising unique properties for monitoring and imaging large and dense objects such as SNF dry cask, cargo scanning, and reactor monitoring. In this chapter, Geant4 simulation results for various applications in SNM monitoring and SNF dry cask imaging using a momentum integrated muon tomography are discussed. Two momentum integrated muon tomographic methods are presented using material identification and generalized mPoCA algorithms, in Sections 5.1 and 5.2, respectively. The material classification mPoCA imaging algorithm is ideal for investigating unknown or smuggled nuclear materials whereas the generalized mPoCA is more efficient for imaging known nuclear materials such as spent nuclear fuel dry casks.

5.1 Nuclear Material Monitoring and Imaging

Cosmic ray muons have been considered as a potential high-energy radiation probe for monitoring and interrogation of dense, well-shielded special nuclear materials (SNM). Due to their high-penetrative nature, cosmic ray muons can easily penetrate shielded nuclear materials with minimal absorption and with leaving the target objects intact. Unless the objective of SNM monitoring is a visualization such as a fast SNM scanning in a cargo container, the statistical analysis will significantly reduce the measurement times for decision-making process. Therefore, methods for the statistical decision-making and the effect of momentum measurement in the SNM monitoring for nuclear security applications are presented in Section 5.1.1. Section 5.1.2 details the muon tomography for nuclear material imaging using the material classification mPoCA method which is described in Section 4.1.

5.1.1 Shielded nuclear material monitoring

To investigate the effect of momentum measurement in the special nuclear material monitoring, significant quantities (SQ) of high-, low-enriched uranium, and plutonium surrounded by lead shielding are designed for simulations. The parameters of SNMs (HEU, LEU, and Pu) and Pb used in Monte-Carlo simulations are tabulated in Table 5.1. All SNMs and non-SNM are assumed to have a spherical shape surrounded by lead shielding thicknesses of 0, 5, 10, 20, and 30 cm as shown in Figure 5.1. The effective radiation length for SNMs with a lead shielding layer is given by

$$\frac{r_{obj}\rho_{obj}}{X_{0,obj}} = \frac{r_{\mathrm{SNM}}\rho_{\mathrm{SNM}}}{X_{0,\mathrm{SNM}}} + \frac{L_{Pb}\rho_{Pb}}{X_{0,Pb}} \quad (\mathrm{SNM} = \mathrm{HEU, LEU, and\ Pu}) \tag{5-1}$$

$$r_{obj} = r_{SNM} + L_{Pb} \tag{5-2}$$

where $X_{0,i}$, ρ_i, and r_i are radiation length, density, and radius of ith component when i is SNMs, Pb, or both (object = SNM + Pb), and L_{Pb} is the thickness of lead shielding. The radii of SNMs were determined based on their reported SQs (IAEA, 2001). The total radius of object is a sum of SNM radius and lead shielding thickness. To compare the effective radiation length of SNMs with various thicknesses of lead shielding, we used a radiation length number (4-13). X_0 and R as a function of lead shielding thickness, L_{Pb}, are shown in Figure 5.2.

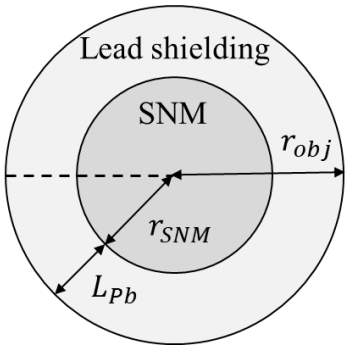

Figure 5.1. Cross section of spherical SNMs (HEU, LEU, and Pu) surrounded by a lead shielding, L_{Pb} (Junghyun Bae & Chatzidakis, 2021b).

Table 5.1. Density, radiation length (X_0), and significant quantity (SQ) of selected special nuclear materials and lead.

	LEU	HEU	Pu	Pb
Density [g/cm3]	19.1	19.1	19.84	11.35
X_0[cm]	0.3166	0.3166	0.2989	0.5612
SQ (IAEA, 2001)	75 kg	25 kg	8 kg	-

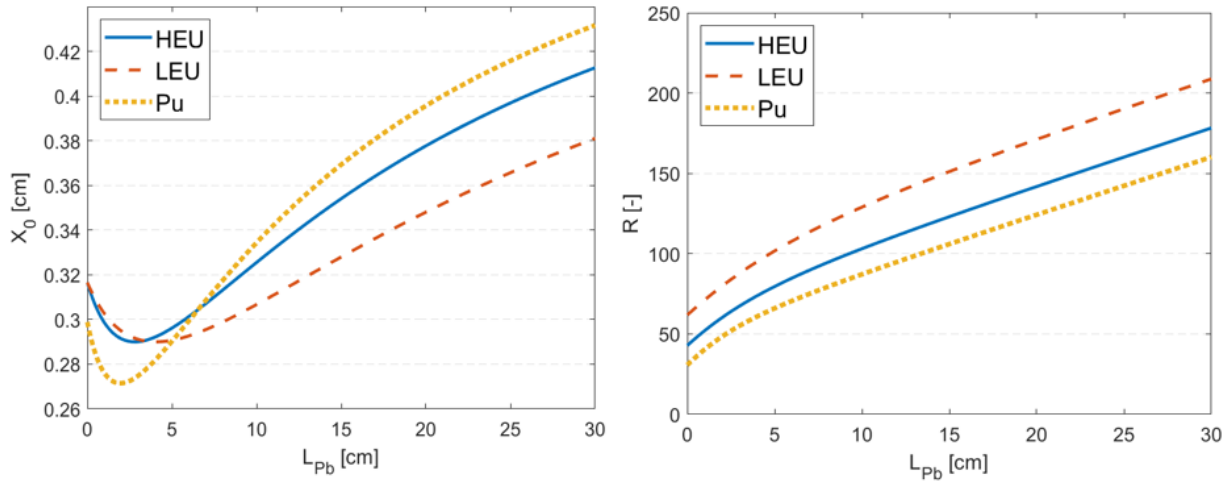

Figure 5.2. The effective radiation length, X_0 (left), and radiation length number, R (right), for HEU, LEU, and Pu as a function of lead shielding thickness, L_{Pb} (Junghyun Bae & Chatzidakis, 2021b).

Effect of Lead Shielding

Five thicknesses of lead shielding, 0, 5, 10, 20, and 30 cm, around SNMs were considered. Figure 5.3 shows the results of muon scattering angle variance distributions for Pb, LEU, HEU, and Pu with a 5 and 30 cm lead shielding when momentum measurement resolution, σ_p, is 0.5 GeV/c, the number of muons, N, is10^3, and the number of iterations, M, is 10^3. The definition and derivation of the scattering angle variance distribution are detailed in Appendix C. Without a lead shielding, SNMs are successfully separated from lead sample. However, the scattering angle variance distributions are substantially overlapped each other when a 30 cm-thick lead shielding is present and they are no longer distinguishable from Pb or one another. The material separation and identification, however, are enhanced by increasing measurement times and improving the momentum measurement resolution.

Effect of Measurement Time

To demonstrate the effect of measurement times, two scenarios are considered, 10^3 and 4×10^3 without momentum knowledge and their scattering angle variance distributions are shown in Figure 5.4. None of materials is able to be identified using 10^3 muons without muon momentum knowledge whereas Pb is separated from SNMs with a longer measurement time.

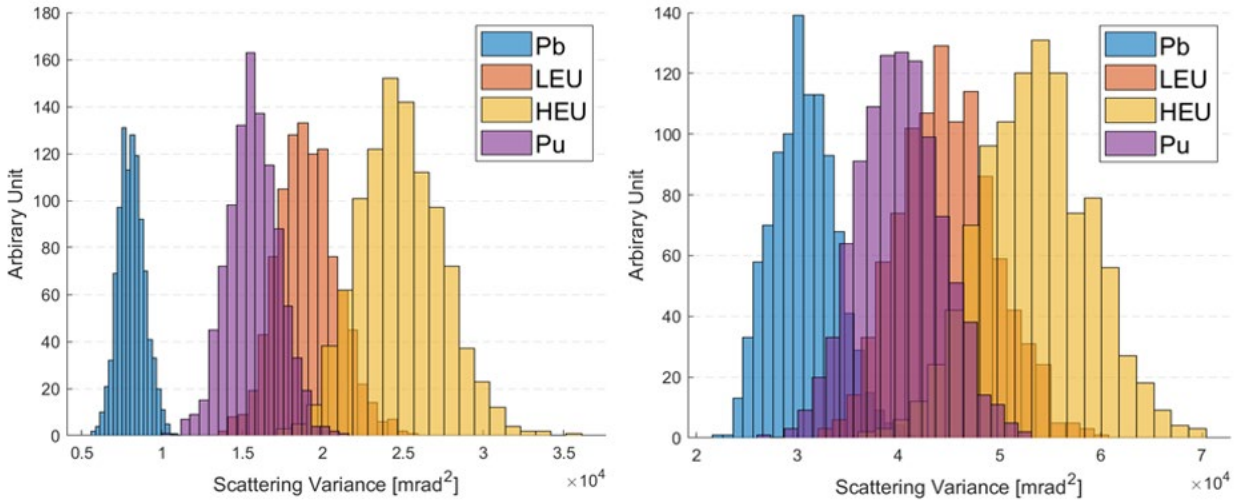

Figure 5.3. Scattering angle variance distributions for Pb, LEU, HEU, and Pu with a 5 cm (left) and 30 cm (right) lead shielding using 1×10^3 muons with a momentum resolution of 0.5 GeV/c (Junghyun Bae & Chatzidakis, 2021b).

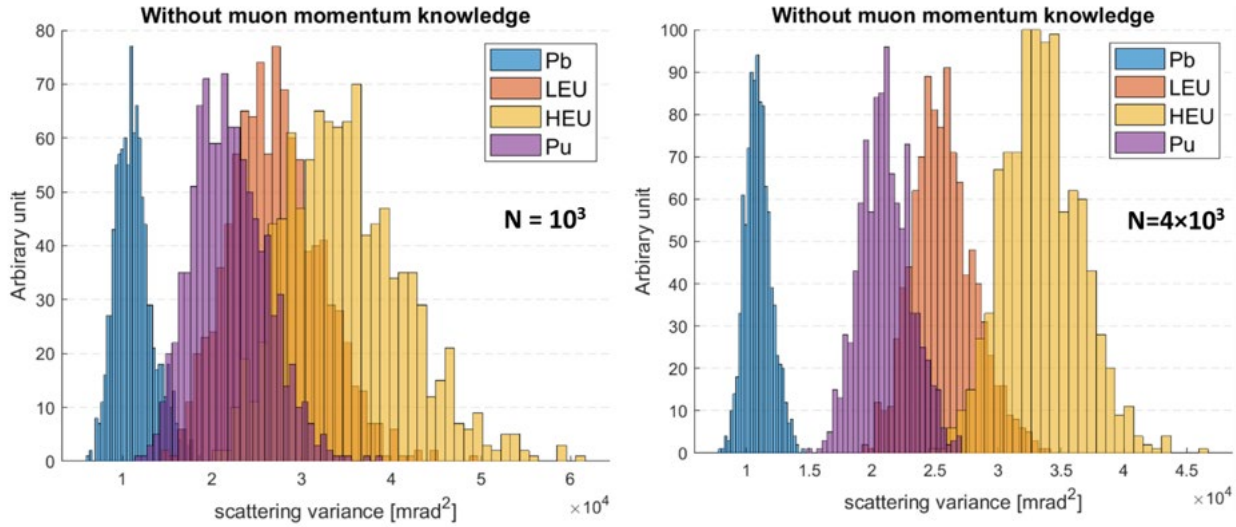

Figure 5.4. Scattering angle variance distributions for Pb, LEU, HEU, and Pu with a 5 cm thick lead shielding using 10^3 (left) and 4×10^3 muons (right) without muon momentum knowledge (Junghyun Bae & Chatzidakis, 2021b).

Separation and Identification of SNMs

For the further investigation of separation and identification of nuclear materials, three threshold lines are drawn between two neighboring scattering angle variance distributions: (i) Pb–Pu, (ii) Pu–LEU, and (iii) LEU–HEU for Pb and Pu, Pu and LEU, LEU and HEU, respectively. Scattering angle variance distributions for SNMs with a 30 cm-thick lead shielding and their receiver operating characteristic (ROC) curves are shown in Figure 5.5. When a muon momentum knowledge is utilized in the SNM monitoring, SNMs are easily separated from non-SNM and each SNM is clearly identified with a high detection rate and low false alarm rate. However, without a muon momentum knowledge, none of materials is distinguished.

Area under curves (AUC) for separation and identification as a function of lead shielding thickness are plotted and shown in Figure 5.6. The AUC for LEU-HEU decreases from 1 to 0.78 without muon momentum measurement whereas it only decreases to 0.89 with a muon momentum knowledge. This highlights the advantage of measuring muon momentum in both SNM separation and identification in SNM monitoring. In addition, Figure 5.7 shows AUC curves as a function the number of muons for two SNM identifications with a muon momentum measurement when they are surrounded by 30 cm lead shielding. The intersection of AUC curves and horizontal dashed line represent the number of muons required to achieve AUC = 0.9. For instance, to separate LEU and HEU with high confidence level (3σ), it requires 4×10^3 muons whereas only 1×10^3 muons are needed with a muon momentum knowledge. For the Pu and LEU separation, it requires 2.5×10^3 and 8.5×10^3 muons, respectively. Although the required number of muons for monitoring relies on various factor, i.e., AUC criteria, types of SNM separations, and shielding thickness, scanning times can be shortened by a factor of 3 to 4 when measuring muon momentum with a measurement resolution of 0.5 GeV/c or better.

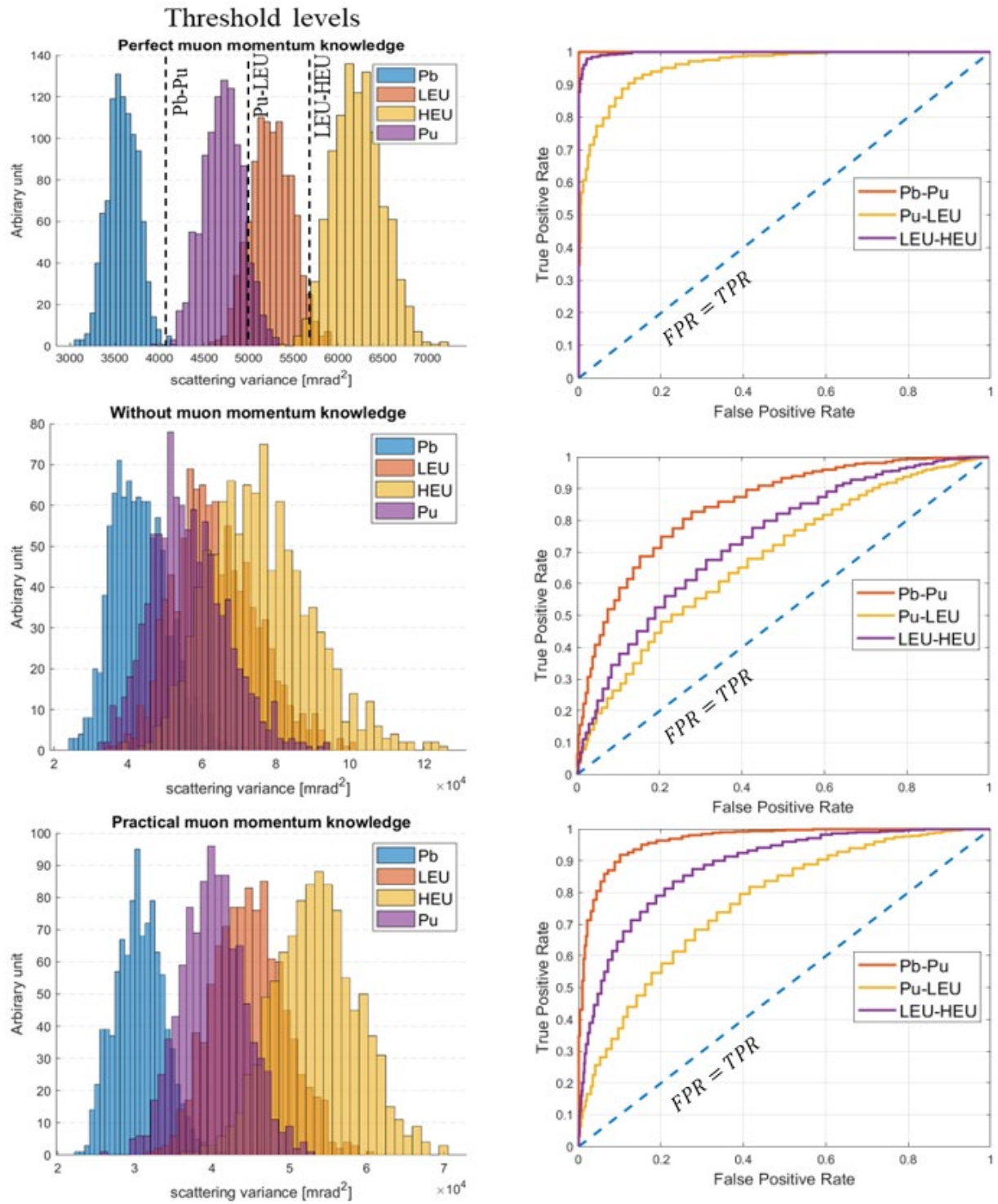

Figure 5.5. Muon scattering angle variance distributions of SNMs and Pb with a 30 cm thick lead shielding (left) and three ROC curves for each threshold level for two materials (right). Threshold levels for separation between two materials (Pb-Pu, Pu-LEU, and LEU-HEU) are also included (Junghyun Bae & Chatzidakis, 2021b).

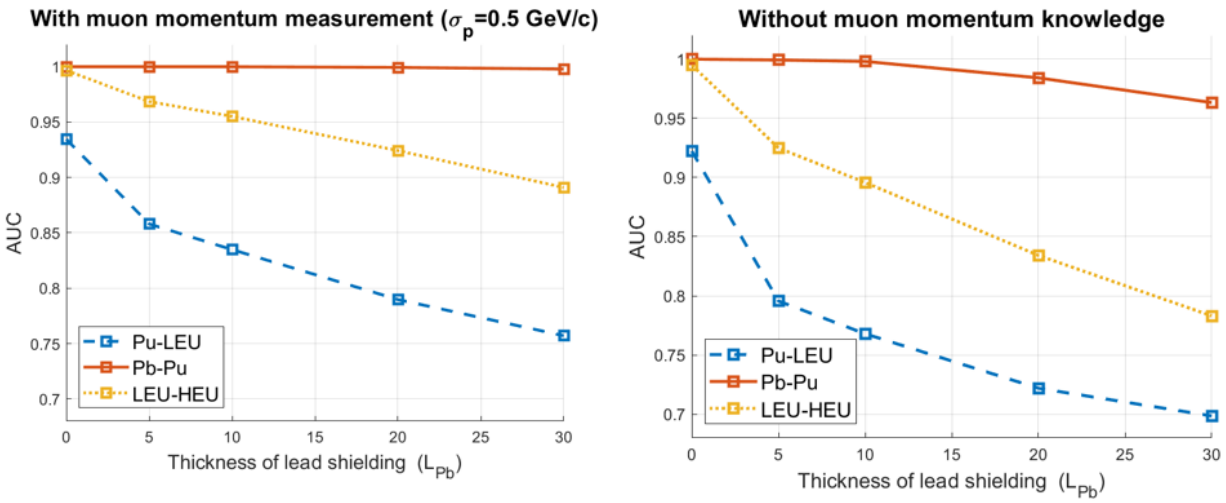

Figure 5.6. Area under curves (AUC) for Pb-Pu, Pu-LEU, and LEU-HEU as a function of thickness of lead shielding with a muon momentum measurement (left) and without a momentum measurement (right) (Junghyun Bae & Chatzidakis, 2021b).

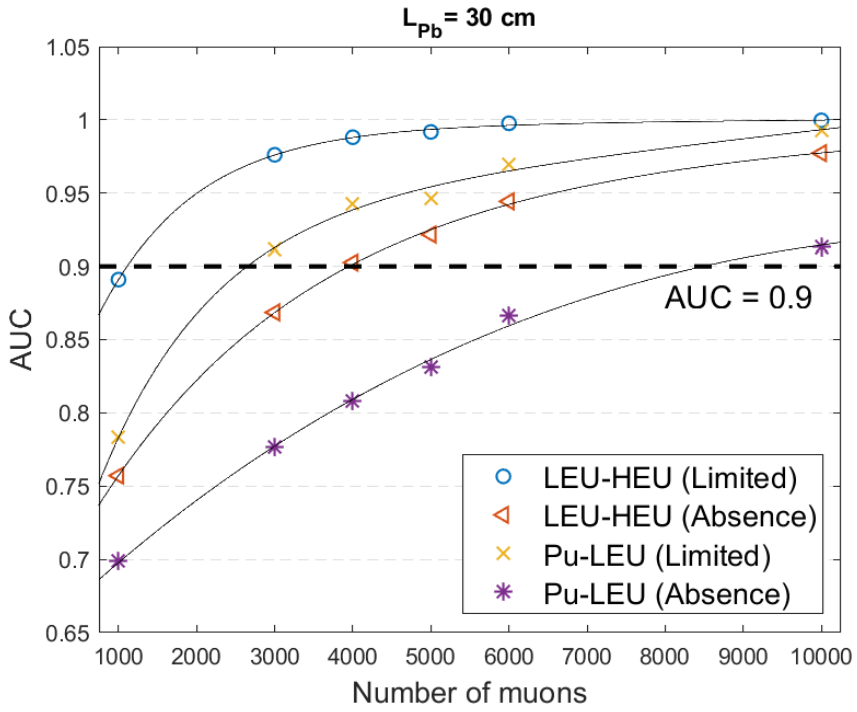

Figure 5.7. Area under curves (AUC) for LEU-HEU and Pu-LEU separation as a function of number of muons for limited and absent muon momentum knowledge with L_{Pb} = 30 cm. The intersections with curves and horizontal dashed line represent the number of muons required to achieve AUC = 0.9 (Junghyun Bae & Chatzidakis, 2021b).

5.1.2 Geant4 simulations for SNM imaging

In this section, to explore the benefits of muon momentum measurement in special nuclear material imaging, the images of SQ of LEU sample surrounded by 5 cm-thick lead shielding are reconstructed using an original PoCA and mPoCA imaging algorithms. We used 10^5 muon samples in Geant4 to simulate stochastic muon transports and muon tomographic images. To demonstrate the effect of momentum measurement, the muon tomographic images are reconstructed using a (i) PoCA algorithm with a cosmic ray muon spectrum when p_μ = 0.2 – 100.0 GeV/c, (ii) PoCA algorithm with mono-energetic muon, p_μ = 3 GeV/c, and (iii) mPoCA algorithm when materials are classified in three groups, M_1, M_2, and M_3, for SNMs, shielding materials, and surroundings, respectively. The layout of spherical LEU sample with a 5 cm thick lead shielding and three reconstructed images are shown in Figure 5.8 (Junghyun Bae & Chatzidakis, 2022c). As discussed in Section 4.1, in the mPoCA algorithm, the most probable material group is recorded instead of scattering angle value in each voxel. The imaging resolution is significantly improved and the boundaries between spherical LEU sample and lead shielding are visually distinguished because the number of noise voxels in the air gap decreases.

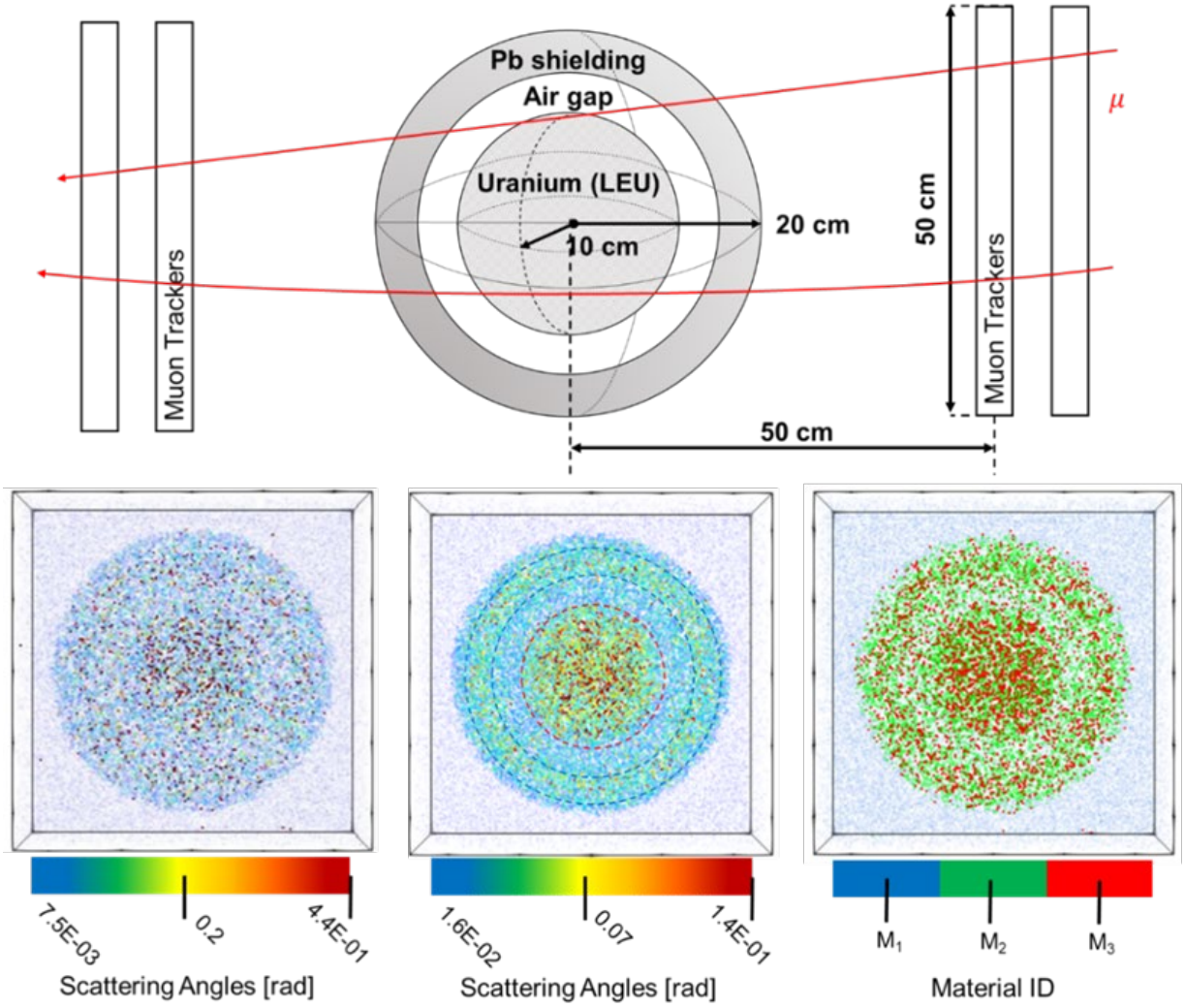

Figure 5.8. The layout of spherical LEU sample surrounded by a 5 cm thick lead shielding (top). Three reconstructed images (cross-sectional images) using a (i) PoCA algorithm with a cosmic ray muon spectrum when p_μ = 0.2 – 100.0 GeV/c (left), (ii) PoCA algorithm with mono-energetic muon momentum, p_μ = 3 GeV/c (center), and (iii) mPoCA algorithm with a cosmic ray muon spectrum when p_μ = 0.2 – 100.0 GeV/c (right) are shown. The number of muons is 10^5 (Junghyun Bae & Chatzidakis, 2022c).

Material identification

To demonstrate the performance of material classification mPoCA imaging algorithm, we benchmarked one image reconstruction experiment which was initially performed by K. Borozdin et al. (Borozdin et al., 2003) (details of experiment and simulation can be found in the paper by Schultz (Larry J Schultz, 2003) using Geant4 simulations. Materials used in this experiment and simulations are tungsten, structural steel, and plastic. Cylindrical tungsten (radius = 5.5 cm, height

= 5.7 cm) is placed on the plastic plate (60×60 cm^2) and two steel beams (5×5×50 cm^3) are used on both sides to hold a plastic plate as shown in Figure 5.9. In our simulations, 5×10^4 and 10^5 muon samples are generated, however, only 70 to 80% of muons are utilized for imaging reconstruction because not all generated muons are recorded by all four muon trackers which are placed on top and bottom of target materials. Examples of muon interactions and trajectories with target geometries in Geant4 simulations are shown in Figure 5.9 (right). In addition to previous model benchmarking, we designed a more challenging scenario to demonstrate the advantages of mPoCA algorithm in material identification application. In this example, four cylindrical materials (radius = 5 cm, height = 5 cm) which are made of aluminum, steel, lead, and uranium, are evenly placed from the center as shown in Figure 5.9 (bottom).

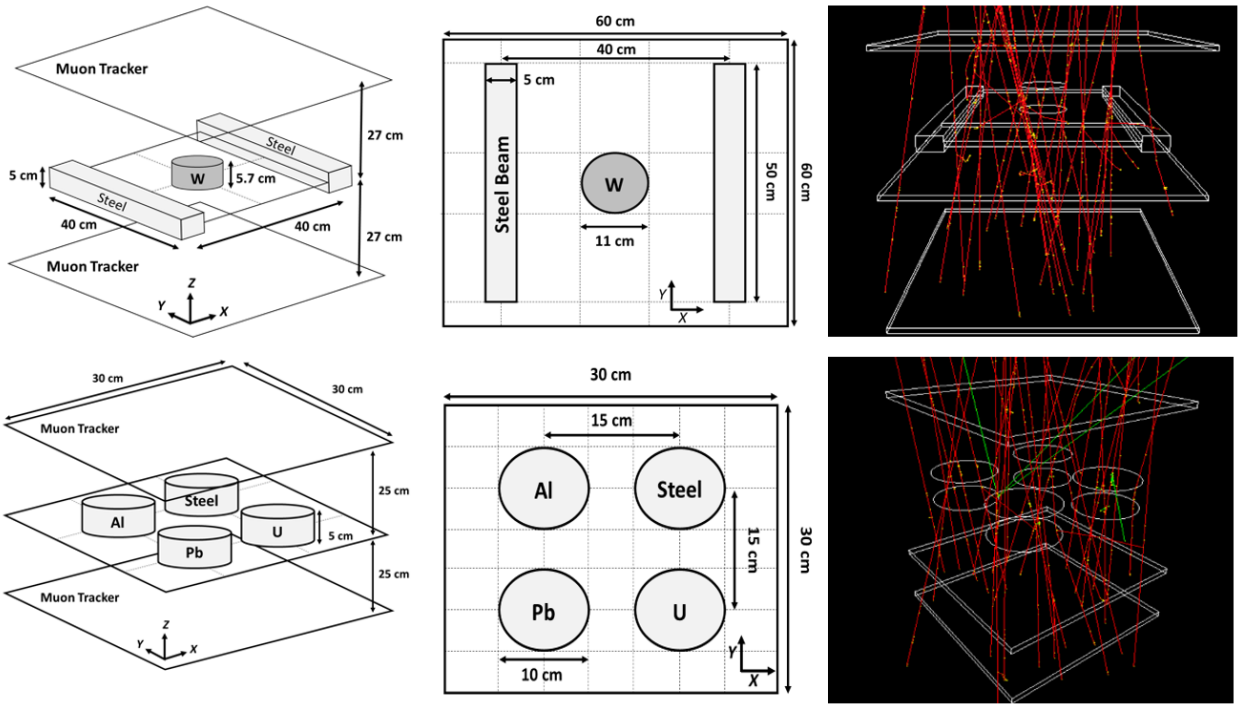

Figure 5.9. Shcematic drawings of target material configurations and geomtereis used in Geant4 simulations: (i) a cylindrical tungsten is placed on the plastic plate and two steel beams are used on both sides to hold a plastic plate and (ii) four cylindrical materials, aluminum, steel, lead, and uranium, are evenly placed from the center. 3D (left), XY (center) perspective, and visualized 30 muon samples in Geant4 simulations (right) for both models are shown.

The image reconstructions for two models were performed using MATLAB (algorithm development) and ParaView (image reconstruction) (Ahrens et al., 2005; Ayachit et al., 2019). The overview of completed momentum integrated muon tomography system for monitoring SNMs using Cherenkov muon spectrometer is shown in Figure 5.10. In this example, four scenarios are considered: (i) original PoCA algorithm with 3 GeV mono-energetic muons (number of muon samples, $N_\mu = 10^5$), (ii) original PoCA algorithm with cosmic muon spectrum ($N_\mu = 10^5$), (iii) mPoCA algorithm with cosmic muon spectrum ($N_\mu = 5\times10^4$), and (iv) mPoCA with cosmic muon spectrum ($N_\mu = 10^5$). In use of the original PoCA algorithm, a designated PoCA point voxel is colored based on muon scattering angle whereas a unique color is assigned for each material class in the material identification mPoCA imaging algorithm. In the first simulation, a tungsten, steel beams, and air are clearly visualized in all scenarios because the geometry and configuration are relatively simple, and they have a large difference in density ($\rho_W = 19.3$ and $\rho_{steel} = 7.9$ g/cm^3). It is noted that continuous and discrete color maps are used in Figure 5.11 for the original PoCA and mPoCA algorithms, respectively. Types of two solid materials are not distinguished in the second scenario (PoCA and cosmic muon spectrum) whereas all three material classes, heavy, light solids, and fluid, are clearly discriminated using colors, red, yellow, and blue, in the fourth scenario (material identification mPoCA and cosmic muon spectrum).

Next, the results of image reconstruction for four materials (aluminum, steel, lead, and uranium) are shown in Figure 5.12. Without a muon momentum knowledge (second row), a location and geometry of sample materials are roughly estimated, however, it is challenging to visually identify their density or types of materials. In the material identification mPoCA algorithm, we categorized materials in four classes in colors, M_1 (blue), M_2 (green), M_3 (yellow), and M_4 (red), which represent, (i) gas or liquid ($Z < 11$), (ii) light structural materials ($Z \sim 20$), (iii) heavy structural or shielding materials ($Z \sim 74$), and (iv) potential special nuclear materials ($90 < Z$) as discussed in Section 4.1. All five materials (air is included) are visually distinguished which was nearly impossible without a momentum knowledge because Pb and U are hardly distinguished using a broad muon scattering range, 0.01 to 0.05 rad. When mono-energy muons are used, all materials are easily identified because scattering angle distribution only depends on material property, hence, a muon scattering range is narrowed to 0.03 to 0.04 rad. A half number of muons (5×10^4) are simulated using a mPoCA algorithm (third scenario) and the results are compared with that of the original PoCA using 10^5 muons (second scenario). Although noise level and imaging

resolution are similar, all five materials can be identified using a material identification mPoCA imaging algorithm.

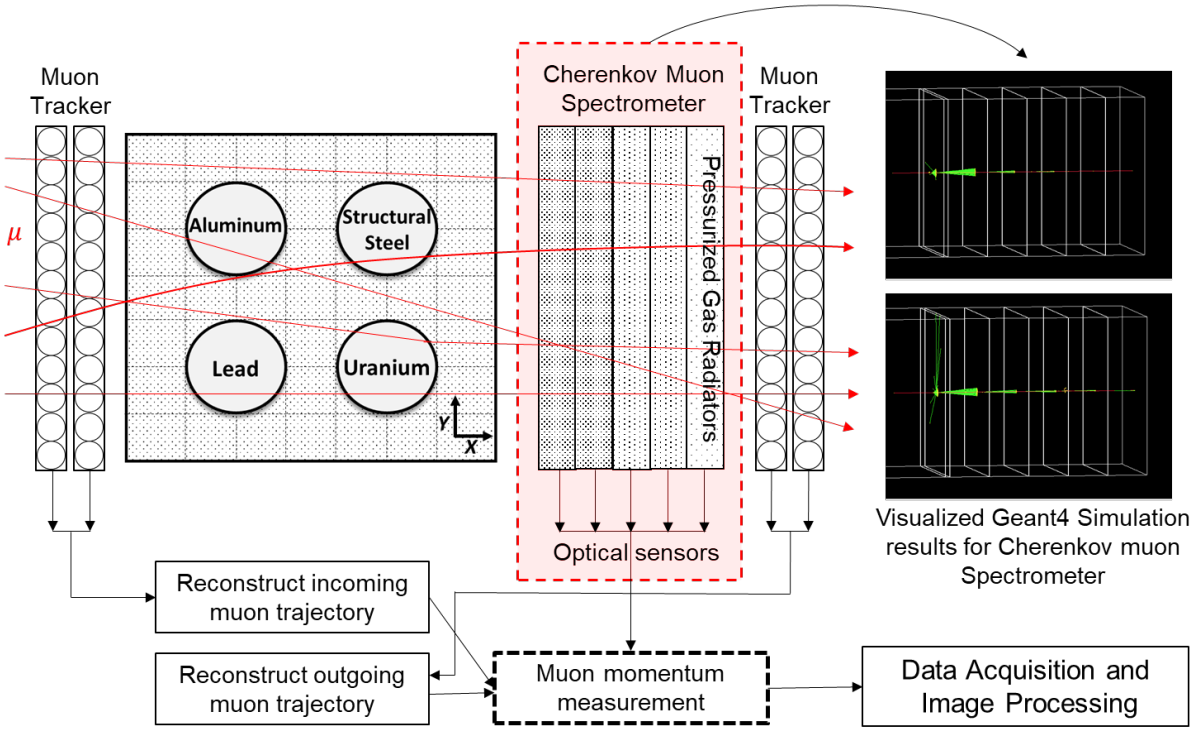

Figure 5.10. The overview of momentum integrated muon tomography system for monitoring SNMs using Cherenkov muon spectrometer (highlighted in red) (Junghyun Bae & Chatzidakis, 2022c).

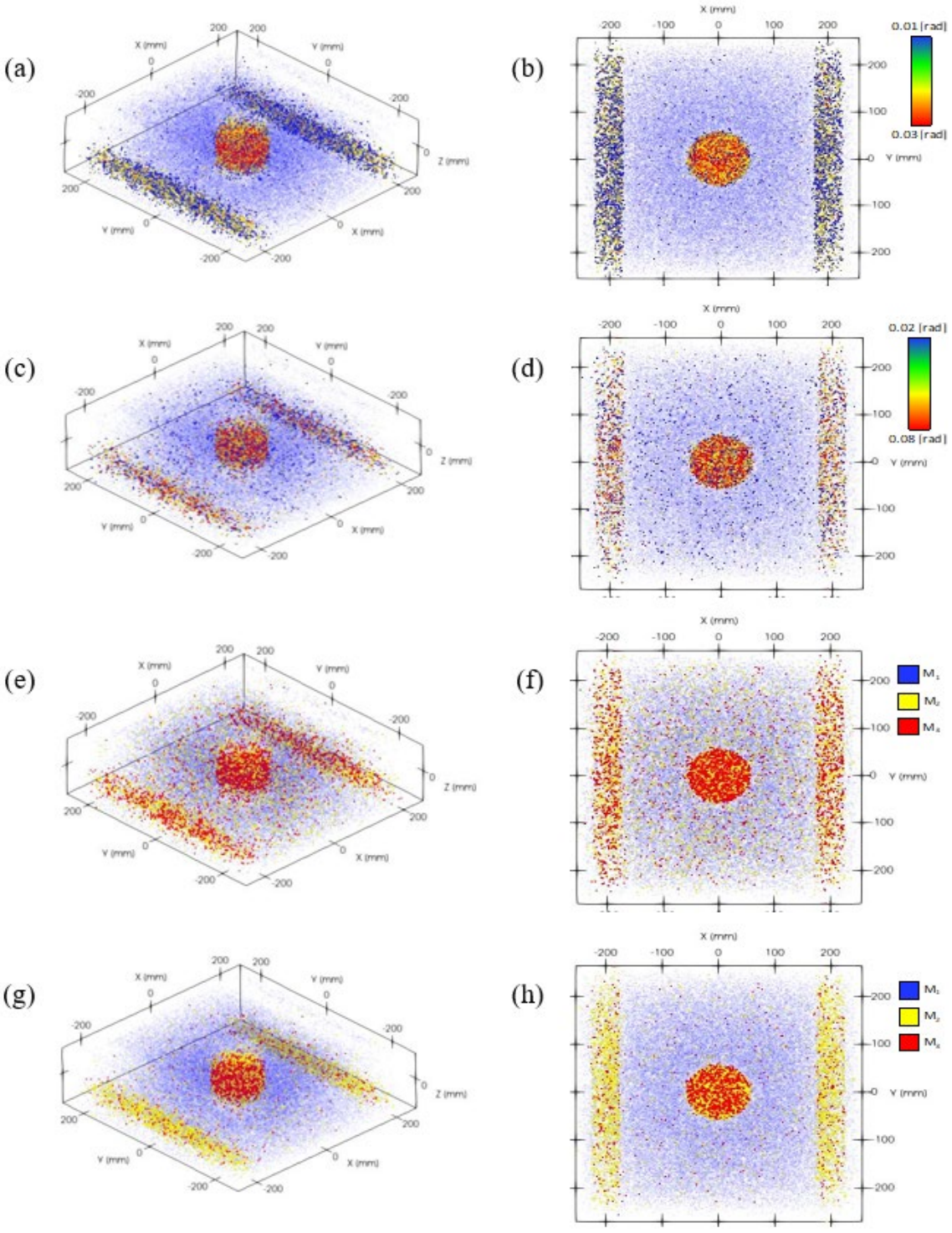

Figure 5.11. Reconstructed images a cylindrical tungsten and two steel beams using original PoCA (a – d) and mPoCA (e – h): 10^5 mono-energy muons, 3 GeV (a, b), (ii) 10^5 muons with cosmic muon spectrum (c, d), (iii) 5×10^4 muons (e, f), and (iv) 10^5 muons (g, h) with cosmic muon spectrum. It is noted that continuous and discrete color maps are used for PoCA and mPoCA, respectively. Types of materials are indistinguishable when muon momentum knowledge is not considered (Junghyun Bae & Chatzidakis, 2022b).

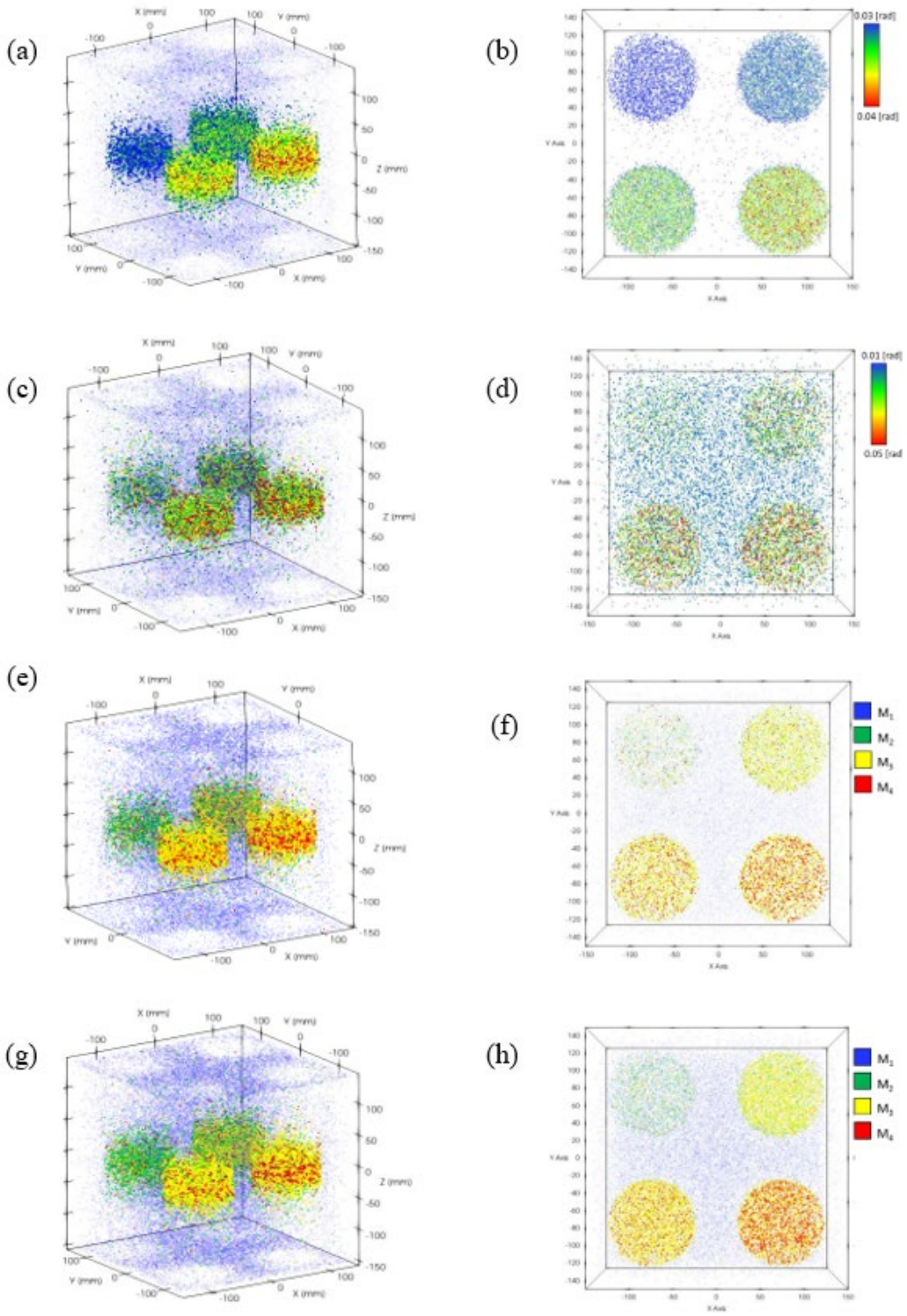

Figure 5.12. Reconstructed 3D and cross-sectional (x-y plane at z = 0) images of four cylindrical target materials, Al, steel, Pb, and U using original PoCA (a – d) and mPoCA (e – h): 10^5 mono-energy muons, 3 GeV (a, b), (ii) 10^5 muons with cosmic muon spectrum (c, d), (iii) 5×10^4 muons (e, f), and (iv) 10^5 muons (g, h) with cosmic muon spectrum. All five materials (including surrounding air) are successfully identified and visualized using different colors (a, b, g, and h).

5.2 Spent Nuclear Fuel Dry Cask Imaging

5.2.1 Geant4 modeling and simulations

Spent nuclear fuels (SNF) are stored in various designs of storage depending on fuel type, capacity, usage, and manufacturers (EPRI, 2010). In general, the SNF dry cask consists of two major components, a stainless-steel canister and vertical concrete cask. The canister separates 24–37 pressurized water reactor (PWR) SNF assemblies with borated stainless-steel latticed walls (Srinivasan et al., 2004). The empty space is filled with helium gas because it is highly inert and hardly activated by neutrons. The outer-most surface of the dry cask is made of thick concrete (800 to 1000 mm) to shield radiation, especially gammas from the SNFs and remain the total radiation dose equivalent rate at the site less than 0.25 mSv per year at the controlled boundary of the system (U.S.NRC, 2021). There are upward airways between the canister and concrete shielding to remove decay heat from the SNF.

In this work, we used a commercial SNF dry cask canister model that stores up to 24 PWR fuel assemblies (FA). Each FA includes 15 × 15 UO_2 fuel rods (ρ_{UO2} = 10.97 g/cm^3) which have a radius, pitch, and length of 5.35, 14.3, and 3658 mm, respectively. The overall dimension of each FA is 2145×2145×3658 mm^3. The array of FAs is surrounded by a hollow concrete shielding ($\rho_{concrete}$ = 2.3 g/cm^3) with the inner and outer radii of 863.5 and 1685 mm. In simulations, we only modeled 23 PWR FAs which means one of the middle FAs is excluded and the Cherenkov muon spectrometer was placed above the SNF cask as shown in Figure 5.13. The Monte-Carlo particle transport simulation code, Geant4, was used to simulate cosmic ray muon interactions with dry cask structures and SNFs. In Geant4 simulations, we additionally provide the well-developed cosmic ray muon energy spectrum and angular distribution so that each generated muon particle has a characteristic momentum and initial flight direction (incident angle) because they are not included in the Geant4 library (S. Chatzidakis & Tsoukalas, 2016; S Chatzidakis et al., 2015). To measure positions and momentum for each muon event during simulations, we modelled two-fold muon trackers above and below the SNF dry cask and Cherenkov muon spectrometer (J. Bae & Chatzidakis, 2021; Junghyun Bae & Chatzidakis, 2022b). The two-fold muon trackers consist of 4 × 4 m^2 two upper and lower scintillators. The distance between upper and lower trackers is 6.0 m and that of two scintillators is 0.3 m. A Cherenkov muon spectrometer is located 0.1 m below the upper tracker in order to measure incoming muon momentum. The active area of the Cherenkov

spectrometer is 4 × 4 m^2 and the overall length is 1.0 m. Then the SNF dry cask is placed between the muon spectrometer and lower tracker. The overall length of SNF dry cask and diameter are 3.66 m and 3.37 m. The overview of the implementation of Cherenkov muon spectrometer in the momentum integrated muon tomography for SNF dry cask imaging and visualized Geant4 simulations are shown in Figure 5.13. In our simulations, 10^5 and 10^6 cosmic ray muon samples were generated for monitoring the SNF dry cask which represent approximately 5–10 minutes and 1–2 hours scanning times in this monitoring system.

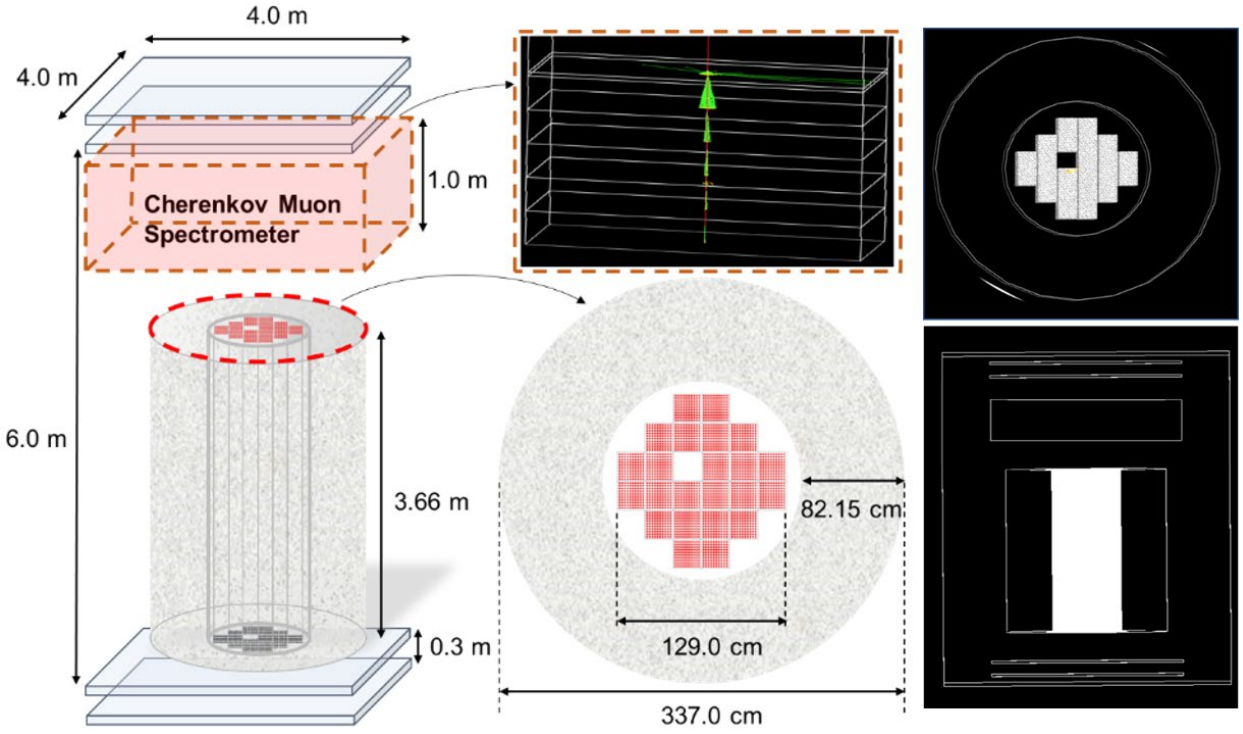

Figure 5.13. Overview of the momentum integrated muon tomography system using the Cherenkov muon spectrometer for SNF dry cask imaging (one FA is missing) and the visualized Geant4 model.

5.2.2 Results

The generalized momentum integrated PoCA algorithm (Section 4.2) was used to reconstruct images of SNFs and its container. To simulate the practical scenario, we only used 23 FAs, one of the middle FAs is missing, because it is more challenging than any other scenarios such as half-loaded, one row of FAs is missing, or one of the outer FAs is missing. Although 10^5 and 10^6 muon samples were generated in Geant4 simulations, only approximately 57% of muons are used for the SNF dry cask imaging because not all muons were recorded in both upper and lower muon trackers due to large incident and scattering angles. In the momentum integrated PoCA imaging algorithm, both scattering angle and momentum are recorded, then *M*-values are calculated using (4-12) for each muon event.

The results of image reconstruction of the SNF dry cask when one of the central FAs is absent using the original PoCA and mPoCA with 10^5 and 10^6 muon samples are shown in Figure 5.14. The horizontal cross section images (x-y plane) of the SNF dry cask at the center are shown in Figures 5.14-(a) and (c). The color scale represents the scattering angle density. In Figures 5.14-(b) and (d), on the other hand, the generalized mPoCA imaging algorithm was applied with 10^5 and 10^6 muon samples, and *M*-values was used instead of scattering angles to reconstruct images. In the first scenario, the overall cylindrical shape of the cask and evidence of nuclear material existence in the center are identified using 10^5 muons and the original PoCA algorithm as shown in Figure 5.14-(a). In the second scenario, we can visually identify the structure of concrete shielding and the locations of FAs in the cask. However, it needs more investigation to specify the exact location of the missing FA in the cask as shown in Figure 5.14-(b). In the third scenario, we used 10 times more muon samples without momentum information. Although the overall structures of concrete shielding, FAs, and air gap are visually identified, it fails to find the position of the missing FA as shown in Figure 5.14-(c). In the fourth scenario, the interior structure of the SNF dry cask is successfully reconstructed. Not only the position of missing FA is clearly identified but also the images of spacing for each FA are reconstructed as shown in Figure 5.14-(d).

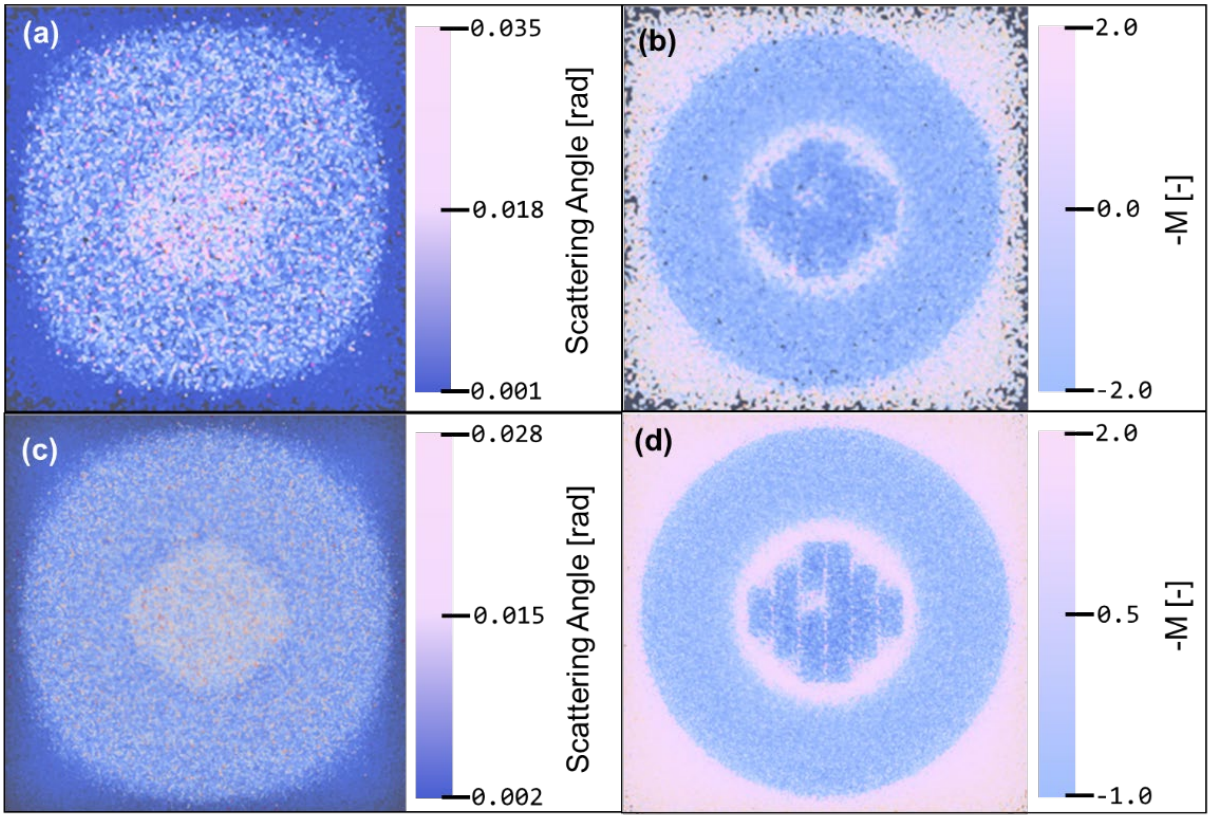

Figure 5.14. The reconstructed cross-sectional images (x-y plane) of SNF dry cask at the center (z = 0) when one FA is missing using 10^5 (upper row) and 10^6 (lower row) muons. Scattering angles (left column) and *M*-values (right column) are used for colormaps.

The computed results for muon scattering angles and *M*-values are plotted as a function of x-position (-2000 to 2000 mm) to quantitatively investigate the structures of SNF dry cask. The results of *M*-values at various locations at the center of the cask (z = 0 mm) are shown in Figure 5.15. We chose three different vertical locations (y-axis), (i) 2 FAs (y = -645 mm), (ii) 6 FAs (y = -215 mm), and (iii) 5 FAs (y = +215 mm) which represents "one FA is missing" scenario, to plot *M*-values as a function of horizontal position (x-axis) in the cask. The results for all four scenarios are presented in Figure 5.16. It is noted that the position of the missing FA is found using 10^5 muons without momentum in Figure 5.16-(c) which was not visually identified in Figure 5.14-(c).

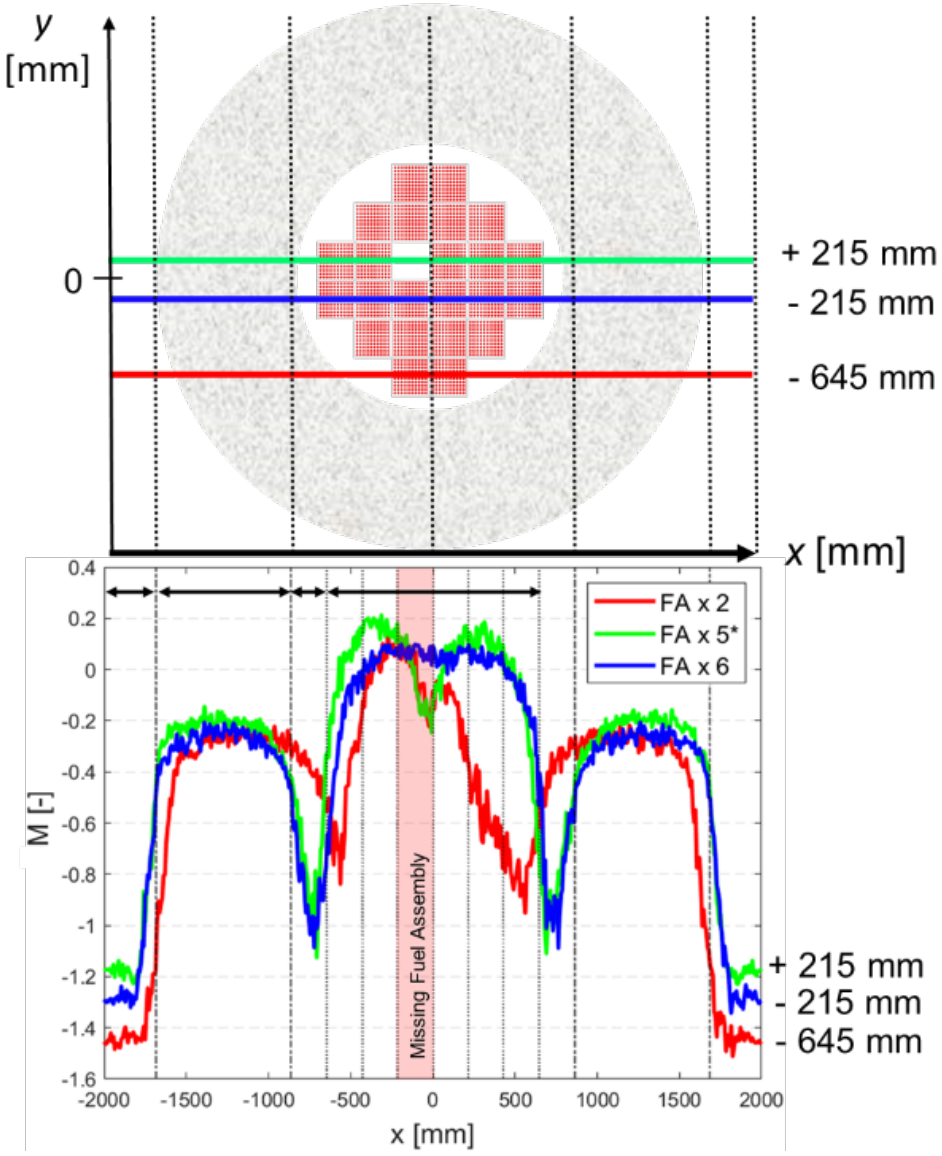

Figure 5.15. The image of SNF dry cask with a missing FA (top) and corresponding M-value plot (bottom) when x = -2000 to 2000 mm and various y-positions, 215 (green), -215 (blue), and -645 mm (red). From top to bottom, 5 FAs (one missing FA out of 6), 6 FAs row, and 2 FAs row, respectively.

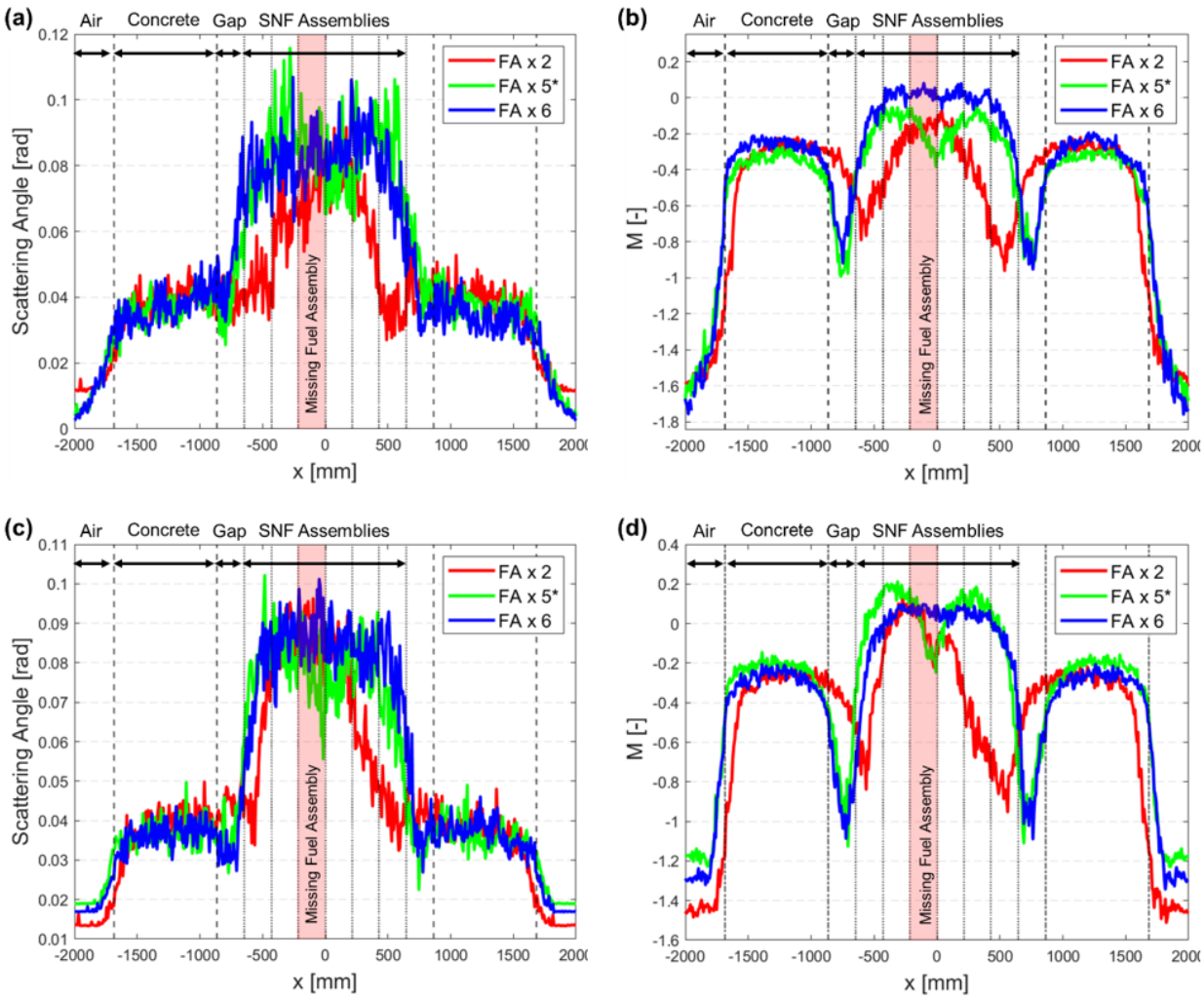

Figure 5.16. M-plots for SNF dry cask when one of middle FAs is missing using 10^5 (upper row) and 10^6 (lower row) muons. Scattering angles (left column) and M-values (right column) are used.

To advance the quantitative investigation of the effect of momentum measurement, the average scattering angles and *M*-values of two empty spaces for (i) missing FA and (ii) gap between FAs and concrete shielding with 2σ uncertainties for 10^5 and 10^6 muon samples are presented in Figure 5.17. The dashed horizontal lines and shaded areas represent the mean scattering angles with 2σ uncertainties for the central six FA rows (-645 to 645 mm) and concrete shielding (±863.5 to ±1685 mm), respectively. In addition, there is a dotted line as a reference level to indicate the surrounding air level, or empty space. Without muon momentum, none of the empty

spaces are completely separated from the central FA row and shielding with 2σ uncertainties as shown in Figure 5.17 (left). On the other hand, both empty spaces are clearly separated from the surrounding structure because the 2σ shaded areas become narrow when M-values are used. It means the missing FA can be identified with a 90% confidential level using 10^5 muon samples which was unsure in the previous approaches, reconstructed images and *M*-value plot.

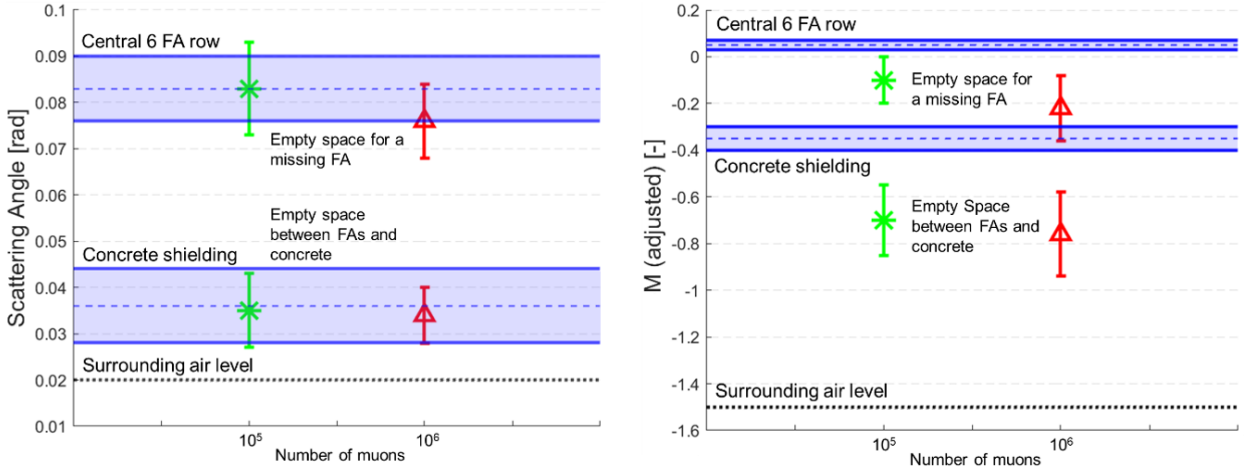

Figure 5.17. The mean scattering angles (left) and M-values (right) for (i) central 6 FA row, (ii) concrete shielding, (iii) empty space for a missing FA, and (iv) empty space between FAs and concrete with 2σ uncertainties. As a reference, surrounding air levels are also plotted in figures.

5.3 Summary

The applicability and implementation of the Cherenkov muon spectrometer in muon tomography, or momentum integrated muon tomography system, were presented in this chapter. To simulate the practical scenarios in the nuclear security applications, (i) lead shielded nuclear materials and (ii) SNF dry cask without one fuel assembly (FA), were modeled using the Monte-Carlo particle transport code, Geant4. Section 5.1.1 outlined the statistical analysis methods using muon scattering angle variance distributions, ROC curves, and AUC to monitor lead shielded special nuclear materials. In Section 5.1.2, the reconstructed images of a lead shielded LEU and various materials using a material identification mPoCA were presented. We demonstrated that a potential nuclear material can be identified even it is completed surrounded by 5 cm lead shielding. In addition, five types of materials, air, steel, steel, lead, and uranium, were visually distinguished

using the mPoCA algorithm which was not possible using the original PoCA algorithm. Section 5.2 described a practical and challenging example in the spent nuclear fuel management application which is one out of 24 FAs is missing. A missing FA was visually identified using the generalized mPoCA algorithm with 10^5 muons. A visual inspection to find one missing FA is not possible using the original PoCA even with 10^6 muons. To advance the quantitative investigation to find a missing FA in the cask, scattering angle (PoCA) and *M*-value (mPoCA) plots were analyzed and the results showed that the measurement times can be reduced by a factor of 10 or more by measuring muon momentum.

6. CONCLUSION

6.1 Summary and Conclusion

This dissertation provided three key ideas, (i) a new paradigm of muon momentum measurement using multi-layer pressurized gas Cherenkov radiators, (ii) mPoCA imaging algorithm, and (iii) a momentum integrated muon scattering tomography system for nuclear security and material management applications. The necessary background and knowledge regarding cosmic ray muons, muon physics, radiation detection and instrumentations, and muon radiography were presented in Chapter 2.

In Chapter 3, theory and principles in the development of Cherenkov muon spectrometer were detailed. We demonstrated that actual muon momentum can be estimated by analyzing Cherenkov radiation light signals from all radiators that have consecutive threshold momentum levels for muons. The necessary muon threshold momentum levels were achieved by pressurizing or depressurizing gas Cherenkov radiators. After a thorough investigation of the properties of various candidates, CO_2, C_3F_8, C_4F_{10}, and R1234yf, we chose CO_2 gas as our Cherenkov gas radiator because it covers a wide range of threshold momenta and it is commercially available in large quantities at a minimal cost. In addition, a glass Cherenkov radiator was inevitably chosen to provide the lowest threshold momentum level, p_{th} = 0.1 GeV/c, because it is not possible to achieve this level with high-pressure CO_2 without phase change at room temperature. Therefore, as a prototype, six threshold momentum levels, p_{th} = 0.1, 1.0, 2.0, 3.0, 4.0, and 5.0 GeV/c, were designed using a SiO_2 and five pressurized CO_2 radiators. We performed extensive Geant4 simulations to evaluate the performance and feasibility of the proposed Cherenkov muon spectrometer. In our analysis, except the Cherenkov radiation by muons, all other optical photon emissions, i.e., scintillation, transition radiation, and Cherenkov radiation by secondary particle, were considered as noise. The results showed that the resolution of momentum measurement is ±0.5 GeV/c with a mean CR of 87% within the momentum ranges of 0.1–10.0 GeV/c. We also demonstrated that the relative resolution can be improved by 3.35% using 100 radiators. However, the increased number of radiators negatively impacts the SNR.

Chapter 4 detailed two momentum-integrated PoCA algorithms (mPoCA). The material classification mPoCA has a benefit when a target object is covered or unknown because it is

specialized to identify the types of materials by analyzing and comparing with a reference database. However, it increases computational costs because an additional material classification process is required. On the other hand, the generalized mPoCA does not increase the computational time for reconstructing images because it only replaces the scattering angle value with *M*-value in an assigned voxel.

Chapter 5 presented various simulation results in nuclear security and spent nuclear fuel management applications. We used the Genat4 Monte-Carlo particle transport code to generate 10^5 and 10^6 cosmic ray muons and simulate muon interactions with modeled FAs and cask structures. The generalized mPoCA algorithm was used for image reconstructions. It was shown that reconstructed images using the original PoCA algorithm failed to visually identify the location of missing FA. However, it was systematically identified by comparing the FA row in which a missing FA is located (5 FAs) with the normal FA row (6 FAs) using 10^6 muons. On the other hand, in the reconstructed images from the momentum integrated PoCA algorithm, not only the location of a missing FA was successfully found but also empty spaces, i.e., air or helium gaps, between FAs and structures were visually identified.

In conclusion, we demonstrated the potential of measuring muon momentum in nuclear material management applications throughout this dissertation. We presented analytical and numerical models to develop a fieldable muon spectrometer using multi-layer pressurized Cherenkov gas radiators. Based on the capability to measure muon momentum in the field, a new imaging algorithm, mPoCA, for muon scattering tomography was suggested. In the end, we provided an example of the implementation of Cherenkov muon spectrometer in the muon scattering tomography system for SNF monitoring. With the Cherenkov muon spectrometer and mPoCA imaging algorithm, the imaging resolution was significantly improved and scanning time was decreased by a factor of 10 or more.

6.2 Future Work

6.2.1 Prototype of Cherenkov muon spectrometer

This dissertation includes the extensive preliminary results of an analytical study, numerical analysis, and Geant4 simulations. To improve the feasibility and reliability of our proposed Cherenkov muon spectrometer, a physical prototype and experimental data must be

included. The schematic diagram, electronics block diagram, and details in material selections for building our proposed Cherenkov muon spectrometer are presented in Figures 3.2, 3.3, 3.18, and Table 3.4.

Materials

For the initial prototype design, pressurized CO_2 gas and SiO_2 Cherenkov radiators were selected. As discussed in Chapter 3, CO_2 is an inert gas and has a relatively high refractive index and low scintillation efficiency. The SiO_2 glass radiator was inevitably used to achieve the lowest momentum threshold level (or highest refractive index) which is not possible using any pressurized gas radiator. For a pressurized gas container, cylindric aluminum housing will be used to endure high pressure. All surfaces of the containers will be layered with black aluminum liners which serve as strong light absorbers because they have more than 90% absorbability in the EM wavelength range of 400–700 nm. On the bottom of the container, however, a wavelength shifter will be placed to convert high-frequency Cherenkov lights to low-frequency photons. The secondary photons will be guided to SiPM using a light guides or optical fibers. The size of the container will be approximately 100×100×20 cm^3 for CO_2 radiators and 100×100×1 cm^3 for solid radiators.

Calibration and testing

To verify the performance of the Cherenkov muon spectrometer, a calibration process must be performed. Because it is challenging to generate muons in the laboratory, indirect calibration methods will be implemented.

Cosmic muon momentum spectrum

The cosmic ray muon spectrum is well-known as shown in Figure 2.3. If the cosmic muon spectrum is successfully reconstructed using our Cherenkov muon spectrometer, it means it is properly calibrated. However, despite the cosmic ray muon flux of ~10,000 m^{-2} min^{-1} at sea level, the measurable count rate would be significantly less than 10,000 m^{-2} min^{-1} because a detectable solid angle is less than 2π (hemisphere). The detailed discussion regarding a measurable solid angle for cosmic ray muons is found in Appendix B.

High energy electrons

Electrons have an approximately 207 times lighter rest mass than muons. Therefore, the Cherenkov threshold momentum level of electrons is also approximately 207 times lower than that of muons in the same medium. Therefore, it is possible to indirectly calibrate our Cherenkov muon spectrometer using high-energy electrons. For example, the threshold momentum of pressurized CO_2 with a 10 atm has the refractive index of 1.0044 and the corresponding Cherenkov threshold momentum for muons is 1.125 GeV/c whereas it is only 5.543 MeV/c for electrons. However, an electromagnetic shower initiates when a high-energy electron (above a few MeV) enters a material mainly due to the Bremsstrahlung photon emission (Landau & Rumer, 1938). This cascade continues until the electron loses enough energy and the characteristic depth of the cascade is called, radiation length, X_0, which was discussed in Section 2.2.3. In addition, since none of the natural beta decays reaches that momentum level without acceleration, we will explore the possible collaboration with National Labs and Universities to use electron accelerators, e.g., Argonne National Lab or RPI.

6.2.2 Advanced signal analysis

Background noise analysis

Once the Cherenkov muon spectrometer is successfully built, (i) system noise, (ii) temperature and pressure sensitivity, and (iii) background radiation analyses must be performed. Because our proposed Cherenkov muon spectrometer is expected to be used with the existing muon tomography system for monitoring and imaging radioactive materials, the responses of the spectrometer in extreme conditions also must be studied.

APPENDIX A. DERIVATION OF THE EFFECTIVE SOLID ANGLE MODEL FOR MUON FLUX ESTIMATION

The effective muon solid angle depends on both size and distance of two detectors and also it continuously varies on the detector surface as shown in Figure A.1. Since the muon flux variance along the azimuthal angle is insignificant, we assumed that the solid angle solely depends on the distance from the detector centerline on the surface. To compute the 3D effective muon solid angle, we found the projected plane angle at a point on the detector surface. The projected plane angle is a function of the distance from the detector centerline, r, whereas it is independent of the height of detector under the assumption that all muons are detected when they traverse detectors regardless of their deposited energy. The projected plane angle, θ, is given by

$$\theta(r)\ [rad]\ = \operatorname{atan}\left(\frac{r_d + r}{D}\right) + \operatorname{atan}\left(\frac{r_d - r}{D}\right) \tag{A-1}$$

where r_d is the radius of the detector surface. The area-averaged projected plane angle, θ_{avg}, and half-projected plane angle, γ, over the detector surface becomes

$$\theta_{avg} = \frac{1}{\pi r_d^2}\int_{A_d} r\theta(r)dA_d \tag{A-2}$$

$$\gamma = \frac{\theta_{avg}}{2} = \frac{1}{2L}\left[\ln\frac{4L^2+1}{(L^2+1)^2} + \frac{1}{L}\operatorname{atan}(2L) + 2\left(L - \frac{1}{L}\right)\operatorname{atan} L\right] \tag{A-3}$$

$$L \equiv r_d/D \tag{A-4}$$

where A_d is the detector surface area and L is the ratio of r_d to D. Because γ depends on not only r_d but also the D, a new parameter, L, is defined.

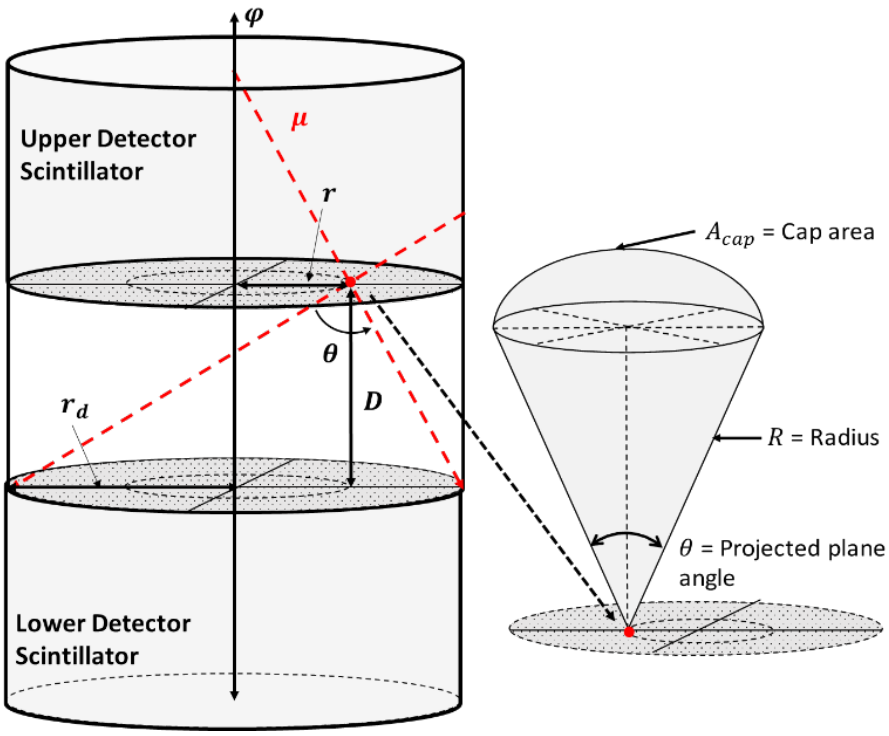

Figure A.1 Example of cosmic ray muon trajectory (left) and the effective solid angle at the point on the detector surface (right) (Junghyun Bae & Chatzidakis, 2022a).

Because the azimuthal angular dependency to the muon flux is negligible, the solid angle when the half-plane projected angle is γ,

$$\Omega = 2\pi \int_0^{\gamma} \sin\phi \, d\phi \tag{A-5}$$

The range of the pointing angle of a centerline, φ, extends from 0° to 90°. As the range of the pointing angle is uniformly divided by N number of angles

$$\varphi_i = \frac{\pi i}{2N}\Big|_{i=1,2,\ldots,N} \tag{A-6}$$

By integrating the zenith angular dependent cosmic muon flux model, i.e., $I(\varphi)/I_0$ with (A-5) and (B-6), the effective solid angle over the entire azimuthal angle becomes (2-9) in Section 2.1.3. The correlation between cosmic ray muon count rate (CR) and the effective solid angle is given by

$$CR = \rho\Omega_{\text{eff}} \tag{A-7}$$

In the range between L = 0.15 and 0.4, both effective solid angle model and experiment data linearly increase as L increases. When the conversion constant, ρ, found using the experimental data is used, (A-7) becomes

$$CR \approx 7.52 \times 10^3 \left[\frac{\text{Counts/day}}{\text{sr}}\right] \times \Omega_{\text{eff}}\,[\text{sr}] \tag{A-8}$$

where Ω_{eff} can be found in (2-8). Because the effective solid angle linearly increases when $0.2 < L < 0.8$, (A-8) can be simplified by

$$CR = 7.52 \times 10^3 \times (CL + k) \tag{A-9}$$

The constants, C and k, as a function of the zenith angle are shown in Figure A-2.

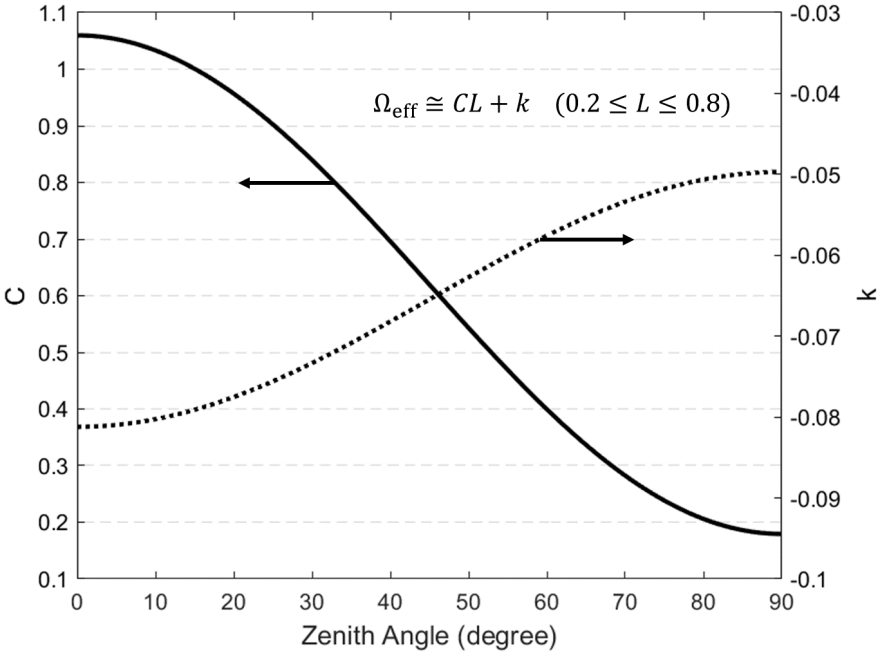

Figure A.2 Constants, C and k, used in (A-9) as a function of zenith angle when 0.2 < L < 0.8 (Junghyun Bae & Chatzidakis, 2022a).

APPENDIX B. VERIFICATION OF CHERENKOV MUON SPECTROMETER USING THE ANALYTICAL APPROACH

To verify the proposed idea discussed in Sections 3.1 to 3.3, the analytical approach was performed before performing the Geant4 simulations. This section contains a problem illuminating the practical example of a muon spectrometer using multi-layer pressurized gas Cherenkov radiators. The solution provides the necessary analytical models, methodologies, and constants to successfully compute light yields from Cherenkov radiation, scintillation, and transition radiation.

B.1 Problem Description

Find the mean numbers of photons from Cherenkov radiation, scintillation, and transition radiation. The incoming muon of energy, 4 GeV (a mean energy of cosmic ray muons) travels and it is detected by the Cherenkov muon spectrometer which consists of pressurized CO_2. The pressure and temperature of CO_2 gas in the spectrometer is 10 atm (1,013,250 Pa) and 300 K. Assume that muon travels the infinitely large surface through the radiator and the vertical length of radiator container is 10 cm. There is no self-absorption (no photon is absorbed within the radiator), but photons are 100% absorbed in the light absorbers. In addition, assume that the detector efficiency is 100% for the visible, ultraviolet, and x-ray photons.

B.2 Refractive Index and Cherenkov Conditions

The molecular polarizability, α, of CO_2 is found in Table 3.2 in Section 3.2. The molecular refractivity, A_m, and the refractive index of pressurized CO_2 when p = 10 atm and T = 300 K, can be computed using (3-8) and (3-9) in Section 3.1.2

$$A_m = \frac{4\pi}{3} N_A \alpha = \frac{4\pi}{3} (6.022 \times 10^{23})(2.59 \times 10^{30}\ m^3) = 6.533 \times 10^{-6}\ \mathrm{m^3/mol} \quad \text{(B-1)}$$

$$n_{CO_2} \approx \sqrt{1 + \frac{3A_m p}{RT}} = \sqrt{1 + \frac{3(6.533 \times 10^{-6}\ m^3/mol)(1{,}013{,}250\ Pa)}{(8.3145\ J/mol)(300\ K)}} = 1.0040 \quad \text{(B-2)}$$

In addition, β_{th} and p_{th} can be calculated using (3-3) and (3-5) in Section 3.1.1.

$$\beta_{th} = \frac{1}{n} = 0.9960 \quad \text{(B-3)}$$

$$p_{th}c = \frac{m_\mu c^2}{\sqrt{n^2 - 1}} = 1.180\ GeV \quad \text{(B-4)}$$

$$\therefore p_{th} = 1.180\ GeV/c. \quad \text{(B-5)}$$

Therefore, the incident muon momentum and velocity, p_μ and β_μ are

$$p_\mu c = \sqrt{E_\mu^2 - m_\mu c^2} \cong 3.9986\ GeV \quad \text{(B-6)}$$

$$\therefore p_\mu = 3.9986\ GeV/c \quad \text{(B-7)}$$

The corresponding muon velocity is

$$\beta_\mu = \sqrt{\frac{(p_\mu c/m_\mu c^2)^{\,2}}{(p_\mu c/m_\mu c^2)^{\,2} + 1}} \cong 0.9997 \quad \text{(B-8)}$$

The results show that the incoming muon with energy 4 GeV is energetic enough to induce Cherenkov radiation in the given pressurized CO_2 gas radiator.

B.3 Cherenkov Radiation

When we can measure the Cherenkov lights with a wavelength range of λ = 200–700 nm, a mean number of photon emission by Cherenkov effect can be estimated using (3-13)

$$\sin^2\theta_c = 1 - \frac{1}{\beta_\mu^2 n^2} = 7.357 \times 10^{-3} \tag{B-9}$$

$$\frac{dN_{ch}}{dx} \cong 1150 \sin^2\theta_c \cong 8.46 \tag{B-10}$$

Because the length, *dx*, is 10 cm, the expected total number of Cherenkov photons (VIS + UC) is, N_{ch} = 84.6

B.4 Scintillation

The linear muon energy loss in the pressurized CO_2 radiator can be estimated using Bethe equation, (2-11). The necessary constants and quantities are tabulated in Table 2.2 in Section 2.1. For CO_2 gas and E_μ = 4 GeV, a mean energy loss per unit length of a muon is,

$$-\left.\frac{dE}{dx}\right|_{avg} = 0.8159\ MeV\ g^{-1}\ cm^2 \tag{B-11}$$

for ρ_{CO2} (at p = 10 atm) = 0.02088 g/cm3,

$$-\frac{dE}{dx} \approx 17.04\ keV/cm \tag{B-12}$$

The mean number of scintillation photons can be calculated by using (3-15) and finding scintillation efficiency for CO_2 in Table 3.3. Because the length of radiator container is 10 cm, the total number of scintillation photons is

$$N'_{sc} = (5.09\ MeV^{-1})(17.04\ keV)(10\ cm) = 0.87 \quad \text{(B-13)}$$

We assumed that the radiator container has an infinitely large surface and all surfaces are 100% light absorbers except the bottom surface. Therefore, only a half of emitted photons are detectable, then N_{sc} = 0.46.

B.5 Transition Radiation

The Lorentz factor, γ, is given by

$$\gamma_\mu = \frac{1}{\sqrt{1-\beta_\mu^2}} \cong 40.83 \quad \text{(B-14)}$$

The mean number of emitted photons due to the transition radiation can be computed using (3-17)

$$N'_{tr} = \frac{z^2\alpha}{\pi}\left[(\ln\gamma - 1)^2 + \frac{\pi^2}{12}\right] \cong 0.02 \quad \text{(B-15)}$$

We assumed the photon detector efficiency is 100% for the electromagnetic wavelength of interest. Also, assuming both forward and backward transition radiations are detectable, the total expected number of transition photons are doubled, then N_{tr} = 0.04.

B.6 Summary

Therefore, the mean numbers of photons from Cherenkov radiation, scintillation, and transition radiation when a muon of energy 4 GeV travels in the 10 cm CO_2 gas (T = 273K, p = 10 atm) Cherenkov muon spectrometer, are N_{ch} = 84.6, N_{sc} = 0.46, and N_{tr} = 0.04. The Cherenkov light emission dominates other two major light emission mechanisms and it demonstrates the

functionality of Cherenkov muon spectrometer. The numerical results from Monte-Carlo simulations are shown in Tables B.1 to B.5.

Table B.1. Monte-Carlo simulation results of nine 4 GeV monoenergetic muons. Each number represents expected total photon yields.

	Muon Number								
Bin #	***1***	***2***	***3***	***4***	***5***	***6***	***7***	***8***	***9***
#1	305	274	333	329	278	331	305	280	319
#2	27	22	27	42	32	32	34	31	36
#3	123	114	141	119	109	118	124	138	107
#4	43	55	41	59	45	50	41	58	51
#5	24	19	29	25	28	21	29	27	31
#6	35	28	21	30	30	35	36	23	29
#7	12	18	15	14	8	13	15	20	18
#8	3	1	7	4	7	8	3	4	9
#9	0	0	0	0	0	0	0	0	0
#10	0	0	0	0	1	0	0	0	0
#11	0	1	0	0	1	0	0	0	0

Table B.2. Monte-Carlo simulation results of nine 4 GeV monoenergetic muons. Each number represents expected Cherenkov photon yields

	Muon Number								
Bin #	***1***	***2***	***3***	***4***	***5***	***6***	***7***	***8***	***9***
#1	298	265	327	324	275	327	302	273	315
#2	24	20	27	39	27	27	32	30	30
#3	122	114	141	117	108	118	122	138	106
#4	43	54	40	59	44	49	40	57	51
#5	24	19	29	24	27	21	29	27	30
#6	35	28	21	30	30	35	35	23	29
#7	12	17	15	14	8	13	14	20	18
#8	3	1	7	4	7	8	3	3	9
#9	0	0	0	0	0	0	0	0	0
#10	0	0	0	0	0	0	0	0	0
#11	0	0	0	0	0	0	0	0	0

Table B.3. Expected number of the Cherenkov photons for various muon momenta in each radiator. It is noted that no Cherenkov light is observed if $p_\mu < p_{th}$.

p_{th} $[GeV/c]$	Radiator	Size [cm]	n	N_{ch} $[photons]$					
				Muon momentum p $[GeV/c]$					
				0.4	**1.1**	**2.1**	**3.1**	**4.1**	**5.1**
0.1	Glass	1	1.4548	568.7	601.6	605.2	606.0	606.3	606.4
0.5	Glass	1	1.0221		39.0	46.3	47.9	48.5	48.8
1.0	CO_2	10	1.00557		21.7	97.4	113.4	120.2	122.5
1.5	CO_2	10	1.00248			27.0	43.1	50.0	52.2
2.0	CO_2	10	1.00139			2.0	18.1	25.0	27.3
2.5	CO_2	10	1.00089				6.7	13.6	15.8
3.0	CO_2	10	1.00062				0.5	7.4	9.7
3.5	CO_2	10	1.00046					3.7	6.0
4.0	CO_2	10	1.00035					1.1	3.4
4.5	CO_2	10	1.00028						1.8
5.0	CO_2	10	1.00022						0.5

Table B.4. Expected number of the scintillation photons for various muon momenta in each radiator. It is noted that scintillation light is observed even if $p_\mu < p_{th}$.

p_{th} $[GeV/c]$	Radiator	Size [cm]	N_{sc} $[photons]$					
			Muon momentum p $[GeV/c]$					
			0.4	**1.1**	**2.1**	**3.1**	**4.1**	**5.1**
0.1	Glass	1	7.8	8.7	9.5	10.0	10.3	10.6
0.5	Glass	1	4.7	5.2	5.7	6.0	6.2	6.4
1.0	CO_2	10	0.9	1.0	1.1	1.1	1.2	1.2
1.5	CO_2	10	0.4	0.4	0.5	0.5	0.5	0.5
2.0	CO_2	10	0.2	0.2	0.3	0.3	0.3	0.3
2.5	CO_2	10	0.1	0.2	0.2	0.2	0.2	0.2
3.0	CO_2	10	0.1	0.1	0.1	0.1	0.1	0.1
3.5	CO_2	10	0.1	0.1	0.1	0.1	0.1	0.1
4.0	CO_2	10	0.1	0.1	0.1	0.1	0.1	0.1
4.5	CO_2	10	0.0	0.0	0.1	0.1	0.1	0.1
5.0	CO_2	10	0.0	0.0	0.0	0.0	0.0	0.0

Table B.5. Expected number of the transition radiation photons for various muon momenta in each radiator. It is noted that transition radiation is observed even if $p_\mu < p_{th}$.

p_{th} $[GeV/c]$	Radiator	Size [cm]	N_{tr} $[photons]$					
			Muon momentum p $[GeV/c]$					
			0.4	**1.1**	**2.1**	**3.1**	**4.1**	**5.1**
0.1	Glass	1	0.00	0.01	0.02	0.03	0.04	0.04
0.5	Glass	1	0.00	0.01	0.02	0.03	0.04	0.04
1.0	CO_2	10	0.00	0.01	0.02	0.03	0.04	0.04
1.5	CO_2	10	0.00	0.01	0.02	0.03	0.04	0.04
2.0	CO_2	10	0.00	0.01	0.02	0.03	0.04	0.04
2.5	CO_2	10	0.00	0.01	0.02	0.03	0.04	0.04
3.0	CO_2	10	0.00	0.01	0.02	0.03	0.04	0.04
3.5	CO_2	10	0.00	0.01	0.02	0.03	0.04	0.04
4.0	CO_2	10	0.00	0.01	0.02	0.03	0.04	0.04
4.5	CO_2	10	0.00	0.01	0.02	0.03	0.04	0.04
5.0	CO_2	10	0.00	0.01	0.02	0.03	0.04	0.04

APPENDIX C. DERIVATION OF THE SCATTERING ANGLE VARIANCE DISTRIBUTION

According to the MCS approximation, all materials have a unique characteristic of muon scattering angle variance distribution. The degree of separation between two scattering angle variance distributions represents the system's material identification capability. The muon scattering angle distribution $S(x_i)$ for N muons is given by

$$\sum_{i=1}^{N} f_i\left(x_i \middle| 0, \sigma_{\theta,i}^2\right) = S(x_i) \tag{C-1}$$

where x_i and $\sigma^2_{\theta,i}$ are the scattering angle and scattering angle variance of ith Gaussian distribution. $S(x_i)$ can be approximated when sample size is large enough

$$S(x_i) \sim S(x_i \mid 0, s^2) \text{ when } N \gg 1 \tag{C-2}$$

This is analogous to describing an undefined function using Fourier series. Integration of each expected Gaussian distribution, f_i develops a $S(x_i)$. When we consider a perfect muon spectrometer, N number of f_i will be used to describe $S(x_i)$. On the other hand, one or a few (it depends on measurement resolution) f_i will be used for the absent and limited muon spectrometer, respectively. The result of the muon scattering angle distribution is $D(x_i)$. Assuming $D(x_i)$ follows the Gaussian approximation

$$D(x_i) \sim D(x_i \mid 0, s_D^2) \tag{C-3}$$

We introduce a parameter which can represent the difference between the results of the muon scattering angle distribution and estimation. Δs^2 is the difference between variance of resulting distribution, s^2_D and estimated distribution, s^2.

$$\Delta s^2 = |s_D^2 - s^2| \tag{C-4}$$

$$E[\Delta s^2] = \frac{1}{M}\sum_{j=1}^{M} \Delta s_j^2 = \mu \tag{C-5}$$

$$Var[\Delta s^2] = \frac{1}{M}\sum_{j=1}^{M} \left(\Delta s_j^2 - \mu\right)^2 = \sigma^2 \tag{C-6}$$

The mean and variance of Δs^2 increase when two distributions do not agree each other. Distribution of Δs^2 is expressed as

$$X\left(\Delta s_j^2\right) \sim X\left(\Delta s_j^2 \middle| \mu, \sigma^2\right) \text{ when } M \gg 1 \tag{C-7}$$

REFERENCES

Abbon, P., Alexeev, M., Angerer, H., Baum, G., Birsa, R., Bordalo, P., Bradamante, F., Bressan, A., Chiosso, M., Ciliberti, P., Colantoni, M., Dafni, T., Torre, S. D., Delagnes, E., Denisov, O., Deschamps, H., Dibiase, N., Duic, V., Eyrich, W., … Rebourgeard, P. (2011). Particle identification with COMPASS RICH-1. *Nuclear Inst. and Methods in Physics Research, A*, *631*, 26–39. https://doi.org/10.1016/j.nima.2010.11.106

Abe, K., Hayato, Y., Iida, T., Iyogi, K., Kameda, J., Kishimoto, Y., Koshio, Y., Marti, L., Miura, M., Moriyama, S., Nakahata, M., Nakano, Y., Nakayama, S., Obayashi, Y., Sekiya, H., Shiozawa, M., Suzuki, Y., Takeda, A., Takenaga, Y., … Wilkes, R. J. (2014). Calibration of the Super-Kamiokande detector. *Nuclear Instruments and Methods in Physics Research, Section A: Accelerators, Spectrometers, Detectors and Associated Equipment*, *737*, 253–272. https://doi.org/10.1016/j.nima.2013.11.081

Abratenko, P., Acciarri, R., Adams, C., An, R., Anthony, J., Asaadi, J., & Auger, M. (2017). Determination of muon momentum in the MicroBooNE LArTPC using an improved model of multiple Coulomb scattering. *Journal of Instrumentation*, *12*.

Adriani, O., Banerjee, S., & Bourilkov, D. (2002). The L3 + C detector , a unique tool-set to study cosmic rays. *Nuclear Instruments and Methods in Physics Research A*, *488*, 209–225.

Aefsky, S. (2012). Alignment of the Muon Spectrometer in ATLAS. *Physics Procedia*, *37*, 51–56. https://doi.org/10.1016/j.phpro.2012.02.355

Agostinelli, S., Allison, J., Amako, K., Apostolakis, J., Araujo, H., Arce, P., Asai, M., Axen, D., Banerjee, S., Barrand, G., Behner, F., Bellagamba, L., Boudreau, J., Broglia, L., Brunengo, A., Burkhardt, H., Chauvie, S., Chuma, J., Chytracek, R., … Zschiesche, D. (2003). GEANT4 - A simulation toolkit. *Nuclear Instruments and Methods in Physics Research, Section A: Accelerators, Spectrometers, Detectors and Associated Equipment*, *506*(3), 250–303.

Ahrens, J., Geveci, B., & Law, C. (2005). *ParaView: An End-User Tool for Large Data Visualization: Vol. LA-UR-03-1*.

Alharbi, M. K. M., Burgess, P., Taggart, M. P., & Sellin, P. J. (2020). Retrofitting an environmental monitor with a silicon photomultiplier sensor. *Journal of Radiological Protection*, *40*, N31–N38.

Allison, J., Amako, K., Apostolakis, J., Araujo, H., Dubois, P. A., Asai, M., Barrand, G., Capra, R., Chauvie, S., Chytracek, R., Cirrone, G. A. P., Cooperman, G., Cosmo, G., Cuttone, G., Daquino, G. G., Donszelmann, M., Dressel, M., Folger, G., Foppiano, F., … Peirgentili, M. (2006). Geant4 developments and applications. *IEEE Transactions on Nuclear Science*, *53*(1), 270–278.

Allkofer, O. C., Andresen, R. D., & Dau, W. D. (1968). The muon spectra near the geomagnetic equator. *Canadian Journal of Physics*, *46*, 301–305.

Alvarez, L. W., Anderson, J. A., Bedwei, F. El, Burkhard, J., Fakhry, A., Girgis, A., Goneid, A., Hassan, F., Iverson, D., Lynch, G., Miligy, Z., Moussa, A. H., Sharkawi, M., & Yazolino, L. (1970). Search for hidden chambers in the pyramids. *Science*, *167*, 832–839.

Amato, L., Ambrosino, F., Bonechi, L., & Cimmino, L. (2017). *Imaging of underground cavities with cosmic-ray muons from observations at Mt . Echia (Naples)*.

Anderson, C. D., & Neddermeyer, S. H. (1936). Cloud Chamber Observations of Cosmic Rays at 4300 Meters Elevation and Near Sea-Level. *Physical Review*, *50*(4), 263–271. https://doi.org/10.1103/PhysRev.50.263

Anghel, V., Armitage, J., Baig, F., Boniface, K., Boudjemline, K., Bueno, J., Charles, E., Drouin, P., Erlandson, A., Gallant, G., Gazit, R., Godin, D., Golovko, V. V, Thompson, M., & Waller, D. (2015). A plastic scintillator-based muon tomography system with an integrated muon spectrometer. *Nuclear Inst. and Methods in Physics Research, A*, *798*, 12–23.

Anghel, V., Armitage, J., Botte, J., Boudjemline, K., Bryman, D., Charles, E., Cousins, T., Erlandson, A., Gallant, G., Jewett, C., Jonkmans, G., Liu, Z., Noel, S., Oakham, G., Stocki, T. J., Thompson, M., & Waller, D. (2010). Cosmic Ray Muon Tomography System Using Drift Chambers for the Detection of Special Nuclear Materials. *IEEE NSS MIC*, 547–551.

Asaturyan, R., Ent, R., Fenker, H., Gaskell, D., Huber, G. M., Jones, M., & Mack, D. (2005). The aerogel threshold Cherenkov detector for the High Momentum Spectrometer in Hall C at Jefferson Lab. *Nuclear Inst. and Methods in Physics Research, A*, *548*, 364–374.

Autran, J. L., Munteanu, D., Saoud, T. S., & Moindjie, S. (2018). Characterization of atmospheric muons at sea level using a cosmic ray telescope. *Nuclear Inst. and Methods in Physics Research, A*, *903*(February), 77–84.

Ayachit, U., Ahrens, J., Bauer, A., Boeckel, B., Choudhary, A., Demarle, D., Geveci, B., Lipsa, D., Loring, B., Maxwell, T., Moreland, K., Nouanesengsy, B., Philip, S., Patchett, J., Pouderoux, J., Quammen, C., Shetty, N., Sherman, B., Waldon, S., … Jordan, S. (2019). *The ParaView Guide Community Edition v.5.6*.

Bae, J., & Chatzidakis, S. (2021). Fieldable Muon Momentum Measurement using Coupled Pressurized Gaseous Cherenkov Detectors. *Transactions of American Nuclear Society*, *125*(1), 400–403.

Bae, Junghyun, & Chatzidakis, S. (2021a). A Cosmic Ray Muon Spectrometer Using Pressurized Gaseous Cherenkov Radiators. *IEEE Nuclear Science Symposium and Medical Imaging Conference*.

Bae, Junghyun, & Chatzidakis, S. (2021b). The Effect of Cosmic Ray Muon Momentum Measurement for Monitoring Shielded Special Nuclear Materials. *INMM/ESARDA Joint Annual Meeting*.

Bae, Junghyun, & Chatzidakis, S. (2022a). A New Semi-Empirical Model for Cosmic Ray Muon Flux Estimation. *Progress of Theoretical and Experimental Physics*, *2022*(4).

Bae, Junghyun, & Chatzidakis, S. (2022b). Fieldable muon spectrometer using multi-layer pressurized gas Cherenkov radiators and its applications. *Scientific Reports*, *12*(2559). https://doi.org/https://doi.org/10.1038/s41598-022-06510-2

Bae, Junghyun, & Chatzidakis, S. (2022c). Momentum-Dependent Cosmic Ray Muon Computed Tomography Using a Fieldable Muon Spectrometer. *Energies*, *15*(2666). https://doi.org/10.3390/en15072666

Bae, Junghyun, & Chatzidakis, S. (2022d). Non-linear Cherenkov Muon Spectrometer Using Multi-Layer Pressurized C3F8 Gas Radiators. *Transactions of American Nuclear Society*.

Bae, Junghyun, Chatzidakis, S., & Bean, R. (2021). Effective Solid Angle Model and Monte Carlo Method: Improved Estimations to Measure Cosmic Muon Intensity at Sea Level in All Zenith Angles. *International Conference on Nuclear Engineering*.

Baesso, P., Cussans, D., Thomay, C., & Velthuis, J. (2014). Toward a RPC-based muon tomography system for cargo containers. *Journal of Instrumentation*, *9*. https://doi.org/10.1088/1748-0221/9/10/C10041

Bahmanabadi, M. (2019a). A method for determining the angular distribution of atmospheric muons using a cosmic ray telescope. *Nuclear Inst. and Methods in Physics Research, A*, *916*(November 2018), 1–7. https://doi.org/10.1016/j.nima.2018.11.010

Bahmanabadi, M. (2019b). A method for determining the angular distribution of atmospheric muons using a cosmic ray telescope. *Nuclear Inst. and Methods in Physics Research, A*, *916*, 1–7.

Baldetti, F., Cecchini, S., Giacomelli, G., Grianti, F., Mandrioli, G., Margiotta, A., & Patrizii, L. (1988). The MACRO detector at the Gran Sasso laboratory. *Nuclear Instrumnts and Methods in Physics Research*, *264*, 18–23.

Benettoni, M., Bettella, G., Bonomi, G., Calvagno, G., Calvini, P., Checchia, P., Cortelazzo, G., Cossutta, L., Donzella, A., Furlan, M., Gonella, F., Pegoraro, M., Rigoni Garola, A., Ronchese, P., Squarcia, S., Subieta, M., Vanini, S., Viesti, G., Zanuttigh, P., … Zumerle, G. (2013). Noise reduction in muon tomography for detecting high density objects. *Journal of Instrumentation*, *8*(12). https://doi.org/10.1088/1748-0221/8/12/P12007

Bengtson, B., & Moszynski, M. (1974). Energy-transfer and Light-collection Characteristics for Different Types of Plastic Scintillators. *Nuclear Instruments and Methods*, *117*, 227–232.

Bethe, H. A. (1953). Molière's Theory of Multiple Scattering. *Physics Review*, *89*(6), 1256–1266.

Birks, J. B. (1951). Scintillations from Organic Crystals: Specific Fluorescence and Relative Response to Different Radiations. *Proceedings of the Physical Society. Section A*, *64*, 874–877.

Biscossa, A., Cambiaghi, M., Conta, C., Ferrari, R., Fraternali, M., Freddi, A., Iuvino, G., Lanza, A., Livan, M., Negri, A., Polesello, G., Rimoldi, A., Vercellati, F., Vercesi, V., Bagnaia, P., Bini, C., Capradossi, G., Ciapetti, G., Dezorzi, G., … Zhao, T. (1998). Calypso : a full-scale MDT prototype for the ATLAS muon spectrometer. *Nuclear Instruments and Methods in Physics Research A*, *419*, 331–335.

Boezio, M., Bonvicini, V., Schiavon, P., Vacchi, A., & Zampa, N. (2003). Energy spectra of atmospheric muons measured with the CAPRICE98 balloon experiment. *PHYSICAL REVIEW D*, *6*, 1–15.

Bonneville, A., Kouzes, R. T., Yamaoka, J., Rowe, C., Guardincerri, E., Durham, J. M., Morris, C. L., Poulson, D. C., Plaud-Ramos, K., Morley, D. J., Bacon, J. D., Bynes, J., Cercillieux, J., Ketter, C., Le, K., Mostafanezhad, I., Varner, G., Flygare, J., & Lintereur, A. T. (2017). A novel muon detector for borehole density tomography. *Nuclear Inst. and Methods in Physics Research A*, *851*, 108–117.

Borozdin, K. N., Hogan, G. E., Morris, C., William, C., Saunders, A., & Schultz, L. J. (2003). Radiographic imaging with cosmic-ray muons. *Nature*, *422*(277), 20–22.

Burden, D. L., & Hieftje, G. M. (1998). Cerenkov Radiation as a UV and Visible Light Source for Time-Resolved Fluorescence. *American Chemical Society*, *70*(16), 3426–3433.

Campi, D., Curé, B., Gaddi, A., Gerwig, H., Hervé, A., Klyukhin, V., Maire, G., Perinic, G., Brédy, P., Fazilleau, P., Kircher, F., Levésy, B., Fabbricatore, P., Farinon, S., & Greco, M. (2007). Commissioning of the CMS Magnet. *IEEE Transactions on Applied Superconductivity*, *17*(2), 1185–1190.

CERN, & LHCC. (1997). *ATLAS muon spectrometer : Technical Design Report*.

Chatzidakis, S., Hausladen, P. A., Croft, S., Chapman, J. A., Jarrell, J. J., Scaglione, J. M., Choi, C. K., & Tsoukalas, L. H. (2017). Classification and Imaging of Spent Nuclear Fuel Dry Casks Using Cosmic Ray Muons. *Nuclear Plant Instrumentation, Control and Human-Machine Interface Technologies*, 237–245.

Chatzidakis, S., & Tsoukalas, L. H. (2016). *A Geant4-MATLAB Muon Generator for Monte-Carlo Simulations*. *September 2015*, 4–6. https://doi.org/10.13140/RG.2.2.31871.41128

Chatzidakis, S, Chrysikopoulou, S., Tsoukalas, L. H., & Carlo, M. (2015). Developing a cosmic ray muon sampling capability for muon tomography and monitoring applications. *Nuclear Inst. and Methods in Physics Research A*, *804*, 33–42.

Chatzidakis, Stylianos, Choi, C. K., & Tsoukalas, L. H. (2016). Analysis of Spent Nuclear Fuel Imaging Using Multiple Coulomb Scattering of Cosmic Muons. *IEEE Transactions on Nuclear Science*, *63*(6), 2866–2874.

Chatzidakis, Stylianos, Hausladen, P. A., Croft, S., Chapman, J. A., Jarrell, J. J., Scaglione, J. M., Choi, C. K., & Tsoukalas, L. H. (2017). Exploring the Use of Muon Momentum for Detection of Nuclear Material Within Shielded Spent Nuclear Fuel Dry Casks. *American Nuclear Society Annual Meeting*, *116*, 190–193.

Chatzidakis, Stylianos, Liu, Z., Hayward, J. P., & Scaglione, J. M. (2018). A generalized muon trajectory estimation algorithm with energy loss for application to muon tomography. *Journal of Applied Physics*, *123*. https://doi.org/10.1063/1.5024671

Chatzidakis, Stylianos, Liu, Z., Jarrell, J. J., Scaglione, J. M., & Hayward, J. P. (2017). Maximum-a-Posteriori Cosmic Ray Muon Trajectory Estimation with Energy Loss for Muon Tomography Applications. *IEEE Nuclear Science Symposium and Medical Imaging Conference*, 20–21.

Chatzidakis, Stylianos, & Tsoukalas, L. H. (2015). Monte Carlo Simulations of Cosmic Ray Muons for Dry Cask Monitoring. *American Nuclear Society Annual Meeting*, *112*, 534–536.

Cheng, H. M. and K. (2000). The Day-night Variation of Cosmic Rays Intensity at Sea Level under the Influence of Meteorological Fronts and Troughs. *10 Internat. Congress of IRPA*.

Cherenkov, P. A. (1934). Visible emission of clean liquids by action of gamma radiation. *Dokl. Akad. Nauk SSSR*, *2*(451).

CMS-Collaboration. (2010). Measurement of the charge asymmetry of atmospheric muons with the CMS detector. *CMS PAS MUO-10-001*.

Craun, R. L., & Smith, D. L. (1970). ANALYSIS OF RESPONSE DATA FOR SEVERAL ORGANIC SCINTILLATORS. *NUCLEAR INSTRUMENTS AND METHODS*, *80*, 239–244.

Davies, H., Bethe, H. A., & Maximon, L. C. (1954). Theory of Bremsstrahlung and Pair Production. II. Integral Cross Section for Pair Production. *PHYSICAL REVIEW*, *93*(4), 788–795.

Engelmann, J. J., Ferrando, P., Soutoul, A., Goret, P., Juliusson, E., Koch-Miramond, L., Lund, N., Masse, P., Peters, B., Petrou, N., & Rasmussen, I. L. (1990). Charge Composition and Energy Spectra of Cosmic-Ray Nuclei for Elements from Be to Ni - Results from HEAO-3-C2. *Astronomy and Astrophysics*, *223*, 96–111.

EPRI. (2010). Industry Spent Fuel Handbook. *Technical Report 1021048*.

Erlandson, A., Boniface, K., Anghel, V. N. P., Jonkmans, G., Thompson, M., & Livingstone, S. (2018). One-Sided Muon Tomography — A Portable Method for Imaging Critical Infrastructure with a Single Muon Detector. *CNL NUCLEAR REVIEW*, *7*(1), 1–9.

Frank, I. Tamm, I. (1937). Coherent visible radiation of fast electrons passing through matter. *Comptes Rendus (Dokl.) Academic Science*.

Geant4 Collaboration. (2017). *Physics Reference Manual (Release 10.4)*.

George, E. P. (1955). Cosmic rays measure overburden of tunnel. *Commonwealth Engineer*, *455*.

Ginzburg, V. L., & Frank, I. M. (1947). Radiation of an electron or atom moving along the axis of a channel in a dense medium. *Doklady Akademii Nauk SSSR*, *56*(7), 699–702.

Goudsmit, S., & Saunderson, J. L. (1940). Multiple Scattering of Electrons. *Physical Review*, *57*(6), 552. https://doi.org/10.1103/PhysRev.57.552.2

Graf, N., Lebedev, A., Abrams, R. J., Akgun, U., Aydin, G., Baker, W., Barnes, P. D., Bujak, A., Carey, D., Dukes, C., Duru, F., Feldman, G. J., Godley, A., Gustafson, H. R., Gutay, L., Hartouni, E., Hanlet, P., Hansen, S., Heffner, M., … Wu, K. (2010). Charged Kaon Mass Measurement using the Cherenkov Effect. *Nuclear Inst. and Methods in Physics Research, A*, *615*, 27–32.

Greis, J. R. (2017). *Multiple Coulomb Scattering of Muons in MICE*. University of Warwick.

Grieder, P. K. F. (2001). Cosmic Rays at Earth. In *Elsevier Science*. Elsevier Science.

Grupen, C., Hashim, N., Jost, B., Maciuc, F., Luitz, S., & Mailov, A. (2008). Cosmic Ray Results from the CosmoALEPH Experiment. *Nuclear Physics B*, *176*, 286–293. https://doi.org/10.1016/j.nuclphysbps.2007.11.014

Guardincerri, E., Rowe, C., Schultz-Fellenz, E., Roy, M., George, N., Morris, C., Bacon, J., Durham, M., Morley, D., Plaud-Ramos, K., Poulson, D., Baker, D., Bonneville, A., & Kouzes, R. (2017). 3D Cosmic Ray Muon Tomography from an Underground Tunnel. *Pure and Applied Geophysics*, *174*, 2133–2141.

Gustafsson, J. (2005). *Tomography of canisters for spent nuclear fuel using cosmic-ray muons*. Uppsala University.

Hagiwara, K., Hikasa, K., Nakamura, K., Tanabashi, M., & Aguilar-Benitez, M. (2002). Review of Particle Properties (Particle Data Group). *PHYSICAL REVIEW D*, *66*.

Harvey, A. H., Paulechka, E., & Egan, P. F. (2018). Candidates to replace R-12 as a radiator gas in Cherenkov detectors. *Nuclear Instruments and Methods in Physics Research, Section B:*, *425*, 38–42.

Hayes, D. J. (2018). *Cherenkov Detectors at Jefferson Lab*. College of William and Mary.

Hebecker, D., Archinger, M. G., Böser, S., Brostean-kaiser, J., Fösig, C., Karg, T., Köpke, L., Kowalski, M., Looft, A., & Sand, K. (2016). A Wavelength-shifting Optical Module (WOM) for in-ice neutrino detectors. *EPJ Web of Conferences*, 4–7.

Highland, V. L. (1975). Some Practical Remarks on Multiple Scattering. *Nuclear Instruments and Methods*, *129*, 497–499.

IAEA. (2001). *IAEA Safeguard Glossary* (Issue 3).

Iijima, T, Adachi, I., Dolenec, R., Petelin, A., Fujita, K., Goris, A., Kuratani, A., Mazuka, Y., Miyazawa, Y., Nishida, S., Kawai, H., Korpar, S., Kozakai, Y., & Kriz, P. (2008). Studies of a proximity focusing RICH with aerogel radiator for future Belle upgrade. *Nuclear Inst. and Methods in Physics Research, A*, *595*, 92–95. https://doi.org/10.1016/j.nima.2008.07.095

Iijima, Toru. (2010). Recent topics of particle identification and photodetection. *Nuclear Inst. and Methods in Physics Research, A*, *623*, 48–56. https://doi.org/10.1016/j.nima.2010.02.149

Inami, K. (2011). TOP counter prototype R&D. *Nuclear Inst. and Methods in Physics Research, A*, *639*(1), 298–301. https://doi.org/10.1016/j.nima.2010.09.138

Jelley, J. V. (1958). *Čerenkov Radiation and its Applications*.

Jelley, J. V. (1961). Čerenkov radiation: Its origin, properties and applications. *Contemporary Physics*, *3*(1), 45–57.

John David Jackson. (1962). *Classical Electrodynamics*. Wiley.

K. Nakamura et al. (2010). The Review of Particle Physics. *J. Phys*, *G 37*(075021).

Kamaev, O., Rand, E. T., Ende, B. M. Van Der, Thompson, M., Livingstone, S., & Golovko, V. V. (2019). Complementary non-destructive detection of nuclear materials with passive neutron and gamma-ray detectors, and a large-volume muon tomography system. *Nuclear Inst. and Methods in Physics Research, A*, *944*.

Kaptanoglu, T., Luo, M., & Kelin, J. (2019). Cherenkov and scintillation light separation using wavelength in LAB based liquid scintillator. *Journal of Instrumentation*, *14*.

Kate, H. H. J. (2006). The ATLAS Superconducting Magnet System : Status of Construction & Installation. *IEEE Transactions on Applied Superconductivity*, *16*(2), 499–503.

Knoll, G. F. (2010). *Radiation Detection and Measurement* (4th ed.). Wiley.

Kume, N., Miyadera, H., Morris, C. L., Bacon, J., Borozdin, K. N., Durham, J. M., Fuzita, K., Guardincerri, E., Izumi, M., Nakayama, K., Saltus, M., Sugita, T., Takakura, K., & Yoshioka, K. (2016). Muon trackers for imaging a nuclear reactor. *Journal of Instrumentation*, *11*(9). https://doi.org/10.1088/1748-0221/11/09/P09008

L. A. Kulchitsky, & Latyshev, G. D. (1942). The Multiple Scattering of Fast Eletrons. *PHYSICAL REVIEW*, *61*.

L'Annunziata, M. F. (2016). *Radioactivity*.

Landau, L., & Rumer, G. (1938). The Cascade Theory of Electronic Showers. *Proceedings of the Royal Society A*, *166*, 213–228. https://doi.org/https://doi.org/10.1098/rspa.1938.0088

Lesparre, N., Gibert, D., Marteau, J., Carbone, D., & Galichet, E. (2010). Geophysical muon imaging: feasibility and limits. *Geophysical Journal International*, *183*, 1348–1361.

Lewis, H. W. (1950). Multiple Scattering in an Infinite Medium. *Physical Review*, *78*(5), 526–529. https://doi.org/10.1103/PhysRev.78.526

Lippmann, C. (2012). Particle identification. *Nuclear Inst. and Methods in Physics Research, A*, *666*, 148–172. https://doi.org/10.1016/j.nima.2011.03.009

Litchfield, R. P. (2014). Status of the AlCap experiment. *Proceedings of Science*.

Liu, Z., Hayward, J., Liao, C., & Yang, H. (2017). Detection of Missing Assemblies and Estimation of the Scattering Densities in a VSC-24 Dry Storage Cask with Cosmic-Ray-Muon-Based Computed Tomography. *Journal of Nuclear Material Management*, *45*(12).

Lynch, G. R., & Dahl, O. I. (1991). Approximations to multiple Coulomb scattering. *Nuclear Instruments and Methods in Physics Research*, *58*(7991), 6–10.

Marteau, J., Gibert, D., Lesparre, N., Nicollin, F., Noli, P., & Giacoppo, F. (2012). Muons tomography applied to geosciences and volcanology. *Nuclear Inst. and Methods in Physics Research, A*, *695*, 23–28.

Meyer, M. A. (1961). MULTIPLE COULOMB SCATYERING FROM FINITE NUCLEI. *Nuclear Physics*, *28*, 512–518.

Molière, G. (1948). Theorie der Streuung schneller geladener Teilchen II Mehrfach-und Vielfachstreuung. *Zeitschrift Für Naturforschung A*, *3*(2), 78–97.

Morii, H., Mizouchi, K., Nomura, T., & Sasao, N. (2004). Quenching effects in nitrogen gas scintillation. *Nuclear Instruments and Methods in Physics Research A*, *526*, 399–408. https://doi.org/10.1016/j.nima.2004.02.015

Morishima, K., Kuno, M., Nishio, A., Kitagawa, N., Manabe, Y., Moto, M., Takasaki, F., Fujii, H., Satoh, K., Kodama, H., Hayashi, K., Odaka, S., Procureur, S., Attié, D., Bouteille, S., Calvet, D., Filosa, C., Magnier, P., Mandjavidze, I., … Guerriero, E. (2017). Discovery of a big void in Khufu's Pyramid by observation of cosmic-ray muons. *Nature*, *386–390*, 4–14.

Morris, C. L., Brown, E. N., Agee, C., Bernert, T., Bourke, M. A. M., Burkett, M. W., Buttler, W. T., Byler, D. D., Chen, C. F., Clarke, A. J., Cooley, J. C., Gibbs, P. J., Imhoff, S. D., Jones, R., Kwiatkowski, K., Mariam, F. G., Merrill, F. E., Murray, M. M., Olinger, C. T., … Zellner, M. B. (2016). New Developments in Proton Radiography at the Los Alamos Neutron Science Center (LANSCE). *Experimental Mechanics*, *56*(1), 111–120. https://doi.org/10.1007/s11340-015-0077-2

Morris, Christopher L, Bacon, J., Borozdin, K., Fabritius, J., Miyadera, H., Perry, J., & Sugita, T. (2014). Horizontal cosmic ray muon radiography for imaging nuclear threats. *Nuclear Instruments and Methods in Physics Research B*, *330*, 42–46.

Motoki, M., Sanuki, T., Orito, S., Abe, K., Anraku, K., & Asaoka, Y. (2003). Precise measurements of atmospheric muon fluxes with the BESS spectrometer. *Astroparticle Physics*, *19*, 113–126. https://doi.org/10.1016/S0927-6505(02)00195-0

Neddermeyer, S. H., & Anderson, C. D. (1937). Note on the Nature of Cosmic-Ray Particles. *Physical Review*, *51*(884). https://doi.org/10.1103/PhysRev.51.884

Neil, G. (1998). Thomas Jefferson National Accelerator Facility FEL Industrial Applications. *Joint Accelerator Conferences*, 88–92.

Nishiyama, R., Taketa, A., Miyamoto, S., & Kasahara, K. (2016). Monte Carlo simulation for background study of geophysical inspection with cosmic-ray muons. *Geophysical Journal International*, *206*(2), 1039–1050. https://doi.org/10.1093/gji/ggw191

P.A. Zyla et al. (2020). The Review of Particle Physics (2020). *Progress of Theoretical and Experimental Physics*, *8*.

Particle Data Group. (2020). *Atomic and Nuclear Properties of Materials for more than 350 materials*. https://pdg.lbl.gov/2020/AtomicNuclearProperties/index.html

Paschen, F. (1889). Ueber die zum Funkenübergang in Luft, Wasserstoff und Kohlensäure bei verschiedenen Drucken erforderliche Potentialdiffenrenz. *Annalen Der Physik*, *273*, 69–96.

Poulson, D., Bacon, J., Durham, M., Guardincerri, E., Morris, C. L., & Trellue, H. R. (2019). Application of muon tomography to fuel cask monitoring. *Philosophical Transactions of the Royal Society A: Mathematical, Physical and Engineering Sciences*, *377*(2137). https://doi.org/10.1098/rsta.2018.0052

Poulson, D., Durham, J. M., Guardincerri, E., Morris, C. L., Bacon, J. D., Morley, D., & Hecht, A. A. (2017). Cosmic ray muon computed tomography of spent nuclear fuel in dry storage casks. *Nuclear Inst. and Methods in Physics Research A*, *842*, 48–53.

Prince, J. L., & Links, J. M. (2006). *Medical Imaging Signals and Systems* (1st ed.). Pearson Education.

R. Donghia. (2017). The Mu2e experiment at Fermilab : Design and status. *IL NUOVO CIMENTO*, *40C*(176), 1–7.

R.L.Gluckstern. (1963). Uncertainties in track momentum and direction, due to multiple scattering and measurement errors. *Nuclear Instruments and Methods*, *24*, 381–389.

Ragoni, S. (2018). Production of pions, kaons and protons in Xe–Xe collisions at √sNN = 5.44 TeV. *Proceedings of Science*, *321*, 0–4.

Raizer, Y. P. (1991). *Gas Discharge Physics*. Springer.

Richter, M., Mclinden, M. O., & Lemmon, E. W. (2011). Thermodynamics Properties of 2,3,3,3-Tetrafluoroprop-1-ene (R1234yf): Vapor Pressure and p-p-T Measurement and an Equation of State. *Journal of Chemical and Engineering Data*, *56*, 3254–3264.

Rossi, Bruno and Greisen, K. (1941). Cosmi-Ray Theory. *Review of Modern Physics*, *13*.

Rossi, B. (1964). *Cosmic Rays*. McGraw-Hill Book Company.

Rossi, B. (1965). *High-energy particles*. Englewood Cliffs.

Rutherford, E. (1911). The Scattering of α and β Particles by Matter and the Structure of the Atom. *Philosophical Magazine and Journal of Science*, *21*(125).

Sakamoto, F., Iijima, H., DOBASHI, K., IMAI, T., UEDA, T., WATANABE, T., & UESAKA, M. (2005). Emittance and Energy Measurements of Low- Energy Electron Beam Using Optical Transition Radiation Techniques. *Japanese Journal of Applied Physics*, *44*(3), 1485–1491.

Salvucci, A. (2011). Measurement of muon momentum resolution of the ATLAS detector. *Hadron Collider Physics Symposium*.

Sato, T. (2015). Analytical Model for Estimating Terrestrial Cosmic Ray Fluxes Nearly Anytime and Anywhere in the World : Extension of PARMA/EXPACS. *PLoS ONE*, *10*(12), 1–33.

Sato, T. (2016). Analytical model for estimating the zenith angle dependence of terrestrial cosmic ray fluxes. *PLoS ONE*, *11*(8), 1–22.

Schouten, D. (2018). Muon geotomography : selected case studies. *Philosophical Transactions A*, *377*.

Schultz, L J, Borozdin, K. N., Gomez, J. J., Hogan, G. E., & Mcgill, J. A. (2004). Image reconstruction and material Z discrimination via cosmic ray muon radiography. *Nuclear Instruments and Methods in Physics Research A*, *519*, 687–694.

Schultz, Larry J. (2003). Cosmic Ray Muon Radiography. In *Portland State University*.

Schultz, Larry J, Blanpied, G. S., Borozdin, K. N., Fraser, A. M., Member, S., Hengartner, N. W., Klimenko, A. V, Morris, C. L., Orum, C., & Sossong, M. J. (2007). Statistical Reconstruction for Cosmic Ray Muon Tomography. *IEEE Transactions on Image Processing*, *16*(8), 1985–1993.

SensL. (2011). *An Introduction to the Silicon Photomultiplier*.

Smith, J. A., & Duller, N. M. (1959). Effects of pi meson decay-absorption phenomena on the high-energy mu meson zenithal variation near sea level. *Journal of Geophysical Research*, *64*(12), 2297–2305.

Sowerby, B. D. (1971). Cerenkov Detectors for Low-Energy Gamma Rays. *Nuclear Intruments and Methods*, *97*, 145–149.

Srinivasan, R., Sisley, S. E., & Hopf, J. E. (2004). Transporting Existing VSC-24 Canisters Using a Risk-Based Licensing Approach. *14th International Symposium on the Packaging and Transportation of Radioactive Materials*, *116*.

Stewart, A., Sullivan-greene, E. O., & Saveliev, V. (2006). Study of the Properties of New SPM Detectors. *Proceedings of SPIE*, *61190*. https://doi.org/10.1117/12.645649

Stowell, P., Fargher, S., Steer, C., & Thompson, L. F. (2021). Scintillating thermal neutron detectors for cosmic ray soil moisture monitoring. *Journal of Instrumentation*, *16*(11). https://doi.org/10.1088/1748-0221/16/11/P11039

T. K. Gaisser et al. (2016). *Cosmic rays and particle physics*. Cambridge University Press.

Tanaka, H. K. M., Nagamine, K., Nakamura, S. N., & Ishida, K. (2005). Radiographic measurements of the internal structure of Mt . West Iwate with near-horizontal cosmic-ray muons and future developments. *Nuclear Instruments and Methods in Physics Research A*, *555*, 164–172.

Tsai, Y. (1974). Pair production and bremsstrahlung of charged leptons. *Review of Modern Physics*, *46*(4), 815–851.

U.S.NRC. (2021). Standards for Protection Against Radiation. *Regulations 10 CFR Part 20*.

Vanini, S., Calvini, P., Checchia, P., Rigoni, A., Klinger, J., Zumerle, G., Bonomi, G., Donzella, A., & Zenoni, A. (2018). Muography of different structures using muon scattering and absorption algorithms. *Philosophical Transactions of the Royal Society A*, *377*.

Wadaa, T., Miyaib, H., Tuji, S., Yamamotoc, I., & Saitod, K. (1996). An altazimuthal counter telescope with a magnet spectrometer tracing Cygnus X-3. *Nuclear Instruments and Methods in Physics Research A*, *374*, 245–253.

Wang, G., Schultz, L. J., Qi, J., & Member, S. (2009). Bayesian Image Reconstruction for Improving Detection Performance of Muon Tomography. *IEEE Transactions on Image Processing*, *18*, 1080–1089.

Wentzel, G. (1926). Zwei Bemerkungen uber die Zerstreuung korpuskularer Strahlen als Beugungserscheinung. *Zeitschrift F□ur Physik*, *40*(8), 590–593.

Wilkinson, F. (2004). *Emission Tomography*.

Yang, G., Clarkson, T., Gardner, S., Ireland, D., Kaiser, R., Mahon, D., Jebali, R. Al, Shearer, C., & Ryan, M. (2019). Novel muon imaging techniques. *Philosophical Transactions of the Royal Society A: Mathematical, Physical and Engineering Sciences*, *377*(2137). https://doi.org/10.1098/rsta.2018.0062

Yukawa, H. (1935). On the Interaction of Elementary Particles. *Progress of Theoretical Physics*, *17*(48). https://doi.org/10.1143/ptps.1.24

VITA

Education

Doctor of Philosophy, Nuclear Engineering — Anticipated May 2022
Purdue University, West Lafayette, Indiana
Dissertation Topic: A Novel Muon Spectrometer Using Multi-Layer Pressurized Gas Cherenkov Radiators for Muon Tomography
Advisor: Prof. Stylianos Chatzidakis

Master of Science, Nuclear Engineering — May 2016
University of California, Berkeley, California
Thesis Title: Offshore Co-generation of Electricity and Desalinated Water: Floating Fluoride-Salt-Cooled High-Temperature Reactors (FHR)
Advisor: Prof. Per Peterson

Bachelor of Science in Nuclear and Quantum Engineering — May 2015
Korea Advanced Institute of Science and Technology (KAIST), Republic of Korea
Thesis Title: Optimization of Signal to Noise Ratio by Analyzing Gamma Spectrum from PIN diode
Advisors: Prof. Mansung Yim and Prof. Gyuseong Cho

Experience

Graduate Research Assistant — Aug 2020 – Present
Development of a high-resolution muon spectrometer using multi-layer pressurized gas Cherenkov radiators.

- Underground research laboratory muon detector project (collaboration with ORNL and PNNL)
- Algorithm development: momentum integrated PoCA algorithm for muon scattering tomography
- Effective solid angle model for cosmic ray muons flux estimation

Graduate Teaching Assistant — Jan 2019 – May 2020

- Nuclear Engineering Radiation Experiment I (NUCL 205)
- Nuclear Engineering Radiation Experiment II (NUCL 305)
- Advanced Nuclear Engineering Radiation Experiment (NUCL 504: Graduate level)

Graduate Research Assistant — Aug 2017 – Jan 2019

- Investigation of the thermohydraulic limits of PUR-1 reactor which is LEU plate-fueled, pool type, and cooled by natural circulation using CFD
- Computational Fluid Dynamics (CFD) analysis of thermohydraulic performances within spent nuclear fuel (SNF) dry casks with additives.

Military Service — Nov 2010 – Sep 2012

- Bravo Battery, 6-52 Air Defense Artillery, 35th Brigade, 8th United States Army
- Served as KATUSA sergeant in the CBRN (Chemical, Bacteriological, Radiological and Nuclear) Defense Unit

Skills

[1] Monte-Carlo particle transport simulation codes

- GEANT4 | MCNP

[2] Data Acquisition, Analysis, and Visualization

- ROOT | QT | R | Origin | ParaView

[3] Multiphysics, CFD, Thermohydraulic Simulation

- COMSOL-Multiphysics | ANSYS-FLUENT | RELAP5-3D

[4] Programming

- C/C++ | MATLAB | Python

Invited Activities

Invited to present in the GEN IV International Forum (GIF) July 2022

Invited reviewer for peer-reviewed journal (Nuclear Science and Engineering) April 2022 – Present

Invited reviewer for peer-reviewed journal (AIP Advances) Aug 2021 – Present

Invited article for *Energies*: Momentum-Dependent Cosmic Ray Muon Computed Tomography Using a Fieldable Muon Spectrometer

Scholarships, Awards, and Honors

- American Physical Society Braslau Family Travel Grant Mar 2022
- Best Presentation Award, US-Korea Conference on Science and Technology Dec 2021
- Winner of "Pitch your PhD" competition in the 2021 ANS Winter meeting Dec 2021
- Best Paper Award, 28th International Conference on Nuclear Engineering Sept 2021
- Conference Travel Fund from the College of Engineering, Purdue University Aug 2021
- IEEE Nuclear Science Symposium and Medical Imaging Conference Trainee Grant July 2021
- Purdue Graduate School CARES scholarship July 2021
- Korean-American Science and Engineering Association (KSEA) Scholarship April 2021
- Purdue University College of Engineering Magoon Excellence in Teaching Award Mar 2021
- Purdue Outstanding Graduate Scholarship Mar 2021
- American Nuclear Society (ANS) Outstanding Graduate Scholarship Aug 2020
- Roy G. Post Foundation Scholarship Mar 2020
- Prof. Audeen Fentiman Award for Conference June 2018
- Full-years Korean government national scholarships 2013 – 2015

Oral Presentations

[INVITED] J. Bae, "A High-Resolution Muon Spectrometer Using Multi-Layer Gas Cherenkov Radiators", GEN IV International Forum, July 2022, Online.

J. Bae and S. Chatzidakis, "A High-Resolution Muon Spectrometer Using Multi-Layer Gas Cherenkov Radiators", American Physical Society (APS) March Meeting, March 2022, Chicago, IL, USA.

J. Bae and S. Chatzidakis, "Applied Gas Cherenkov Radiators to Measure Cosmic Ray Muon Momentum", United States and Korea Conference, December 2021, Anaheim, CA, USA.

J. Bae and S. Chatzidakis, "Fieldable Muon Momentum Measurement using Coupled Pressurized Gaseous Cherenkov Detectors", American Nuclear Society (ANS) Winter Meeting, December 2021, Washington D.C., USA.

J. Bae and S. Chatzidakis, "A Cosmic Ray Muon Spectrometer Using Pressurized Gaseous Cherenkov Radiators", IEEE Nuclear Science Symposium and Medical Imaging Conference (NSS-MIC), October 2021, Online.

J. Bae and S. Chatzidakis, "The Effect of Cosmic Ray Muon Momentum Measurement for Monitoring Shielded Special Nuclear Materials", Institute of Nuclear Material Management (INMM) Annual Meeting, August 2021, Online.

J. Bae, S. Chatzidakis, and R. Bean, "Effective Solid Angle Model and Monte Carlo Method: Improved Estimations to Measure Cosmic Muon Intensity at Sea Level in All Zenith Angles", International Conference on Nuclear Engineering (ICONE) 28, August 2021, Online.

J. Bae, R. Bean, and R. Abboud, "A Critical and CFD Analysis of a Dry Storage Cask with Advanced Spent Nuclear Fuel Cask Additives", Waste Management Symposium (WMS), March 2020, Phoenix, AZ, USA.

J. Bae and R. Bean, "Analytical Methods in Safeguards for Nuclear Nonproliferation and Complete, Verifiable, Irreversible Denuclearization (CVID) of North Korea", Institute of Nuclear Material Management (INMM) Annual Meeting, July 2019, Palm Desert, CA, USA.

J. Bae, R. Bean, and R. Abboud, "A Criticality Analysis of a Dry Storage Cask with Advanced Nuclear Fuel Cask Additive", American Nuclear Society (ANS) Annual Meeting, June 2018, Philadelphia, PA, USA.

PUBLICATIONS

[1] **J. Bae** and S. Chatzidakis, "Momentum-Dependent Cosmic Ray Muon Computed Tomography using a Fieldable Muon Spectrometer", Energies, **15** (7), 2666 (2022).

[2] **J. Bae** and S. Chatzidakis, "Fieldable Muon Spectrometer Using Multi-Layer Pressurized Gas Cherenkov Radiators and Its Applications", Scientific Reports, **12,** 2559 (2022).

[3] **J. Bae** and S. Chatzidakis, "A New Semi-Empirical Model for Cosmic Ray Muon Flux Estimation", Progress of Theoretical and Experimental Physics, **2022,** 4 (2022).

[4] **J. Bae** and R. Bean, "Investigation of Thermohydraulic Limits on Maximum Reactor Power in LEU Plate-Fueled, Pool Type Research Reactor", Nuc. Sci. Eng. (2022).

[5] **J. Bae**, R. Bean, and R. Abboud, "CFD Analysis of Dry Storage Cask with Advanced Spent Nuclear Fuel Cask Additives", Annals of Nuclear Energy, **145** (2020).

[6] **J. Bae** and S. Chatzidakis, "A Compact High-Resolution Muon Spectrometer Using Multi-Layer Gas Cherenkov Radiators", Under Review (2022).

[7] **J. Bae** and S. Chatzidakis, "Momentum Integrated PoCA Algorithm for Muon Scattering Tomography", Under Review (2022).

[8] **J. Bae** and S. Chatzidakis, "Cosmic Muon Momentum Measurement Using the Multiple Pressurized Gaseous Cherenkov Detectors", IEEE NSS-MIC Conf. Records (2021).

[9] **J. Bae** and S. Chatzidakis, "Fieldable Muon Momentum Measurement using Coupled Pressurized Gaseous Cherenkov Detectors", Trans. Am. Nuc. Soc. **125** (1), 400-403 (2021).

[10] **J. Bae** and S. Chatzidakis, "The Effect of Cosmic Ray Muon Momentum Measurement for Monitoring Shielded Special Nuclear Materials", INMM proceedings, (2021).

[11] **J. Bae**, S. Chatzidakis, R. Bean, "Effective Solid Angle Model and Monte Carlo Method: Improved Estimations to Measure Cosmic Muon Intensity at Sea Level in All Zenith Angles", ICONE28 proceedings, **4** (2021).

[12] **J. Bae** and R. Bean, "Analytical Methods in Safeguards for Nuclear Nonproliferation and Complete, Verifiable, Irreversible Denuclearization (CVID) of North Korea", INMM proceedings (2019).

[13] **J. Bae**, R. Bean, and R. Abboud, "A Criticality Analysis of a Dry Storage Cask with Advanced Nuclear Fuel Cask Additive", Trans. Am. Nuc. Soc. **118**, 147-150 (2018).

[14] A. Anwar, **J. Bae**, S. Chatzidakis, "Study of Neutron Detectors for Virtual Labs in Nuclear Engineering", ANS Student Conference (2022)

[15] A. Anwar, Z. Dahm, **J. Bae**, S. Chatzidakis, M. Sharpe, X. Zhou, G. Takahashi, "Developing High Fidelity, Real-Time Nuclear-Based Virtual Laboratories Using Physics-Based Modeling and Authentic 3d Machine Interfaces", NESTed proceedings (2021).